

Final Report on NASA contract NAS8-36169

Determination of Atmospheric Moisture Structure and Infrared Cooling  
Rates from High Resolution MAMS Radiance Data

for the period of  
7 November 1986 to 18 September 1991

submitted by

W. Paul Menzel

Christopher C. Moeller

William L. Smith

Cooperative Institute for Meteorological Satellite Studies (CIMSS)

University of Wisconsin

1225 West Dayton Street

Madison, Wisconsin 53706

December 1991

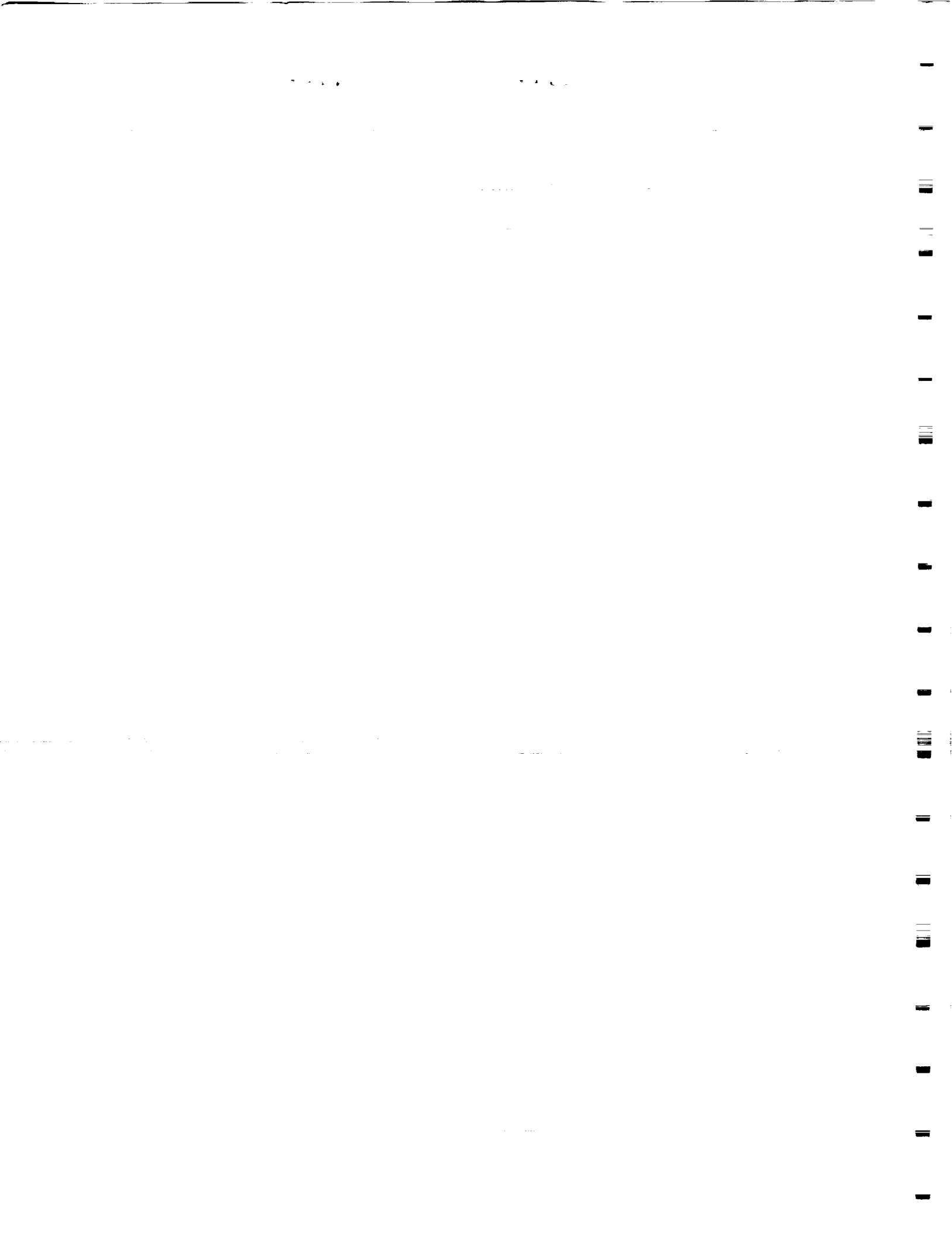
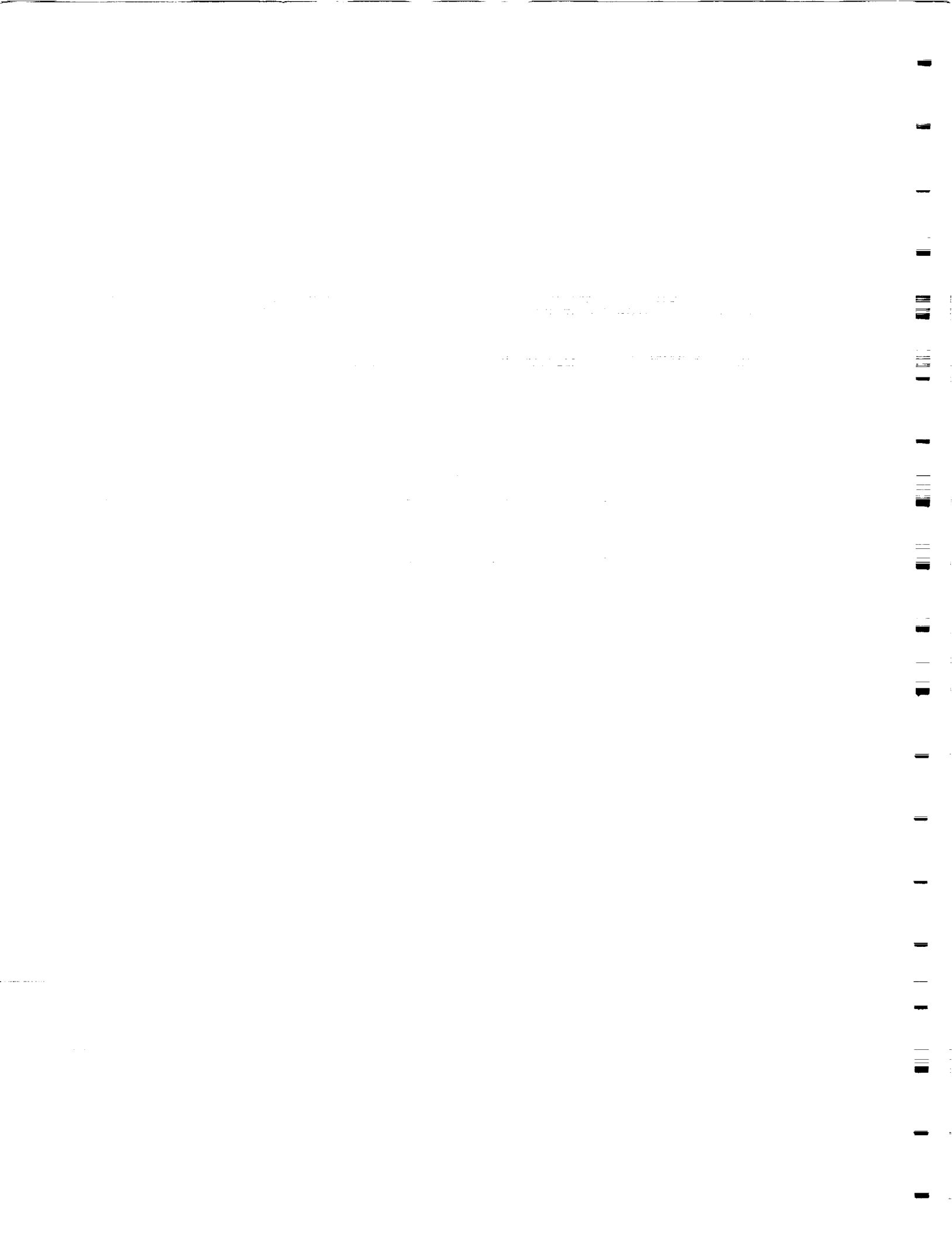


## Table of Contents

I.	INTRODUCTION	1	
II.	RESEARCH ACCOMPLISHMENTS	2	
	A.	COHMEX Data Collection	2
	B.	HIS Research Results	2
		1. HIS/FASCODE Comparisons	2
		2. HIS Retrievals	3
	C.	MAMS Research Results	4
		1. MAMS Instrument Improvements and Data Comparisons	4
		2. COHMEX Data Archive	5
		3. MAMS/VAS Retrieval Products	5
		4. MAMS/VAS Fluxes	7
		5. MAMS/VAS Cloud Clearing Activities	9
III.	LIST OF PUBLICATIONS RESULTING FROM NAS8-36169	10	
IV.	REFERENCES	13	
	APPENDIX A - NASA SUPPORTED PUBLICATIONS	15	



## I. INTRODUCTION

With the advancement of remote sensing from space as a tool for monitoring the earth's atmosphere and surface, new and better information is constantly becoming available for investigating meteorological processes and their spatial and temporal scales of preference in the earth-atmosphere system. Much information has been gained in understanding synoptic and mesoscale variability; the Multispectral Atmospheric Mapping Sensor (MAMS) is contributing to this understanding by looking at very small mesoscale (meso  $\gamma$ : 2-20 km) horizontal variability in the atmosphere and at the earth's surface. The High-resolution Interferometer Sounder (HIS) is contributing by producing high vertical resolution profiles of atmospheric temperature and moisture. These two research instruments, flown on NASA U2 and ER2 high altitude aircraft, are helping to identify advantageous design and deployment characteristics for future operational satellite programs.

This program has applied MAMS high resolution data to the problem of monitoring atmospheric quantities of moisture and radiative flux at small spatial scales. MAMS, with 100m horizontal resolution in its four infrared channels, was developed to study small scale atmospheric moisture and surface thermal variability, especially as related to the development of clouds, precipitation, and severe storms. HIS data has been used to develop a high spectral resolution infrared sounding retrieval algorithm for producing high resolution vertical profiles of atmospheric temperature and moisture. The results of this program are that high spectral resolution soundings significantly improve the vertical resolution of atmospheric profiles, and that high spatial

resolution data shows small horizontal scale variability is clearly present in the atmosphere and on the surface.

## II. RESEARCH ACCOMPLISHMENTS

### A. COHMEX Data collection

MAMS and HIS were flown on NASA U2 and ER2 aircraft during the COoperative Huntsville Meteorological EXperiment (COHMEX) (Williams et al. 1987). A listing of the flights is shown in Table 1. Funding from the contract was used to support science teams for the HIS and MAMS, as well as instrument field teams for the HIS during COHMEX. Science support teams contributed to the experiment through flight go/no-go decision-making based on the objectives of the field experiment, and by specifying flight patterns and locations for MAMS and HIS data collection as well as coordinating data collection activities among the many data sources available during COHMEX. The data collected during COHMEX was the primary source of data for scientific studies under this contract.

### B. HIS Research Results

#### 1. HIS/FASCODE Comparisons

Comparisons of HIS spectra to FASCOD2 (Clough et al. 1986) spectra have been under intense study. In general, it is concluded that HIS and FASCODE agree remarkably well, a tribute to the current state of spectral line files and line-by-line code. However, several discrepancies have been identified and are reported in Revercomb et al. 1990. A copy of this paper is included in Appendix A.

## 2. HIS Retrievals

A significant effort has been made to develop efficient retrieval algorithms for producing atmospheric profiles of temperature and moisture using HIS spectra. Atmospheric profiles for COHMEX days of June 15 and June 19, 1986 have been produced. These days were chosen because good quality HIS data of contrasting atmospheric conditions (boundary layer cumulus development on June 15; clear conditions on June 19) was available. Statistics of HIS atmospheric profiles, along with comparisons to simulated atmospheric profiles (from HIS spectra) for the HIRS and GOES I/M instruments are given in Huang et al. (submitted). In this work, it is shown that the HIS atmospheric profiles are approximately five times better in vertical resolution and two times better in accuracy than HIRS and GOES I/M atmospheric profiles. The retrieval methodology is also transferable to the retrieval of atmospheric trace gas concentrations. Future EOS infrared sounder data has also been simulated and studied using HIS spectra (Huang et al. 1991). Efforts to improve the retrieval methodology are ongoing.

Table 1. Listing of MAMS and HIS flights during COHMEX.

<u>Date</u>	<u>location</u>	<u>MAMS?</u>	<u>HIS?</u>	<u>Comments</u>
6-15-86	COHMEX	Y	Y	both on U2
6-17-86	Local ocean		Y	
6-18-86	COHMEX	Y		
6-19-86	COHMEX	Y	Y	repeat coverage
6-20-86	Chesapeake		Y	Tstorms
6-23-86	COHMEX		Y	Tstorms
6-26-86	COHMEX	Y	Y	repeat coverage
6-29-86	Atlantic		Y	Ocean buoys
7-1-86			Y	test hop
7-3-86	COHMEX	Y	Y	both on U2
7-4-86	Chesapeake		Y	TMS mission
7-05-86	Atlantic	Y	Y	both on U2
7-08-86	COHMEX	Y	Y	both on ER2
7-11-86	COHMEX	Y	Y	both on ER2
7-12-86	COHMEX	Y	Y	both on ER2
7-14-86	COHMEX		Y	night flight
7-15-86	Lake Oneida		Y	
7-17-86	COHMEX		Y	aborted
7-20-86	COHMEX	Y	Y	both on ER2
7-21-86	East coast	Y	Y	ocean buoys

### C. MAMS Research Results

#### 1. MAMS Instrument Improvements and Data Comparisons

Improvements to the radiometric performance have been made during the life of this contract. These include the use of a full axe blade mirror, 10 bit digitization, and improved external blackbody sampling. While hardware improvements were not funded by the contract, tests of MAMS data quality following hardware and procedural improvements were conducted. Science efforts under this contract benefitted through improved data quality. Comparisons to VAS, AVHRR, and HIS radiometric data were made. These improvements and the impact they have had on the data quality, as well as instrument intercomparisons are discussed in NASA Tech Memo 100352, which was produced in part under this contract.

## 2. COHMEX Data Archive

Data from six selected MAMS COHMEX flights were archived at the Cooperative Institute for Meteorological Satellite Studies (CIMSS) at the University of Wisconsin. The archive procedure consisted of breaking the data up into separate straight line flight tracks, fixing identifiable data errors in housekeeping (calibration, time, etc.) and video (missing lines) data, and attaching earth location information to the data ("navigating" the data). This saved considerable data processing during subsequent use of the data. Table 2 lists the MAMS archived data.

---

Table 2. MAMS COHMEX archived tape inventory.

<u>Tape</u>	<u>Date</u>	<u>Location</u>	<u>Comments</u>
MC136	6/15/86	COHMEX	popcorn cumulus
MC138	6/18/86	COHMEX	high pressure overhead
MC140	6/19/86	COHMEX	developing cumulus
MC147	6/26/86	COHMEX	mature Tstorm
MC155	7/03/86	COHMEX	synthetic navigation
MC159	7/05/86	ATLANTIC	many missing lines

---

## 3. MAMS/VAS Retrieval Products

Mesoscale atmospheric variability was investigated by making 100 meter resolution atmospheric temperature and moisture profiles using MAMS and geostationary satellite borne VISSR Atmospheric Sounder (VAS) data. MAMS and VAS data collected during COHMEX (June 19, 1986) were combined in a retrieval algorithm that allowed the high resolution MAMS data to be substituted for similar VAS spectral channels. VAS CO<sub>2</sub> sounding channels not contained on MAMS provided most of the vertical resolution in the profiles, while the MAMS data, with its 100 meter

resolution, provided the horizontal resolution. MAMS/VAS derived image products of skin temperature, precipitable water (atmospheric moisture), and lifted index (atmospheric stability) were made from the retrievals. The imagery showed several interesting features. In particular, a tongue of low level moist air pushing into the COHMEX region from the south was captured in the precipitable water product. This feature was also observed in the COHMEX radiosonde network, however not with the definition provided by the 100 meter resolution MAMS/VAS moisture product. Interestingly, an area of low level cumulus formed in the moist tongue region within a few hours of the imagery. The MAMS/VAS lifted index product showed a bias towards unstable values when compared to the COHMEX radiosondes, as has been seen previously with VAS lifted index products. The skin temperature product showed a definite heat island in the urban land-use region of Nashville, TN.

Meso  $\beta$  (20-200 km) and meso  $\gamma$  (2-20 km) scale gradients in the MAMS/VAS moisture, stability, and surface skin temperature products were evaluated using a structure function analysis. Among the significant findings of this analysis, the meso  $\gamma$  scale moisture and skin temperature gradients clearly exceeded the strength of the Meso  $\beta$  scale gradients. This is important information for investigations of mesoscale meteorological events. Meso  $\gamma$  scale stability gradients were marginally stronger than the Meso  $\beta$  scale gradients. However, this may only have occurred because the VAS data (with its much coarser 8 km horizontal resolution) influences the stability product more than the other products. Also, for all the products, detectable gradient information was found at resolutions down to 300 meters, the smallest resolution at which the gradients were evaluated. These results, while

from only a single case study, indicate that significant atmospheric variability exists at very small scales. The importance of this variability to small scale meteorological phenomena has not been thoroughly assessed. Further investigations into mesoscale atmospheric gradients are warranted by these findings.

A comparison of the MAMS/VAS moisture gradients was made to gradients of VAS-only atmospheric moisture data. It was found that the VAS-only gradients were significantly weaker, especially for meso  $\gamma$  and smaller meso  $\beta$  scales (<50 km). This indicates that significant atmospheric moisture gradient information is being missed in operational practice by the VAS instrument and suggests a need for an improved resolution operational sounding instrument in geostationary orbit. A paper has been submitted to the Int. Journal of Remote Sensing on this topic; a copy is included in the appendix of this report.

#### 4. MAMS/VAS Fluxes

Atmospheric radiative fluxes were studied by producing 100 meter resolution MAMS/VAS net fluxes at 1000 mb, 700 mb, and 300 mb. Regression coefficients from previously developed relationships between VAS data and simulated radiation fluxes were applied, using VAS data with MAMS spectral channels substituted for similar VAS spectral channels as predictors. A repeat overpass of MAMS data collected over COHMEX on June 19, 1986 was used. Results showed that 1000 mb and 700 mb net fluxes were highly related demonstrating a strong influence of surface temperature on the net flux at these levels. The 300 mb net flux was smoother than the 700 mb or 1000 mb net fluxes, demonstrating the effect of atmospheric absorption. Cooling rates from the net flux

data showed very little variation in the 1000 - 700 mb layer, reflecting the high correlation between the 1000 mb and 700 mb net fluxes. Cooling rates for the 700 - 300 mb layer were more variant. Also, midday net fluxes at 1000 mb and 700 mb decreased with time in the eastern third of the flight track. This agreed with the location of a moist tongue being advected into the COHMEX region (described above) and also with the development of the low level cumulus field. Net fluxes at 1000 mb and 700 mb increased with time in the western two-thirds of the flight track. Simulations showed that a decrease of net flux at a level can result from increased moisture below the level; an increase in net flux can be caused by decreasing moisture below the level.

A shortcoming of the radiation net flux effort was its inability to produce reasonable fluxes over small low level cumulus clouds. This occurred because the 8 km resolution of VAS channel 5, which is susceptible to low level cloudiness, was insufficient to resolve individual cumulus clouds. Other VAS channels affected by the low level clouds were replaceable by MAMS data. This points out the importance of high resolution data for quantitative analysis in and around cloudy fields of view.

The net flux products (and cooling rates) in this effort combine information available separately in satellite temperature and moisture products. The net flux product however represents a different way of packaging this information which may be useful to radiative budget studies of the earth-atmosphere system and modelling efforts which attempt to assimilate radiative data. Using the radiometric data directly in a regression algorithm, instead of producing atmospheric

temperature and moisture profiles from the radiometric data and then computing fluxes, saved considerable computation time.

#### 5. MAMS/VAS Cloud Clearing Activities

MAMS COHMEX data was used to investigate the effect of low level clouds on VAS retrievals. MAMS data from June 15, 1986 was used. On this day the COHMEX region was covered by an extensive low level scattered to broken cumulus cloud field. MAMS  $11\mu\text{m}$  and  $12\mu\text{m}$  "cloud cleared" radiances were used to replace cloud contaminated VAS  $11\mu\text{m}$  and  $12\mu\text{m}$  radiances. MAMS data was "cloud cleared" by applying brightness temperature thresholds to the MAMS data, which can see between the clouds with its high resolution. The non-cloudy MAMS fields of view were then averaged to simulate the VAS field of view. MAMS averaged non-cloudy field of view temperatures were 1 - 3 K warmer than the VAS cloud contaminated data. Cloud contaminated retrievals were compared to "cloud cleared" retrievals. The impact of cloud clearing the  $11\mu\text{m}$  and  $12\mu\text{m}$  data was most evident in the moisture profile. Temperature profile modification was generally negligible. The moisture profile showed a general 5% increase in moisture in the lowest 300 - 500 mb (about 1 - 2mm of total column precipitable water). While the response of the moisture profiles to the cloud clearing is encouraging, a lack of vertical resolving power in the lower atmosphere in the retrievals limited the potential impact. Temperature and moisture profile impact would likely be increased if the VAS  $13.3\mu\text{m}$  data (VAS channel 5) were cloud cleared by a similar MAMS channel (MAMS currently does not have a  $13.3\mu\text{m}$  channel). This channel is an important contributor to the low level temperature profile but is sensitive to low level cloud

contamination. The impact of unresolved cloud on sounding data from instruments carrying more lower atmospheric sounding channels than VAS may be significantly greater, increasing the need to use high spatial resolution data for atmospheric sounding.

### III. LIST OF PUBLICATIONS RESULTING FROM NAS8-36169

Huang, H.-L., W. L. Smith, and H. M. Woolf, 1992: Vertical resolution and accuracy of atmospheric infrared sounding spectrometers.

Accepted for publication in J. Applied Met., Feb 1992.\*

Huang, H.-L., W. L. Smith, H. M. Woolf, and J. M. Theriault, 1991:

Theoretical computation of trace gases retrieval random error from measurements of high spectral resolution infrared sounder. Digest of Topical Meeting on Optical Remote Sensing of the Atmosphere, November 18-21, 1991, Williamsburg, VA, Optical Society of America, Washington, DC, Vol 18, 48-50.\*

Jedlovec, G. J., K. B. Batson, R. J. Atkinson, C. C. Moeller, W. P.

Menzel, and M. W. James, 1989: Improved capabilities of the Multispectral Atmospheric Mapping Sensor (MAMS). NASA Technical Memorandum 100352, Marshall Space Flight Center, Huntsville, AL, 71pp.

Jedlovec, G. J., W. P. Menzel, R. J. Atkinson, G. S. Wilson, and J.

Arveson, 1986a: The Multispectral Atmospheric Mapping Sensor (MAMS): Instrument description, calibration, and data quality. NASA Technical Memorandum 86565, Marshall Space Flight Center, Huntsville, Alabama. 37pp.

Jedlovec, G. J., W. P. Menzel, G. S. Wilson, and R. J. Atkinson, 1986b:

Detection of mountain induced mesoscale wave structures with high

resolution moisture imagery. **Second Conference on Satellite Meteorology/Remote Sensing and Applications**, May 13-16, 1986, Williamsburg, VA, AMS, Boston, 365-369.\*

Menzel, W. P., G. J. Jedlovec, and G. S. Wilson, 1986: Verification of small scale features in VAS imagery using high resolution MAMS imagery. **Second Conference on Satellite Meteorology/Remote Sensing and Applications**, AMS, Boston, MA, 108-111.\*

Moeller, C. C., W. P. Menzel, and K. I. Strabala, 1991: High resolution depiction of atmospheric and surface variation from combined MAMS and VAS radiances. Submitted to Int. J. Remote Sensing (in review).\*

Moeller C. C., W. P. Menzel, and K. I. Strabala, 1990: High resolution atmospheric and surface variability from combined MAMS and VAS radiances. **Digest of Topical Meeting on Optical Remote Sensing of the Atmosphere**, Feb. 12-15, 1990, Incline Village, NV, Optical Society of America, Washington, DC, Vol 4, 92-95.\*

Revercomb, H. E., R. O. Knuteson, W. L. Smith, H. M. Woolf, and H. B. Howell, 1990: Spectroscopic inference from HIS measurements of atmospheric thermal emission. **Digest of Topical Meeting on Optical Remote Sensing of the Atmosphere**, Feb. 12-15, 1990, Incline Village, NV, Optical Society of America, Washington, DC, Vol 4, 590-593.\*

Revercomb, H. E., H. Buijs, H. B. Howell, D. D. Laporte, W. L. Smith, and L. A. Sromovsky, 1988: Radiometric calibration of IR Fourier transform spectrometers : solution to a problem with the High-resolution Interferometer Sounder (HIS). Appl. Opt., 27, 3210-3218.\*

Smith, W. L., H. E. Revercomb, D. D. Laporte, L. A. Sromovsky, S.

Silverman, H. M. Woolf, H. B. Howell, R. O. Knuteson, and H.-L.

Huang, 1991: GHIS - The GOES High resolution Interferometer

Sounder. J. Applied Met., 29, 1189-1204.\*

\* Copy included in Appendix A.

#### IV. REFERENCES

- Clough, S. A., F. X. Kneizys, E. P. Shettle, and G. P. Anderson, 1986:  
Atmospheric spectral transmittance and radiance: FASCOD2.  
Proceedings of Sixth Conference on Atmospheric Radiation, AMS,  
Boston, MA.
- Huang, H.-L., W. L. Smith, and H. M. Woolf, 1992: Vertical resolution  
and accuracy of atmospheric infrared sounding spectrometers.  
Accepted for publication in J. Applied Met., Feb 1992.
- Huang, H.-L., W. L. Smith, G. R. Diak, and H. M. Woolf, 1991: Future  
hybrid infrared and microwave satellite sounding system - a  
theoretical analysis of its capability. **Seventh Symposium on  
Meteorological Observations and Instrumentation: Special Sessions  
on Laser Atmospheric Studies**, Jan. 14-18, 1991, New Orleans, LA,  
AMS, Boston, MA
- Jedlovec G. J., K. B. Batson, R. J. Atkinson, C. C. Moeller, W. P.  
Menzel, and M. W. James, 1989: Improved capabilities of the  
Multispectral Atmospheric Mapping Sensor (MAMS). NASA Technical  
Memorandum 100352, Marshall Space Flight Center, Huntsville, AL,  
71pp.
- Moeller, C. C., W. P. Menzel, and K. I. Strabala, 1991: High resolution  
depiction of atmospheric and surface variation from combined MAMS  
and VAS radiances. Submitted to Int. J. Remote Sensing (in  
review).
- Revercomb, H. E., R. O. Knuteson, W. L. Smith, H. M. Woolf, and H. B.  
Howell, 1990: Spectroscopic inference from HIS measurements of  
atmospheric thermal emission. **Digest of Topical Meeting on  
Optical Remote Sensing of the Atmosphere**, Feb. 12-15, 1990,

Incline Village, NV, Optical Society of America, Washington, DC,  
Vol 4, 590-593.

Williams, S. T., H. M. Goodman, K. R. Knupp, and J. E. Arnold, 1987:  
SPACE/COHMEX Data Inventory Document. NASA Technical Memorandum  
4006, Marshall Space Flight Center, Huntsville, AL (available  
NTIS), 480pp.

APPENDIX A - NASA SUPPORTED PUBLICATIONS

# Radiometric calibration of IR Fourier transform spectrometers: solution to a problem with the High-Resolution Interferometer Sounder

Henry E. Revercomb, H. Buijs, Hugh B. Howell, D. D. LaPorte, William L. Smith, and L. A. Sromovsky

A calibrated Fourier transform spectrometer, known as the High-Resolution Interferometer Sounder (HIS), has been flown on the NASA U-2 research aircraft to measure the infrared emission spectrum of the earth. The primary use—atmospheric temperature and humidity sounding—requires high radiometric precision and accuracy (of the order of 0.1 and 1°C, respectively). To meet these requirements, the HIS instrument performs in-flight radiometric calibration, using observations of hot and cold blackbody reference sources as the basis for two-point calibrations at each wavenumber. Initially, laboratory tests revealed a calibration problem with brightness temperature errors as large as 15°C between 600 and 900 cm<sup>-1</sup>. The symptom of the problem, which occurred in one of the three spectral bands of HIS, was a source-dependent phase response. Minor changes to the calibration equations completely eliminated the anomalous errors. The new analysis properly accounts for the situation in which the phase response for radiance from the instrument itself differs from that for radiance from an external source. The mechanism responsible for the dual phase response of the HIS instrument is identified as emission from the interferometer beam splitter.

## I. Introduction

The capability of measuring absolute radiance with an infrared Fourier transform spectrometer is important to the High-Resolution Interferometer Sounder (HIS) program,<sup>1,2</sup> which is applying interferometry to measure the upwelling emission spectrum of the earth for retrieving the temperature, humidity, and other parameters of the atmosphere and surface. The primary objective of the HIS program is to improve significantly the vertical resolution of temperature and humidity profiles determined from satellite platforms by increasing the spectral resolution of observed radiances. The interferometer is a natural choice for the job. Interferometers have proved their merit in space with successful measurements of the emission spectra of planetary atmospheres, not only of the earth,<sup>3,4</sup> but also of Venus,<sup>5</sup> Mars,<sup>6</sup> Jupiter, Saturn and Uranus.<sup>7</sup>

The multiplex and throughput advantages of the interferometer<sup>8</sup> make it possible to make radiometrically precise observations at a much higher spectral resolution than that of current filter radiometers (tens of cm<sup>-1</sup>). To improve the vertical resolution in the troposphere and lower stratosphere by at least a factor of 2 over that of current temperature profiling radiometers (3–8 km), a resolving power ( $\lambda/\Delta\lambda$ ) of ~1000 is needed in the spectral range from 3.7 to 17 μm. (The 15-μm CO<sub>2</sub> absorption band is the primary band for temperature sounding, the combined 4.3-μm CO<sub>2</sub> and 4.5-μm N<sub>2</sub>O bands are used to enhance the temperature resolution in the lower troposphere, and the 6.7-μm H<sub>2</sub>O absorption band gives humidity soundings.) High radiometric precision is required because radiometric noise and time-dependent and wavelength-dependent calibration errors are magnified in the inversion process to derive atmospheric parameters. To obtain temperature profiles with rms errors of <1°C from high-resolution measurements requires noise-equivalent-temperature errors and calibration reproducibilities of the order of 0.1°C and absolute errors of less than about 1°C.

Several important steps have been taken toward developing an improved temperature and humidity sounding satellite instrument. The feasibility of building an instrument to achieve the radiometric performance needed from a geosynchronous satellite plat-

H. Buijs is with BOMEM, Inc., 625 Marais, Ville de Vanier, Quebec G1M 2Y2, Canada; H. B. Howell is with NOAA/NESDIS Systems Design & Applications Branch, 1225 West Dayton Street, Madison, Wisconsin 53706; D. D. LaPorte is with Santa Barbara Research Center, 75 Coromar Drive, Goleta, California 93117; and the other authors are with University of Wisconsin, Space Science & Engineering Center, 1225 West Dayton Street, Madison, Wisconsin 53706.

Received 19 December 1987.

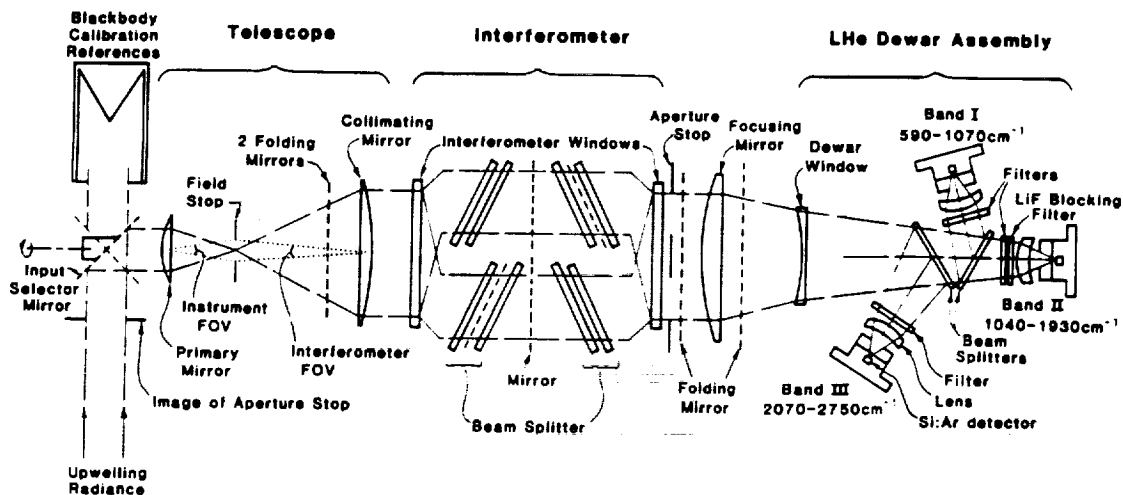


Fig. 1. Functional schematic of HIS optics. The primary mirror, collimating mirror, and focusing mirrors are shown as lenses to simplify the drawing. Plane reflecting surfaces are shown as dashed lines, and the two paths of the interferometer are functionally represented. The complete instrument is ~2.7 m (9 ft) long and fits into the 45.7-cm (18-in.) diam wing pods of the NASA U-2 aircraft.

form has been demonstrated.<sup>9</sup> An aircraft model HIS has been developed and flown on dozens of flights of the NASA U-2 research aircraft as a direct demonstration of the scientific value of such an instrument<sup>10</sup> and that the radiometric noise and calibration requirements are achievable.<sup>11</sup> The instrument was flown with many other atmospheric sensing instruments in two major NASA field programs, the combined Huntsville Meteorological Experiment (COHMEX) for studying severe storms and the First ISCCP Regional Experiment (FIRE) for studying the effect of cirrus clouds on climate. The unique ability of this instrument to measure accurately the emission spectrum from a flexible high-altitude platform with a large complement of other instrumentation should make it an important resource for many types of experiment for several years. Currently, plans for modifying the newest NOAA geosynchronous sounding instrument to incorporate an interferometer are being investigated to realize improvements in the satellite sounding data for weather forecasting before the next century.

This paper describes information about the radiometric calibration of the HIS aircraft instrument, which may be useful to other IR interferometer applications. Early laboratory testing of the aircraft instrument revealed that wavelength-dependent calibration errors of up to 15°C occurred between 600 and 900 cm<sup>-1</sup> when blackbodies at 300 and 77 K were used to determine the radiance of a 280 K blackbody from the magnitude spectra of each source (Sec. II). These large errors, which were originally believed to require hardware changes to the instrument, have been completely eliminated by the processing technique described in Sec. III. The instrument characteristic responsible for the initial calibration errors is also identified there. The implications of the new calibration analysis technique for interferometer design and performance are summarized in the final section.

## II. HIS Radiometric Calibration and the Problem

### A. Calibration Approach and Laboratory Test Results

The basic approach for determining absolute radiances from the HIS nadir-viewing interferometer is the same as that used for filter radiometers and has been used successfully for other interferometric applications.<sup>3-7,12</sup> The detectors and electronics are designed to yield an output which is linear in the incident radiance for all wavenumbers in the optical passband of the instrument, and two blackbody reference sources are viewed to determine the slope and offset which define the linear instrument response at each wavenumber.

In the HIS U-2 instrument, calibration observations of the two onboard reference blackbodies are made every 2 min. There are four double-sided optical-path scans of each reference source for every twelve scans of the earth. As shown in Fig. 1, which summarizes the optical configuration, the blackbodies are viewed by rotating the telescope field of view (FOV) from below the aircraft to inside a blackbody aperture using a 45° plane mirror. There are no uncalibrated optical surfaces, since the earth is viewed through an open aperture in the pod, which provides an aerodynamic shell.

The small size of the optical beam at the blackbody positions makes the design of accurate radiation standards relatively easy. The reference blackbodies are thermoelectrically controlled blackened copper cavities. The insulated copper walls of the blackbody cavities give good temperature uniformity, and because of the cavity effect, the normal emissivity is very close to one (Table I). The temperatures are sensed with accurately calibrated platinum resistance thermometers (PRTs) embedded in the base of each cavity. (During testing, a second PRT in the side of the cavity was used to verify adequate temperature uniformity.)

Table I. Characteristics of the HIS Aircraft Instrument

Spectral range (cm <sup>-1</sup> ) <sup>a</sup>	
Band I	590-1070
Band II	1040-1930
Band III	2070-2750
Field of view diameter (mrad)	
Telescope	100
Interferometer	30
Blackbody reference sources	
Emissivity	>0.998
Aperture diameter (cm)	1.5
Temperature stability (K)	±0.1
Temperatures (K)	240, 300
Autoaligned interferometer:	Modified BOMEM BBDA2.1
Beam splitter	
Substrate	KCl
Coatings (1/4 λ at 3.3 μm)	Ge + Sb <sub>2</sub> S <sub>3</sub>
Maximum delay (double-sided current configuration) (cm)	
Band I (hardware limit is ±2.0)	±1.8
Bands II and III (limited by data system)	+1.2, -0.8
Michelson mirror optical scan rate (cm/s)	
	0.6-1.0
Aperture stop (at interferometer exit window)	
Diameter (cm)	4.1
Central obscuration area fraction	0.17
Area (cm <sup>2</sup> )	10.8
Area-solid angle product (cm <sup>2</sup> -sr)	
	0.0076
Detectors	
Type	Ar-doped Si
Diameter (cm)	0.16
Temperature (K)	6
Nominal instrument temperature (K)	
	260

<sup>a</sup> The ranges shown are design ranges. The current bandpass filters were chosen from available stock filters and will be changed as new filters are acquired.

One important additional requirement when applying a two-point calibration with blackbody references to an interferometer, as opposed to an instrument measuring spectra directly, is that the instrument responsivity should be independent of optical delay (or that any delay dependences should be accurately known). Avoiding sources of delay-dependent response was a major objective in designing the HIS instrument. To accomplish this, care was taken in the optical stop design and alignment to prevent the effective aperture stop size from changing with the motion of the Michelson mirror. The best location for the aperture stop, which is focused on the detectors, was found to be at the exit window of the interferometer module (see Fig. 1). Furthermore, the FOV of the interferometer is restricted to 30 mrad to limit self-apodization.

Now we turn to the mathematical expressions for the calibration. First, a formalism which leads to the use of magnitude spectra in the expression for calibrated radiance is presented to show where this commonly used approach can create a problem, as occurred with the early (1985) HIS calibrations. Assuming linearity as expressed above, the output interferogram  $F$  can be

expressed in terms of the incident spectral radiance  $L_\nu$  as follows, using a continuous representation:

$$F(x) = \frac{1}{2} \int_{-\infty}^{\infty} C_\nu \exp[i\phi(\nu)] \exp(i2\pi\nu x) d\nu, \quad (1)$$

where the uncalibrated magnitude spectrum ( $C_\nu \equiv C_{-\nu}$ ) is given by

$$C_\nu = |F| = r_\nu(L_\nu + L_\nu^0), \quad (2)$$

and where  $x$  = optical path difference (delay),

$\nu$  = wavenumber,

$\phi(\nu)$  = phase response of instrument [ $\phi(\nu) = \phi(-\nu)$ ],

$r_\nu$  = responsivity of instrument,

$L_\nu^0$  = offset from instrument emission, referred to input,

$\sim$  = complex Fourier transform.

The phase characterizes the combined optical and electrical dispersion of the instrument and here is assumed to be the same for scene and background emissions. Although this assumption is commonly made, it will later be shown to be invalid for the HIS instrument. Equation (2) expresses the linear relationship between the uncalibrated spectrum and spectral radiance. The two unknowns to be determined from the two calibration observations are the responsivity and the offset radiance. The offset radiance defined here is the radiance, which, if introduced at the input of the instrument, would give the same contribution as the actual emission from various parts of the optical train. Equation (2) written for both the hot and cold blackbody views can be solved to yield

$$r_\nu = (C_{\nu h} - C_{\nu c})/[B_\nu(T_h) - B_\nu(T_c)], \quad (3)$$

$$L_\nu^0 = C_{\nu c}/r_\nu - B_\nu(T_h) = C_{\nu h}/r_\nu - B_\nu(T_c), \quad (4)$$

where  $B_\nu$  is the Planck blackbody radiance, and subscripts  $h$  and  $c$  label the quantities associated with the hot and cold blackbody. [Note that for simplicity the blackbodies are assumed to have unit emittance here. To account for actual emittances  $\epsilon$ , the Planck radiances should be replaced with  $\epsilon B + (1 - \epsilon)B(T_a)$ , where  $T_a$  is the ambient temperature.] Solving Eq. (2) for the source radiance and substituting from Eqs. (3) and (4) yield the basic calibration relationships:

$$L_\nu = C_\nu/r_\nu - L_\nu^0, \quad (5)$$

$$L_\nu = [(C_\nu - C_{\nu c})/(C_{\nu h} - C_{\nu c})][B_\nu(T_h) - B_\nu(T_c)] + B_\nu(T_c). \quad (6)$$

The ground calibration tests to be reported here consisted of measuring the radiance from a blackbody at ~280 K using calibration blackbodies at 300 and 77 K. The uncalibrated spectra are shown for two of the three HIS spectral bands in Figs. 2 and 3 (see Table I for the nominal spectral coverage of each band). These bands were chosen because band I displays the problem to be discussed here, and band II does not. (Band III also does not.) Both the magnitude and phase are determined directly from a complex Fourier transformation of the measured two-sided interferogram. As will be explained further in Sec. III, the

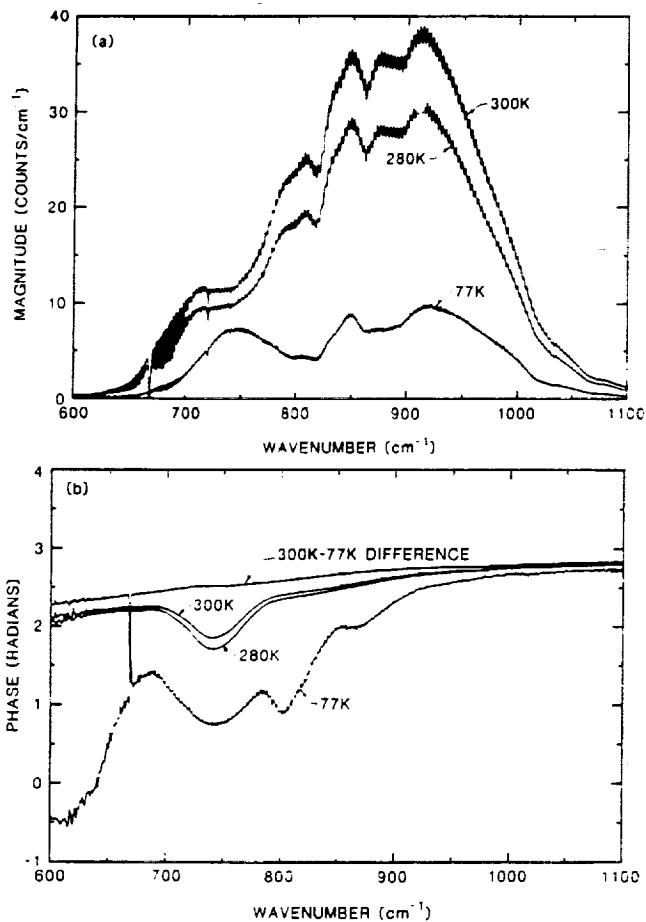


Fig. 2. Uncalibrated magnitude (a) and phase (b) spectra of blackbody sources for HIS spectral band I. The curves are labeled by the temperature of the source. The phase labeled 300K-77K Difference is the phase of the difference of the 300 and the 77 K spectra. The magnitude spectra are shaped by a Gaussian numerical filter and display  $\text{CO}_2$  absorption features and channeling as discussed in the text. Note the substantial differences among the phase responses.

linear phase contribution arising from an ambiguity in the sample offset from the zero path difference (ZPD) has also been removed.

The magnitude spectra have various features which need explanation. Because testing was conducted in air, the instrument transmittance is significantly affected by the 1-2 m of air in the path from the blackbodies to the detectors. (Of the total optical path between the blackbodies and the detector/Dewar assembly, only the interferometer itself is enclosed and backfilled with dry nitrogen to protect the beam splitter; at flight altitudes of 20 km, atmospheric absorption is insignificant.) Therefore, the magnitude spectrum for band I (600-1100  $\text{cm}^{-1}$ ) shows  $\text{CO}_2$  absorption between 600 and 750  $\text{cm}^{-1}$ , and band II (1100-1800  $\text{cm}^{-1}$ ) shows water vapor absorption beyond 1300  $\text{cm}^{-1}$ . The absorption for the 668- $\text{cm}^{-1}$   $\text{CO}_2$  line and for several  $\text{H}_2\text{O}$  lines is so strong in air that the signal is almost zero, and the phase is poorly defined. The general Gaussian shape of the magnitude spectra is caused by the numerical filtering which is performed in the instrument digital electronics. (A hardware con-

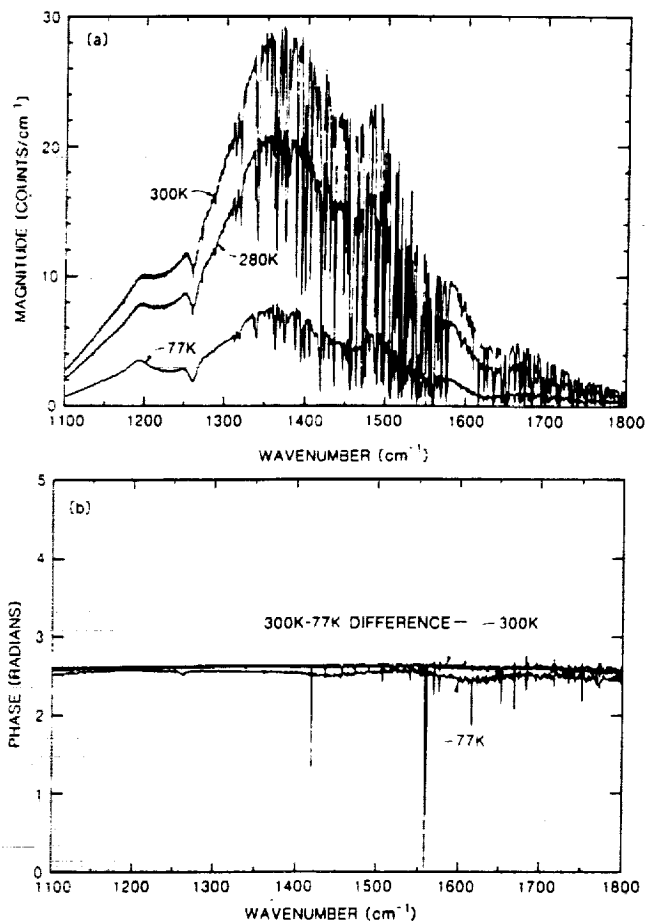


Fig. 3. Uncalibrated magnitude (a) and phase (b) spectra of blackbody sources for HIS spectral band II. The curves are labeled as in Fig. 2. Here also the magnitude spectra are shaped by a numerical filter and display channeling as discussed in the text. The very deep and numerous lines in the magnitude spectra are due to  $\text{H}_2\text{O}$  absorption. In contrast to band I, the phase spectra are very similar and quite linear.

volution is performed for signal-to-noise preserving sample volume reduction by factors of 14, 8, and 8 in the three spectral bands.)

The sinusoidal components superimposed on the magnitude spectra are channeled spectra caused by the parallel surfaces of the arsenic-doped silicon detectors. (The band III detector has an antireflective coating, and the spectra do not display channeling.) The channeled spectra are very stable because the detectors, which are operated in a liquid He Dewar, have a very small coefficient of expansion and experience only small temperature variations. As will be shown in the next section, channeling does not affect calibrated spectra.

The phase spectra for bands I and II differ markedly. For band II the phases are nearly linear, the behavior expected with an ideal beam splitter having zero dispersion and with an electrical response having a pure time delay. Band I phases, on the other hand, show significant deviations from linearity and also vary as the source radiance is varied. The nonlinearity is optical, not electrical, in origin because the sign of the

deviations from linearity depends on delay scan direction. The phase spectra shown are for one scan direction. The corresponding phases for the other direction are approximately a mirror image about  $\pi$  rad.

### B. Problem

It is probably not surprising, in light of the anomalous band I phases, that direct application of the normal calibration procedure (based on magnitude spectra) to the laboratory test data does not work uniformly well. The band I spectrum derived in this way is shown in Fig. 4. The spectrum is presented as a brightness temperature to make any errors stand out as a deviation from the measured blackbody temperature of 280.2 K. Errors of tens of degrees occur, and the similarity of the wavelength dependence of the errors to the nonlinearities of the phase is apparent. Figure 5 shows that the calibrated spectra for the HIS bands with nearly linear phase spectra are extremely accurate when calibrated in the same way. The region of large variance from 280.2 K beyond 1400  $\text{cm}^{-1}$  for band II and centered near 2350  $\text{cm}^{-1}$  for band III is caused by water vapor and  $\text{CO}_2$  in the optical path and does not occur when the instrument is operated at flight altitude. Apparently, the normal calibration approach cannot handle measurements with phase anomalies like those of band I.

### III. Solution

#### A. New Calibration Analysis

The band I phase spectra shown in Fig. 2(b) indicate that the phase becomes more nearly linear as the source radiance becomes larger. This behavior suggests that the total measured interferogram and the corresponding complex spectrum have two components; a normal phase component for radiance from the source and an anomalous phase component for radiance from the instrument itself. Of course, the radiance from the instrument can originate from many individual components with different phase characteristics, but they can be lumped together into one term with one phase.

The new calibration analysis is a generalization which properly accounts for a dual phase response, if it is present. It is really a minor modification of the procedure presented in Sec. II. The difference is that the complete complex spectra obtained from Fourier transforming the measured interferograms are used for calibration, not just the magnitudes. Let the complex uncalibrated spectrum be represented by

$$C_r = \tilde{F}_r = r_s [L_r + L_r^0 \exp[i\phi^0(\nu)]] \exp[i\phi(\nu)], \quad (7)$$

where  $\phi^0$  is the difference from the normal phase of the anomalous phase associated with the combined radiance from the many emitting components of the instrument. Then it is clear, under the same instrument stability assumptions on which the basic calibration approach depends, that the anomalous phase contribution can be eliminated along with the instrument radiance offset by differencing complex spectra from

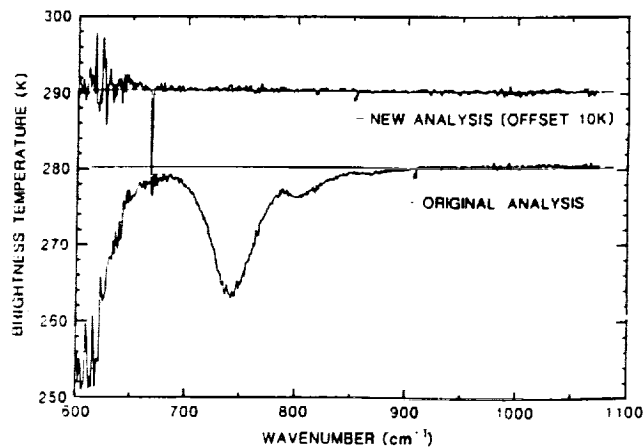


Fig. 4. Brightness temperature spectra for band I. The spectrum with the large deviations from the measured 280.2 K temperature of the blackbody source is derived from the original calibration analysis using magnitude spectra. The spectrum which accurately reproduces a constant brightness temperature is from the modified analysis presented here. The large variance between 600 and 650  $\text{cm}^{-1}$  is caused by the low instrument transmittance in that region. Changes have since been made to improve the throughput in this region.

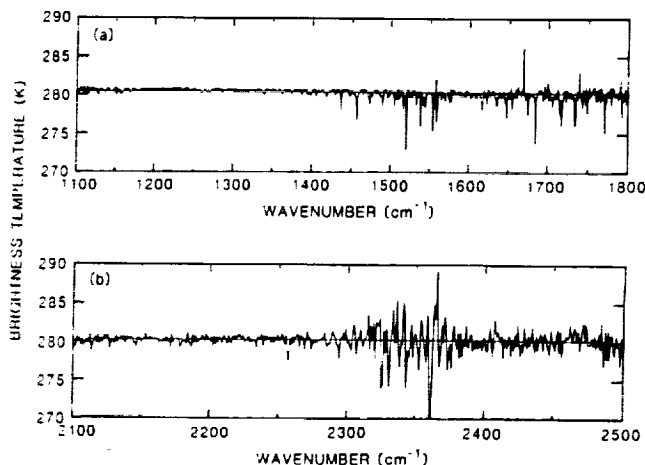


Fig. 5. Brightness temperature spectra for band II (a) and band III (b). The calibration for these bands is good and essentially identical for the standard and modified analyses. The larger variance beyond 1400  $\text{cm}^{-1}$  for band II and centered at 2350  $\text{cm}^{-1}$  for band III are due to  $\text{H}_2\text{O}$  and  $\text{CO}_2$  in the path of the interferometer.

different sources. The difference spectra are identical to the difference spectra which would result if there were no anomalous phase contribution. The equations for the difference spectra from Eq. (7) are

$$C_r - C_{cr} = r_s [L_r - B_r(T_c)] \exp[i\phi(\nu)], \quad (8)$$

$$C_{hr} - C_{cr} = r_s [B_r(T_h) - B_r(T_c)] \exp[i\phi(\nu)]. \quad (9)$$

The new expression for the responsivity, which follows immediately from Eq. (9) by taking the magnitude of both sides, is

$$r_s = |C_{hr} - C_{cr}| / [B_r(T_h) - B_r(T_c)]. \quad (10)$$

Compared to Eq. (3), the difference of magnitude spec-

tra is replaced by the magnitude of difference spectra. The offset which follows directly by substituting the responsivity into Eq. (7) is

$$L_p^0 \exp[i\phi(\nu)] = C_{h_i} \exp[-i\phi(\nu)]/r_c - B_p(T_c). \quad (11)$$

Note that while the instrument responsivity remains a real function in this formalism, the offset is now complex. Finally, the basic calibration expression which follows by taking the ratio of Eq. (8) to (9) is

$$L_p = \text{Re}[(C_p - C_{c_i})/(C_{h_i} - C_{c_i})][B_p(T_h) - B_p(T_c)] + B_p(T_c). \quad (12)$$

For ideal spectra with no noise, this expression for the calibrated radiance would be real, since the phases of the ratioed difference spectra are the same. This cancellation of the phases avoids the square root of two noise amplification, which can be associated with taking the magnitude of spectra with nonzero phase. Because the phase of the ratio of difference spectra is zero to within the noise, the calibrated spectrum can equally well be defined in terms of the real part of the ratio (as shown) or in terms of the magnitude of the ratio.

This technique solves the problem. Application to the measurements presented in the last section yields an accurately calibrated spectrum for band I. The new brightness temperature spectrum, compared to the old in Fig. 4, shows no sign of the large dip centered at  $740 \text{ cm}^{-1}$ . Also, the phase associated with radiance from the source (the phase of difference spectra) is found to be reasonably linear as shown in Fig. 2. The impact on the band II and III spectra for a 280 K blackbody is negligible. However, the small phase dependence on source for band II would probably cause a detectable error for colder sources.

It should be pointed out that ambiguities in the phase from one spectrum to the next must be eliminated before applying this technique. For the HIS instrument, which does not use a white light source to maintain a fixed offset between ZPD and the delay of a numerically filtered point, a discrete ambiguity occurs. This translational ambiguity is linear in wavenumber and takes the form

$$\phi_k = \pi mk/MR, \quad (13)$$

where  $k$  is an integer,  $m$  is the spectral sample number,  $M$  is the number of points in the spectrum, and  $R$  is the numerical filter sample reduction factor. The ambiguity is removed by determining the  $k$  for each spectrum, which nearly eliminates the phase slope. Ambiguities of  $\pi$  rad, which occur in instruments with ambient temperature detectors, are not usually a consideration for the HIS application which uses LHe cooled detectors.

Also, note that if a white light source is used to control numerical filtering so that the same delays are measured on subsequent scans, the differencing to eliminate instrument background can be performed on the interferograms. Then anomalous phases would have no effect on spectra. Differencing interferograms is also the way to handle a potential dual phase problem, if one-sided OPD scanning is used.

## B. Source of the Anomalous Phase Spectrum

It is of interest to explore the cause of the anomalous band I phase to assess the applicability of the new analysis technique to other FTIR applications. Also, it may be possible to relax constraints on interferometer optical design, since some apparent hardware problems can be eliminated by analysis.

Phase nonlinearities can of course occur from dispersion in beam splitter/compensator substrates, if their thicknesses are not well matched. This effect cannot explain the HIS data. The linearity of the phases for bands II and III suggests that the beam splitter/compensator matching is quite good. More important, dispersion from this origin does not give phase spectra which depend on the source.

To explain the HIS data, a mechanism is needed for which radiance from the instrument can yield a phase spectrum which is different from that for an external source. Apparently, the plane of wavefront division in the beam splitter depends on the source of the radiation. We have identified two mechanisms by which a source dependence might occur: (1) dependence of the beam splitter coating properties on the angle of incidence and (2) emission from the beam splitter coatings.

The first mechanism, angle dependence, has been ruled out as an important factor for the HIS configuration. A test was performed to measure off-axis radiation. It consisted of viewing a  $LN_2$  source with the instrument in its normal configuration and with the field stop removed. The spectrum with the field stop removed is dominated by radiance from the Dewar window entering the interferometer exit window, not radiance from the field stop as in the normal configuration. The difference in the spectra for these two configurations is the spectrum of radiation from the field stop. The phase of the difference is essentially identical to that of radiance from an external source (Fig. 2), indicating no significant dependence on the angle of incidence.

The second possible mechanism, beam splitter coating emission, appears to be a likely candidate for explaining the anomalous phase. Beam splitter emission could lead to the effective wavefront division occurring at the point of emission with coherent radiation being emitted into both legs of the interferometer. Emission at a different depth in the beam splitter than normal wavefront division would create an anomalous phase.

There is evidence that the HIS beam splitter has absorption in the wavenumber region where phases are anomalous. Although the absorption of the beam splitter used for the measurements presented here has not been measured directly, transmittance measurements for other beam splitters of the same construction are available. Figure 6 shows the transmittance of one such beam splitter compared to a sinusoidal fit used to extrapolate the expected transmittance in the absence of absorption into the region of the narrow absorption feature centered at  $\sim 740 \text{ cm}^{-1}$ . The minimum reflectance at  $3000 \text{ cm}^{-1}$  is consistent with the

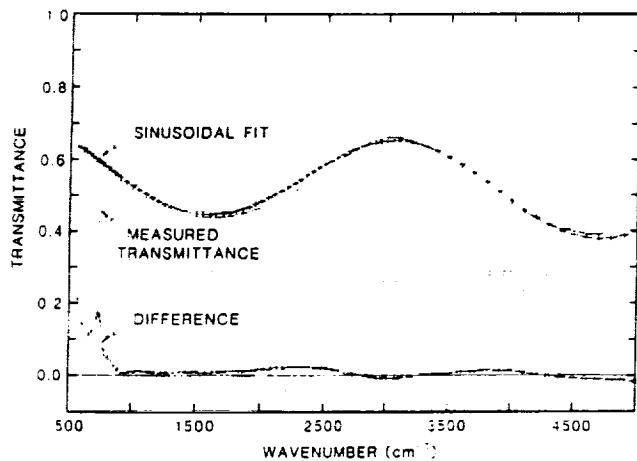
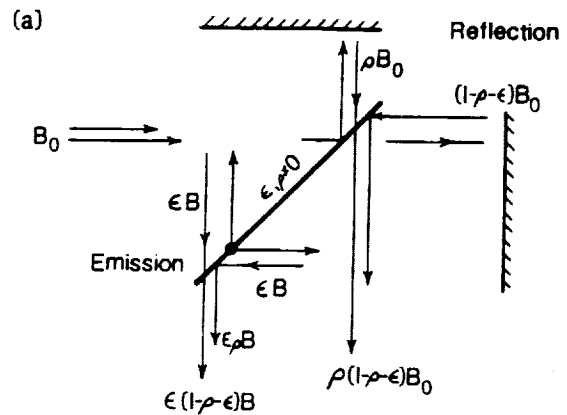


Fig. 6. Transmittance of a beam splitter of the same construction as the HIS instrument beam splitter. The absorption feature centered at  $\sim 740 \text{ cm}^{-1}$  is responsible for the dual phase response of the instrument. The sinusoidal fit to the transmittance is used to approximate the reflectance for beam splitter emittance and efficiency calculations.

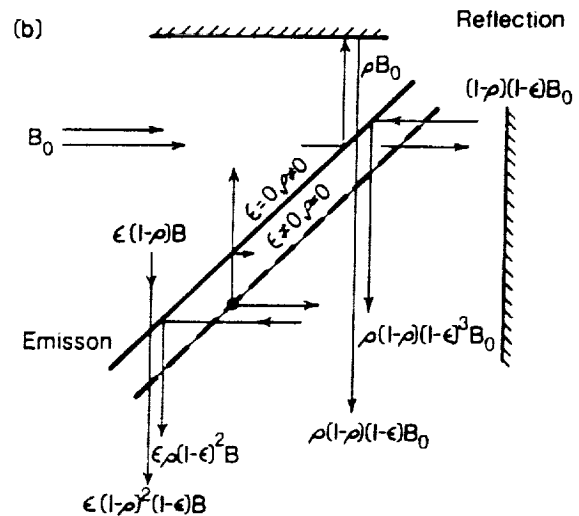
thickness of the beam splitter coatings, 0.25 wavelength at  $3.3 \mu\text{m}$  of Ge and the same of  $\text{Sb}_2\text{S}_3$ . While germanium has a weak absorption feature centered near  $740 \text{ cm}^{-1}$ , the absorptance of up to 0.1 or 0.2 implied by these data is surprising, because the thickness of the coatings is not large enough for substantial bulk absorption. Maybe the indicated absorption is caused by a surface effect or contamination.

It is possible to obtain information on the beam splitter emittance and efficiency directly from measurements of the HIS instrument itself, if a model of the beam splitter is assumed. The two simple models illustrated in Fig. 7 have been used for this purpose. Rays illustrating the reflection process for an external source and the emission process are shown for both. Model 1 represents the beam splitter/compensator as a single plane with nonzero reflectance  $\rho$  and emittance  $\epsilon$ . It is too simple to explain a phase anomaly, because there is a single surface for wavefront division due to both reflection and emission. Model 2 uses two plane surfaces, one which can reflect but not emit and one which can emit but not reflect. A beam splitter representable by this model would create an anomalous phase.

Emittances and efficiencies are determined from the ratio of the uncalibrated magnitude spectrum for emission from the beam splitter (referred to interferometer input) to that of a blackbody at the same temperature. The blackbody spectrum, free of emission contributions, is obtained in the normal manner by differencing the complex spectrum of an ambient temperature blackbody from the spectrum of a liquid nitrogen blackbody. The beam splitter spectrum is obtained by subtracting a scaled blackbody spectrum from the liquid nitrogen spectrum with the scale factor chosen to give approximately zero from  $950$  to  $1100 \text{ cm}^{-1}$  where absorption is expected to be small. The ratio defined in this way is equal to the ratio of the expressions for the emitted and reflected output given



MODEL 1: ONE PLANE SURFACE



MODEL 2: TWO PLANE SURFACES

Fig. 7. Simplified beam splitter models for emittance and efficiency calculations. The expressions in terms of the emittance  $\epsilon$  and reflectance  $\rho$  represent the amplitudes of the beam at various locations. The rays on the left represent the emission process, and those on the right represent the passage of an external beam.

in Fig. 7 (e.g., ratio =  $\epsilon/\rho$  for model 1). Using the reflectivity from the sinusoidal fit of Fig. 6 [fit =  $(1 - \rho)$ ], the expression for the ratio can be solved for the emittance. The efficiency of the beam splitter is then given by the product of the complete beam splitter reflectivity and transmittance divided by the ideal output amplitude of 0.25 for a reflectance of 0.5 and no absorptance.

The emittances and efficiencies deduced from interferometer measurements using these models are shown in Fig. 8. The emittances estimates are in reasonable agreement with those obtained from the direct transmittance data of Fig. 6, giving further support for the conclusion that there is beam splitter emission acting approximately as modeled. Notice

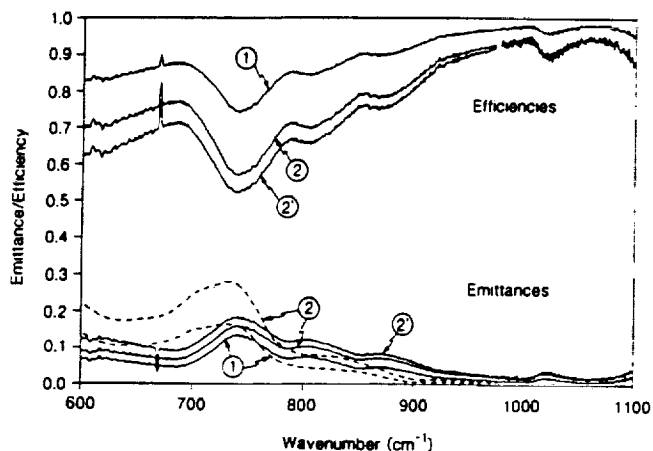


Fig. 8. Beam splitter emittance and efficiency estimates labeled by the model assumed. Model 2' is the same as model 2 with the emitting and reflecting surfaces reversed in order. The dashed emittance curves are from the data of Fig. 6, and the solid curves are from measurements with the HIS instrument.

that due to the multiple passes through the absorbing layer, the efficiency can get as low as 50% at  $740\text{ cm}^{-1}$ .

Further verification of the influence of beam splitter absorption on the HIS instrument is provided by comparison of the measured instrument responsivity to that calculated based on the transmittance of each optical element and on the detector responsivities, as shown in Fig. 9. The Gaussian numerical filter function has been divided out of the measured responsivity (note the effects of  $\text{CO}_2$  absorption and channeling discussed earlier). The responsivity calculated assuming the beam splitter to be uniformly efficient is noticeably too large between  $650$  and  $900\text{ cm}^{-1}$  where the band I phase anomaly occurs. The beam splitter efficiencies from Fig. 8 reduce the responsivity over the correct wavenumber region, with the model 2 calculation giving very good agreement with the measured responsivity.

Both the deduced emittances and the efficiencies give a strong case for the emission explanation of anomalous phases. However, a piece of puzzle that does not fit very well is the size of the phase anomalies. The optical thickness ( $x = \delta\phi/2\pi\nu$ ) corresponding to the observed phase anomalies ( $\delta\phi$ ) at  $740\text{ cm}^{-1}$  is  $3.9\text{ }\mu\text{m}$ . Model 2 suggests that, if the absorption is in the coatings, the additional optical path difference should be  $<1.9\text{ }\mu\text{m}$ , the optical thickness of the combined beam splitter coatings divided by the cosine of the  $30^\circ$  angle of incidence. This peculiarity and the mechanism for the absorption are remaining mysteries.

#### IV. Implications and Summary

It is not known whether the problem identified here is common or rare in other FTIR applications. The errors resulting from this problem could possibly be small enough to go unnoticed but might be significant when evaluating detailed performance. Comparing the phase spectra for a cold and a warm source is a simple test for diagnosing the problem.

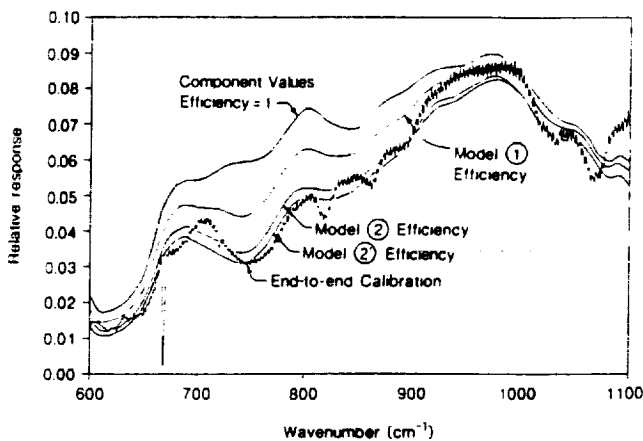


Fig. 9. Comparison of instrument responsivity calculated from optical component transmittances and detector responsivity to the end-to-end responsivity from calibration measurements. The beam splitter efficiencies used in the calculated responsivities are those deduced from measurements with the HIS interferometer itself. The calculations using model 2 seem to account properly for actual beam splitter efficiencies.

The new calibration analysis technique has been discussed here in the context of the HIS application, involving absolute radiance measurements. It may also be important for applications in which the transmittance or reflectance of a sample is measured. As pointed out by Tanner and McCall,<sup>13</sup> emission from the samples or the surroundings can create significant errors for these types of measurement. However, the radiance contribution from the background can be eliminated, if the spectra for two different reference sources are differenced. By determining the difference spectra using complete complex spectra as described in the last section, any anomalous phase contributions of radiance from the interferometer will also be eliminated.

There are some aspects of interferometer design that may be influenced by the analysis approach presented here and by knowledge that beam splitter emission can modify the phase response. First, the constraints on beam splitter coating materials can probably be relaxed to include materials with some absorption. Second, interferometer designs may be able to rely on a better capability to handle errors associated with the phase. It is conceivable that having a well-behaved phase is not so important when a proper calibration is performed with double-sided scanning.

In summary, the phase response of one spectral band of the HIS FTIR instrument appears to vary with the source radiance, becoming more linear the higher the radiance contribution from the source. This dependence creates substantial radiance errors when magnitude spectra are used to perform a two-point calibration using blackbody reference sources. The errors are eliminated, yielding good calibration results, when a minor modification to this technique is applied. The new technique explicitly accounts for the possibility that a dual phase response can occur. That is, the phase response for radiance from the instrument can

differ from that for radiance from a source. The origin of the different phase response for radiance from the HIS instrument is identified as emission from the beam splitter.

The authors thank the members of the instrument team at the Space Science and Engineering Center, BOMEM, Inc., the Santa Barbara Research Center, and the University of Denver, whose care in fabricating and aligning the HIS instrument made accurate radiometric calibration realizable. Thanks also to Frank Murcay for many helpful discussions. The HIS program is jointly funded by NOAA contract NA-84-DGC-00095 and NASA contract NAS5-27608.

### References

1. W. L. Smith, H. E. Revercomb, H. B. Howell, and H. M. Woolf, "Recent Advances in Satellite Remote Sounding," *International Radiation Symposium '84: Current Problems in Atmospheric Radiation*, G. Fiocco, Ed. (A. Deepak, Hampton, VA, 1984), p. 388.
2. W. L. Smith, H. E. Revercomb, H. B. Howell, and H. M. Woolf, "HIS—A Satellite Instrument to Observe Temperature and Moisture Profiles with High Vertical Resolution," in *Fifth Conference on Atmospheric Radiation* (American Meteorological Society, Boston, 1983).
3. R. A. Hanel, B. Schlachman, F. D. Clark, C. H. Prokesh, J. B. Taylor, W. M. Wilson, and L. Chaney, "The Nimbus III Michelson Interferometer," *Appl. Opt.* **9**, 1767 (1970).
4. R. A. Hanel, B. Schlachman, D. Rodgers, and D. Vanous, "Nimbus 4 Michelson Interferometer," *Appl. Opt.* **10**, 1376 (1971).
5. D. Oertel *et al.*, "Infrared Spectrometry of Venus from Venera-15 and Venera-16," *Adv. Space Res.* **5**, 25 (1985).
6. R. A. Hanel *et al.*, "Mariner 9 Michelson Interferometer," *Appl. Opt.* **11**, 2625 (1972).
7. R. A. Hanel *et al.*, "Infrared Spectrometer for Voyager," *Appl. Opt.* **19**, 1391 (1980).
8. J. W. Brault, "Fourier Transform Spectroscopy," *High Resolution Astronomy*, Proceedings, Fifteenth Advanced Course in Astronomy and Astrophysics, Saas-Fee, M. Huber, A. Benz, and M. Mayor, Eds. (1985).
9. "A Design Feasibility Study for the High-Resolution Interferometer Sounder (HIS)," Santa Barbara Center Final Report for contract UAA 871R55 5 (10 July 1981, updated 19 July 1982, updated 15 Feb. 1983).
10. W. L. Smith, H. E. Revercomb, H. M. Woolf, H. B. Howell, D. D. LaPorte, and K. Kageyama, "Improved Geostationary Satellite Soundings for the Mesoscale Weather Analysis/Forecast Operations," in *Proceedings, Symposium on Mesoscale Analysis and Forecasting*, Vancouver, Canada, 17-19 Aug. 1987, ESA SP-282 (1987).
11. H. E. Revercomb, D. D. LaPorte, W. L. Smith, H. Buijs, D. G. Murcay, F. J. Murcay, and L. A. Sromovsky, "High-Altitude Aircraft Measurements of Upwelling IR Radiance: Prelude to FTIR from Geosynchronous Satellite," *Mikrochim. Acta* in press, 000 (Springer-Verlag, Wien, 1987).
12. D. D. LaPorte and R. Howitt, "Ambient Temperature Absolute Radiometry using Fourier Transform Spectrometers," *Proc. Soc. Photo-Opt. Instrum. Eng.* **364** (1982).
13. D. B. Tanner and R. P. McCall, "Source of a Problem with Fourier Transform Spectroscopy," *Appl. Opt.* **23**, 2363 (1984).

51-46  
N92-34096  
P-4

SPECTROSCOPIC INFERENCES FROM HIS MEASUREMENTS  
OF ATMOSPHERIC THERMAL EMISSION

H. E. Revercomb, R. O. Knuteson, W. L. Smith  
University of Wisconsin, Space Science and Engineering Center  
1225 West Dayton Street  
Madison, WI 53706

H. M. Woolf, and H. B. Howell  
NOAA/NESDIS Systems Design and Applications Branch  
1225 West Dayton Street  
Madison, WI 53706

1. INTRODUCTION

Radiometrically accurate observations of the earth's emission spectrum from 3.8 to 16.6 microns have been made using the High-resolution Interferometer Sounder (HIS) to look downward from the NASA U2/ER2 aircraft or upward from the ground. These observations have been used to demonstrate the substantially improved vertical resolution of temperature and water vapor soundings derived from high resolution spectra (resolving power from 1800 to 3800), as compared to soundings from the low resolution filter radiometer observations used in current satellite sounders.<sup>1,2,3</sup>

The HIS observations have also demonstrated that Fourier Transform - Infrared (FTIR) instruments are especially well suited to absolute emission measurements of broad spectral bands at high resolution.<sup>4,5,6</sup> A fundamental advantage of FTIR instruments for accurate calibration is wavelength integrity, the same property which has made FTIR the standard for very high resolution absorption measurements.

While the HIS was primarily designed for atmospheric temperature and water vapor profiling, its broad spectral coverage and high accuracy (absolute brightness temperature errors of less than 0.5°C and a reproducibility approaching 0.1°C at most wavelengths) lead to a wide range of important applications, including monitoring tropospheric trace gases, surface and cloud spectral properties, and surface temperatures, in addition to spectroscopy.

2. SPECTROSCOPY

The long wavelength part of a HIS downwelling radiance spectrum is compared to a calculated spectrum in Fig. 1. The calculation uses the AFGL HITRAN/86 line file and FASCOD2 line-by-line program with atmospheric state data from in situ measurements. In general, agreement between HIS and FASCOD2 spectra is remarkably good, a tribute to the current state of spectral line files and line-by-line codes.

The detailed radiance differences of observations from FASCOD2 calculations are shown in Figs. 2 and 3 for a range of atmospheres. Note that the largest differences are reproducible over a wide range of conditions, including even uplooking and downlooking viewing conditions.

The top two differences in Figs. 2 and 3 are from uplooking observations (note the reversed sign). The in situ atmospheric temperature and humidity measurements for these observations are very good because NCAR Cross-chained Loran Atmospheric Sounding System (CLASS) balloons were launched from the same

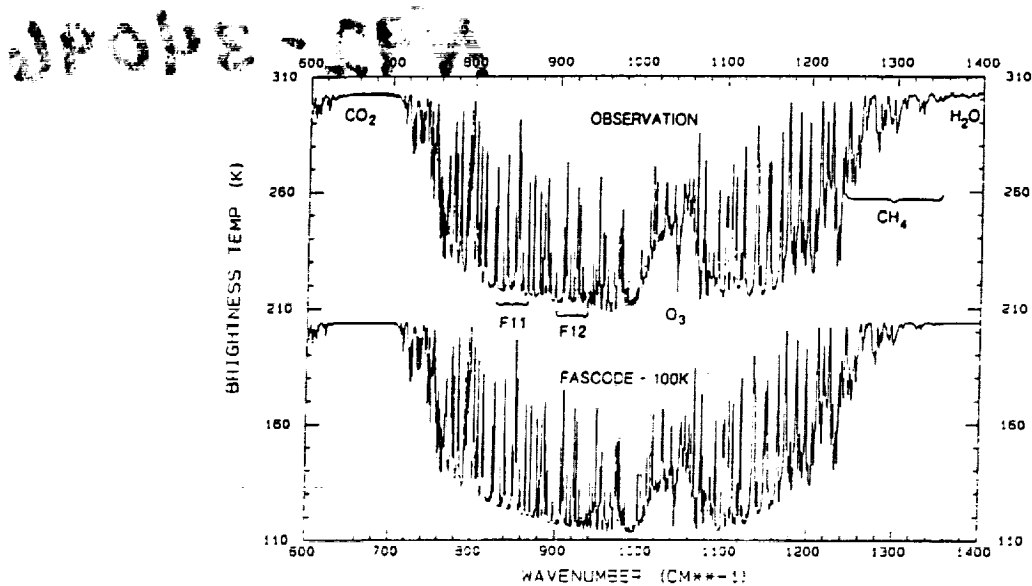


Fig 1. HIS uplooking spectrum compared to FASCOD2 calculation.

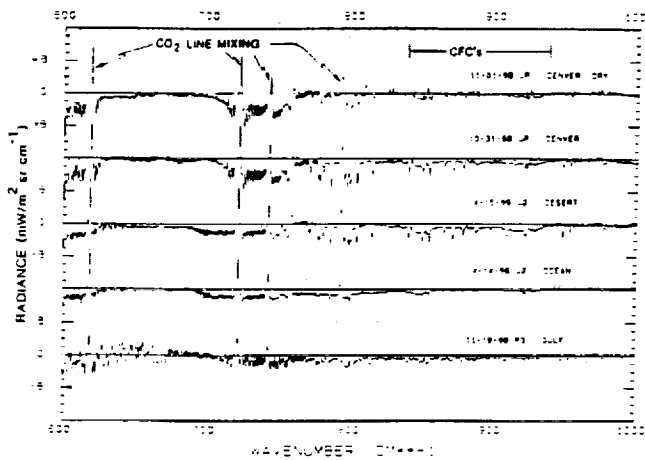


Fig 2. Radiance differences (HIS-FASCOD2).

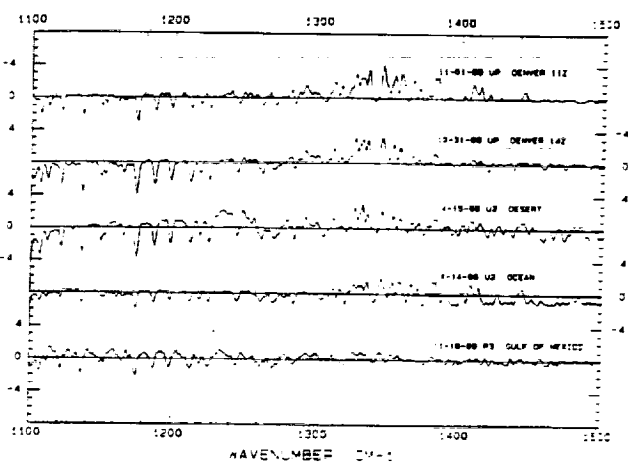


Fig 3. Radiance differences.

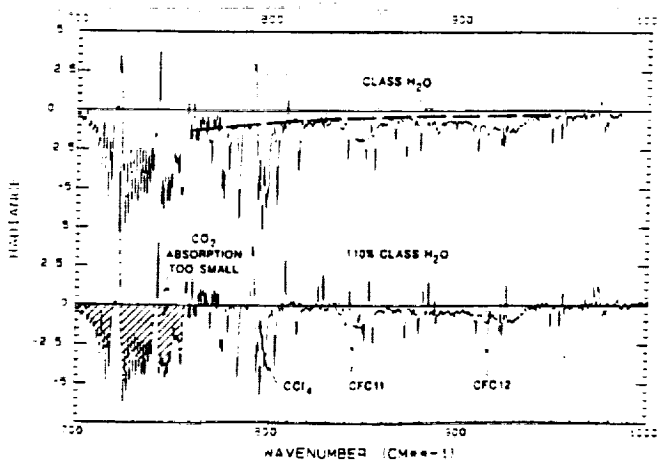


Fig 4. Radiance differences (HIS-FASCOD2).

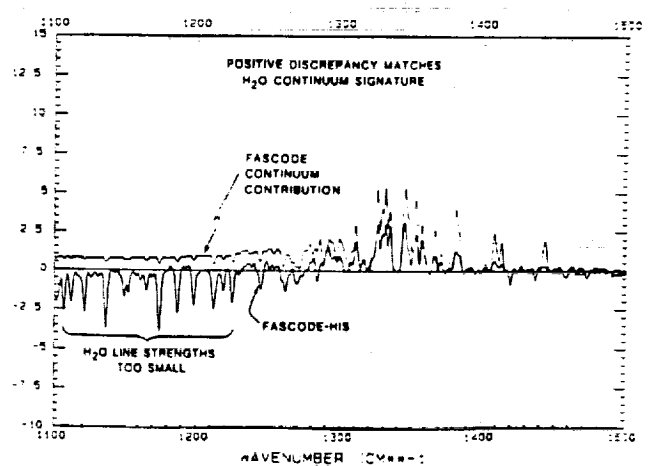


Fig 5. Radiance differences.

site where the HIS was located.<sup>7</sup> The last comparison labelled Gulf was flown at 400 mb over the Gulf of Mexico aboard the NOAA P3 aircraft during an integration test flight and is somewhat noisy. It is included because, again in this situation, the atmospheric measurements made by sensors onboard the plane and by NCAR dropsondes are very good and because it is an example of a reasonably wet atmosphere (the wetness of the atmospheres shown generally increases from the top of the figure to the bottom).

The largest residuals between observations and calculations have been identified with either spectroscopic or atmospheric uncertainties. Two examples are labelled in Fig. 2. The effects of line mixing on the effective line shapes in the CO<sub>2</sub> Q-branches was not accounted for in FASCOD2. The latest version (FASCOD3), soon to be available from AFGL, does account for line mixing. The effects of absorption by chlorofluorocarbons (CFC's), not currently included in FASCOD2, are also labelled.<sup>8</sup> These features are shown in more detail in Fig. 4, along with absorption by carbon tetrachloride.

The major new conclusions which have been drawn from these comparisons are illustrated in Figs. 4 and 5. Figure 4 shows that only a 10% adjustment of the H<sub>2</sub>O amount is needed to bring the calculated and observed spectra into excellent agreement regarding the longwave H<sub>2</sub>O continuum. This adjustment is on the order of the uncertainty in the H<sub>2</sub>O profile. Over most of the spectral range, the residual differences are small after accounting for this adjustment, the larger effects discussed above, and small H<sub>2</sub>O line parameter uncertainties. However, a major difference still remains from about 700 to 760 cm<sup>-1</sup>. The correlation of this region with the absorption of CO<sub>2</sub> and the symmetric effect on the other side of the CO<sub>2</sub> band (Fig. 2), strongly suggests that the line absorption of CO<sub>2</sub> needs to be increased in the model.

Figure 5 shows that the positive discrepancy between 1250 and 1425 cm<sup>-1</sup>, which is largest for the driest atmospheres, is related to the H<sub>2</sub>O continuum, because the continuum contribution (the difference between a FASCOD2 calculation without and with a continuum) accounts for the shape of the positive discrepancy. The continuum in this region is dominated by the foreign-broadened continuum, unlike the longwave region where the self-broadened continuum dominates. Therefore, it is possible to reduce the continuum for this region by the large amount needed (60%), without destroying the agreement already discussed in the longwave window.

Finally, the consistent differences at the H<sub>2</sub>O lines from 1100 to 1230 cm<sup>-1</sup> implies the need to increase the line strengths of water vapor in this region by about 30%. It is important to note that even large adjustments of the atmospheric water vapor amount cannot eliminate both this problem and the continuum problem simultaneously, because they require changes in the opposite sense.

### 3. CONCLUSIONS

Reproducible differences between HIS observations and FASCOD2 line-by-line calculations lead to the following conclusions:

- (1) The FASCOD2 water vapor continuum in the longwave window region from 10 to 13 microns (750 to 1000 cm<sup>-1</sup>) gives reasonable agreement with radiance observations.

- (2) The model H<sub>2</sub>O continuum from 7 to 8 microns (1250 to 1425 cm<sup>-1</sup>) needs adjustment to reduce its contribution by about 60%.
- (3) CO<sub>2</sub> absorption in the region from 13.1 to 14.3 microns (700 to 760 cm<sup>-1</sup>) is too small in the model.
- (4) Water vapor line strengths in the region from 8.1 to 9.1 microns (1100 to 1230 cm<sup>-1</sup>) need to be increased about 30%.

#### REFERENCES

- <sup>1</sup>Smith, W. L., H. E. Revercomb, D. D. LaPorte, L. A. Sromovsky, S. Silverman, H. M. Woolf, H. B. Howell, R. O. Knuteson, and H.-L. Huang, 1989: GHIS - The GOES High resolution Interferometer Sounder. Submitted to J. Appl. Meteor.
- <sup>2</sup>Smith, W. L., H. M. Woolf, H. B. Howell, H.-L. Huang, and H. E. Revercomb, 1989: The simultaneous retrieval of atmospheric temperature and water vapor profiles - applications to measurements with High spectral resolution Interferometer Sounder (HIS). RSRM 87; Advances in Remote Sensing Retrieval Methods. A. Deepak, H. Fleming, J. Theon (Eds.). A. Deepak Publishing, Hampton, VA.
- <sup>3</sup>Smith, W. L., H. M. Woolf, H. B. Howell, H. E. Revercomb, and H.-L. Huang, 1988: High resolution interferometer sounder - the retrieval of atmospheric temperature and water vapor profiles. Proceedings of the Third Conf. on Satellite Meteorology and Oceanography, Anaheim, CA, February 1-5, AMS, Boston, MA.
- <sup>4</sup>Revercomb, H. E., W. L. Smith, L. A. Sromovsky, R. O. Knuteson, H. Buijs, D. D. LaPorte, and H. B. Howell, 1989: Radiometrically accurate FTS for atmospheric emission observations. 7th International Conf. on Fourier Transform Spectroscopy, Fairfax, VA, June 19-23, in press.
- <sup>5</sup>Revercomb, H. E., H. Buijs, H. B. Howell, R. O. Knuteson, D. D. LaPorte, W. L. Smith, L. A. Sromovsky, and H. M. Woolf, 1988: Radiometric calibration of IR interferometers: experience from the High-resolution interferometer sounder (HIS) aircraft instrument. RSRM 87; Advances in Remote Sensing Retrieval Methods. A. Deepak, H. Fleming, J. Theon (Eds.), A. Deepak Publishing, Hampton, VA.
- <sup>6</sup>Revercomb, H. E., H. Buijs, H. B. Howell, D. D. LaPorte, W. L. Smith, and L. A. Sromovsky, 1988: Radiometric calibration of IR Fourier transform spectrometers: solution to a problem with the High-resolution Interferometer Sounder (HIS). Appl. Optics, 27, 3210-3218.
- <sup>7</sup>Smith, W. L., H. E. Revercomb, H. B. Howell, H. M. Woolf, R. O. Knuteson, R. G. Dedecker, M. J. Lynch, E. R. Westwater, R. G. Strauch, K. P. Moran, B. Stankov, M. J. Falls, J. Jordan, M. Jacobsen, W. F. Dabberdt, R. McBeth, G. Albright, C. Paneitz, G. Wright, P. T. May, and M. T. Decker, 1989: GAPEX - A Ground-based Atmospheric Profiling Experiment. Accepted for publication in March 1990 issue of Bull. Amer. Meteor. Soc.
- <sup>8</sup>Clough, S. A., R. D. Worsham, W. L. Smith, H. E. Revercomb, R. O. Knuteson, H. M. Woolf, G. P. Anderson, M. L. Hoke, and F. X. Kneizys, 1988: Validation of FASCODE calculations with HIS spectral radiance measurements. International Radiation Symposium, Lille, France, August 18-24.

VERTICAL RESOLUTION AND ACCURACY OF ATMOSPHERIC INFRARED  
SOUNDING SPECTROMETERS

Hung-Lung Huang, William L. Smith and Harold M. Woolf

Cooperative Institute for Meteorological Satellite Studies  
University of Wisconsin, Madison

ABSTRACT

A theoretical analysis is performed to evaluate the accuracy and vertical resolution of atmospheric profiles obtained with the HIRS/2, GOES I/M and HIS instruments. In addition, a linear simultaneous retrieval algorithm is used with aircraft observations to validate the theoretical predictions. Both theoretical and observational results clearly indicate that the accuracy and vertical resolution of the retrieval profile would be improved by high spectral resolution and broad spectral coverage of infrared radiance measurements.

The HIS is found to possess the equivalent of 10 pieces each of temperature and water vapor independent precise measurements. The characteristics for temperature include a vertical resolution of 1-6 km with an accuracy of 1K, and for water vapor a vertical resolution of 0.5-3 km with an accuracy of 3K in dewpoint temperature. The HIS is a factor of almost five times better in vertical resolution and a factor of two times better in accuracy than the GOES I/M and HIRS/2 filter radiometers.

## 1. Introduction

Radiance measurements by satellite borne multispectral infrared radiometers are used to sense atmospheric temperature and moisture profiles (Kaplan, 1959; Wark and Fleming, 1966; Smith and Woolf, 1976; Susskind et al., 1984). Because the radiances arise from very thick layers of the atmosphere, the poor vertical resolution and associated accuracy of the derived profiles limit their use in Numerical Weather Prediction (NWP) (Bengtsson 1979; Phillips et al., 1979; Smith 1991). The presence of clouds which absorb infrared radiation further complicates the derivation of the sounding profiles from the radiance observations (Chahine, 1974/77/82) and also limits their utility in NWP.

The poor vertical resolution of current operational satellite sounding instruments is attributable, in part, to low spectral resolution. Due to this coarse spectral resolution, the radiometer does not sense radiation between individual absorption lines so that the emitted radiance reaching the satellite is a mixture of radiation from the high atmosphere, due to the strong absorption near line centers, and radiation from the lower atmosphere, from between the absorption lines. Thus, the relatively poor spectral resolution of current instruments causes a vertical smearing of the atmospheric structure.

To minimize vertical smearing and thereby approach the ultimate vertical sounding resolution and accuracy achievable with passive measurements, a sounding instrument

must possess a spectral resolving power (defined by  $\lambda/\delta\lambda$ , where  $\lambda$  is wavelength) of at least 1000. For example, a spectral resolution of  $0.7 \text{ cm}^{-1}$  is required in the 600-700  $\text{cm}^{-1}$  (15  $\mu\text{m}$ ) thermal emission band of  $\text{CO}_2$ . This spectral resolution can be achieved using a Michelson interferometer (Smith et al., 1979/83/90) or a large detector array grating spectrometer (Chahine et al., 1990). The High-resolution Interferometer Sounder (HIS) and Advanced InfraRed Sounder (AIRS) are experimental instruments designed to demonstrate improved sounding performance from high spectral resolution and continuous broad spectral coverage. An aircraft model of HIS is a Michelson interferometer with a spectral resolving power of approximately 2000, covering a spectral range of 3.7-16.7  $\mu\text{m}$  (Smith et al., 1983). The AIRS is to achieve measurement characteristics similar to HIS by incorporating new cooled focal plane detector array technology into a grating spectrometer (Chahine et al., 1990).

In this paper, the linear simultaneous retrieval algorithm (Smith et al., 1987/91) along with the theoretical vertical resolution (Backus and Gilbert, 1970, Conrath, 1972, Thompson, 1982, and Rodgers, 1987) and error analysis (Rodgers, 1987 and Smith et al., 1991) are used to quantify the vertical resolution and accuracy provided by three different sounding instruments: (1) the GOES I/M sounding radiometer; (2) the HIRS/2 aboard the NOAA satellites; and (3) the HIS sounding instrument proposed for future GOES implementation.

## 2. Data

HIS data have been successfully collected from NASA U2/ER2 aircraft flights (Smith et al., 1987; Revercomb et al., 1988). With observations at a six second sampling interval from the height of 65,000 ft, an instantaneous ground resolution of 2 km is achieved. Figure 1 shows a clear sky spectrum of brightness temperature observed during the COoperative Huntsville Meteorological EXperiment (COHMEX), with a spectral resolution of about  $0.5 \text{ cm}^{-1}$  from  $600\text{-}1100 \text{ cm}^{-1}$  ( $9.1\text{-}16.7 \text{ }\mu\text{m}$ ), and  $1.0 \text{ cm}^{-1}$  resolution from  $1100\text{-}2700 \text{ cm}^{-1}$  ( $3.7\text{-}9.1 \text{ }\mu\text{m}$ ) (Huang, 1989). Major absorbing constituents are labeled accordingly, namely,  $\text{CO}_2$ ,  $\text{H}_2\text{O}$ ,  $\text{O}_3$ ,  $\text{N}_2\text{O}$ ,  $\text{CH}_4$  and  $\text{CO}$ . The selected weighting functions for the three HIS infrared bands are presented in Figures 2 and 3. These curves express the vertical derivative of atmospheric transmittance with respect to the natural logarithm of pressure and are calculated from a line-by-line model FASCODE II (Clough et al., 1986) using FASCODE standard atmosphere profile conditions. As for the GOES I/M and HIRS/2 data, they are simulated from the HIS radiance spectra by convolution with their spectral response functions.

## 3. Retrieval Algorithm, Vertical Resolution and Error

### Analysis Methods

#### a. Linear Simultaneous Retrieval Algorithm

A computationally efficient retrieval methodology has been developed by Smith et al., (1991), which is a unique linear algorithm that simultaneously retrieves temperature and absorbing constituent profiles (i.e. water vapor, ozone, methane et al.) from observations of spectral radiances. The Radiative Transfer Equation (RTE) linearization results from a definition for the deviation of the true gas concentration profiles from an initial state in terms of the deviation of their "effective" temperature profiles from the true atmospheric temperature profile. The "effective" temperature profile for any absorbing constituent is defined as that temperature profile which satisfies the observed radiance spectra under the assumption that the initial absorber concentration profile is correct. Differences between the effective temperature, derived for each absorbing constituent, and the true atmospheric temperature are proportional to the error in the initial state of the gas concentration profiles. The gas concentration profiles are thus determined after inversion of the linearized RTE from the retrieved effective temperature profiles assuming that one of the assumed concentration profiles is known (i.e. CO<sub>2</sub>).

Following the algorithm of Smith et al., 1991, the linearized RTE is

$$\delta T_{B\nu} = \beta_{\nu}^0(p_S) r_{\nu}^0(p_S) \delta T_S - \sum_{i=1}^N \int_0^{p_S} \beta_{\nu}^0(p) \delta T_i(p) r_{\nu}^0(p) d \ln r_{\nu,i}^0(p)$$

where  $\beta_{\nu}^0(p) = [\partial B_{\nu}(T^0) / \partial T] / [\partial B_{\nu}(T_B^0) / \partial T]$ ,

$N$  = the number of optically active atmospheric constituents,

$N=2$  when only the uniformly mixed gases (mainly  $\text{CO}_2$ )

and water vapor are considered,

$p_s$  = pressure with subscript  $s$  denoting the surface,

$r_{\nu}(p)$  = the total transmittance of the atmosphere above  
atmospheric pressure level  $p$ ,

$\delta(\ )$  = the difference between the true quantity and the  
initial state denoted by a superscript 0,

$\Sigma(\ )_i$  = the summation of  $i$  quantities,

$r_{\nu i}$  = the transmittance of the atmosphere for the  $i$ th  
absorbing constituent,

$T_{B\nu}$  = the brightness temperature at spectral frequency  $\nu$

$T(p)$  = the true atmospheric temperature profile,

$T_i(p)$  = the effective temperature of the  $i$ th absorbing  
constituent,

$U_i(p)$  = path length profile of the  $i$ th absorbing constituent

$$U_i(p) = 1/g \int_0^p q_i(p') dp',$$

$g$  = acceleration due to gravity,

$q_i(p)$  = mixing ratio of the  $i$ th absorbing constituent,

$\delta T_i(p) = T_i(p) - T^0(p)$ .

In matrix form, again, following Smith et al., 1991, the  
generalized statistical/physical solution of equation (1) is

$$t_r = Ct_b \quad (2a)$$

and the retrieval coefficient matrix C is

$$C = (A^* E^{-1} A + S^{-1})^{-1} A^* E^{-1} \quad (2b)$$

where subscript r denotes retrieved quantity. The elements of the weighting function matrix A are

$$A_{r,0} = \beta_{r,0}^0(p_s) r_{r,0}^0(p_s)$$

$$A_{r,j} = -\beta_{r,j}^0(p_{ij}) r_{r,j}^0(p_{ij}) \ln r_{r,i}^0(p_{i..j}), \quad j=1,2,\dots,N \cdot M_i,$$

where N is the number of constituents and  $M_i$  is the number of quadrature pressure levels denoted to each constituent. S is the sample statistical covariance matrix and E is the covariance of the brightness temperature error ( )<sup>\*</sup> denotes the matrix transpose, and ( )<sup>-1</sup> denotes the matrix inverse.

#### b. Analysis of Retrieval Vertical Resolution

The vertical resolution of the various sounding instruments is analyzed using the concepts of Backus and Gilbert (1970), Conrath (1972), Thompson (1982) and Rodgers (1987). The retrieved temperature can be expressed as a smooth version of the true temperature profile,

$$T_r(p_i) = \sum_j R(p_i, p_j) T(p_j) \quad (3)$$

where  $T_r(p_i)$  is the retrieved temperature at pressure level i,  $T(p_j)$  is the true temperature profile, and  $R(p_i, p_j)$  is the vertical resolution function or averaging kernel for

level  $p_i$ . (3) describes the retrieved temperature at any level  $p_i$  as a vertical average of the true temperature profile weighted by the vertical resolution function  $R$  for the level  $p_i$ . In terms of the sounding retrieval algorithm given by (2)  $t_r = Ct_b$ , and the RTE (1), written in matrix notation as  $t_b = At$ , then one can rewrite  $t_r$  as

$$t_r = CA t$$

$$= R t.$$

with

$$R = (A^* E^{-1} A + S^{-1})^{-1} A^* E^{-1} A \quad (4)$$

It has been found that the concept of resolution is vague and has many possible definitions (Thompson, 1982 and Rodgers, 1987). Backus and Gilbert (1970) defined the "spread" as a measure of the resolution and used to quantify the vertical resolution of a retrieval system using satellite radiance measurements. However, Newman (1979) and Thompson (1982) have pointed out that the definition of spread suffers from several mathematical deficiencies which are caused by the oscillatory sidelobes of resolution functions that results in an unreliable estimations of the resolution. The mathematical difficulties become increasing severe with increasing spectral resolution and measurement precision. The computations of spread of HIS, HIRS/2 and GOES I/M (not shown) also confirm these findings.

It is these difficulties that motivate the development of an alternative technique to define an effective vertical

resolution, which would directly apply to any satellite retrieval system. The appendix gives an abbreviated derivation of this technique (Purser, personal communication) which will be discussed in complete detail in a subsequent article. If one lets  $J$  be the trace of matrix  $R$ , than  $J$  can be thought as the total effective degrees of constraint (independent precise measurement) imposed by the satellite data. The measure of the local effective data density is

$$\rho_i = \sum_j F_{i,j} R_{j,j}$$

where

$$F_{i,j} = R_{j,i}^2 / \left( \sum_k R_{j,k}^2 \delta Z_k \right),$$

$\delta Z_k$  is the height increment at the level  $k$ . And the vertical resolution defined in terms of data density is simply,

$$W_i = 1/\rho_i \tag{5}$$

### c. Analysis of Retrieval Error

Within the framework of the linear simultaneous inversion theory, a retrieval error analysis algorithm is developed following the concepts of Rodgers (1987).

The covariance of the retrieval temperature error  $G$ ,  $G = \langle (t - t_r)(t - t_r)^* \rangle$ , can be obtained from

$$t_r = ct_b = C(t'_b + e) = C(AT + e) = CAT + Ce,$$

where angle bracket denotes expectation operator, and  $e$  is assumed to be the brightness temperature measurement error, as

$$\begin{aligned} G &= (t - CA t - Ce)(t - CA t - Ce)^* \\ &= [(I - CA)t - Ce][(I - CA)t - Ce]^* \end{aligned}$$

where  $I$  is the identity matrix. By assuming temperature,  $t$ , and random brightness temperature error,  $e$ , are uncorrelated, then

$$\begin{aligned} G &= (I - CA)tt^*(I - CA)^* + Cee^*C^* \\ &= (I - CA)S(I - CA)^* - CEC^* = V + M. \end{aligned}$$

Here

$$V = (I - CA)S(I - CA)^* \quad (6)$$

$$M = CEC^* \quad (7)$$

and  $S = tt^*$  and  $E = ee^*$ .  $V$  and  $M$  can be defined as the vertical resolution component error and the measurement noise component error, respectively (Rodgers, 1987). The total root mean square (rms) error is the square root of the diagonal elements of matrix  $G$ , if ignoring inter-level correlations, and can be written as

$$G = (A^*E^{-1}A - S^{-1})^{-1} \quad (8)$$

(8) is obtained by using the matrix identity

$$I - (X+Y)^{-1}X = (X+Y)^{-1}Y.$$

The vertical resolution error results from those components of the profile that cannot be recovered by the retrieval process. In other words, the accuracy of the retrieved profiles is limited by the vertical resolution of observations. This vertical resolution related error is the square root of the diagonal elements of the matrix  $V$  (Rodgers, 1987). The contribution to the retrieval error due to radiance measurement error is given by the square root of the diagonal elements of the matrix  $M$  (Rodgers, 1987). It should be noted that the systematic retrieval error due to the imperfection of the linearized RTE and inverse model is not included in  $G$ .

#### 4. Results

##### a. Results of Retrieval Vertical Resolution and Error

###### Analysis

Retrieval vertical resolution and error are determined for HIS, GOES I/M and HIRS/2 sounding instruments. A radiance error equivalent to a brightness temperature measurement error (or noise) of 0.25K at a scene temperature of 260K is assumed for all measurement situations. The sample covariance matrix  $S$  is derived from 400 mid-latitude global climatological atmospheric profiles (Smith et al., 1974). The global sample mean profile and FASCODE II (Clough et al., 1986) are used to calculate the spectrum of atmospheric transmittance profiles for all three instruments

considered and used for all vertical resolution and error analysis computations. The uniformly mixed constituents ( $\text{CO}_2$ ,  $\text{N}_2\text{O}$ ,  $\text{CH}_4$ ,  $\text{SO}_2$  and  $\text{CO}$ ) are combined to form a single transmittance profile so that together with water vapor the number of atmospheric transmittance components was two (ozone absorption regions are excluded in this analysis). Forty pressure levels between 0.1 hpa to 1000 hpa are considered for each of the two constituents.

Results of the retrieval vertical resolution functions  $R$  for temperature and water vapor are shown in figure 4 and 5, respectively. For temperature vertical resolution, one can see little difference in these functions (except near the surface) between HIRS/2 and GOES I/M sounding conditions. In general, both HIRS/2 and GOES I/M sounders only are able to resolve very broad vertical layers of the temperature profile. However, examination of HIS temperature vertical resolution functions (figure 4c) reveals that HIS possesses many more fine layers of temperature profile information. Similar conclusions can be made for water vapor vertical resolution functions of HIRS/2, GOES I/M and HIS. Nevertheless, the GOES I/M sounder seems to be able to obtain a little more vertical water vapor information than the HIRS/2, because of its additional tropospheric moisture channel (7.43  $\mu\text{m}$ ).

Table 1 presents the total effective degrees of constraint (precise independent measurements) for temperature and water vapor retrievals. It is found that

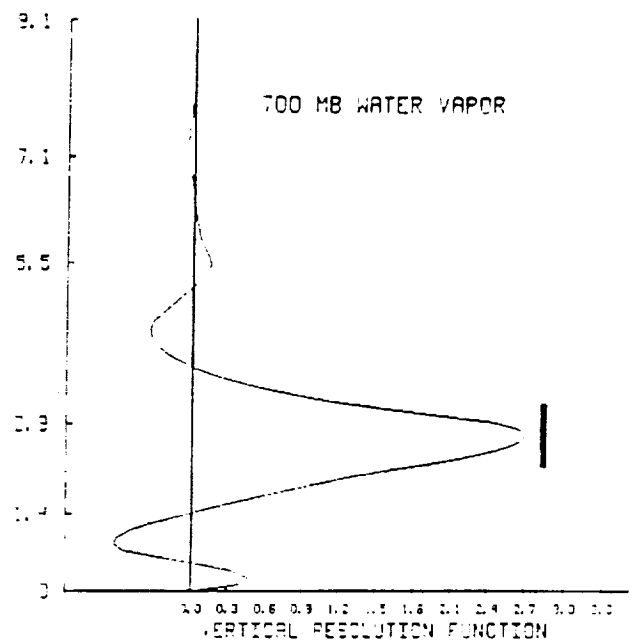
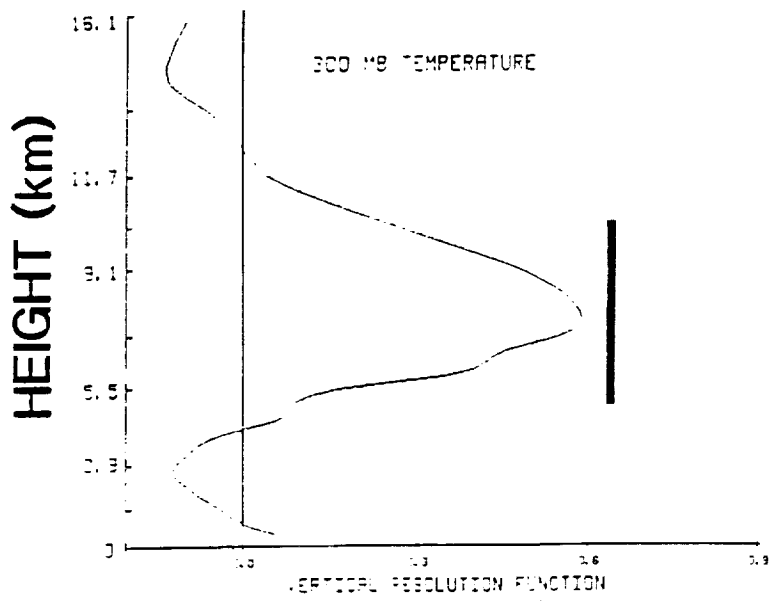


Fig 6

ORIGINAL PAGE IS  
OF POOR QUALITY

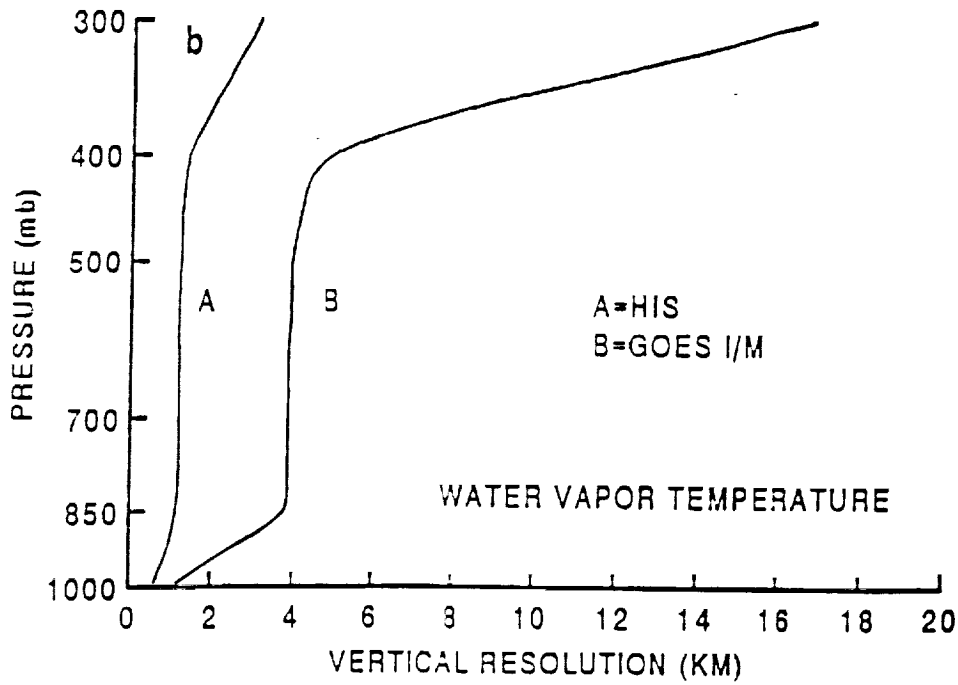
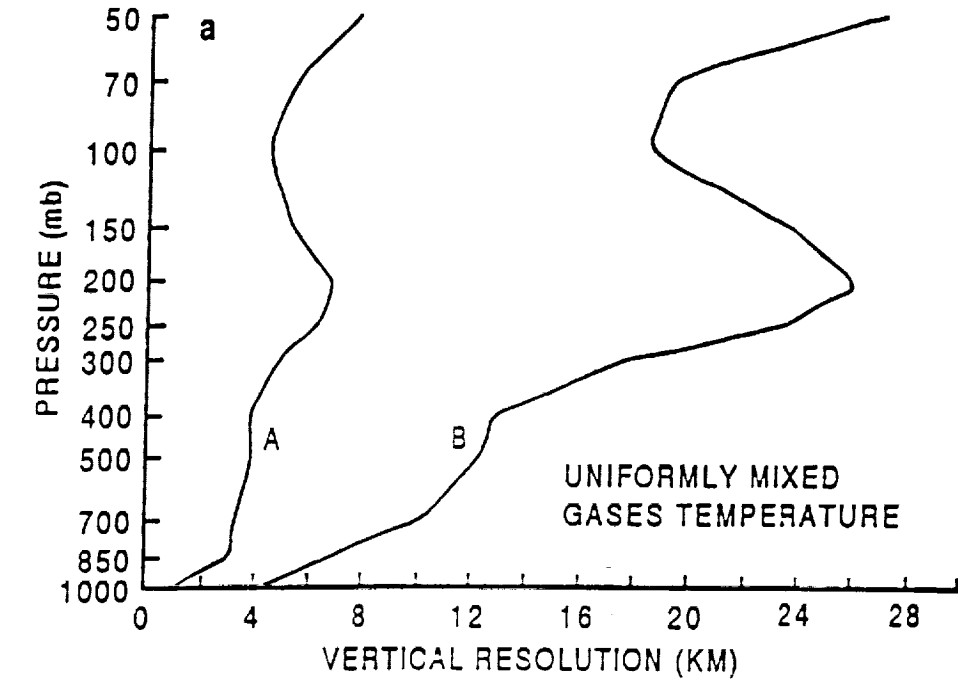


Fig 7

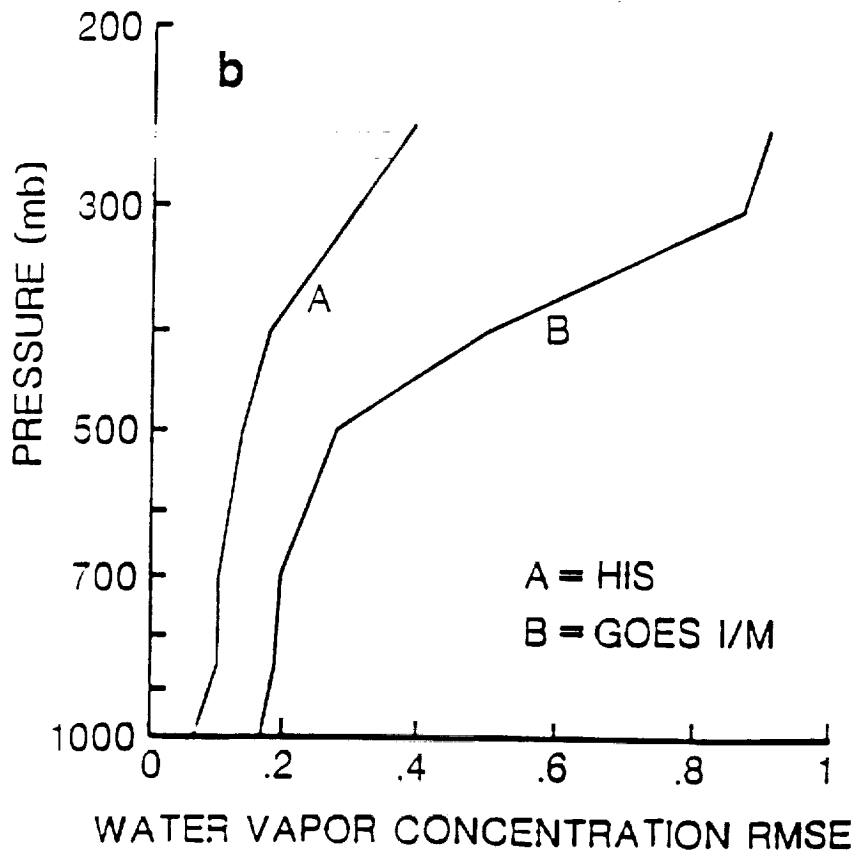
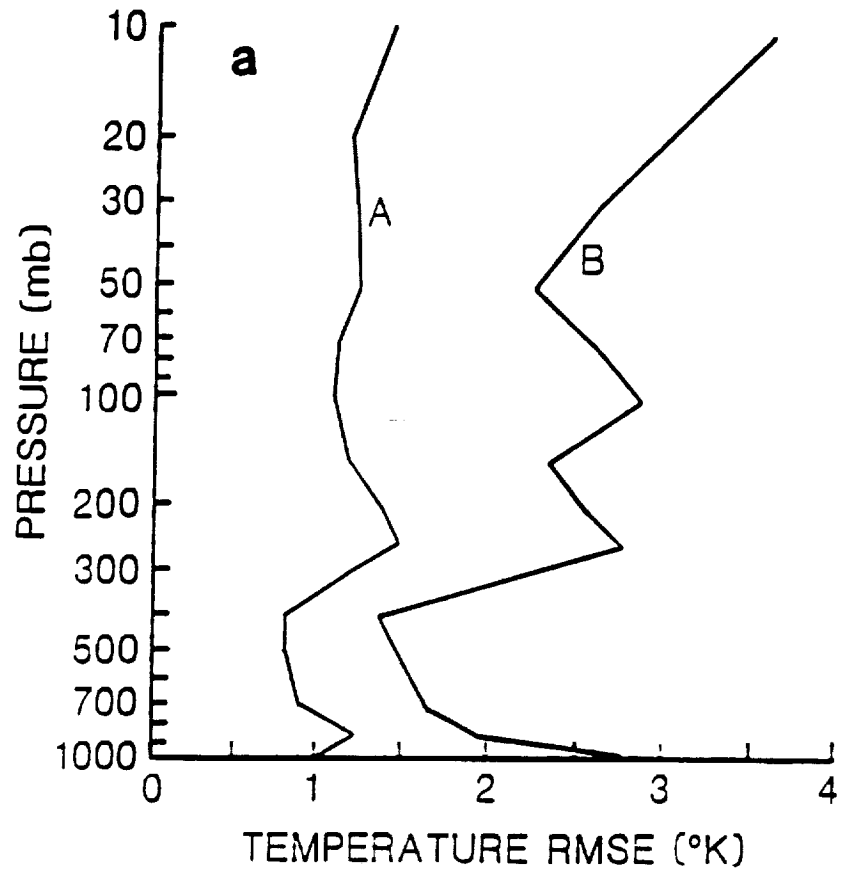


Fig 8

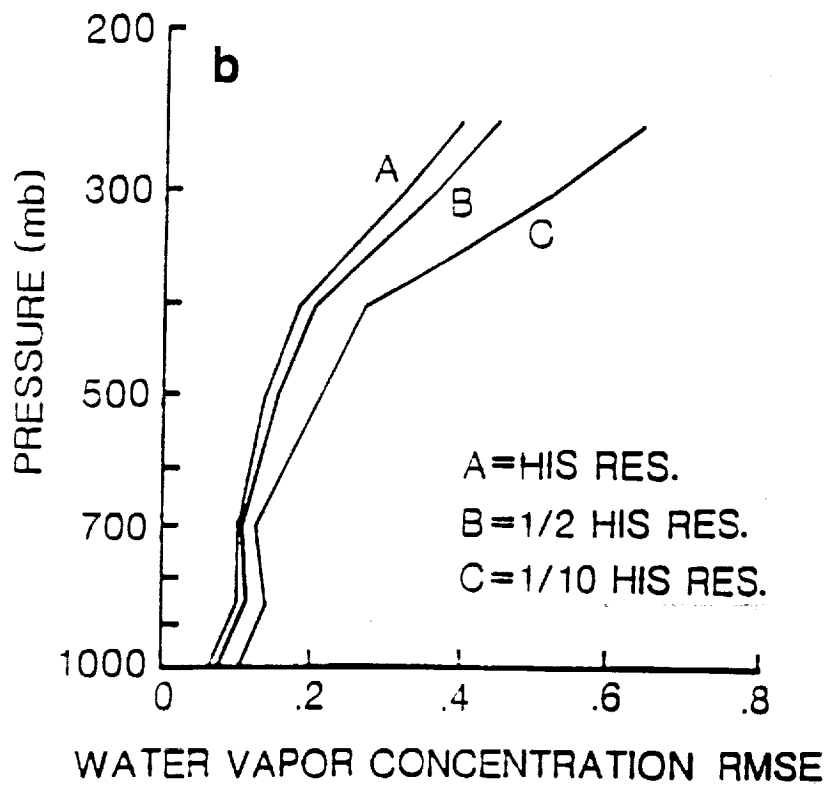
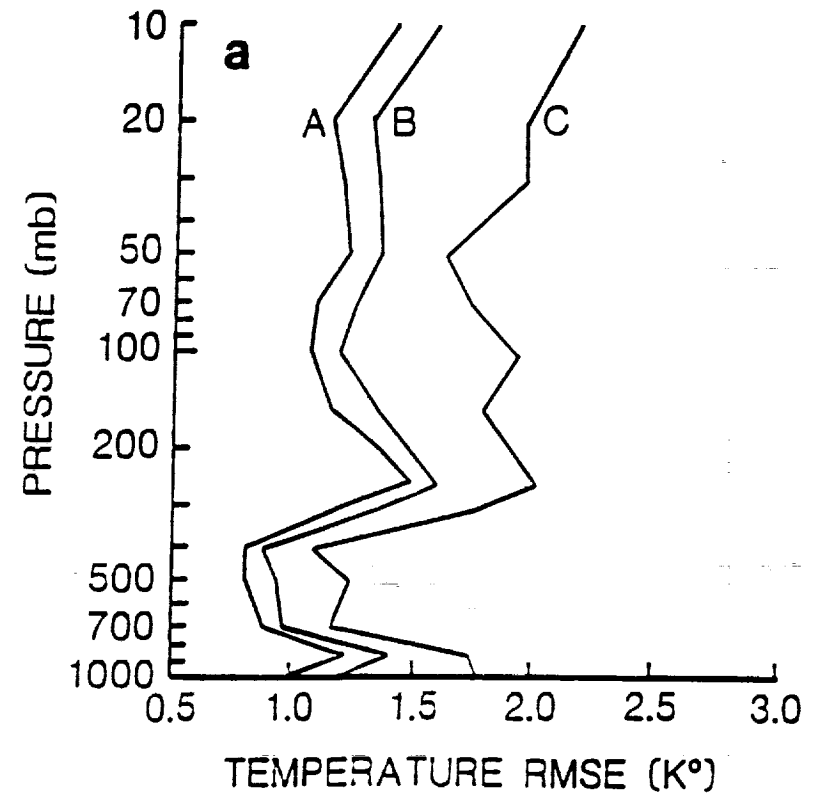


Fig 9

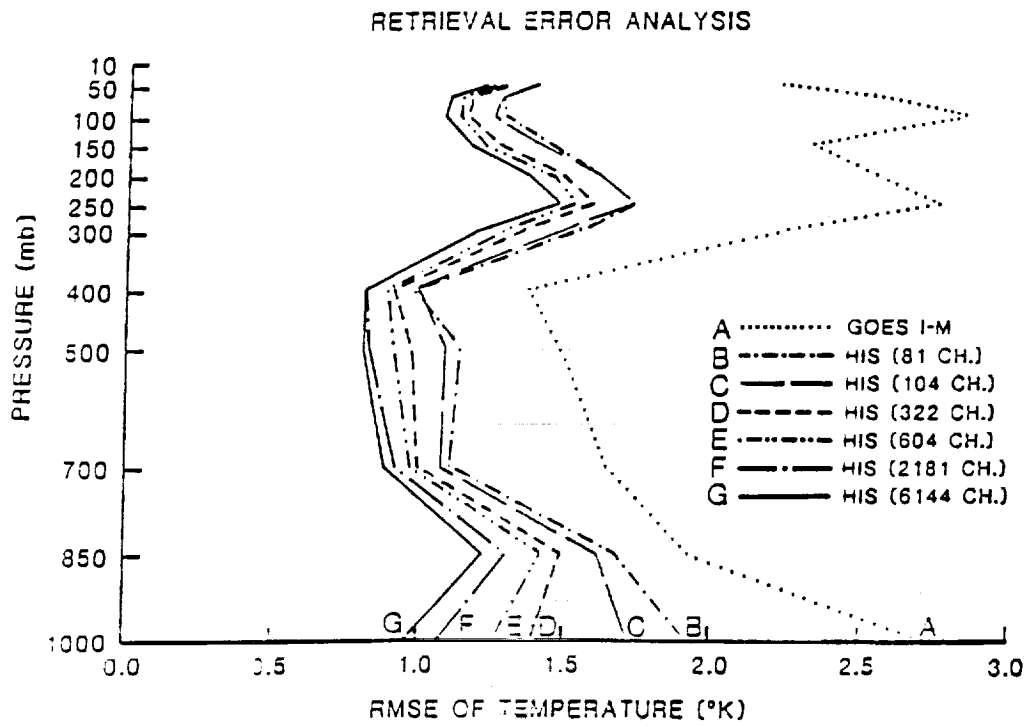


Fig 10

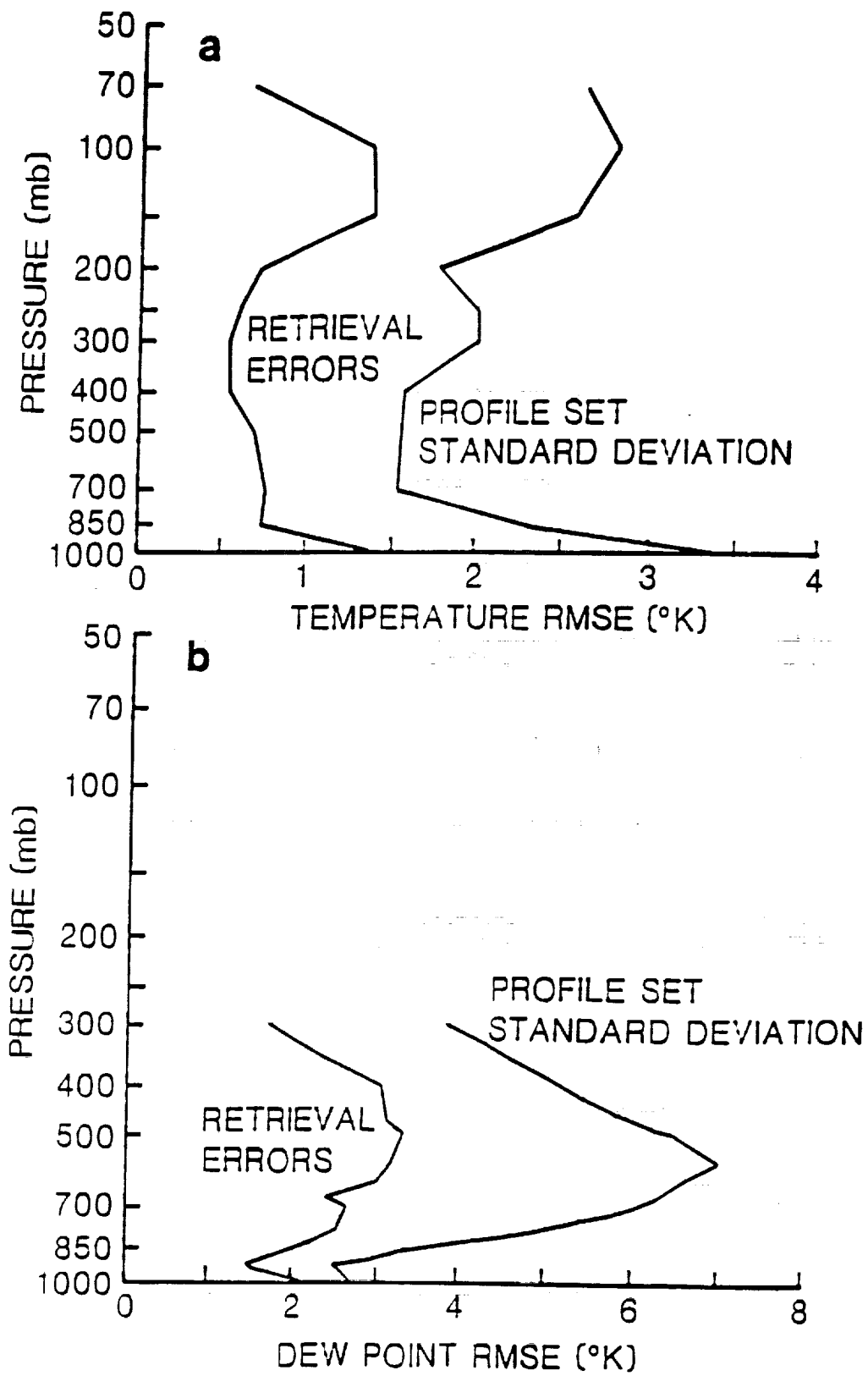


Fig 11

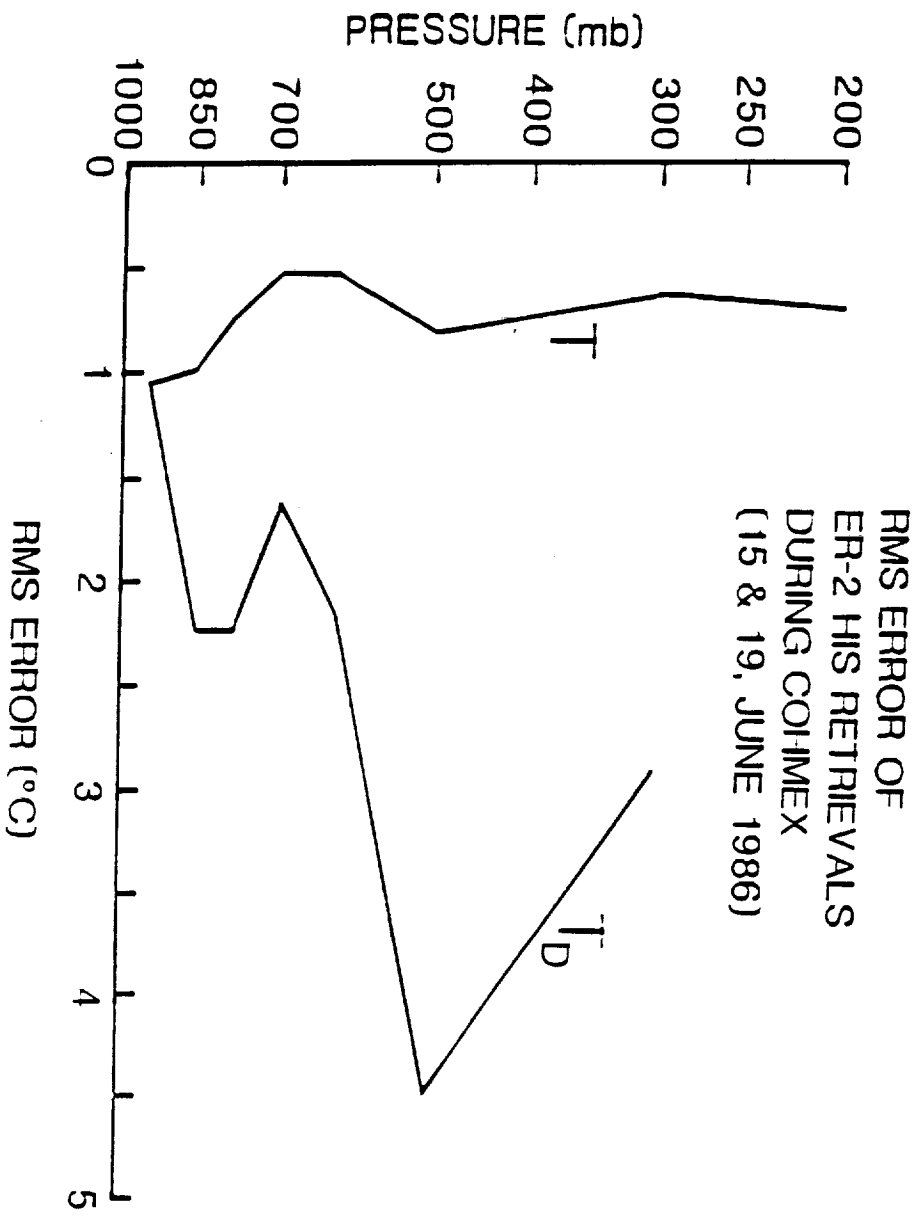


Fig 12

both HIRS/2 and GOES I/M are only able to obtain approximately two pieces each of temperature and water vapor retrievals. In particular, GOES I/M seems to possess less temperature information than HIRS/2 (1.8 vs. 2.2). In contrast to temperature, GOES I/M possesses more water vapor information than HIRS/2 (2.7 vs. 1.3). The total effective independent measurement possesses by HIS, however, has ten for each of temperature and water vapor. This indicates a factor of almost five improvement of the HIS over that of GOES I/M and HIRS/2.

Vertical resolution functions of 300 hpa temperature and 700 hpa water vapor together with their vertical resolution  $W$  obtained from (5) are shown in figure 6. The lengths of the fine vertical bars are the vertical resolution  $W$ . The examples presented in figure 6 demonstrate the reliable estimation of the vertical resolution which their function has oscillatory sidelobes. Figure 7 shows the vertical resolution computed from (5) which is defined in terms of data density and is in the unit of km. It can be seen that a major improvement in the vertical resolution of temperature and water vapor retrieval profiles is demonstrated by the HIS instrument approach.

Figure 8 shows the total rms error of HIS and GOES I/M temperature and water vapor concentration profiles. This result suggests that, consistent with the vertical resolution analysis shown earlier, sounding accuracy is improved by a factor of 2-3 over that of current radiometers

by using measurements with high spectral resolution and broad spectral coverage.

Figure 9 demonstrates the resulting total random rms error of temperature and water vapor profiles for different spectral resolutions of HIS measurements. These three spectral resolutions are the full HIS, half HIS and one tenth of HIS spectral resolution, each with the same noise (0.25 k) and spectral coverage (600-2700  $\text{cm}^{-1}$ ). The sensitivity of the retrieval error to spectral resolution is large, with the higher spectral resolution providing the most accurate sounding product.

Different "optimal" sets of HIS channels have been selected to investigate retrieval error sensitivity to the total number of spectral channels used. For each "optimal" case, those channels whose weighting functions have the greatest sensitivity to each of the forty sounding levels between 0.1 to 1000 hpa were selected for long wavelength (15  $\mu\text{m}$ ), mid wavelength (6.3  $\mu\text{m}$ ) and short wavelength (4.3  $\mu\text{m}$ ) bands, respectively (Huang, 1989). Figure 10 presents rms error of temperature for different sets of "optimal" channels. Curve A in this figure is the result obtained by using 19 GOES I/M channels and is presented as a reference. Curves B to G are based on optimally selected HIS channel sets of 81, 104, 322, 604, 2181 and 6144 (complete set). As shown in this figure, the addition of more "optimally chosen" channels does provide more independent retrieval information and results in a smaller retrieval error.

#### b. Results Of Synthetic and Aircraft Observation Retrievals

Figure 11 shows the rms error of sounding retrievals from HIS radiance spectra synthesized from an independent set of 38 special radiosondes during COHMEX. The temperature and dew point soundings were retrieved using the solution of (2) based on a dependent statistical set of 153 different COHMEX radiosondes. The guess profile used for retrieval is the mean of these 153 soundings. Figure 12 shows an estimate of the rms error of retrievals from actual HIS measurements from the NASA ER-2 aircraft for the two COHMEX days, 15 and 19 June 1986. The results in Figure 12 were obtained by Bradshaw and Fuelberg (1990) using statistical structure function analysis. As can be seen by comparing figures 11 and 12 for the COHMEX region, observational results confirm the theoretically expected accuracies close to 1 K for temperature and 3 K for dewpoint temperature.

#### 5. Conclusions

The theoretical retrieval vertical resolution and profile accuracy of GOES I/M, HIRS/2 and HIS are quantified and compared by using a linear simultaneous retrieval algorithm and vertical resolution and error analysis techniques. These observed and simulated retrievals indicate that high spectral resolution and broad spectral coverage are indeed the key to both the improved vertical resolution and the profile accuracy that results.

In conclusion, the passive remote atmospheric sounding of HIS is found to possess the equivalent of 10 pieces each of temperature and water vapor independent precise measurements. The characteristics for temperature include a vertical resolution of 1-6 km with an accuracy of 1K, and for water vapor a vertical resolution of 0.5-3 km with an accuracy of 3K in dewpoint temperature. The HIS is a factor of almost five times better in vertical resolution and a factor of two times better in accuracy than the GOES I/M and HIRS/2 filter radiometers.

Acknowledgments. The authors are grateful for stimulating discussions with professor Owen Thompson. The authors are indebted to R.J. Purser, CIMSS/UW for developing the theory of effective resolution provided in the appendix to this paper. This research was supported by NASA Grant NAS8-36169 and NAGW-1831.

## APPENDIX

### A Theory of Effective Resolution

Let vertical resolution functions matrix  $R$  be defined as in (4), and from the fact that the precision matrices  $(A^*E^{-1}A)$  and  $S^{-1}$  are nonnegative symmetric matrices it follows that each eigenvalue  $\lambda$  of  $R$  is bounded within the interval  $[0,1]$  and since the sum of nonvanishing eigenvalues is simply the trace of the matrix,

$$J = \text{Tr}(R) \tag{A1}$$

it can be found that

$$0 \leq J \leq M \tag{A2}$$

where  $M$  is the number of independent measurements. The case  $J=0$  occurs in the singular limit of vanishing measurement precision,  $E^{-1} \rightarrow 0$ , and implies no effect of the satellite measurements on the retrieval, while the case  $J=M$  occurs only in the case of infinite measurement precision,  $E \rightarrow 0$ , and implies a retrieval that always fits all measurements exactly. Thus it seems at least intuitively reasonable to consider  $J$  to be a measure of the total effective degrees of constraint imposed by the satellite data used in the retrieval.

It would be useful to be able to extrapolate from the measure  $J$  of the effective total quantity of satellite data to a measure of the local effective retrieval density. The simplest choice that integrates to  $J$  would be,

$$\rho'_i = R_{i,i} / \delta Z_i \quad (A3)$$

where  $\delta Z_i$  is the height increment of the level  $i$ . In theory there is no guarantee that some components  $R_{i,i}$  are not negative and in practice the distribution  $\rho'$  is invariably noisy. However, it is observed (Purser, personal communication) that, averaged locally over a scale comparable with that implied by the structure of the corresponding rows and columns of  $R$ , the typical magnitudes of  $\rho'$  genuinely reflect the local density of distinct measurements when these measurements are precise and are themselves localized. A serviceable measure of local effective data density  $\rho$  is therefore given by applying a unimodular nonnegative smoothing operator  $F$  to  $\rho'$ , that is,

$$\rho_i = \sum_j F_{i,j} R_{j,j} \quad (\text{A4})$$

with

$$\sum_i F_{i,j} \delta Z_i = 1 \quad (\text{A5})$$

For the univariate data one need look no further than R itself to find the material from which to construct a smoother with the desired qualities. Of the two natural definitions,

$$F^{(a)}_{i,j} = R^2_{i,j} / \sum_k R^2_{k,j} \delta Z_k \quad (\text{A6})$$

$$F^{(b)}_{i,j} = R^2_{j,i} / \sum_k R^2_{j,k} \delta Z_k \quad (\text{A7})$$

the first is more universal in the sense that it continues to apply when the retrieval formalism is generalized to an "optimal interpolation" (Daley, 1991) that incorporate point-like measurements (such as radiosonde temperature observations), but the second method has been found to yield superior estimates when, as in the present study, attention is confined exclusively to remotely sensed data whose weighting functions (the rows of A) are mainly much smoother than the covariance profiles (rows of S). It is the second form, (A7), that is therefore adopted here.

#### REFERENCES

- Backus G. and Gilbert, 1970: Uniqueness in the inversion of inaccurate gross earth data. Phil. Trans. Roy. Soc. London, A266, 123-192.
- Bengtsson, L., 1979: Problems of using satellite information in numerical weather prediction. Proc. of a Technical Conference, ESA SP-143, 87-100.

- Bradshaw, J.T. and H.E. Fuelberg, 1990: HIS analysis of mesoscale phenomena. Preprints of Fifth Conference on Satellite Meteorology and Oceanography, AMS, London, 5pp.
- Chahine, M.T., 1974: Remote sounding of cloudy atmospheres. I. The single cloud layer. J. Atmos. Sci., 31, 233-243.
- Chahine, M.T., 1977: Remote sounding of cloudy atmospheres. II. Multiple cloud formations. J. Atmos. Sci., 34, 744-757.
- Chahine, M.T., 1982: Remote sensing of cloud parameters. J. Atmos. Sci., 39, 159-170.
- Chahine, M.T., F.G. O'Callaghan, H.H. Aumann, R.W. Capps, R.D. Haskins, R.J. Pagano, and R.A. Schindler, 1990: Atmospheric Infrared Sounder (AIRS) - Science and Measurement Requirements. Jet Propulsion Laboratory.
- Clough, S.A., F.X. Kneizys, E.P. Shettle, G.P. Anderson, 1986: Atmospheric radiance and transmittance : FASCODE 2. Six Conference on Atmospheric Radiation, AMS, Boston, MA, 141-144.
- Conrath, B.J., 1972: Vertical resolution of Temperature Profiles Obtained from Remote Radiation Measurements. J. Atmos. Sci., 29, 1262-1272.
- Daley, R., 1991: Atmospheric Data Analysis. Cambridge University Press, 457 pp.
- Huang, H.-L., 1989: An analysis of the characteristics of atmospheric profiles obtained with the High-Resolution Interferometer Sounder (HIS). Ph.D. dissertation, University of Wisconsin-Madison, 145 pp.
- Kaplan, L.D., 1959: Inference of atmospheric structure from remote radiation measurements. J. Opt. Soc. Am., 49, 1004-1007.
- Newman, W.I., 1979: The Application of Generalized Inverse Theory to the Recovery of Temperature Profiles. J. Atmos. Sci., 36, 559-565.
- Phillips, N.A., L.M. McMillin, D. Wark, and A. Gruber, 1979: An evaluation of early operational temperature soundings from TIROS-N. Bull. Amer. Meteor. Soc., 60, 1188-1197.
- Revercomb, H.E., H. Buijs, H.B. Howell, D.D. Laporte, W.L. Smith and L.A. Sromovsky, 1988: Radiometric

Calibration of IR Fourier transform spectrometers:  
Solution to a problem with the High-Resolution  
Interferometer Sounder. Appl. Opt., 27, 3210-3218.

Rodgers, C.D., 1987: A general error analysis for profile  
retrieval. RSRM 37, Advances in Remote Sensing  
retrieval Methods, A Deepak Publishing, Hampton, VA.  
285-297.

Smith, W.L., H.M. Woolf, P.G. Abel, C.M. Hayden,  
M. Chalfant, N. Grödy, 1974: NIMBUS-5 sounder data  
processing system, part I: measurement characteristics  
and data reduction procedures. NOAA Technical  
Memorandum NESS 57, Washington D.C..

Smith, W.L. and H.M. Woolf, 1976: The use of  
eigenvectors of statistical covariance matrices  
for interpreting satellite sounding radiometer  
observations. J. Atmos. Sci., 33, 1127-1140.

Smith, W.L., H.B. Howell, and H.M. Woolf, 1979: The Use of  
Interferometric Radiance Measurements for Sounding the  
Atmosphere. J. Atmos. Sci., 36, 566-575.

Smith, W.L., H.E. Revercomb, H.B. Howell and H.M. Woolf,  
1983: HIS - A satellite instrument to observe  
temperature and moisture profiles with high  
vertical resolution. Preprints of Fifth Conference  
on Atmospheric Radiation, AMS, Boston, 9 pp.

Smith, W.L., H.M. Woolf, H.B. Howell, H.-L. Huang, and  
H.E. Revercomb, 1987: The simultaneous retrieval  
of atmospheric temperature and water vapor profiles  
- applications to measurements with the High  
spectral resolution Interferometer Sounder (HIS).  
RSRM 37, Advances in Remote Sensing Retrieval Methods,  
A Deepak Publishing, Hampton, VA. 189-202.

Smith, W.L., H.E. Revercomb, D.D. Laporte, L.A. Sromovsky,  
S. Silverman, H.M. Woolf, H.B. Howell, R.O. Knuteson  
, and H.-L. Huang, 1990: GHIS - The GOES high  
resolution interferometer sounder. J. Appl. Meteo.,  
29, 1189-1204.

Smith, W.L., H.M. Woolf and H.E. Revercomb, 1991 :  
A linear simultaneous solution for temperature and  
absorbing constituent profiles from radiance  
spectra. Appl. Opt., 30, 1117-1123.

Smith, W.L., 1991 : Atmospheric Soundings from Satellites  
- False Expectation or the key to Improved Weather  
Prediction ?. Quart. J. R. Met. Soc., 117, 267-297.

- Susskind J., J. Rosenfield, D. Reuter and M.T. Chahine,  
1984 : Remote sensing of weather and climate  
parameters from HIRS2/MSU on TIROS-N.  
J. Geophys. Res., 890, 4677-4697.
- Thompson, O.E., 1982 : HIRS-AMTS Satellite Sounding System  
Test - Theoretical and Empirical Vertical Resolving  
Power. J. Appl. Meteo., 21, 1550-1561.
- Wark D.Q. and H.E. Fleming, 1966 : Indirect Measurements  
of Atmospheric Temperature Profiles from Satellite :  
I. Introduction. Mon. Weath. Rev., 94, 351-362.

Table Legends

Table 1: The total effective degrees of constraint (precise independent measurements) for temperature and water vapor retrievals obtained from GOES I/M, HIRS/2 and HIS.

	<u>GOES I/M</u>	<u>HIRS/2</u>	<u>HIS</u>
<u>TEMPERATURE</u>	1.3	2.2	10.1
<u>WATER VAPOR</u>	2.7	2.1	10.3

Table 1, the total effective degrees of constraint (precise independent measurements) for temperature and water vapor retrievals obtained from GOES I/M, HIRS/2 and HIS.

## Figure Legends

- Figure 1: Brightness temperature spectra measured by HIS from U2 aircraft over Huntsville, Alabama on 15 JUNE 1986 of COHMEX.
- Figure 2: Temperature component Planck radiance weighting functions for a small set of HIS band 1 and band 3 channels.
- Figure 3: Water vapor component Planck radiance weighting functions for a small set of HIS band 2 channels.
- Figure 4: (a) Temperature vertical resolution functions of GOES I/M sounder.
- Figure 4: (b) Temperature vertical resolution functions of HIRS/2.
- Figure 4: (c) Temperature vertical resolution functions of HIS.
- Figure 5: (a) Water vapor vertical resolution functions of GOES I/M sounder.
- Figure 5: (b) Water vapor vertical resolution functions of HIRS/2.
- Figure 5: (c) Water vapor vertical resolution functions of HIS.
- Figure 6: Vertical resolution functions and their vertical resolution (the fine vertical bars) of HIS 300 hpa temperature and 700 hpa water vapor retrievals.
- Figure 7: (a) Temperature vertical resolution (km) of HIS and GOES I/M sounder.
- Figure 7: (b) Water vapor vertical resolution (km) of HIS and GOES I/M sounder.
- Figure 8: RMS temperature and water vapor concentration retrieval errors of HIS and GOES I/M sounder.
- Figure 9: Temperature and water vapor concentration RMS errors of HIS in full resolution, half of the HIS resolution, and one tenth of the HIS resolution.
- Figure 10: Temperature RMS errors for the use of different optional selections of HIS channels and GOES I/M sounding channels.

Figure 11: Simulated temperature and dew point temperature RMS errors and standard deviation of statistical profile set from the mean profile.

Figure 12: Temperature and dew point temperature RMS error of ER-2 HIS retrievals during COHMEX (15 & 19, JUNE 1986).

HEIGHTNESS TEMPERATURE (°K)

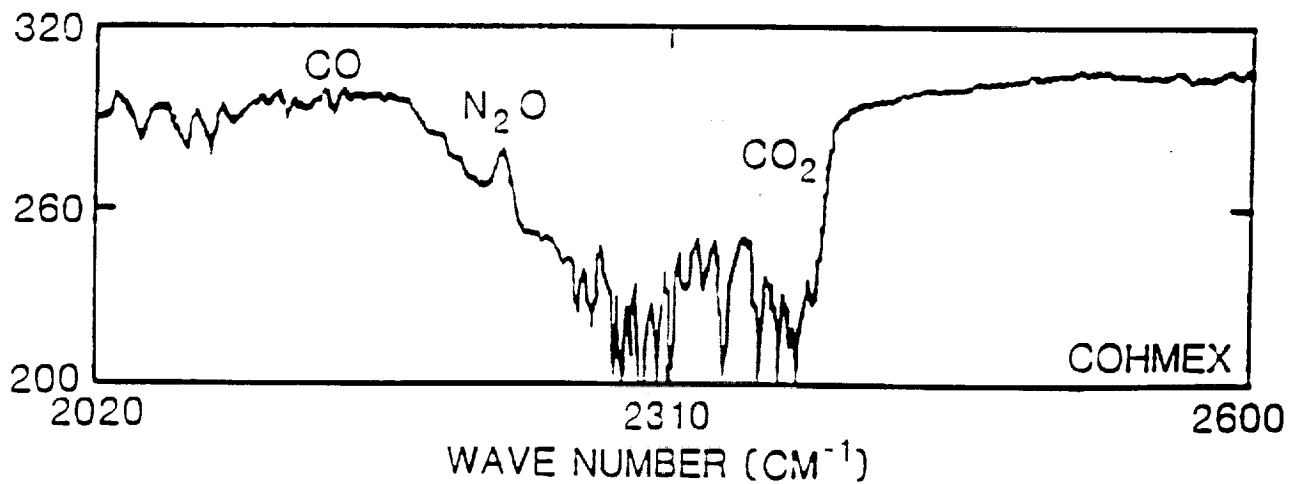
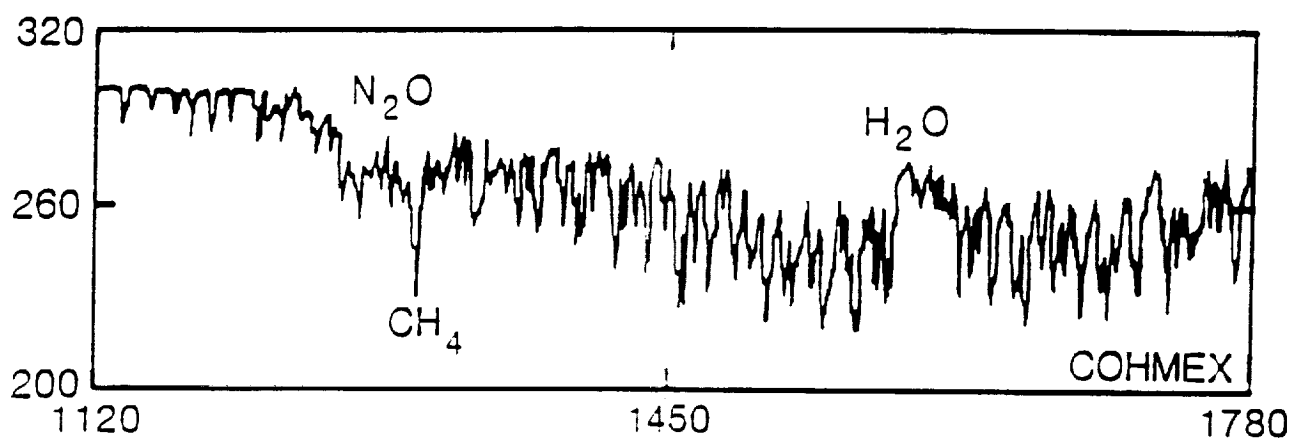
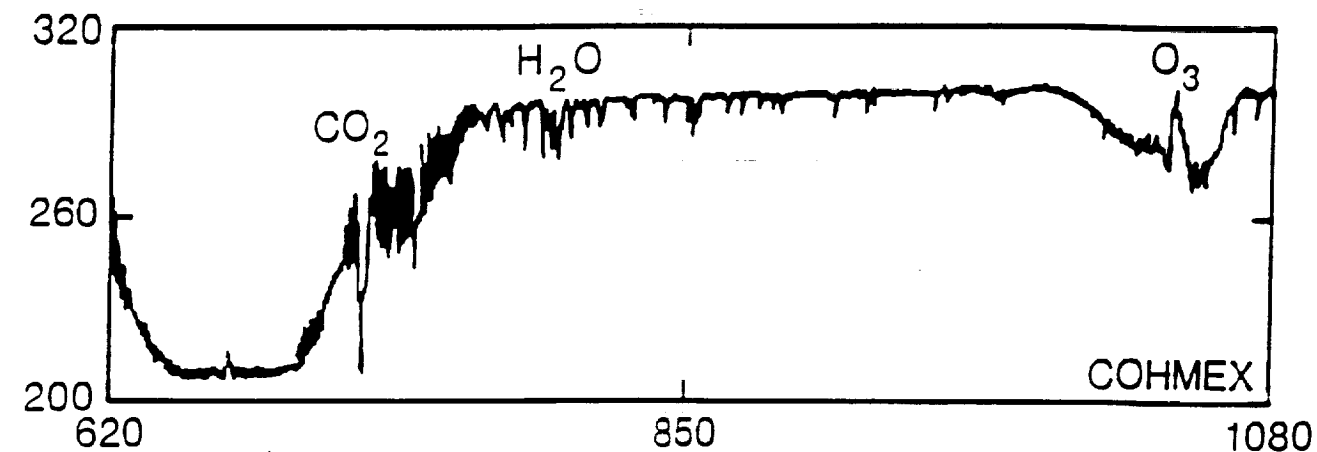


Fig 1

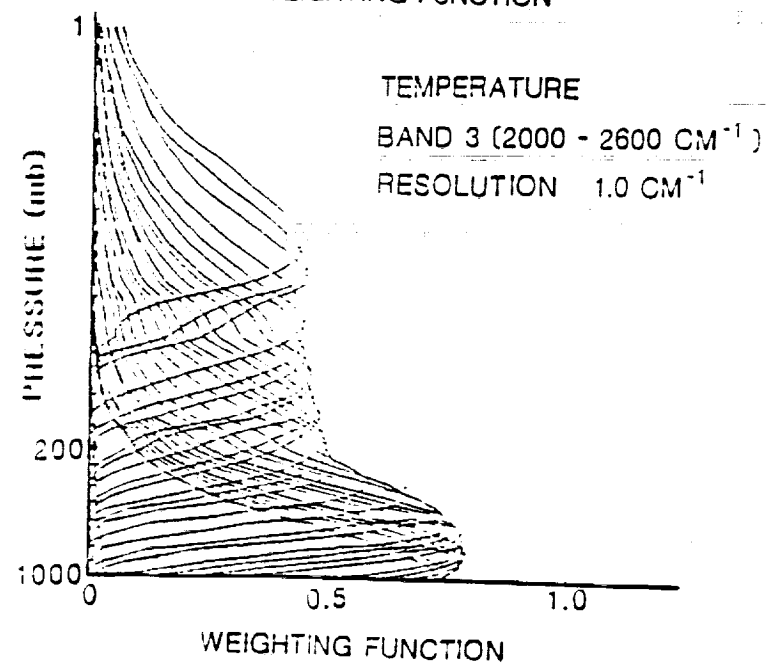
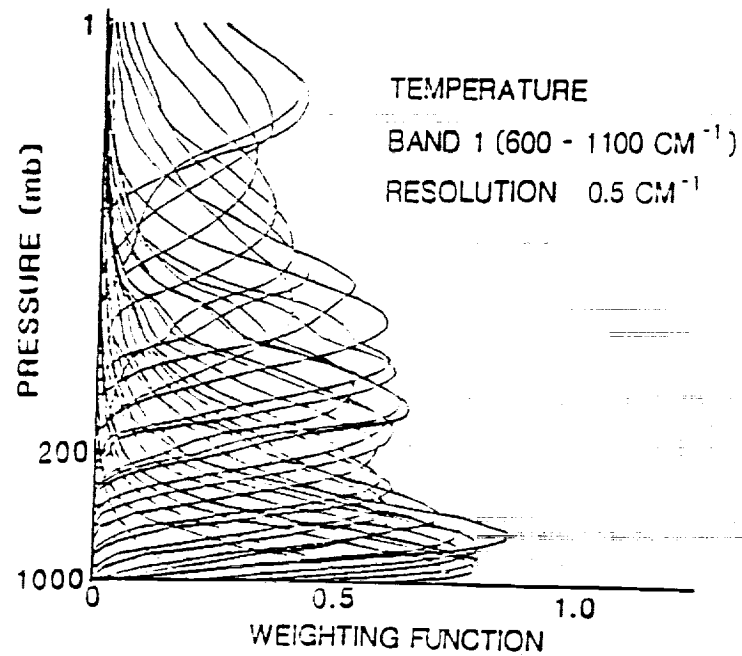


Fig 2

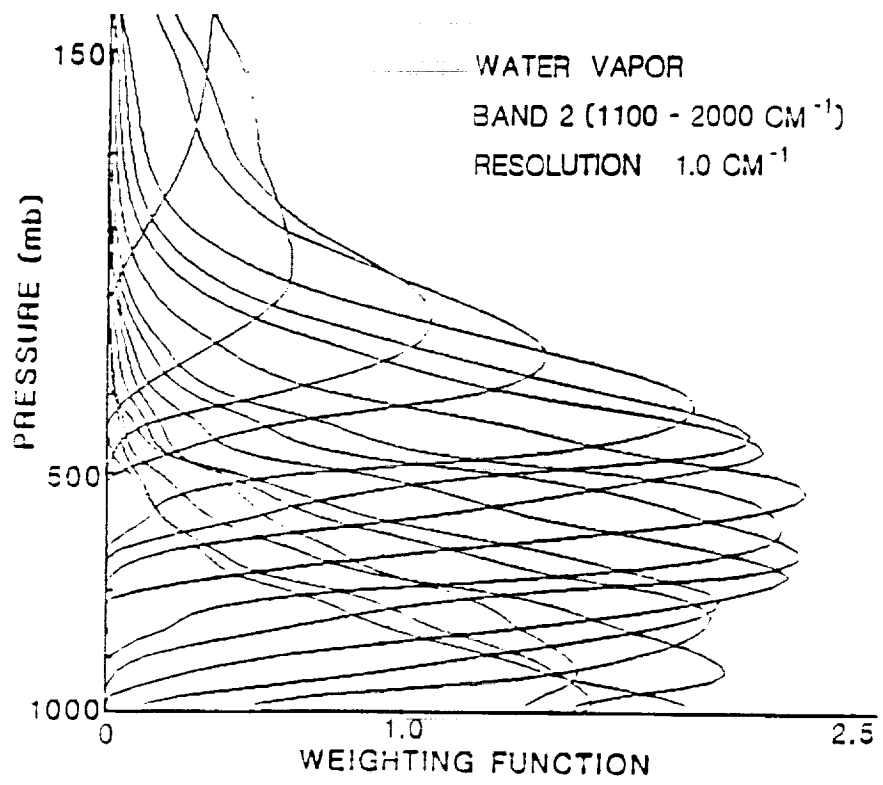


Fig 3

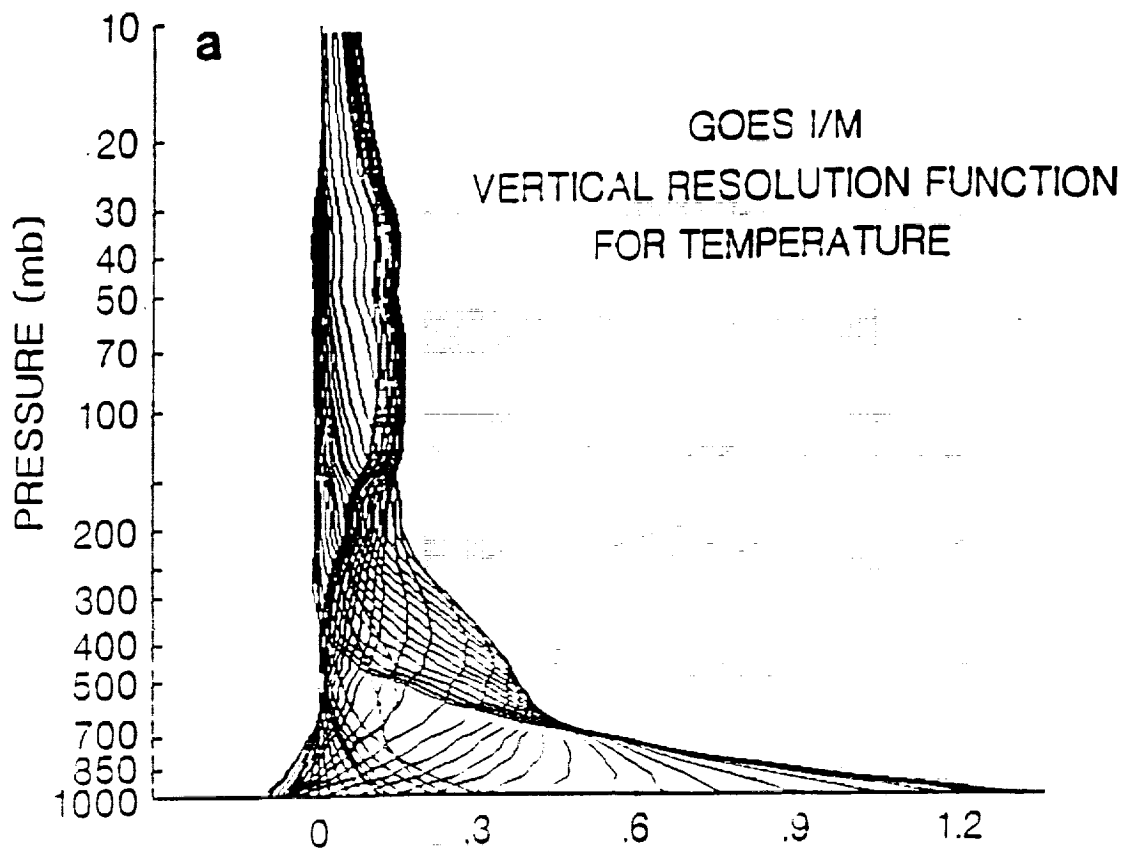


Fig 4(a)

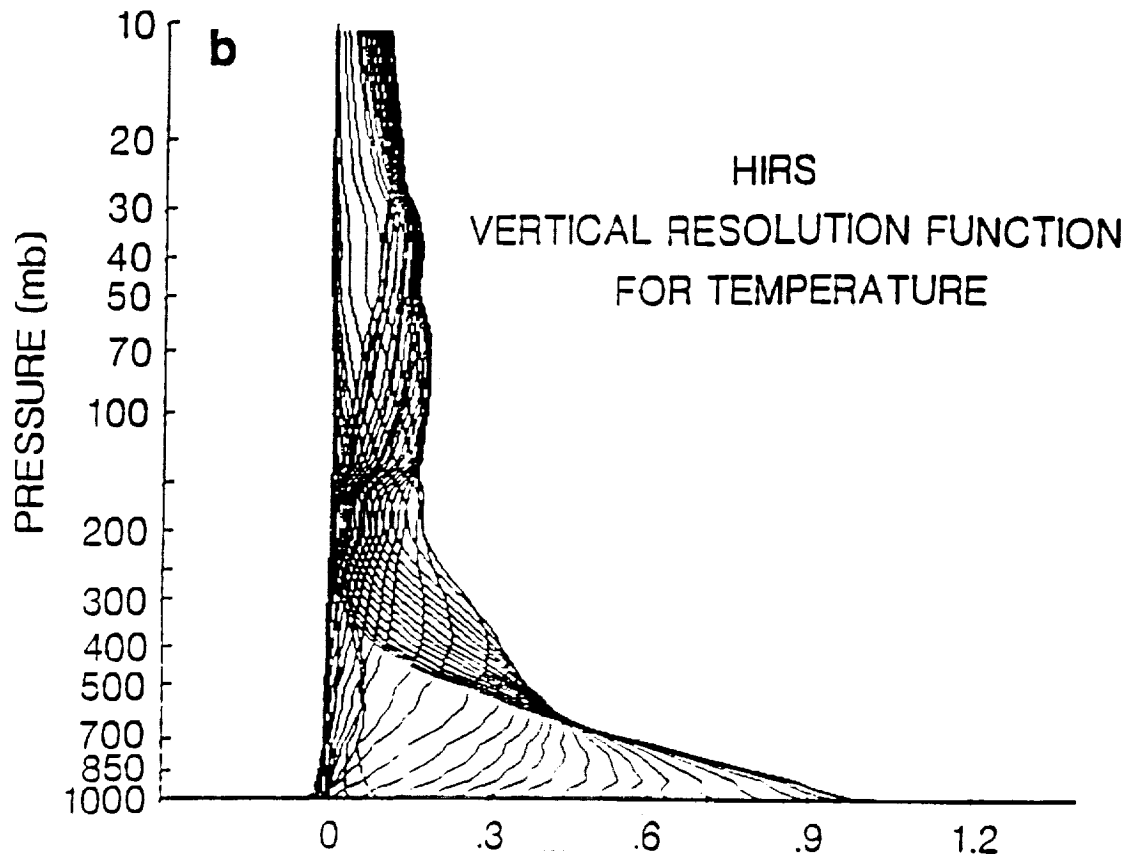


Fig 4(b)

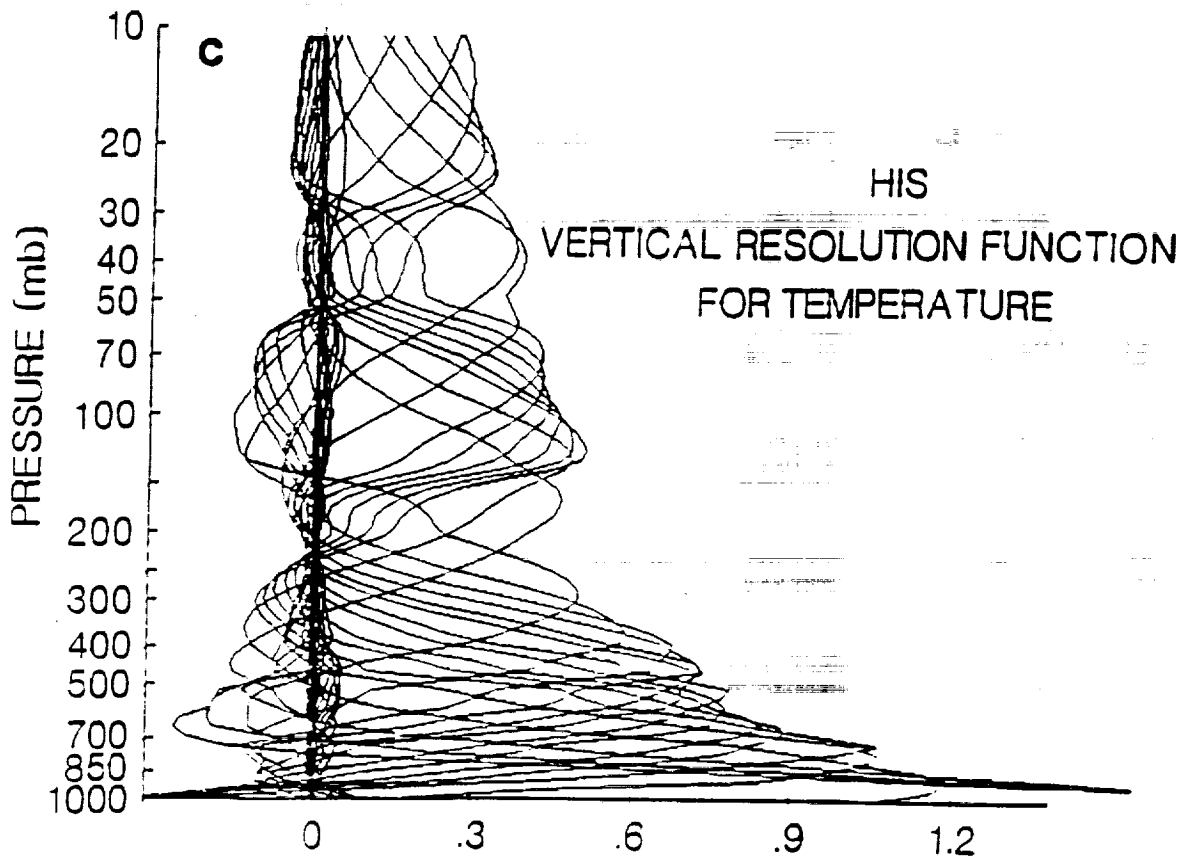


Fig 4(c)

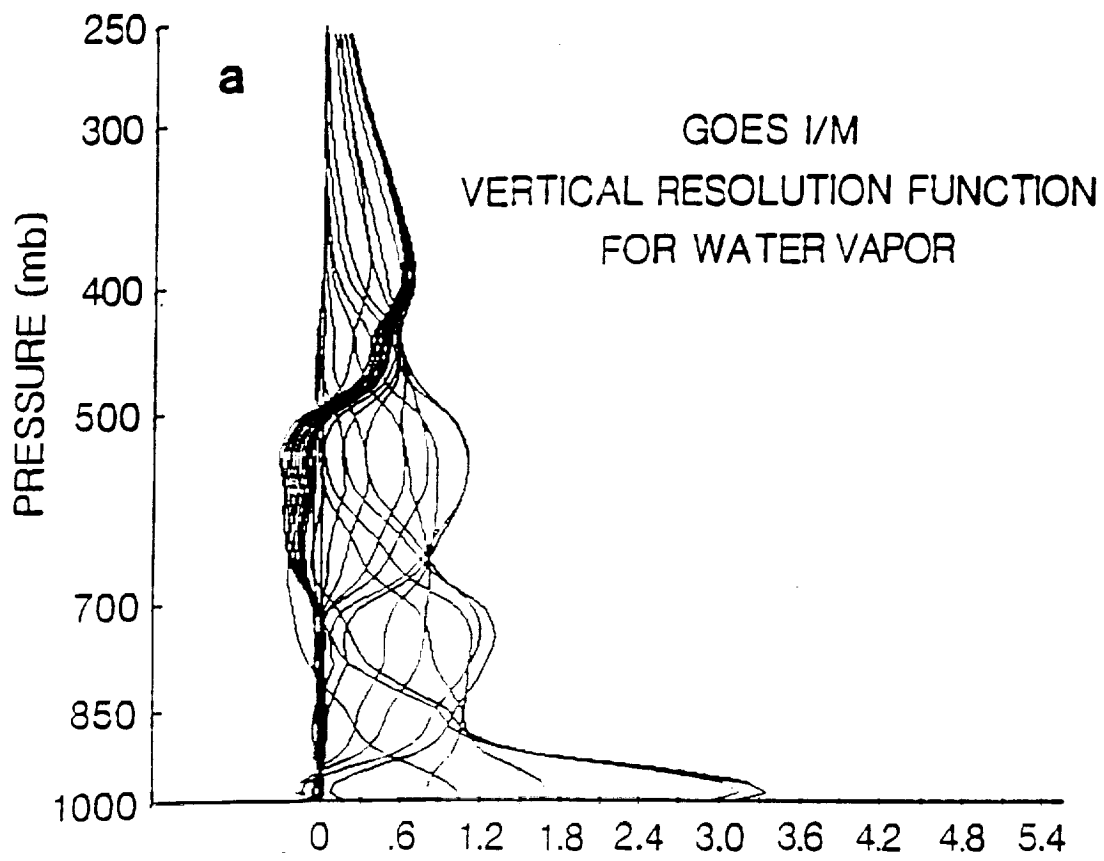


Fig 5(a)

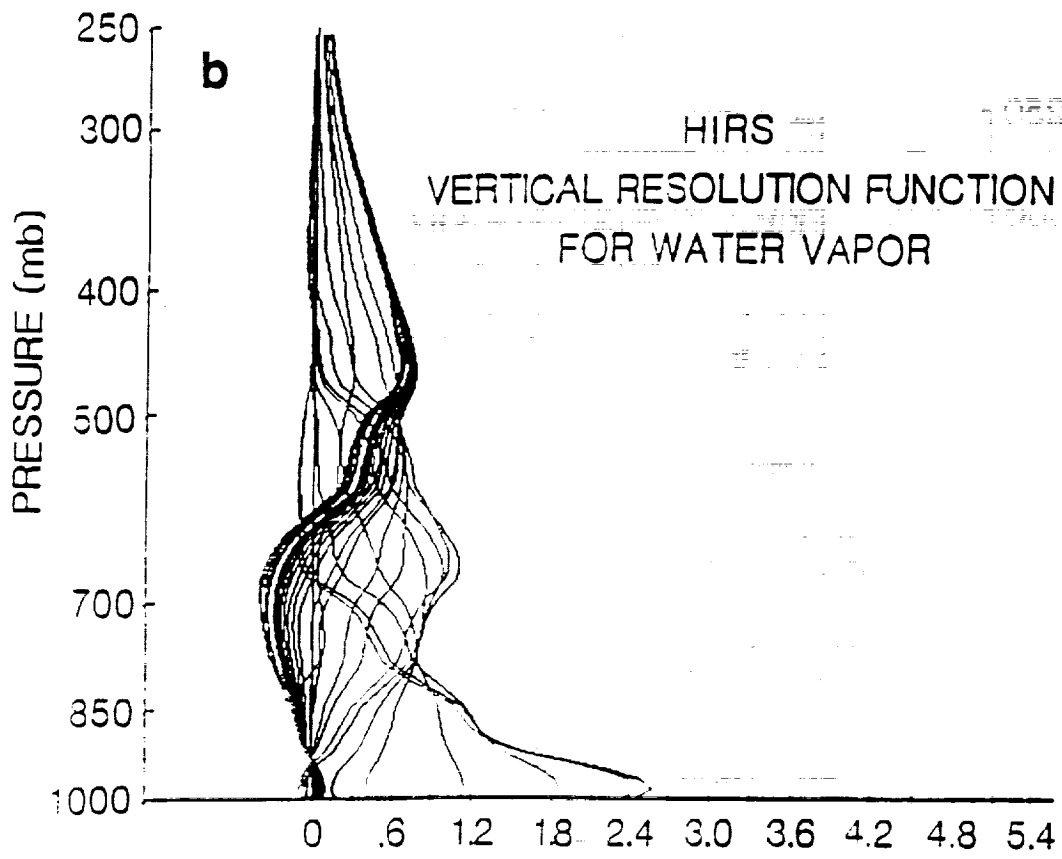


Fig 5(b)

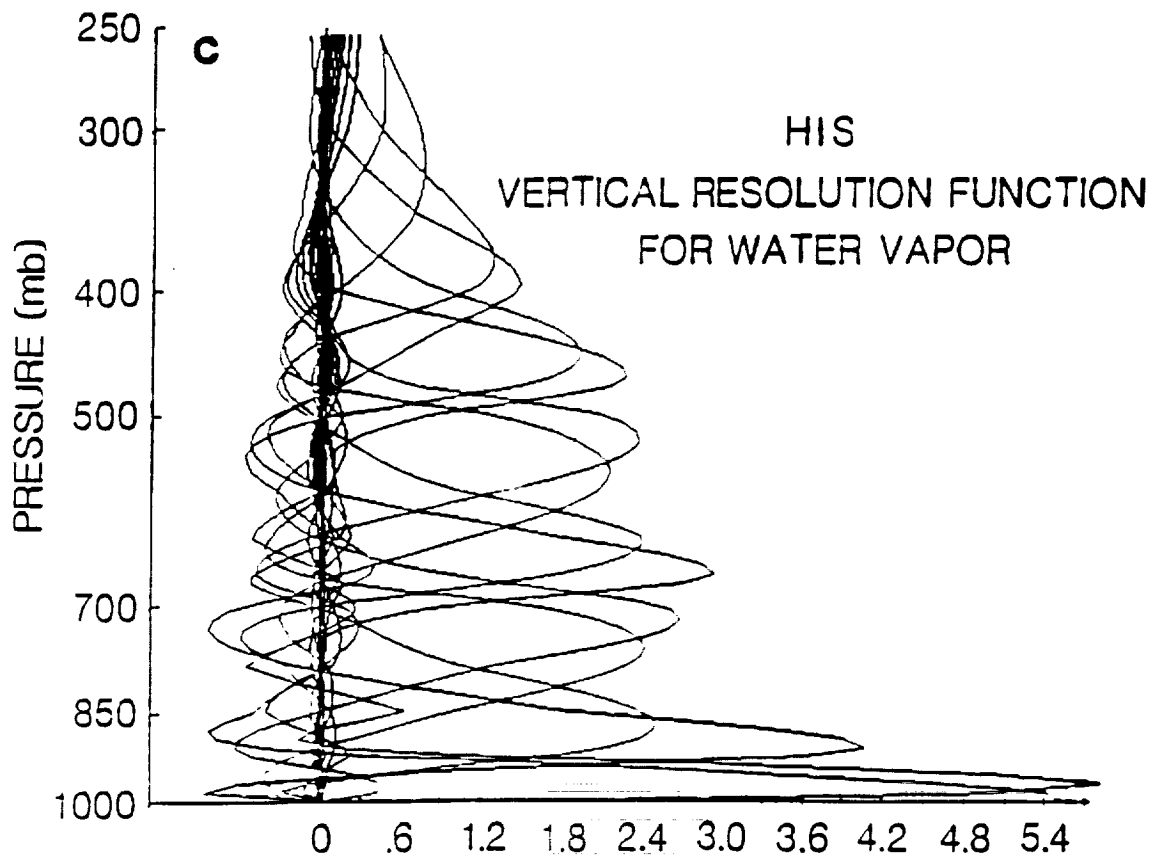


Fig 5(c)

## GHIS—The GOES High-Resolution Interferometer Sounder

W. L. SMITH,\* H. E. REVERCOMB,\* H. B. HOWELL,\* H.-L. HUANG,\* R. O. KNUTESON,\* E. W. KOENIG,<sup>‡</sup>  
D. D. LAPORTE,\*\* S. SILVERMAN,\*\* L. A. SROMOVSKY,\* AND H. M. WOOLF\*

\*Cooperative Institute for Meteorological Satellite Studies, Madison, Wisconsin

\*\*Santa Barbara Research Center, Goleta, California

‡International Telephone and Telegraph Corporation, Fort Wayne, Indiana

(Manuscript received 14 April 1989, in final form 21 June 1990)

### ABSTRACT

A high spectral resolution interferometer sounder (GHIS) has been designed for flight on future geostationary meteorological satellites. It incorporates the measurement principles of an aircraft prototype instrument, which has demonstrated the capability to observe the earth-emitted radiance spectrum with high accuracy. The aircraft results indicate that the theoretical expectation of 1°C temperature and 2°–3°C dewpoint retrieval accuracy will be achieved. The vertical resolution of the water vapor profile appears good enough to enable moisture tracking in numerous vertical layers thereby providing wind profile information as well as thermodynamic profiles of temperature and water vapor.

### 1. Introduction

Because of the temperature and water vapor profiling capabilities needed to meet the 1990s initiative for improved mesoscale weather prediction, the remarkable performance history of Michelson interferometry in space (Hanel et al. 1967, 1971, 1972, 1980; Schäfer et al. 1989), and the recent successful aircraft demonstration of the High-resolution Interferometer Sounder (HIS) technology (Revercomb et al. 1988a, 1988b, 1988c; Smith et al. 1988), the time is right to proceed with plans to place interferometer sounders on geosynchronous satellites. The objective of this paper is to show the performance improvement of the GHIS (GOES High-resolution Interferometer Sounder) over the current satellite sounding instruments, the characteristics of the instrument that emerged from a Phase A study, and the results achieved from tests of the aircraft prototype interferometer sounding instrument.

Higher vertical resolution temperature and moisture soundings from geosynchronous orbit are needed to make full use of the improved wind observations planned for the 1990s. For mesoscale weather prediction, it is important to have observations of temperature, humidity, and wind distributions that together provide information on atmospheric stability, and horizontal and vertical motion fields. Improved wind measurements will soon be available to enhance weather prediction capability in the United States, since NOAA is installing a demonstration network of 30

Doppler radar wind profilers, spaced 500 km apart, across the midwestern United States. The Doppler radars provide wind profiles on an hourly basis with an accuracy of 1 m s<sup>-1</sup> and a vertical resolution of 1 km. However, the profiler will not have the spatial coverage needed for mesoscale or regional models. GOES observations are needed to provide coverage on a finer spatial grid.

To allow atmospheric stability to be determined from GOES-acquired temperature and water vapor measurements with an accuracy consistent with profiler wind accuracy, it can be shown (using the thermal wind relationship) that the temperature and water vapor distribution must be observed with a vertical resolution of 1–2 km and an accuracy of 1°C for temperature and 3°C for dewpoint. The GOES I/M filter wheel instrument will fall far short of meeting these requirements, as will be demonstrated in the following section. Experience with GOES-VAS data confirms the fact that geostationary satellite temperature profile data with the poor spectral (vertical) resolution provided by filter wheel radiometers offer little information on mesoscale phenomena. The primary uses of the VAS instrument for mesoscale applications have been in the definition of the gross water vapor structure from the sounding retrieval process and the diagnosis of the horizontal wind field by tracking cloud and upper-level water vapor motion.

Aside from improving thermodynamic observations from satellites, improved vertical resolution water vapor profiles are needed to supplement wind profile observations over coastal oceanic regions. From geostationary satellites, the GHIS improved water vapor profiles should enable the vertical profile of horizontal

Corresponding author address: Dr. William L. Smith, CIMSS, University of Wisconsin, 1225 W. Dayton Street, Madison, WI 53706.

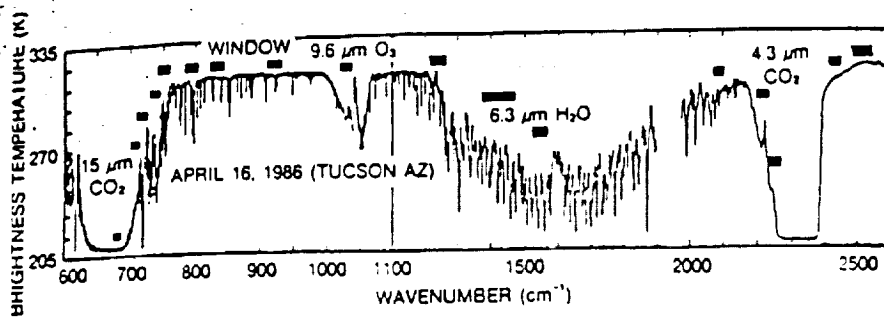


FIG. 1. Radiation brightness temperature spectrum as observed by HIS from the NASA U2 aircraft over Tucson, Arizona with the bandwidths of the GOES I/M filters superimposed.

wind to be achieved by tracking the water vapor motion observed within 1–2 km vertical layers.

In summary, greatly improved temperature and water vapor profile resolution and accuracy from the GOES sounding instrument are needed to meet the mesoscale meteorological data requirements of this decade and beyond. As will be shown, the GHIS can provide the improved performance.

## 2. Performance improvement

To obtain the vertical temperature and moisture profile resolution required, the sounding instrument must achieve near continuous spectral coverage throughout the 600–2600  $\text{cm}^{-1}$  region with a spectral resolution of 0.1% ( $\Delta\lambda/\lambda$ ) (Smith et al. 1979, 1983a). The high spectral resolution is needed to avoid smearing the upwelling radiance contributions from relatively opaque absorption lines with the contributions from more transparent regions in between the absorption lines. For example, in the thermal emission bands of  $\text{CO}_2$ , a spectral resolution of 0.7  $\text{cm}^{-1}$  is needed in the 600–700  $\text{cm}^{-1}$  (15  $\mu\text{m}$ ) region and 2  $\text{cm}^{-1}$  in the 2300–2400  $\text{cm}^{-1}$  (4.3  $\mu\text{m}$ ) region. Although the required spectral coverage and spectral resolution are beyond the capabilities of filter wheel radiometers, they can be achieved using an interferometer.

The HIS aircraft instrument flown aboard the NASA U2 and ER2 aircraft has proven the performance capabilities of a high spectral resolution interferometer. Ground calibration tests and airborne science missions have demonstrated the ability of the HIS to measure radiometrically accurate emission spectra with a resolution far exceeding the performance of contemporary filter radiometers (Revercomb et al. 1988a,b,c). Radiance spectra have been obtained during the more than 40 aircraft missions with a resolution of 0.35  $\text{cm}^{-1}$

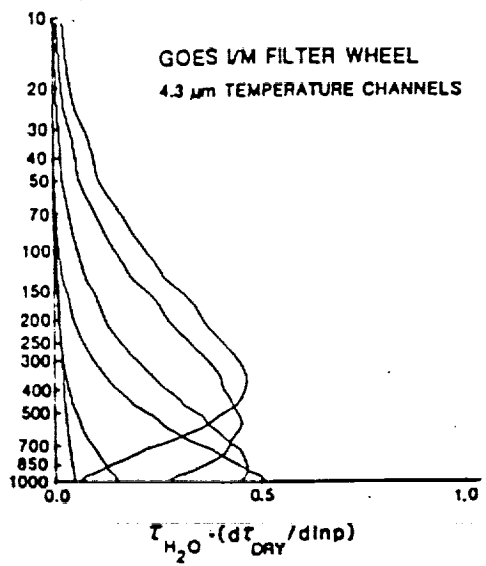
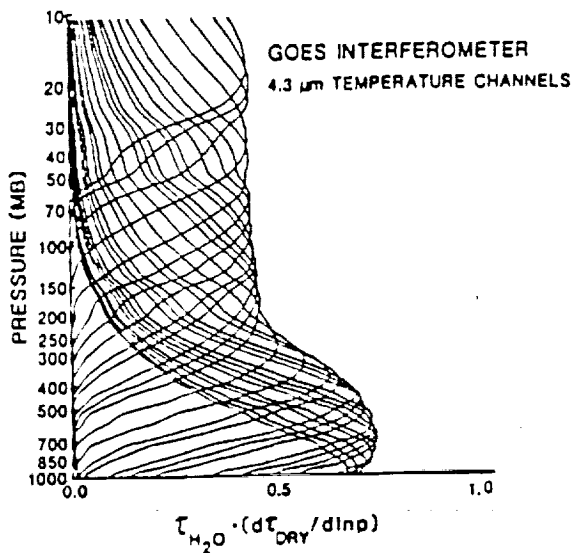
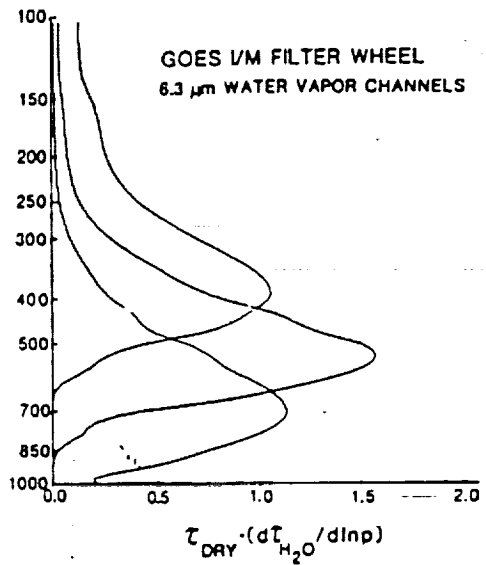
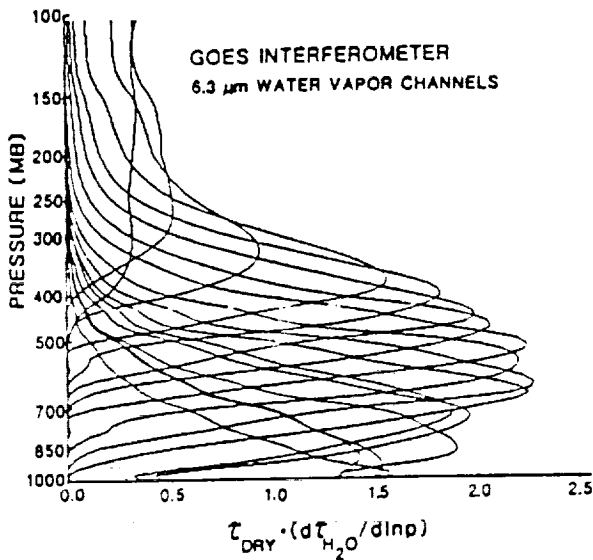
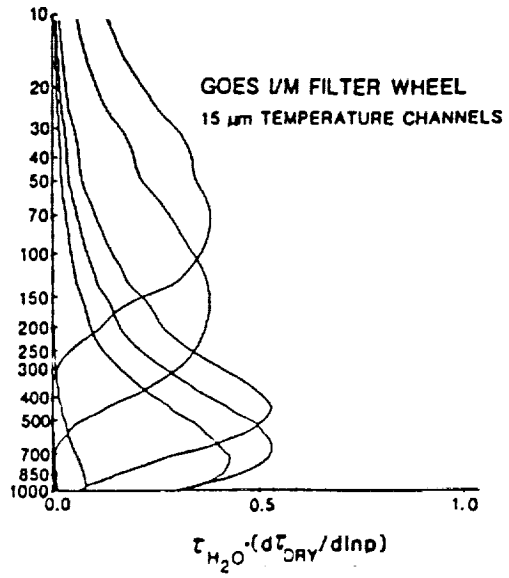
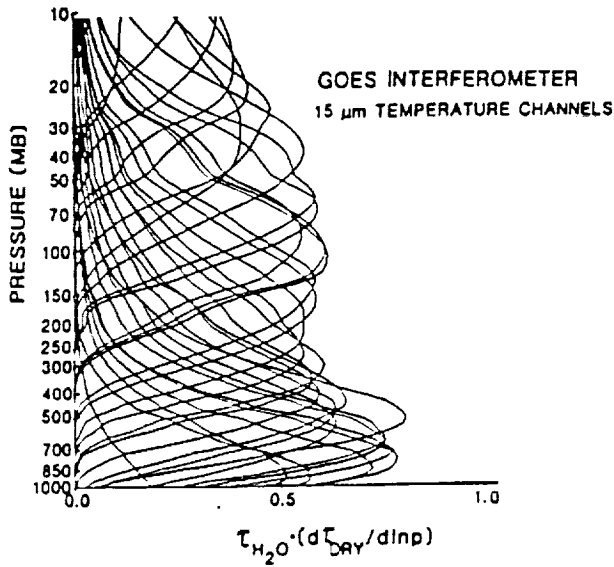
in the 600 to 1100  $\mu\text{m}$  region, as compared to the typical 15.0  $\text{cm}^{-1}$  resolution of filter radiometers, such as the one to be flown on GOES I/M.

Figure 1 shows a typical spectrum of infrared radiation brightness temperature sensed by the HIS. The bandwidths of the filters planned for the GOES I/M sounding radiometer are superimposed. As can be seen, the filter wheel radiometer severely smears the fine-scale spectral radiance structure of the atmosphere. The spectral smearing causes unwanted absorption contamination in atmospheric "windows" used for sensing the earth's surface temperature, and it greatly limits the vertical resolution of temperature and water vapor profiles because it broadens the atmospheric weighting functions (Fig. 2).

Figure 3a shows more clearly the effect of spectral resolution on radiance smearing. It can be seen from these brightness temperature spectra observed with the HIS and portrayed at three different spectral resolutions that the 15  $\text{cm}^{-1}$  resolution of the GOES I/M filter wheel instrument causes an extreme smearing of energy emission from the lower atmospheric levels (brightness temperatures in excess of 240 K) with energy emission from upper atmospheric levels (brightness temperatures below 240 K).

The vertical resolution of atmospheric temperature profiles as sensed by the GOES I/M filter wheel radiometer is compared to that of the interferometer sounder in Fig. 3b. (The vertical resolution was determined using the procedure described by Rodgers 1987.) As can be seen, a factor of 2–3 improvement is achieved by the GHIS. Figure 4 shows results of a retrieval error analysis conducted using the "linear simultaneous retrieval method" and associated error diagnosis scheme described by Smith et al. (1990), and the expected sounding accuracy of the GOES I/M filter instrument compared to the GHIS. Simulations also demonstrating these substantial improvements in accuracy have been

FIG. 2. Comparison of a small selection of GOES Interferometer (GHIS) spectral channel Planck radiance profile weighting functions with those for the GOES I/M filter radiometer. The 15  $\mu\text{m}$ , 6.3  $\mu\text{m}$ , and 4.3  $\mu\text{m}$  designations correspond to the 600–1100  $\text{cm}^{-1}$ , 1100–2000  $\text{cm}^{-1}$ , and 2000–2300  $\text{cm}^{-1}$  regions, respectively.  $t_{\text{H}_2\text{O}}$  and  $t_{\text{DMY}}$  refer to the atmospheric transmittance for water vapor and the uniformly mixed (e.g.,  $\text{CO}_2$ ,  $\text{N}_2\text{O}$ ) optically active gases, respectively.



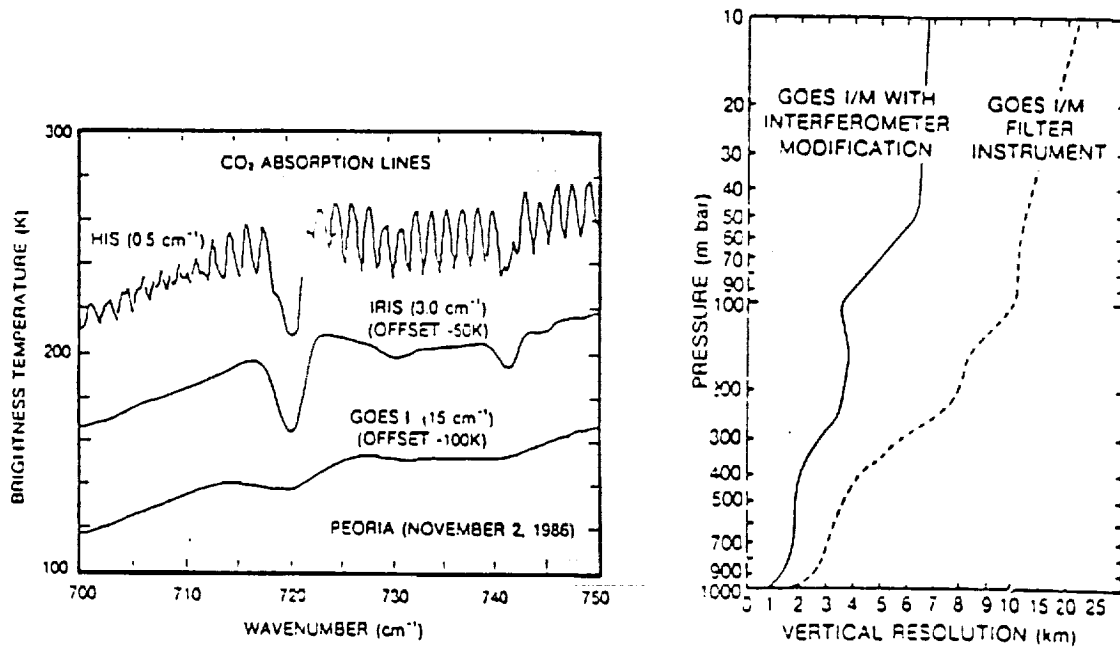


FIG. 3. (a) Spectra showing how emissions from different atmospheric levels are smeared by low-resolution measurements, which cannot resolve the CO<sub>2</sub> lines. (b) Improvement in vertical temperature profile resolution from modifying GOES I/M to use an interferometer.

performed by Fleming and Barnes (1987). (Experimental confirmation of these theoretical expectations is shown in section 4.) As can be seen from Figs. 3 and 4, dramatic improvements in vertical resolution and accuracy will result from the interferometer modification.

Another very important application of the GOES interferometer will be the tracing of fine scale features of the atmosphere's water substance. As will be shown in section 4, the interferometer sounder is capable of sensing water vapor emission with very high vertical resolution. Observations from a geostationary satellite of the dynamic displacement of fine vertical scale water vapor features might be used to construct vertical profiles of horizontal wind velocity as well as to provide a direct measure of the moisture convergence responsible for weather development. This wind profiling capability could be extremely useful over coastal oceanic regions, which are devoid of ground-based wind observations. The moisture structure sensing capability of the interferometer, together with its associated improved temperature profiling performance, are considered crucial for the use of geostationary satellite data in the mesoscale numerical weather prediction models planned for the next decade and beyond.

In addition to greatly improving atmospheric sounding resolution and accuracy, the modified GOES Sounder will provide more accurate measurements of cloud altitudes (Smith and Frey 1990) and atmospheric soundings beneath thin and/or broken clouds. Moreover, detailed observation of the infrared spectrum yield radiances highly sensitive to the concentrations

of atmospheric gases such as ozone, nitrous oxide, carbon monoxide, methane, and Freon 11 and 12 (Revercomb et al. 1988c; Clough 1988), as well as the thermal emission of land and sea surfaces. The interferometer sounder, once implemented aboard the geostationary satellite, will help satisfy observational requirements for climatology, oceanography, and geology as well as operational meteorology.

### 3. GHIS instrument characteristics

One practical approach for implementing the GOES HIS is to modify the existing GOES I/M filter wheel sounder (Koenig 1989). This approach would permit its implementation as early as possible, in order to achieve the urgently needed improved sounding performance. Feasibility studies confirm that the replacement of the GOES sounder filter wheel subassembly with an interferometer module is relatively straightforward and that it is a very attractive way to obtain a major enhancement in vertical sounding resolution and accuracy.

The primary operating characteristics of the GOES sounder as described by Koenig (1989) will be retained. The only functional change will be to expand the flexibility of the scan system to permit an optional longer dwell time at each sounding location, and another optional skip-step mode to permit faster soundings over large areas. As a consequence of the richer dataset collected by the interferometer, the output data rate will increase from 40 000 bits per second to as much as 500 000 bits per second.

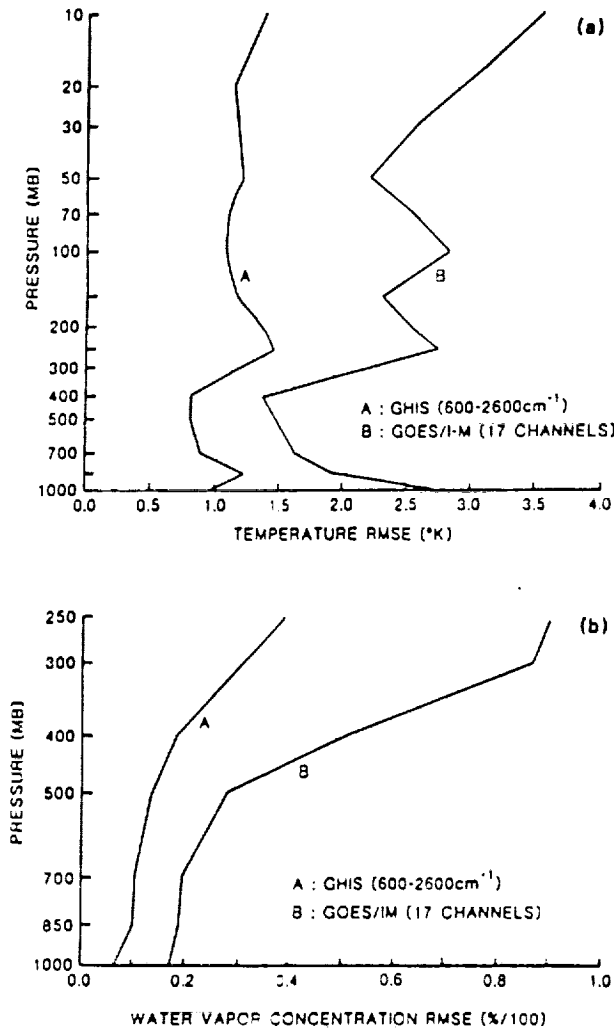


FIG. 4. Improvements in vertical temperature profile (a) and water vapor profile (b) rms retrieval errors from modifying GOES L/M to use an interferometer.

Key features of the GHIS are given in Table 1. Items modified or added for the new system are starred. It may be noted that these changes are a small part of the total system, indicating the compatible nature of the interferometer. The interferometer module will fit in place of the GOES I/M filter wheel assembly, leaving the telescope and detector-cooler assemblies essentially unchanged.

*a. GHIS operating modes*

The current filter wheel design for GOES I/M contains two scene scanning modes. Figures 5a,b show the scan patterns for the existing single step, normal line and single step, skip line modes. Two new scene scanning patterns have been introduced to fully utilize the capabilities of the interferometer while maintaining geographical coverage. The new scan patterns (skip

step, normal line and skip step, skip line) are shown in Figs. 5c,d.

In any one of the four scene scanning patterns, the sounder operator has the choice of three vertical (spectral) resolution modes: low, medium, or high. The three vertical (spectral) resolution modes are defined in Table 2 in terms of the unapodized resolution attained in each band. The normal step, low-resolution mode is designed to provide the same area coverage currently achievable with the filter wheel radiometer, but with improved spectral resolution and dramatically lower noise performance in the long wavelength band (Table 3b). The higher resolution modes require longer dwell times to allow the interferometer moving mirror to traverse the longer optical path range.

The definition of these operating modes is based on a desire to maintain most of the operational characteristics of the GOES I/M sounder.

*b. Interface to existing system*

The modularity of the GOES sounder makes implementation of the interferometer modification quite feasible. The existing scene-mirror optics and its control circuitry will remain unchanged. Some reprogramming

TABLE 1. Key features of sounder.

Simultaneous FOVs	4
FOV defining element	Field stop, 242 $\mu$ rad diam (8.6 km. nadir)
Telescope aperture	31.1 cm (12.25 in) diameter
Channel separation, LW-SW-MW	Dichroic
IR spectral definition	Interferometer*
Visible sounding	Fixed detectors
Radiometric calibration	Space and 290 K IR blackbody
Frequency of space clamp	2 min
Frequency of IR calibration	20 min
IR detector operational temperature (K)	92°, 97°, 102, 107
Field sampling	Four areas N-S on 10-km centers
Scan step angle	280 $\mu$ rad (10 km nadir); Skip-step* and skip-line optional
Step and dwell time	0.1 Seconds; 0.2 s, 0.4 s, 0.8* optional
Scan capability	Full earth and space
Sounding areas	10 km $\times$ 40 km to 60°N-S and 60°E-W
Optical location	Star sensing
Output data quantizing	12 bit all channels*
Output data rate	<500 kbits per second without data compression (lower by 2 to 5 times with compression)*
System power average	112 W
System weight:	
Sensor assembly	202 lb (92.0 kg)
Electronics module	61 lb (27.9 kg)
Power supply	14 lb (6.2 kg)
Interferometer processor*	16 lb (7.3 kg)
<b>Total</b>	<b>293 lb (133.4 kg)</b>

\* Added for interferometer.

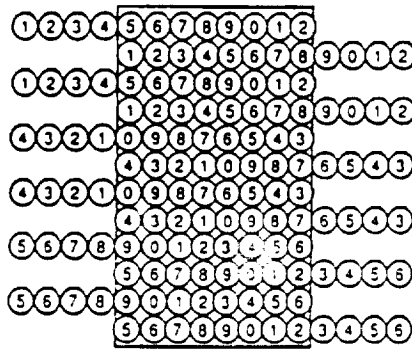


Figure 5a. Single step, normal line

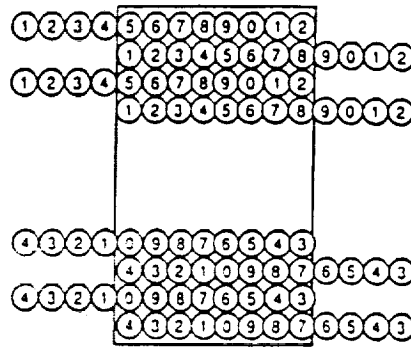


Figure 5b. Single step, skip line

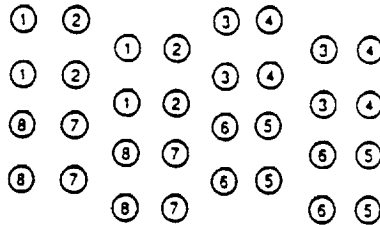


Figure 5c. Skip step, normal line

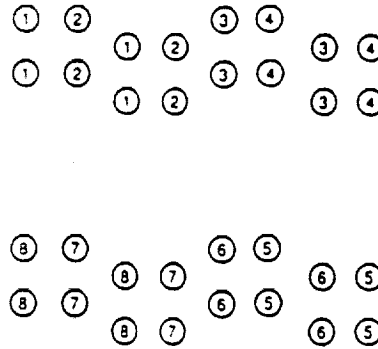


Figure 5d. Skip step, skip line

FIG. 5. Sounding in different scan modes (dwell times of 0.1, 0.4, 0.8 s are selectable at each location). The numbers indicate the order by which the four simultaneous fields of view are sampled.

of the scene mirror will be required to accommodate the new scan modes; however, the GOES design is well suited to accepting such changes. The existing passive cooler, used to cool the aft optics, detectors, and focal plane will be maintained. Also, the physical dimensions of the sensor assembly will remain unchanged. The filter wheel passive cooler will be used to cool the interferometer module. The major change is to remove the filter wheel and relay optics from the input beam and to replace them with an interferometer and its relay optics. Another change is to replace the filter wheel electronics circuitry with circuitry appropriate for controlling the dynamically aligned interferometer and for on-board processing of the data. The last change is to replace the current set of detectors with ones optimized

for the interferometer's long-wavelength (LW), mid-wavelength (MW), and short-wavelength (SW) band passes.

*c. Mass, power, and volume*

The mass of the interferometer and the mass of the electronic control circuitry being added (10 lbs) nearly equals the mass of analogous material being removed (11 lbs). The main additional mass (16 lbs) being added in the interferometer design is for the on-board processing system.

The total system mass is expected to be only about 5% greater than the mass of the current filter wheel sounder.

TABLE 2. Vertical resolution modes.

Spectral resolution	Dwell time (s)	Time/step (s)	Resolution (cm <sup>-1</sup> )		
			Band 1 (620 to 1150 cm <sup>-1</sup> )	Band 2 (1210 to 1740 cm <sup>-1</sup> )	Band 3 (2150 to 2721 cm <sup>-1</sup> )
Low	0.075	0.1	3.33	4.63	4.63
Medium	0.375	0.4	0.67	1.15	1.15
High	0.775	0.8	0.32	1.15	1.15

ORIGINAL PAGE IS OF POOR QUALITY

TABLE 3a. Expected GHIS NEN performance.

Spectral resolution	Dwell time (s)	Time/step (s)	NEN ( $\text{mW}/\text{m}^2 \text{ sr cm}^{-1}$ )		
			Band 1 (620 to 1150 $\text{cm}^{-1}$ )	Band 2 (1210 to 1740 $\text{cm}^{-1}$ )	Band 3 (2150 to 2721 $\text{cm}^{-1}$ )
Low	0.075	0.1	0.14	0.06	0.007
Medium	0.375	0.4	0.32	0.13	0.014
High	0.775	0.8	0.46	0.13	0.014

TABLE 3b. GHIS low resolution mode NEN performance reduced to GOES I/M resolution.

Channel number	Center wavenumber	Resolution $\Delta\nu$	GOES I/M		GHIS
			NEN specified	NEN desired	NEN expected
1	680	13	0.66	0.25	0.083
2	696	13	0.58	0.25	0.084
3	711	13	0.54	0.25	0.085
4	733	16	0.45	0.25	0.080
5	748	30	0.44	0.2	0.060
6	790	50	0.25	0.15	0.048
7	832	50	0.16	0.06	0.051
8	907	25	0.16	0.06	0.079
9	1035	25	0.35	0.12	0.090
10	1345	55	0.16	0.05	0.021
11	1425	80	0.12	0.04	0.019
12	1535	60	0.15	0.04	0.023
13	2188	23	0.013	0.004	0.0037
14	2210	23	0.013	0.004	0.0038
15	2245	23	0.013	0.004	0.0038
16	2420	40	0.008	0.003	0.0032
17	2513	40	0.0082	0.003	0.0032
18	2671	100	0.0036	0.002	0.0022

The modification requires an additional 10.7 W of average power, including 5.2 W for the data processing on board. The interferometer adds no additional peak power requirements, and the additional average power is within the current margin for power available to the sounder.

#### d. Detector performance

Table 3 summarizes the expected noise performance for each spectral resolution mode specified in Table 2. This noise performance has been shown to meet the needs of high resolution sounding (Smith et al. 1983a), and in the low resolution mode will offer a substantial improvement over GOES I/M for the long wavelength band (Table 3b).

Note that the NENs for soundings will be better than those shown in Table 3 by a factor of the square root of the number of field of views (FOVs) used per sounding retrieval.

#### e. Data rate and processing

The expected data rate is based on the use of Digital Signal Processor (DSP) modules to do on-board Fourier

transforms of the interferogram data in real time. Table 4 gives the data rates for the full spectra (all bands included). For each item in the table, the higher number holds if complex spectra are needed for phase corrections of the data (Revercomb et al. 1988a), the lower number if only magnitude spectra are used. In all cases, the data rates are less than 500 kbps. Further reductions in data rate (by a factor of 2 to 5) could be realized with data compression. Another factor of 5 to 10 could be achieved if the radiance spectra were convoluted with a "standard atmosphere" weighting function matrix, as required for sounding retrieval using the linear simultaneous approach (Smith et al. 1990) prior to telemetry to the ground (see section 4). In summary, on-board processing will enable the sounding information to be compressed to fit almost any prescribed data rate constraint.

#### 4. Aircraft prototype instrument

In order to prove the theoretical expectation of improved sounding performance (Smith et al. 1979, 1983a; Smith 1984), NOAA and NASA jointly funded the development of an aircraft prototype High-resolution Interferometer Sounder (HIS). The instrument

TABLE 4. Data rates for the interferometer sounder by operating mode.

Spectral resolution	Total data rate (kbps)	
	Single step, normal line/ skip step, skip line	Skip step, normal line/ skip step, skip line
Low	452/226	226/113
Medium	452/226	362/181
High	336/168	299/149

was completed and tested in 1985 and since then has flown on more than 40 airborne missions of the NASA U2/ER2 high altitude (65 000 feet) aircraft. All of its research flights to date have been flown on the NASA U2/ER2, but the instrument was recently checked out on the NOAA P-3 research aircraft, which has excellent in situ capabilities for temperature, trace gas and aerosol measurements. Here we summarize the characteristics and the radiometric performance of the aircraft HIS instrument, and present examples of the sounding results.

#### a. Description

The specific hardware configuration of the HIS aircraft instrument bears little resemblance to the design for GOES, but the principles are the same. The aircraft HIS views directly downward from inside a pod (about 3 m long and 0.5 m in diameter) mounted either under the wing or under the center line of the fuselage. Many of the important design parameters of the HIS are summarized in Table 5.

Calibration is accomplished by viewing two high emissivity blackbodies, servo controlled at altitude to 300 K and about 240 K. After 12 scans of the earth over the full range of optical path, a 45 degree scene switching mirror rotates the field-of-view from the open earth viewing port to give four scans of the hot and four scans of the cold blackbodies. The blackbodies, built and tested by Eppley Labs, are blackened cavities with thermoelectric cooler/heaters for temperature control and platinum resistance thermometers for monitoring. The temperatures of the interferometer optics are not actively controlled.

The BOMEM Michelson interferometer (Buijs 1979) as modified for this application provides double-sided interferograms from both scan directions. Its auto-alignment system makes it possible to operate in the ambient thermal environment of the pod and in very close proximity to the aircraft jet engine. The optical bench is shock-mounted to dampen high frequency vibration and the interferometer is evacuated to protect the beamsplitter during descent.

The three spectral bands, covering most of the region from 3.8 to 16.6 microns (Table 5), are split inside a single liquid helium dewar, which contains three sets of bandpass cold filters, focusing optics, and arsenic-

doped silicon detectors. The preamplifiers are external and operate near the ambient pod temperature of about 260 K. The gain of each channel is fixed and the signals are digitized with a 16 bit A/D. On-board numerical filtering is used to reduce the sample rate from the HeNe laser rate by factors of 14, 8 and 8 in bands I, II and III.

The data system is controlled with a 6809 microprocessor-based system built at the University of Denver. The three bands of interferometer data and house-keeping parameters are combined and recorded on formatted cassette tapes. Two drives with a capacity of 67 megabytes each are used to provide 9 hours of continuous recording time.

Processing of selected data in the field is performed on IBM-compatible personal computers. Data is transferred to hard disk and is processed with custom software, which displays the measured interferograms and corresponding spectra, and performs calibration to yield radiance or brightness temperature spectra. The calibration procedure uses full complex spectra to avoid errors that can arise from radiance emitted by the warm interferometer (Revercomb et al. 1988a,b).

TABLE 5. Characteristics of the HIS aircraft instrument.

Spectral range (cm <sup>-1</sup> )	
Band I	590-1080
Band II	1080-1850
Band III	2000-2700
Field of view diameter (mr)	
Telescope	100
Interferometer	30
Blackbody reference sources	
Emissivity	>0.998
Aperture diameter (cm)	1.5
Temperature stability (K)	~0.1
Auto-aligned interferometer:	modified BOMEM BBDA2.1
Beamsplitter:	
Substrate	KCl
Coatings (1/4 g at 3.3 mm)	Ge + Sb <sub>2</sub> S <sub>3</sub>
Maximum delay (double-sided) current configuration (cm):	
Band I (hardware limit is ~2.0)	~1.8
Bands II and III (limited by data system)	+1.2, -0.8
Michelson mirror optical scan rate (cm s <sup>-1</sup> ):	0.6
Aperture stop (at interferometer exit window):	
Diameter (cm)	4.1
Central obscuration area fraction	0.17
Area (cm <sup>2</sup> )	10.8
Area-solid angle product (cm <sup>2</sup> sr):	0.0076
Detectors:	
Type	Ar doped Si
Diameter (cm)	0.16
Temperature (K)	6

ORIGINAL PAGE IS  
OF POOR QUALITY

### b. Radiometric performance

The rms detector noise for a single interferogram scan determined from in-flight calibration data is shown in Fig. 6. The noise is expressed in brightness temperature units for the calibration blackbody scene temperature of 260 K. For bands I and II the noise is background limited, with radiation from the instrument providing most of the photons. Band III noise is considerably higher, with an electrical interference contribution between 2150–2350  $\text{cm}^{-1}$ , which is not detector noise.

The other type of noise encountered in flight is sample-position-error noise caused by the effect of aircraft vibrations on the velocity of the scanning Michelson mirror. Since it originates from very near zero path difference, this noise is highly correlated with wavenumber, causing a small rocking of the spectra. It is absent on the ground and would not be present in a spacecraft application. Even in the hostile aircraft environment, this noise can be made small. Its amplitude varies with instrument configuration, but is generally comparable to the detector noise level.

Accurate radiometric calibration over the full spectral range was demonstrated on the ground using a third blackbody. A liquid nitrogen blackbody was used as the cold reference, one on-board blackbody served as the 300 K hot reference, and the temperature of the other on-board blackbody (set between 260 and 280 K) was determined. The unknown temperature can be determined routinely to within about 0.2 to 0.4 K. This procedure relies on a careful optical design and alignment to prevent optical-path-difference dependence of the responsivity, which would degrade the high resolution integrity of the spectra. Self-apodization is kept small by the relatively small field-of-view of the interferometer, and can be accounted for accurately. Additional errors could be present in flight, but comparisons with aircraft altitude temperatures and water surface temperatures are generally within 1 K. An accuracy of better than 0.5°C is possible, except for regions of low brightness temperature in the 4.3- $\mu\text{m}$   $\text{CO}_2$  band.

Figure 7 shows a portion of the HIS spectra recorded 15 April 1986 over the desert Southwest compared to

a spectrum calculated using radiosonde data with the AFGL FASCOD2 line-by-line program (Clough et al. 1986). The finite FOV of the interferometer is accounted for in the calculated spectra. The agreement is remarkably good. The major differences are believed to be due to incomplete information on the temperature, water vapor, and ozone (the large discrepancy between 1010–1070  $\text{cm}^{-1}$ ) of the observed atmosphere, deficiencies in the line-by-line calculations, and the presence of constituents not included in the calculations (e.g., CFC-11 and CFC-12) that contribute to the discrepancies seen between 840–860 and 910–925  $\text{cm}^{-1}$  in Fig. 7. Noise and calibration errors are not believed to be significant.

Another comparison of HIS observations with calculations is shown in Fig. 8. The observations were taken from the NOAA P-3 aircraft over the Gulf of Mexico on 18 November 1988. This flight provided the best supporting measurements of temperature and humidity of any of the HIS observations, via both aircraft sensors and dropsondes. The spectral agreement is generally within two degrees with the exception of the 600–680  $\text{cm}^{-1}$  region, which is influenced by 400 Hz noise from the aircraft power supply, and the 2260–2380  $\text{cm}^{-1}$  region, which is due to the large influence of the electrical and detector noise noted earlier for this spectral region on brightness temperature when viewing low scene temperatures. Note especially the excellent agreement over the 6.3 micron water vapor band occupying most of the HIS Band II.

### c. Example experimental sounding results

#### 1) RETRIEVAL METHODOLOGY

For the retrieval of atmospheric profiles from the HIS, it is desirable to utilize all spectral observations in a simultaneous solution for temperature, water vapor and other desired absorbing constituents (e.g., ozone, methane, etc). Such a general solution has been formulated for treating the HIS spectra and is described in detail elsewhere (Smith et al. 1988, 1990).

For the results shown here, the following perturbation form of the "physical simultaneous" retrieval algorithm is used

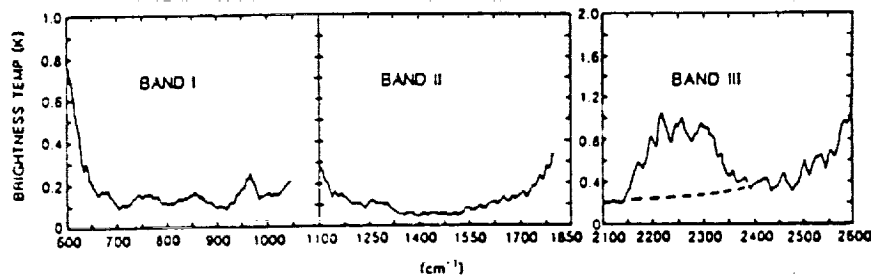


FIG. 6. Detector noise observed with the HIS aircraft instrument.

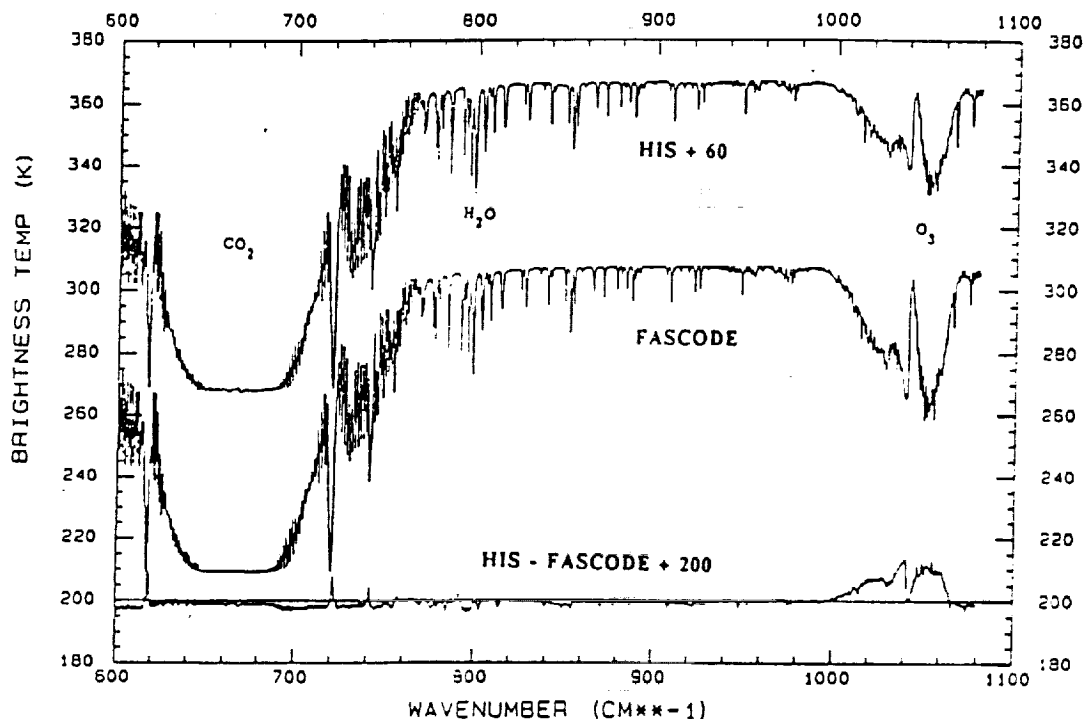


FIG. 7. Blackbody equivalent temperature of upwelling radiance from the nadir viewing HIS instrument aboard the NASA U2 at an altitude of 20 km over the desert southwest on 15 April 1986. Also shown is a line-by-line calculation with AFGL FASCODE2 using a nearby radiosonde. The spectra are apodized to yield an approximate resolution of  $0.7 \text{ cm}^{-1}$ .

$$t = DA_0^T t_b = Dt^* \quad (1)$$

where  $t$  is a vector of the deviations of the desired atmospheric variables (e.g., temperature and dewpoint) from an ensemble mean condition,  $t_b$  is a vector of observed brightness temperature deviations from the mean condition,  $A_0^T$  is the transpose of the profile weighting function matrix, partitioned into "dry" and "wet" components as required for the simultaneous solution, and  $D$  is a "deconvolution" matrix. In its application, we define

$$t^* = A_0^T (t_b + \beta) \quad (2)$$

where  $\beta$  is the systematic error in calculated brightness temperature due to uncertainties in the spectroscopy and errors in the numerical methods used to define the atmospheric transmittance spectra. The elements of  $A_0$  are

$$a_{ij} = W_{ij} / \sum_{i=1}^M W_{ij}$$

with

$$w_{ij} = \int_{\nu_j} \tau(\nu_i, p_j) d \ln \tau_k(\nu_i, p_j) / \sigma_{\nu_i(\nu)}$$

and

$$f_{ij} = \partial B(\nu_i, T_j^0) / \partial T.$$

$B$  is Planck radiance,  $T$  is temperature, and  $M$  is the number of spectral radiance observations. The zero superscript refers to the mean temperature profile condition. The scripts  $i, j, k$  denote spectral wavenumber, atmospheric pressure level, and atmospheric absorbing constituent, respectively. The transmittance of the atmosphere between the instrument and pressure level,  $p_j$ , is  $\tau(\nu_i, p_j)$  whereas that due to an individual absorbing constituent (e.g., water vapor) is  $\tau_k(\nu_i, p_j)$ . The derivative is with respect to the vertical coordinate. Here we treat the spectrum as composed of uniformly mixed constituents ( $k = 1$ ) and water vapor ( $k = 2$ ). Strictly speaking, the first half of the vector  $t$  is the atmospheric temperature profile which satisfies that portion of the observed radiance spectrum influenced by the uniformly mixed gases whereas the second half is the temperature profile which satisfies that portion of the observed radiance spectrum influenced by the water vapor, assuming that the mean water vapor profile used to define  $W_{ij}$  is correct. Thus, if the actual water vapor profile is equal to the mean profile, then the two temperature profiles, uniformly mixed gas and water vapor, are identical. For all other conditions, the actual moisture profile is a function of the discrepancy between the two temperature profile components (Smith et al. 1990). The dewpoint temperature can be approximated from a linear combination of the two temperature profiles. The quantity  $\sigma_{\nu_i(\nu)}$  is the standard

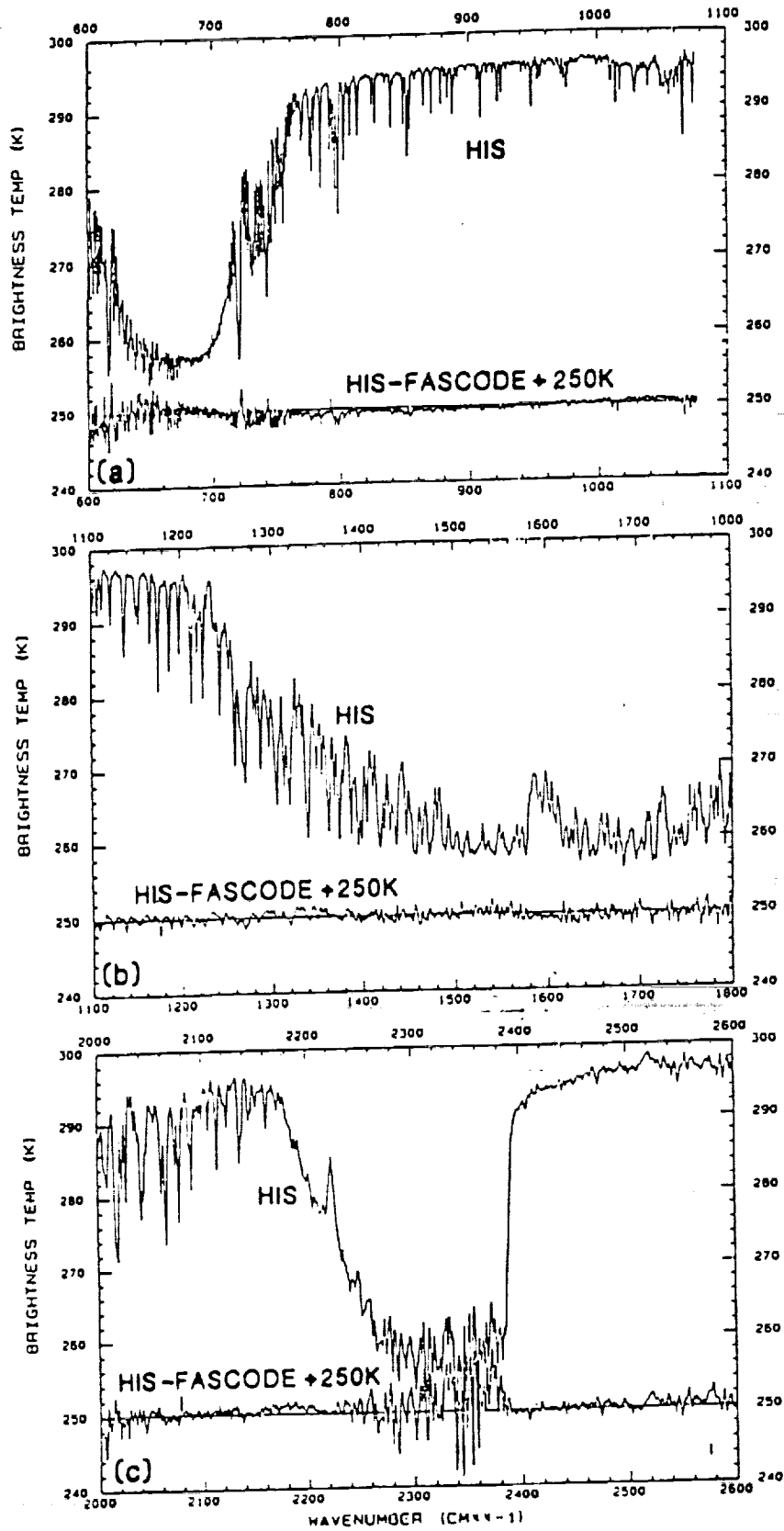


FIG. 8. Spectra for all three bands of the HIS observed from the NOAA P3 aircraft at 7.5 km altitude (400 mb) on 18 November 1988. The difference spectra show the excellent agreement between HIS observations and spectra calculated using FASCOD2.

deviation of the radiance noise due to measurement noise and error in theoretical radiative transfer computations. It is included to weight those spectral regions that have the lowest noise most heavily in the profile solutions.

The vector  $t^*$ , as defined by (2), can be thought of as the vertically smoothed temperature profile as depicted by the convolution of the spectral weighting functions with the radiant brightness temperatures. Numerically,

$$t^*(p_j) = \sum_{i=1}^M W_{ij} t_{bi} / \sum_{i=1}^M W_{ij}, \quad (3)$$

that is, the convoluted temperature profile deviation from the mean is given by the spectrally weighted-average brightness temperature spectrum deviation from the mean spectrum. This form for  $t^*$  is identical to the generalized iterative retrieval solution (Smith 1970) used for processing grating spectrometer and filter wheel radiometer data. However, because of the large number of spectral radiance observations ( $\sim 4000$ ) with the HIS, iteration of (3) is prohibitive due to the very large amount of radiative transfer computation involved to update  $W_{ij}$  and the mean brightness temperature spectrum with the spectrum computed from a prior retrieval. Instead,  $t^*$  serves here as the smooth first approximation of the true profile whose enhanced vertical structure is retrieved through the application of the deconvolution matrix,  $D$ . The  $D$  matrix is determined by matrix inversion of (1)

$$D = (TT^T)(T^*T^*T)^{-1} \quad (4)$$

where  $T$  is a matrix of dry-bulb temperature and dewpoint temperature profile deviations from the mean for a statistical ensemble of soundings and  $T^*$  is a matrix of the smoothed temperature (uniformly mixed gas and water vapor component) profiles from their ensemble mean values.  $T^*$  is specified by radiative

transfer computation of  $W_{ij}$  and  $t_{bi}$ . Random errors of measurement of the same magnitude observed from calibration spectra with the HIS aircraft instrument are simulated using a random number generator and added to  $t_{bi}$  in order to stabilize the solution against actual instrument noise. For the generation of  $T^*$  used in (4),  $\beta$  is assumed to be equal to zero since here  $T^*$  is based solely on radiative transfer theory. However, when  $D$  is applied to real spectral brightness temperature observations,  $\beta$  must be applied to  $t_b$  [Eq. (3)] in order to account for systematic errors in the radiative transfer model.

During the Combined Huntsville Meteorological EXperiment (COHMEX), the HIS flew aboard the NASA U2/ER2 aircraft. A few sample results achieved during COHMEX are presented below to illustrate the sounding capabilities of the HIS.

## 2) SIMULATION RESULTS

Soundings have been derived using HIS radiance spectra simulated from the special radiosondes launched during the COHMEX. The purpose of first investigating retrieval accuracy using synthesized data, rather than actual spectral observations, is that the "truth" is known since the radiosonde profile was used to compute the "observed" spectrum. (Random errors of the same magnitude associated with actual HIS observations are added to the computed radiances to simulate "observed" radiances for the retrieval process.) As shown later, when comparing profile retrievals from actual spectral radiance observations with radiosondes, it is uncertain as to whether the difference is due to errors in the retrieval, the radiosonde, or space and time discrepancies between the two independent observations. Thus, the use of synthetic spectra serves to illustrate the errors expected to result from the sounding retrieval process.

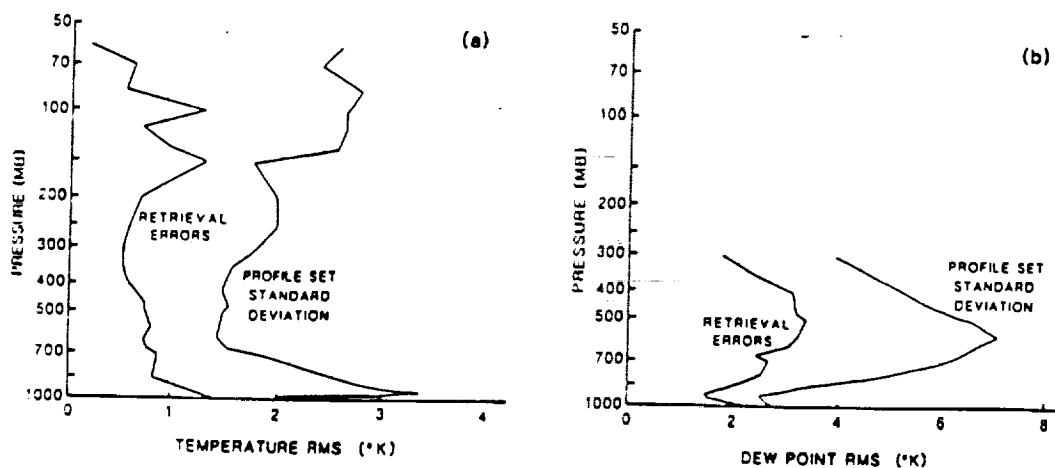


FIG. 9. Rms retrieval errors for (a) temperature and (b) dewpoint compared to standard derivation of the 193 COHMEX radiosondes used in the retrieval error analysis.

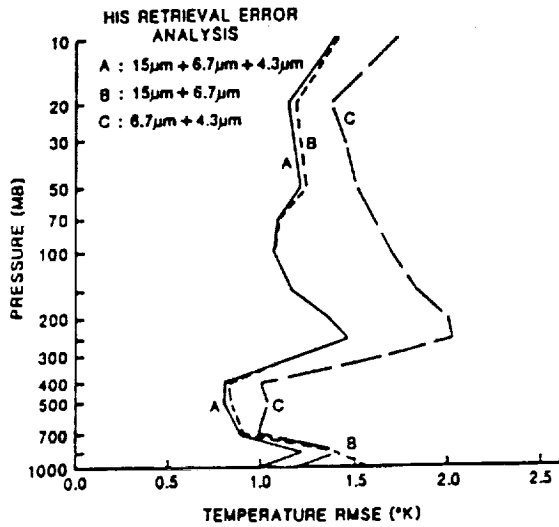


FIG. 10. Comparison of rms errors from simulated temperature retrievals using all GHIS spectral bands (a), omitting the 4.3- $\mu\text{m}$   $\text{CO}_2$  band (b), and omitting the 15- $\mu\text{m}$   $\text{CO}_2$  band (c). The long wavelength band is important at all altitudes, while the short wavelength band only contributes significantly near the surface.

Figure 9 shows rms errors of the sounding retrievals from HIS radiance spectra synthesized from a set of 193 COHMEX radiosonde profiles. The temperature and dewpoint soundings were retrieved using deconvolution matrix,  $D$ , based on the same COHMEX statistical set of 193 radiosonde soundings, and as a result, Fig. 9 represents the lower limit of retrieval error using the linear simultaneous retrieval algorithm. As can be seen for the COHMEX observation region, HIS re-

trieval accuracies close to  $1^\circ\text{C}$  could be achieved for temperature, and  $2^\circ\text{--}3^\circ\text{C}$  for dewpoint temperature. Figure 10 shows rms error curves derived from a global set of soundings (Smith et al. 1990) for three different measurement conditions: 1) all spectral bands ( $600\text{--}2700\text{ cm}^{-1}$ ), 2) bands 1 and 2 ( $600\text{--}2000\text{ cm}^{-1}$ ), and 3) bands 2 and 3 ( $1100\text{--}2700\text{ cm}^{-1}$ ). Best results are achieved when all spectral measurements are used in the retrieval.

Figure 11 shows two example comparisons of synthetic radiance retrievals with individual COHMEX radiosondes. As can be seen, much of the fine scale detail is retrieved from the full HIS radiance spectrum. The vertical structure of water vapor dewpoint is particularly noteworthy.

### 3) EXPERIMENTAL RESULTS

Figure 12 shows two examples of comparisons of radiosondes with retrievals of temperature and dewpoint profiles from actual HIS spectral radiances observed on 19 June 1986. It is noted that the  $D$  matrix and initial (mean) profile used for these retrievals are the same as those used for the simulated radiance retrievals shown earlier. We can see from these comparisons that the agreement of the radiance derived profiles with the radiosonde is close to the theoretical expectation (Fig. 9). Once again, the fine-scale water vapor structure retrieved is particularly noteworthy.

Figure 13 is presented to show the improvement in vertical resolution and accuracy of HIS profile retrievals over those achieved with the current VAS geostationary satellite sounder. The GOES 1/M filter wheel sounder

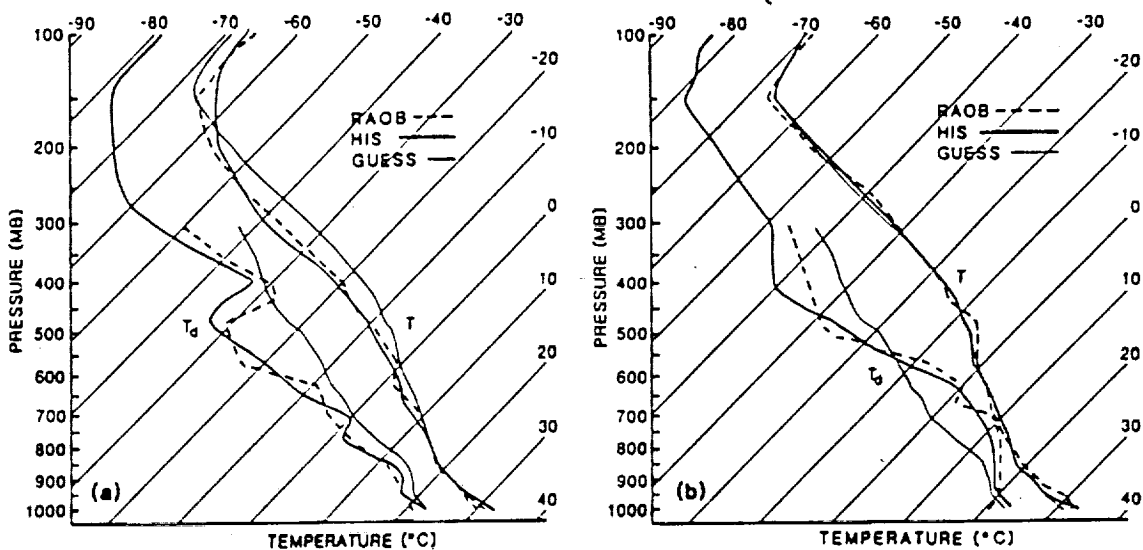


FIG. 11. Examples of two COHMEX radiosondes, (a) and (b) above, compared to the retrievals of temperature and dewpoint obtained from synthetic radiances calculated from them. Notice that most of the fine scale structure is recovered, particularly for water vapor.

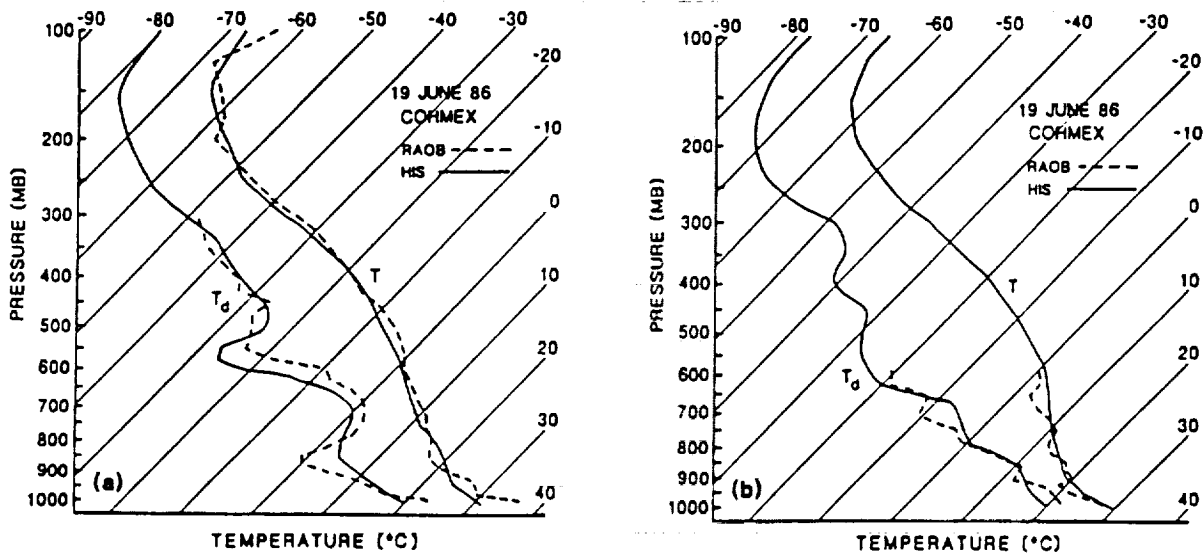


FIG. 12. Examples of two COHMEX radiosondes, (a) and (b) above, compared to retrievals of temperature and dewpoint from actual HIS spectral radiances observed on 19 June 1986.

will produce soundings of vertical resolution similar to VAS. As can be seen, whereas VAS depicts the broad scale profiles of temperature and moisture, HIS is capable of resolving finer scale features of vertical structure. Once again the most noticeable improvement appears in the moisture profile retrieval. The moisture discrepancy between the HIS and radiosonde moisture above the 600-mb level is believed to be due to space and time discrepancies of the measurements rather than due to errors in either sounding. Evidence for this arising from strong space and time gradients of at-

mospheric moisture in this layer is given in Fig. 14 described below.

In order to illustrate the water vapor sensing capability of the HIS, Figs. 14 and 15 show vertical cross sections along the flight tracks of the NASA U2 and ER2 on 15 and 19 June 1989, respectively. Both flight tracks are over northern Alabama and Tennessee, but as can be seen from the HIS data, the meteorological characteristics are quite different for the two days. On 15 June the HIS cross section reveals an intense boundary layer whose top was near the 850-mb level.

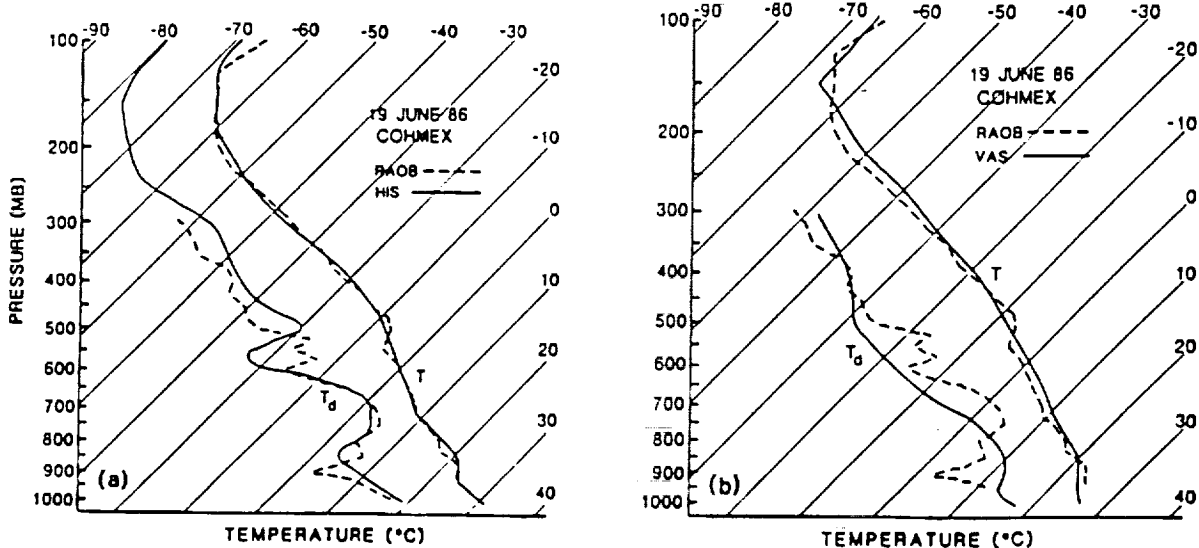


FIG. 13. The improvement in vertical resolution of the HIS (a) is apparent when compared to a coincident satellite retrieval using the VAS filter wheel sounder (b).

DE  
Inc  
low  
lev  
str  
is c  
the  
wit  
ver  
see  
dif  
ex:  
sup  
cl  
ob  
mc  
wi  
res  
str  
are

2  
2  
}

17  
r  
:  
and  
der  
Ve  
de  
fro

Indeed, cloud observations revealed that the top of a low-level scattered cumulus deck was near the 850-mb level. The rapid drying and stabilizing temperature structure just above the boundary layer (850–700 mb) is clearly evident in the HIS cross-section analysis. Also, the largest horizontal variability in moisture occurs within the 200–400 mb layer where the aircraft traverses a moisture front located across central Tennessee. On 19 June the meteorological condition is quite different. The HIS cross section does not reveal the existence of an intense boundary layer and this was supported by the fact that no boundary layer cumulus clouds or haze were observed. Contrary to the 15 June observation, the largest horizontal variability of atmospheric moisture occurs lower in the atmosphere within the 400–700 mb layer. In both cases, the vertical resolution of the retrieved water vapor structure is striking. In this regard, the HIS sounding capabilities are unique; that is, no other sensor is capable of pro-

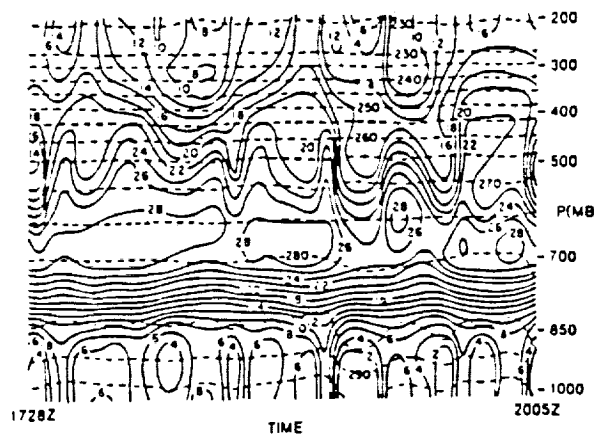
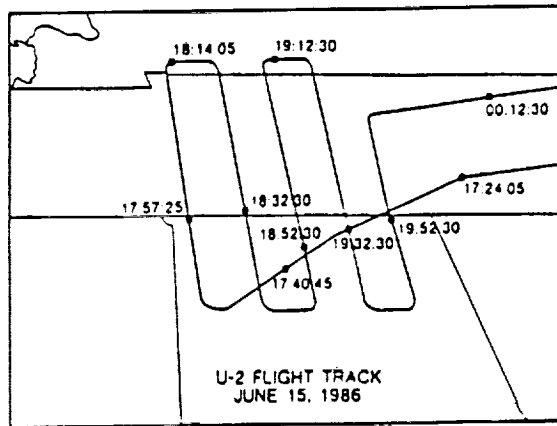


FIG. 14. (a) Flight track of the NASA/U2 over northern Alabama and Tennessee on 15 June 1986. The times of various aircraft are denoted in hours, minutes, and seconds of central daylight time. (b) Vertical/time cross section of atmospheric temperature (dashed) and dewpoint depression (solid) beneath the U2 flight track as retrieved from HIS spectra.

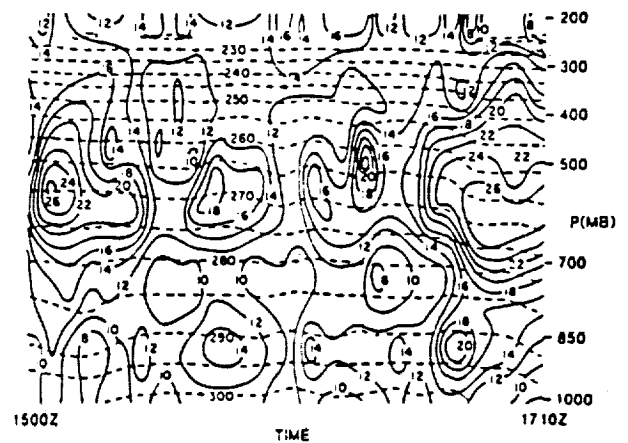
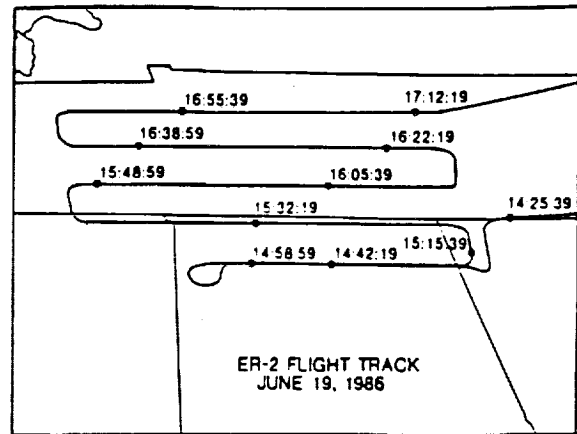


FIG. 15. As in Fig. 14, but for 19 June 1986.

viding the vertical and horizontal sounding detail as achieved with the airborne HIS. From the geostationary satellite, the HIS will provide an unprecedented four-dimensional sounding capability.

5. Conclusions

A design exists to enable implementation of a greatly improved sounding capability from geostationary satellite orbit. Experimental results achieved with an aircraft prototype instrument indicate that the theoretical expectations of 1°C temperature and 2°–3°C dewpoint accuracy can be achieved. Most exciting is the great improvement in sensing the water vapor profile structure. It appears that the vertical resolution is good enough to enable water vapor tracking in numerous vertical layers thereby providing water vapor tracer wind profile data as well as thermodynamic profiles.

REFERENCES

Buijs, H., 1979: A class of high-resolution ruggedized Fourier transform spectrometers. *SPIE*, 191, 116–119.  
Clough, S. A., F. X. Kneizys, E. P. Shettle and G. P. Anderson, 1986:

- Atmospheric radiance and transmittance: FASCOD2. *Sixth Conf. on Atmospheric Radiation*, Amer. Meteor. Soc., 141.
- Fleming, H. E., and L. L. Barnes, 1987: Satellite tomographic remote sensing retrieval methods. *RSRM 87: Advances in Remote Sensing Retrieval Methods*, A. Deepak, H. Fleming and J. Theon, Eds., A. Deepak.
- Hanel, R. A., B. Schlachman, F. D. Clark, C. H. Prokesh, J. B. Taylor, W. M. Wilson and L. Chaney, 1970: The Nimbus III Michelson interferometer. *Appl. Optics*, 9, 1767.
- , —, D. Rodgers and D. Vanous, 1971: Nimbus 4 Michelson Interferometer. *Appl. Optics*, 10, 1376.
- , —, E. Reihan, R. Bywaters, F. Chapman, M. Rhodes, D. Rodgers and D. Vanous, 1972: Mariner 9 Michelson interferometer. *Appl. Optics*, 11, 2625.
- , D. Crosby, L. Herath, D. Vanous, D. Collins, H. Creswick, C. Harris and D. Rhodes, 1980: Infrared spectrometer for Voyager. *Appl. Optics*, 19, 1391.
- Koenig, E. W., 1989: Characteristics of the GOES I-M imager sounder. *Proceedings of the GOES I-M Operational Satellite Conference*, Crystal City, 168-175.
- Revercomb, H. E., H. Buijs, H. B. Howell, R. O. Knuteson, D. D. LaPorte, W. L. Smith, L. A. Sromovsky and H. W. Woolf, 1988a: Radiometric calibration of IR interferometers: experience from the High-resolution Interferometer Sounder (HIS) aircraft instrument. *RSRM 87: Advances in Remote Sensing Retrieval Methods*, A. Deepak, H. Fleming and J. Theon, Eds., A. Deepak.
- , —, D. D. LaPorte, W. L. Smith and L. A. Sromovsky, 1988b: Radiometric calibration of IR Fourier transform spectrometers: solution to a problem with the High-resolution Interferometer Sounder (HIS). *Appl. Optics*, 27, 3210-3218.
- , D. D. LaPorte, W. L. Smith, H. Buijs, D. G. Murcay, F. J. Murcay and L. A. Sromovsky, 1988c: High-altitude aircraft measurements of upwelling IR radiance: prelude to FTIR from geosynchronous satellite. *Mikrochim. Acta*, 11, 439-444.
- Rodgers, C. D., 1987: A general error analysis for profile retrievals. *RSRM 87: Advances in Remote Sensing Retrieval Methods*, A. Deepak, H. Fleming and J. Theon, Eds., A. Deepak.
- Schäfer, K., R. Dubois, R. Haus, K. Dethloff, D. Oertel, H. Becker-Ross, W. Stadthaus, D. Spankuch, V. I. Moroz, L. V. Zasova and I. A. Matsygorin, 1989: Infrared Fourier spectrometer experiment from Venera-15. *Workshop on the Middle and Upper Atmosphere of Venus of the 27th COSPAR Meeting*, Helsinki, *Adv. Space Res.*, in press.
- Smith, W. L., 1970: Iterative solution of the radiative transfer equation for temperature and absorbing gas profiles of an atmosphere. *Appl. Optics*, 9, 1993-1999.
- , and R. Frey, 1990: Cloud altitude determinations from infrared spectral radiances. *J. Appl. Meteor.*, 29, 658-662.
- , H. B. Howell and H. M. Woolf, 1979: The use of interferometric radiance measurements for sounding the atmosphere. *J. Atmos. Sci.*, 36, 566-575.
- , H. M. Woolf and H. E. Revercomb, 1990: A linear simultaneous solution for temperature and absorbing constituent profiles from radiance spectra. *Appl. Optics*, in press. 2
- , H. E. Revercomb, H. B. Howell and H. M. Woolf, 1983: HIS—a satellite instrument to observe temperature and moisture profiles with high vertical resolution. *Fifth Conf. Atmospheric Radiation*, Baltimore, Amer. Meteor. Soc.,
- , H. M. Woolf, H. B. Howell, H.-L. Huang and H. E. Revercomb, 1988: The simultaneous retrieval of atmospheric temperature and water vapor profiles—applications to measurements with the High spectral resolution Interferometer Sounder (HIS). *RSRM 87: Advances in Remote Sensing Retrieval Methods*, A. Deepak, H. Fleming and J. Theon, Eds., A. Deepak,

N92-34097

THEORETICAL COMPUTATION OF TRACE GASES RETRIEVAL RANDOM  
ERROR FROM MEASUREMENTS OF HIGH SPECTRAL RESOLUTION INFRARED  
SOUNDER

Hung-Lung Huang, William L. Smith, Harold M. Woolf  
and J.M. Theriault\*

Cooperative Institute for Meteorological Satellite Studies  
University of Wisconsin-Madison  
1225 West Dayton Street  
Madison, WI 53706  
608-263-5283

DH 568 544

\*DREV-Defence Research Establishment Valcartier  
P.O. Box 8800, Courcelette, Quebec, Canada, G0A 1R0

1. Introduction

The purpose of this paper is to demonstrate the trace gas profiling capabilities of future passive high spectral resolution ( $1 \text{ cm}^{-1}$  or better) infrared ( $600$  to  $2700 \text{ cm}^{-1}$ ) satellite tropospheric sounders. These sounders, such as the grating spectrometer, Atmospheric Infrared Sounders (AIRS) (Chahine et al., 1990) and the interferometer, GOES High resolution Interferometer Sounder (GHIS), (Smith et al., 1991) can provide these unique infrared spectra which enable us to conduct this analysis.

In this calculation only the total random retrieval error component is presented. The systematic error components contributed by the forward and inverse model error are not considered (subject of further studies). The total random errors, which are composed of null space error (vertical resolution component error) and measurement error (instrument noise component error), are computed by assuming one wavenumber spectral resolution with wavenumber span from  $1100 \text{ cm}^{-1}$  to  $2300 \text{ cm}^{-1}$  (the band  $600 \text{ cm}^{-1}$  to  $1100 \text{ cm}^{-1}$  is not used since there is no major absorption of our three gases here) and measurement noise of 0.25 degree at reference temperature of 260 degree K. Temperature, water vapor ozone and mixing ratio profiles of nitrous oxide, carbon monoxide and methane are taken from 1976 US Standard Atmosphere conditions (a FASCODE model). Covariance matrices of the gases are "subjectively" generated by assuming 50% standard deviation of gaussian perturbation with respect to their US Standard model profiles.

Minimum information and maximum likelihood retrieval solutions are used. All terms and definitions except weighting functions outlined in Sec. 2, are identical to those defined in Rodgers (1989), and are not repeated here. Retrieval random error is presented in terms of "level explained variance" for each individual trace gas. However, these preliminary results are by no means complete and are only to be considered as "illustrative".

## 2. Outline of the Computations

The transmittance is computed from a fast regression model (developed at CIMSS) which is based on line-by-line FASCODE 2. Component transmittance profile spectra are created for each radiatively absorbing gas such as H<sub>2</sub>O, O<sub>3</sub>, N<sub>2</sub>O, CO, CH<sub>4</sub>, and CO<sub>2</sub> plus all other absorbing gases. The effective temperature weighting function is then defined as described in Smith et al. (1991), which has the form of

$$K_i(p) = \beta(p) \tau(p) \ln \tau_i(p) \quad (1)$$

where  $i$  represents  $i$ th absorbing gas,  $p$  denotes pressure,  $\tau$  is the total transmittance,  $\tau_i$  is the component transmittance of  $i$ th gas and  $\beta$  denotes scaling factor among radiance, brightness temperature and air temperature. The wavenumber dependence of (1) is to be understood.

Following the development of Rodgers (1989), total random error is the sum of null space error and measurement error. The null space error covariance matrix is

$$S_N = (A-I)S_X(A-I)^T \quad (2)$$

and the measurement error covariance matrix is

$$S_M = DS_eD^T \quad (3)$$

where the averaging kernel  $A=DK$  and  $D$  is the inverse model dependent contribution function that will be defined later. The total random error covariance matrix is

$$S_T = S_N - S_M \quad (4)$$

The "level explained variance" can be expressed as one minus the diagonal element of  $S_T$  divided by the diagonal element of  $S_X$  for each gas  $x$  at each level. Note the neglect of the off-diagonal elements of  $S_T$ .

For the minimum information solution, the contribution function is

$$D = (K^TK - \gamma I)^{-1}K^T \quad (5)$$

where  $\gamma$  is arbitrarily set to  $10^{-3}$ . For the maximum likelihood solution,

$$D = (K^TS_e^{-1}K + S_X^{-1})^{-1}K^TS_e^{-1} \quad (6)$$

## 3. Results and Discussions

Figure 1 represents the retrieval explained variance profile for nitrous oxide, carbon monoxide and methane. Two curves in each panel represents the minimum information and maximum likelihood solutions, respectively. In general, the mid-atmosphere (400 to 850 hpa) has high explained variance

for all three gases. The subtle differences in details between two solutions require further studies.

Random error contributions from the null space and measurement components will be presented in the conference. The averaging kernels will also be discussed. The uncertainties of the a priori statistics and the effects of the smoothing parameter  $\gamma$  on the component errors will be explored. The results presented here are preliminary.

### References

Chahine, M.T., F.G. O'callaghan, H.H. Aumann, R.W. Capps, R.D. Haskins, R.J. Pagano, and R.A. Schindler, 1990 : Atmospheric Infrared Sounder (AIRS) - Science and Measurement Requirements. JPL.

Rodgers, C.D., 1989 : A General Error Analysis for Profile Retrieval. RSRM 87, Advances in Remote Sensing Retrieval Methods, A. Deepak publishing, Hampton, VA, 285-297.

Smith, W.L., H.M. Woolf, and H.E. Revercomb, 1991 : Linear Simultaneous Solution for Temperature and Absorbing Constituent Profiles from Radiance Spectra. Appl. Optics, Vol 30, NO. 9, 1117-1123.

Smith, W.L., H.E. Revercomb, D.D Laporte, L.A. Sromovsky, S. Silverman, H.M. Woolf, H.B. Howell, R.O. Knuteson, and H.-L. Huang, 1991 : GHIS - The GOES High resolution Interferometer Sounder. Accepted for publication in J. Appl. Meteor.

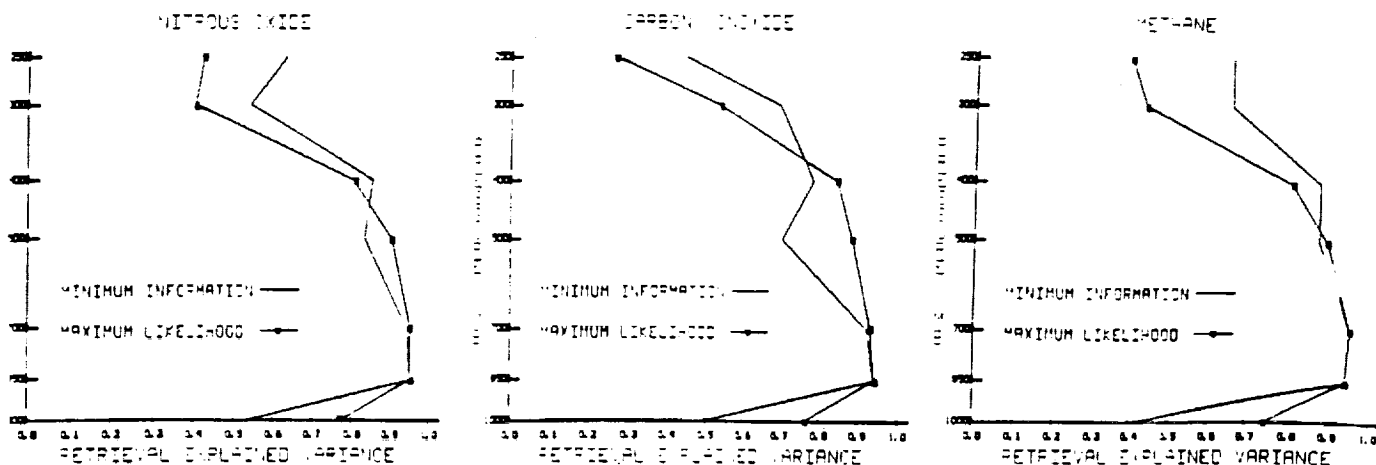


Figure 1, Retrieval explained variance profile of nitrous oxide, carbon monoxide and methane for minimum information and maximum likelihood solutions.

omit

# DRAFT

## HIGH RESOLUTION DEPICTION OF ATMOSPHERIC AND SURFACE VARIATION FROM COMBINED MAMS AND VAS RADIANCES

Christopher C. Moeller,<sup>1</sup>

W. Paul Menzel,<sup>2</sup> and

Kathleen I. Strabala<sup>1</sup>

<sup>1</sup>Cooperative Institute for Meteorological Satellite Studies

<sup>2</sup>NOAA/NESDIS Advanced Satellite Products Project

1225 West Dayton Street

Madison, Wisconsin 53706

### ABSTRACT

High resolution multispectral aircraft data (MAMS) and geostationary sounding data (VAS) have been combined in a physical retrieval method to produce 100 meter resolution derived images of precipitable water, lifted index, and skin temperature for the COHMEX day of June 19, 1986. The method benefits by combining the multispectral sounding capability of VAS with the 100 meter spatial resolution of MAMS. The derived images show significant small scale features including a moist tongue intruding into the COHMEX region and a heat island at Nashville, Tn. Structure function calculations indicate that significant mesoscale variability is not being captured by current geostationary sounding instruments. Geostationary sounding data with at least 1 km resolution or better is needed to monitor this additional mesoscale variation with time.

## 1. INTRODUCTION

Monitoring atmospheric moisture and stability at small scales is an important step to understanding and forecasting mesoscale processes. Few ground-based observing systems can provide the high temporal and spatial coverage necessary to study mesoscale variation; satellite observing systems have shown promise in this endeavor. Moisture and stability products from the geostationary platform VISSR Atmospheric Sounder (VAS) exhibit interesting detail at the meso  $\beta$  (20-200 km) scale (Chesters et al. 1986; Mostek et al. 1986; Smith et al. 1985; Hayden 1988). However, observations of variation at the meso  $\gamma$  (2-20 km) scale remain elusive. Atmospheric processes involved in meso  $\gamma$  scale weather events (such as airmass thunderstorms, cloud development, inversions and land/water interface circulations) are not well observed by VAS data because of its 8 km resolution and radiometric noise. Data averaging reduces the noise but also removes mesoscale variation. Therefore, information leading to a better understanding of such mesoscale phenomena must come from a higher resolution observing system.

The Multispectral Atmospheric Mapping Sensor (MAMS) is well suited to provide mesoscale information about the atmosphere and surface of the earth. This instrument provides high resolution (~100 meter) data over a significant swath (~37 km) and has been used to depict mid-tropospheric water vapor (Menzel et al. 1986);

Jedlovec et al. 1986), total precipitable water (Jedlovec 1990) and sea surface temperature (Moeiler et al. 1989) through the use of its  $6\mu\text{m}$ ,  $11\mu\text{m}$ , and  $12\mu\text{m}$  channels. Similar VAS channels have contributed significantly to precipitable water and lifted index products (Chesters et al. 1986; Robinson et al. 1986). However, Chesters et al., and Robinson et al. also show that other VAS channels are important contributors to these products. This suggests that high resolution derived products be produced by combining multispectral VAS data and high resolution MAMS data. A physical retrieval algorithm developed by Smith et al. (1985) provides the framework to combine VAS and MAMS data by replacing VAS  $6\mu\text{m}$ ,  $11\mu\text{m}$ , and  $12\mu\text{m}$  spectral data with similar MAMS spectral data to generate the derived product images.

This paper presents the procedure by which MAMS and VAS data are used to produce high resolution derived products of precipitable water (PW), lifted index (LI), and skin temperature (TS). Section 2 addresses the characteristics of the VAS and MAMS instruments. Section 3 describes the procedure used to make the derived products, while section 4 presents the application of the procedure to real data, with comparisons to radiosondes collected during the COoperative Huntsville Meteorological EXperiment (COHMEX) (Williams et al. 1987). The spatial and temporal variability of the derived products is evaluated in a structure function analysis (Hillger and Vonder Haar 1979). Data of

June 19, 1986, a day of low level cumulus development over the COHMEX field experiment, is presented.

## 2. INSTRUMENT DESCRIPTIONS AND COMPARISONS

2.1. Both the MAMS and VAS instruments have been described extensively in the open literature so that only a brief discussion of each instrument is presented here.

### 2.1.1. MAMS

The MAMS instrument is a 12 channel scanning radiometer that flies onboard NASA's high altitude ER2 and U2 aircraft at an altitude of about 20 km. Figure 1 shows a depiction of the MAMS scanning geometry. The instrument scans across an 86 degree field of view for a swath width of about 37 km. At 20 km altitude, the data has 100 meter resolution when the 5.0 mrad aperture is used. The MAMS spectral bands are summarized in Table 1. Channels 1-8 are visible/near infrared channels. Channels 9-12 are infrared channels. The infrared channels include surface viewing channels at  $3.7\mu\text{m}$  and  $11.2\mu\text{m}$  as well as water vapor channels for the mid ( $6.6\mu\text{m}$ ) and lower troposphere ( $12.5\mu\text{m}$ ). As noted in the footnotes of Table 1, only three infrared bands can be used on a given flight (the  $3.7\mu\text{m}$  and the  $6.6\mu\text{m}$  channels are readily exchanged between flights). Generally, the  $3.7\mu\text{m}$  channel is used for surface applications (e.g., sea surface temperature); the  $6.6\mu\text{m}$  channel is employed for atmospheric studies (e.g., atmospheric

water vapor). For this study, the  $6.6\mu\text{m}$  detector was used in channels 9 and 10. Channels 11 and 12 form the well-known split window combination.

MAMS visible/near IR data is calibrated by laboratory measurement, usually right before and after aircraft deployments. Infrared data is calibrated on each scan line by viewing two onboard blackbodies of known temperature. A linear detector response is assumed to define the calibration slope and offset. Blackbody counts may be averaged over several lines to reduce noise in the line to line calibration.

Additional discussion of the MAMS instrument and its performance is found in Jedlovec et al. (1989).

#### 2.1.2. VAS

VAS is a 12 channel spin scan radiometer that was deployed on the GOES series of satellites for the purpose of atmospheric sounding and multispectral imaging (Menzel 1980; Smith et al. 1981). The VAS channels are shown in Table 2. VAS consists of temperature sounding channels in the  $15\mu\text{m}$   $\text{CO}_2$  band (channels 1-5), a split window combination (7 and 8), mid-tropospheric water vapor channels (9 and 10), and shortwave channels (6, 11, and 12). In general, VAS channels 1-10 are used to make retrievals with channel 12 used for a skin temperature guess and cloud checks (Hayden 1988). VAS channels 4, 5, 7, 8, 9, and 10 are available at 8 km resolution (others at 16 km resolution). Noise is

generally reduced to less than 1.5 K for all channels by multiple sampling (the dwell sounding mode of operation). Further information on the VAS instrument may be found in Montgomery and Uccellini (1985).

## 2.2. MAMS/VAS Instrument Comparisons

The VAS instrument has several atmospheric sounding channels that the MAMS instrument does not. This additional spectral coverage provides VAS with a better vertical resolution sounding capability than MAMS has. The MAMS data has high horizontal resolution. This resolution advantage over VAS, while perhaps not so important for mid-tropospheric data, is well suited for evaluating the variability of surface and lower tropospheric fields. The spatial variability of MAMS  $11\mu\text{m}$  and  $12\mu\text{m}$  data has been demonstrated by Jedlovec (1990) for June 19, 1986 COHMEX data. In that work thermal variance was shown to level off significantly beyond a field of view size of about 3 km. Thus, the MAMS shows a capability to identify small scale thermal features that are below the resolution of VAS data, which may be important in identifying preferred areas of local convection or low level cloud development.

In replacing VAS spectral data with MAMS spectral data, it is important, because of absorption constituent considerations, that the MAMS and VAS channels have close spectral agreement.

Figure 2 illustrates the spectral characteristics of the similar channels. Both the  $6\mu\text{m}$  and  $11\mu\text{m}$  channels of VAS and MAMS show excellent agreement while the  $12\mu\text{m}$  channels show some deviation which is more noticeable because of their narrow bandwidths. Water vapor absorption in the MAMS  $12\mu\text{m}$  channel will likely be greater than in the VAS  $12\mu\text{m}$  channel. However, this can be accounted for in a MAMS/VAS instrument bias adjustment.

An instrument bias was calculated by comparing collocated VAS and MAMS observed data of June 19, 1986 over the entire MAMS data domain. This bias removes variance between the instruments arising from spectral response, absolute calibration, viewing geometry, and time of observation differences. A set of 69 MAMS and VAS collocated data were considered for the bias calculation. VAS data observed at nominal times of 1600 and 1730 UTC were used to compare with the MAMS data collected between 1530 and 1800 UTC. In order to obtain spatial agreement in footprint size, the VAS spatial weighting function (which includes the effects of impulse response and diffraction) was applied to the MAMS data to simulate the spatial response of a VAS field of view. The results of this comparison showed biases of 2.21, 5.69, and 3.24 K for the  $6\mu\text{m}$ ,  $11\mu\text{m}$ , and  $12\mu\text{m}$  comparisons, respectively. The positive values indicate that the MAMS data is warmer than the VAS data. These bias values are applied to the MAMS data when it is substituted

for the VAS data in the derived imagery production process which is described in the next section.

### 3. ALGORITHM

Previous efforts to make derived imagery products from 8 km VAS data have used retrieval statistics generated from a simultaneous retrieval technique (Smith and Woolf 1984) for an area average (e.g., 100 km by 100 km) of VAS radiances. The retrieval statistics are then applied to individual VAS fields of view (fov) to produce 8 km resolution derived product imagery (Smith et al. 1985). In the formulation, a set of coefficients,  $\alpha_i$ , are produced and are used with pressure dependent basis functions,  $\phi(p)$ , to produce departures of skin temperature  $T_s$ , precipitable water vapor U, and atmospheric temperature T, from some first estimate:

$$\delta T_s = \alpha_0 \phi_0$$

$$\delta U(p) = \sum_{i=1}^N \alpha_i \int_0^p q(p) \phi_i(p) dp$$

$$\delta T(p) = \sum_{i=N+1}^M \alpha_i \phi_i(p)$$

where precipitable water vapor U and mixing ratio q are related by

$$\delta q(p) = g \sum_{i=1}^N \alpha_i q(p) \phi_i(p)$$

$$\delta(p) = - \frac{1}{g} \int_0^p \delta q(p) dp$$

and  $g$  is gravity. See Smith and Woolf for the formulation of the  $\alpha_i$  coefficients. Since  $\alpha_i$  is dependent on the channel brightness temperatures,  $\alpha_i$  can be recalculated at each fov to capture pixel to pixel variation in the skin temperature, precipitable water vapor, and atmospheric temperature fields.  $\alpha_i$  dependence on the atmospheric transmittance (including the transmittance dependence on water vapor), the slope of the Planck function (for converting radiance to temperature), and the expected errors of the radiance observations are not recalculated at each fov (Smith and Woolf 1984). Channel weighting functions are used as basis functions.

In the MAMS/VAS effort, a three channel ( $6\mu\text{m}$ ,  $11\mu\text{m}$ ,  $12\mu\text{m}$ ) retrieval is produced for a  $5 \times 5$  VAS fov area, with  $\alpha_i$  coefficients then computed at each MAMS fov, using the bias corrected MAMS  $6.6\mu\text{m}$ ,  $11.2\mu\text{m}$ , and  $12.5\mu\text{m}$  channel radiances in place of the similar VAS channels. A  $5 \times 5$  retrieval size was chosen because it roughly matches the MAMS 37 km swath width. Those VAS channels not replaced by MAMS data influence the MAMS/VAS retrieval through its first guess, a VAS-only  $5 \times 5$  fov 10 channel retrieval (which uses the NMC Aviation model forecast for its first guess). As with previous retrieval efforts (Hayden 1988), surface data from National Weather Service SVCA observations are used in the retrieval. This data is updated to

the resolution of the MAMS data by adjusting a grid of the SVCA data for MAMS  $11\mu\text{m}$  temperature variation. Cloud checks are performed on the VAS and MAMS data. Cloudy VAS fovs are removed from the 5 x 5 retrieval. No soundings are made at cloudy MAMS pixels.

#### 4. EVALUATION OF TECHNIQUE

##### 4.1. June 19, 1986

The surface weather of June 19 over the COHMEX region is shown in Fig. 3. Dry Canadian high pressure which had moved over the COHMEX region on the 18th began to slide off to the east, reducing the subsidence over the region as well as increasing the low level moisture, especially in the southern part of the COHMEX region. Surface temperatures reached into the upper 80s while surface dew points ranged from the upper 50s to the upper 60s from north to south over the COHMEX region. Synoptic scale atmospheric forcings were weak as surface and upper level winds were light. Although no significant convection occurred, sufficient moisture and surface heating were present to produce low level cumulus over eastern Tennessee beginning about 1700 UTC. During the next several hours this cumulus field expanded to cover much of east central Tennessee and northern Alabama. During the afternoon a few of these cumulus did grow sufficiently to produce brief light showers over the region.

On June 19, the MAMS was flown over the COHMEX region from about 1530 UTC to 1800 UTC. Figure 4 shows the COHMEX region and the MAMS straight line flight tracks that were flown on that day. Table 3 lists information about each flight track. Note that flight tracks F-G and H-I were repeated. During the flight, 100 meter resolution radiometric data with 8-bit precision was collected for the MAMS 6.6 $\mu$ m, 11.2 $\mu$ m, and 12.5 $\mu$ m channels. On this same day, VAS dwell sounding pairs were collected at 1600 UTC and 1730 UTC. These dwell sounding data were combined with the MAMS data as indicated in Table 3 to produce the derived imagery products.

Both the MAMS and VAS navigation were inspected to assure good collocation between the two instruments. MAMS 6.6 $\mu$ m data was corrected for zenith angle effects under an assumption of homogeneity across the MAMS swath width; no correction was applied to the MAMS 11.2 $\mu$ m or 12.5 $\mu$ m data because of a relatively weaker effect in these channels and uncertainty in the correction.

MAMS/VAS retrievals were made using the procedure described in section III for five of the six straight-line flight tracks flown on June 19 by MAMS (the B-C flight track was not processed because it fell in a VAS data void). Figure 5 shows a representative profile as it evolves during the retrieval process. The top panel of Fig. 5 shows the impact of the VAS-only retrieval (which is used as the first guess for the MAMS/VAS retrieval). A

slight modification of the NMC guess moisture profile has occurred while the temperature profile is affected at mid and upper tropospheric levels only. This temperature profile impact is at least partly a result of the VAS CO<sub>2</sub> sounding channels which are not common to the MAMS instrument. Without including these VAS channels, this modification to the guess profile probably would not occur. The bottom of Fig. 5 demonstrates the resulting profile after the MAMS/VAS retrieval. The guess profile shown in the bottom of Fig. 5 is the profile that was produced in the VAS-only retrieval. Changes to the guess profile are confined to lower levels of the troposphere. This reflects the impact of the MAMS 11 $\mu$ m and 12 $\mu$ m data on the MAMS/VAS retrieval. Note that the mid and upper tropospheric profile has not been modified in the bottom panel.

#### 4.2. Analysis of Derived Products

Fields of precipitable water (PW), lifted index (LI) and skin temperature (TS) from the MAMS/VAS retrieval process are shown for June 19 in Figs. 6-8. The data has been remapped into a Mercator projection with a degradation of resolution down to .6 km so that adjacent flight tracks can be shown in a single image format. Each figure consists of a composite of three initial flight tracks (D-E, F-G, H-I) and a composite of two repeated flight tracks (F-G, H-I). The northernmost two flight tracks of

the three flight track image are collocated with the image of the repeated flight tracks. Note that there is about 30 to 40 minutes time difference between adjacent flight tracks which reduces continuity of clouds and features between flight tracks. There is also an indication of a limb effect across each flight track in the figures.

The precipitable water (PW) analysis shows generally higher moisture to the east and south in the imagery. Undetected thin cirrus exists in the NW corner of both the three track and two track composites and is likely responsible for the moisture maximum in that portion of the PW imagery. A moisture maximum of about 34 mm can be seen in east central Tennessee southeast of Nashville, TN (BNA). The gradient to the northwest shows a decrease of about 8-10 mm over a distance of about 100 km with a more concentrated gradient of 6-8 mm over about 20 km to the northwest of the moisture maximum. This moisture pattern was also found by Jedlovec (1990) using a split window variance ratio technique on MAMS June 19, 1986 data. This general moisture pattern shows up in the COHMEX Beta Network radiosondes for 1800 UTC in Fig. 9. It is evident however that the maximum and minimum locations in Fig. 9 are strongly influenced by the location of the COHMEX radiosondes, as would be expected; the high resolution MAMS/VAS product is much more capable of accurately identifying the location of the moisture maximum than the ~100 km spaced

COHMEX Beta Network radiosondes. Radiosonde PW values show fairly good relative agreement with the MAMS/VAS PW field, while absolute comparisons show a small ( $\sim 2$  mm) bias in the MAMS/VAS PW product (for this comparison, the repeated flight track data is used since it is the closest collocation in time to the launch of the radiosondes).

Higher moisture to the southeast is also identifiable in the repeated flight tracks which provide some insight to the time evolution of the field. The moisture has extended somewhat northward and expanded in the east-west direction in the repeat overpass composite. The analysis shows PW values have increased by 1-2 mm in east central Tennessee and that the gradient to the northwest has smoothed somewhat. This time continuity lends credence to the MAMS/VAS product. Low level cumulus began to form at the time of the repeat overpass ( $\sim 1700$  UTC) in east central Tennessee. In the next couple hours this field of cumulus expanded westward to about the center of flight track F-G, in good correlation with the increasing moisture. Figure 10 shows the cumulus field as it looked at 1900 UTC, about one hour after the MAMS data collection ended. 2100 UTC COHMEX radiosondes (not shown) indicated a continuing increase of moisture over east central Tennessee, in agreement with the trend depicted in the MAMS/VAS PW imagery. While the influence of other factors such as topography, surface conditions, etc., should not be overlooked,

atmospheric moisture seems to have played an important role in the development of the cumulus.

The lifted index (LI) analysis (Fig. 7) of the initial flight tracks shows a broad unstable maximum (-2) in east central Tennessee near the location of the moisture maximum. This generally agrees with the relative variation of the COHMEX 1800 UTC radiosonde LI, although a 3-4 K bias towards unstable values is apparent. The general location of the low level cumulus field that developed agrees with the relatively unstable location in east central Tennessee. The repeated flight tracks show that much of the area is destabilizing over the one hour interval. This is likely the result of surface heating. Interestingly, the most rapid destabilization is taking place in the western portion of the flight tracks. This might lead one to expect cloud development further west than actually occurred. However, the cumulus development remained in and around the moisture (Fig. 6) concentrated in east central Tennessee.

Around the cumulus cloud development in east central Tennessee (repeat overpass of the F-G track) the LI values appear to remain constant or actually increase (become more stable) with time. This seems contrary to cloud development and contrasts to a general destabilization over the rest of the COHMEX region. Evidence is insufficient to say whether this is a true atmospheric trend or a result of cloud contamination in the VAS radiances,

which have a larger impact on the LI product than on the PW or TS products. However, this does point out the difficulty of using relatively low resolution data in a highly variant field (in this case impacted by clouds). The need for high resolution data in atmospheric sounding for cloud clearing purposes has been pointed out by Menzel et al. (1984) in a study of VAS retrievals using large detector versus small detector data.

The skin temperature (TS) product of Fig. 8 shows considerable high resolution variability. Land slope and the various land uses in the COHMEX region (e.g., forest, agriculture, urban) contribute strongly towards this variability. In particular, a definite heat island is observed at the location of Nashville, TN (BNA) with skin temperatures 5 to 10 K warmer than the surrounding region. Surface emissivity variation may also contribute to the variability in the skin temperature product since emissivity is assumed uniform at .96 for all the retrievals (Hayden 1988). Note that individual pixel values of TS range by more than 20°C.

Time change of TS shows good continuity of thermal features in Fig. 8. Samples show that individual pixel skin temperatures increase by as little as < 1 K to as much as 5 K or more over the one hour time interval. Over a selected larger clear region (~50000 pixels; ~20 X 25 km) the average skin temperature increase was 2.75 K. Many land types are included in this average, which

is thus not representative of the temperature changes that might occur at individual 100 meter resolution pixels. For comparison, Tarpley (1988) found 30-day average three hour (0900-1200 LST) heating rates of 4-8 K across Kansas in June using 40 X 40 km GOES target areas. Such skin temperature monitoring is useful in radiation budget studies of the surface of the earth. Significant small scale variability in the skin temperature field makes it difficult to identify relationships between cloud development and skin temperature at the meso  $\gamma$  scale. In a study of Oklahoma land types and their relationship to convective cloud formation, Rabin et al. (1990) found convective clouds tended to form earliest over warm, dry land surfaces. In a broad sense, the cumulus on June 19 formed over a region of relatively warm skin temperatures, although there was no cloud development over many other regions of comparably warm skin temperatures in the TS imagery. Given a lack of rainfall in Tennessee over the previous eight days (only isolated convection along the Tennessee/Alabama and Tennessee/Georgia borders on June 17), it is unlikely that surface residual moisture was a significant factor in the location of the cumulus development. This indicates that other factors such as the atmospheric moisture pattern and topography played an important role in the cloud development on June 19. Topography data show that significant relief (500-1000 feet) exists in SE Tennessee and gradually diminishes towards the MAMS flight area to

the west (<500 feet). The initial cloud formation did occur in SE Tennessee over the region of greatest topography; however, the cloud formation continued over much weaker relief as the day wore on. This suggests that topography and atmospheric moisture combined to produce the earliest clouds, but that sufficient instability and moisture was present to produce clouds over relatively weak relief later in the day.

Other noted relationships included a positive correlation (-.75) linking MAMS channel 5 (similar to VISSR visible channel) visible brightness to warmer skin temperatures. This is presumably a relationship between surface vegetation type and skin temperature. A similar relationship was noted by Rabin et al. (1990) over the Oklahoma region. Also, in the cloud development region the skin temperature actually showed a small decrease with time (-.35 K) over a large area, possibly indicating cloud shadowing of the surface.

#### 4.3. Effect of MAMS Noise

The effect of MAMS single sample noise on the derived products was evaluated by using single sample noise estimates for each MAMS channel in the  $\alpha_i$  coefficient calculation. Since the  $\alpha_i$  coefficients represent a departure from a mean condition, a direct impact of noise can be determined by simply allowing the departure to be solely due to noise. An evaluation using several

MAMS/VAS retrievals indicated that the MAMS noise contribution to the PW, TS, and LI products was about .75 mm, .5 K, and .5 K, respectively. This represents about 15%, 5%, and 5% of the variation in each product respectively. Thus, real variation of PW, TS, and LI is easily observed using the MAMS/VAS retrieval methodology.

#### 4.4. Variability of Derived Products

The spatial variability of the PW, LI, and TS fields was evaluated in a structure function calculation. The structure function has been described by several authors (e.g., Hillger and Vonder Haar 1979; Fuelberg and Meyer 1986). Under the assumptions of homogeneity and isotropy, structure becomes a function of only the scalar separation between data points. A graph of structure versus scalar separation depicts spatial gradients. Where the slope of the plot is greater, mean horizontal gradients are stronger over separation distance.

The random noise of the derived products was evaluated by extrapolating the structure function to zero separation (Hillger and Vonder Haar 1979). With an assumption of no spatially correlated error, the structure function at zero separation becomes

$$\text{STR}(0) = 2 \sigma^2$$

where  $\sigma^2$  is the variance of the random noise. Structure function calculations were made at three locations using a 5 km by 5 km domain with a 100 meter separation interval (i.e., 50 X 50 pixel domain). The structure between 100 m and 1 km separation distances was fit with a second order curve and extrapolated to zero separation distance. A second order curve fit was used because it best fit the shape of the structure data. Random noise estimates for the three locations of each product are shown in Table 4 along with the average of the three estimates for each product. The three estimates for each product show some variation making the random noise estimates somewhat uncertain. However, the averaged noise results for PW and LI are consistent with those obtained by using single sample MAMS noise estimates in the retrieval (Section 4.3), while the TS structure noise value is somewhat larger. The explanation for the TS discrepancy may be that the rapidly increasing TS structure at small separations creates uncertainty in the extrapolation to the noise value.

PW, LI, and TS isotropic structure functions for a repeat overflight (1630 and 1730 UTC) are shown in Figs. 11-13, respectively. Flight track F-G was selected for the computation because it encompassed the moisture maximum identified in section 4.2 as well as good visual variability in the LI and TS products. The structure was calculated out to 180 km separations with a separation interval of 300 meters (calculations have indicated

that using the data at higher resolution did not appreciably alter the results). Data pairs per separation interval exceeded 100,000 for all separations. All three products demonstrate significant structure at meso  $\gamma$  separations. The rapid structure increase at small separations reduces the possibility of noise dominating the structure. Hillger and Vonder Haar (1988) noted that simulations showed gradient information was detectable at a level only 10% above the extrapolated structure minimum. Calculations showed the ratio of the structure at the smallest separation (300 m) to that of the average extrapolated minimum is -1.75, 2.10, and 4.60 respectively for the PW, LI, and TS products. Thus real gradients are being observed at even the smallest separations. The moisture maximum in east central Tennessee is likely associated with the structure maximum at about 30 km separation distance. The LI structure shows a relatively weaker maximum at this separation, probably because the instability maximum in east central Tennessee is somewhat more spread out, shifting the variability to larger separations. At large separations PW and LI structure both increase, indicating that atmospheric gradients are present at larger scales. This is consistent with the fact that the atmosphere varies significantly at larger scales (e.g., across air mass boundaries), which has been demonstrated with structure functions by Fuelberg and Meyer (1986) using VAS derived precipitable water products for separations out to 700 km. The

dominance of small scale gradients in the TS structure is not surprising given the highly variant nature of the thermal field in the COHMEX region.

The one hour time evolution of the structure is also shown in Figs. 11-13. The atmospheric quantities, PW and LI, show changes in the shape of the structure curve with time, while the surface temperature, TS, shows a fairly uniform increase of structure with time. While it is difficult to explain changes at particular separations, the overall trends may be informative about basic atmospheric and surface responses to forcings. PW and LI structure slope decrease with time at small scale separations (up to 25 km), indicating a smoothing of gradients with time. The structure maxima at about 30 km separation associated with the moisture and instability features in east central Tennessee are now weaker. Since PW and LI are affected by changes throughout much of the atmospheric column, there is uncertainty concerning the explanation of the reduced gradients with time. However, it can be reasonably speculated that mesoscale moisture expanded spatially with time and smoothed the smaller scale gradients (as is indicated by the PW analysis of Fig. 6). Also, boundary layer vertical and horizontal mixing may be affecting the structure. Surface inhomogeneities cause spatial variations of sensible and latent heat fluxes which lead to horizontal variability of boundary layer temperature and moisture. Mixing processes may

reduce this variability during the day as air is exchanged horizontally between thermals. Physical evidence of boundary layer mixing on June 19 is given by the onset of low level cumulus. This boundary layer mixing would be superimposed on other atmospheric processes such as mesoscale moisture advection. The net effect has been to reduce the smaller scale horizontal temperature and moisture gradients in this case. At larger separations ( $> 50$  km) PW gradients become nearly constant (constant slope). This also indicates gradient smoothing with time, however caution is advised as the separation distance approaches half of the domain size ( $\sim 200$  km). Features with wavelengths approaching 100 km and larger may be aliased in the structure data. Larger separation LI structure shows gradients weakening with time. This reflects the rapid destabilization that took place in western Tennessee over the one hour interval (Fig. 7). The result of this was a smoothing of larger scale gradients. This rapid destabilization may have been caused by larger sensible heat fluxes in western Tennessee. The LI structure change may also reflect temperature changes in the mid-troposphere with time although given the synoptic conditions, such changes would be expected to be small over a one hour interval. The fairly uniform increase of TS structure can be attributed to the inability of the surface to quickly mix thermal gradients; warm surfaces heat up at a faster rate than cool surfaces (which are presumably cooler

because of considerations involving vegetation type, soil moisture content, etc.). The increased surface thermal gradients are seen as increased structure. It is expected that these thermal gradients decrease when the solar input is removed. A slight indication that differential surface heating occurred over larger scale surface inhomogeneities is shown by small maximums of structure at about 70 km and 90 km separation distance.

In the context of these physical explanations, the evolution of the structure functions demonstrate reasonable atmospheric and surface trends. While the PW and LI structure functions might be expected to show more continuity of features with time, these results indicate the atmosphere's ability to evolve rapidly at small scales. Such rapid mesoscale evolution has been pointed out by Fuelberg and Meyer (1986) in both satellite as well as radiosonde PW. However, while most of the structure trend is attributable to physical processes, influences such as limb effects, undetected cloud, noise characteristics, and aliasing at large separations are also affecting the structure.

A comparison of MAMS/VAS and VAS-only structure is shown in Fig. 14 for the PW product. The VAS PW data is taken from special data set soundings produced for the COHMEX scientific community (Veldon et al. 1988). The primary difference between the MAMS/VAS and VAS COHMEX special data set is the spatial resolution (i.e., 100 meter vs. 8 km). It is immediately obvious that the

instrument resolution impact on the PW product is quite large. The MAMS/VAS product demonstrates larger gradients at relatively small separations that the VAS COHMEX data set does not capture. At separations less than 50 km the MAMS/VAS PW structure is roughly twice that of the VAS structure. In addition, larger sample sizes per separation interval should make the MAMS/VAS PW structure less susceptible to noise. Thus, high resolution data provides both a capability to identify small scale atmospheric and surface variability, and reduces the effect of noise on the data through larger sample sizes for analysis at given spatial scales. A similar comparison between MAMS/VAS LI structure and VAS-only LI structure (not shown) showed much more similar structure functions at small separations, probably because the VAS data contributes more to the MAMS/VAS LI product than to the PW product; had a comparison been made for TS, it is expected that results would have been similar to those of the PW product structure comparison. This comparison, while representing only a single case, clearly suggests that gradient information at small scales is not being captured by relatively coarser resolution instruments such as VAS.

## 5. CONCLUSIONS

A technique for combining 100 meter resolution MAMS and 8 km resolution VAS radiances to produce high resolution maps of precipitable water, lifted index and skin temperature has been

demonstrated. Each quantity exhibits real spatial and temporal variation at the meso  $\gamma$  and larger scales. In particular, a moisture maximum in east central Tennessee during the COHMEX day of June 19, 1986 has been identified, as well as a heat island at Nashville, Tennessee. The June 19, 1986 case study of these quantities and their evolution in the context of a developing low level cumulus field indicated that returning moisture on the backside of high pressure had an apparent influence on the development and existence of low level cumulus in the region. This suggests that atmospheric variability is influential in cloud development. A lifted index quantity also demonstrated some ability to identify the location of the cumulus development. Topography was also indicated as an important contributor to the initial cloud development. Skin temperature data was more ambiguous, with clouds forming over a relatively warm region while not forming over other comparably warm regions. A possible effect of cloud shadowing was also noted in the skin temperature data.

Structure function analyses were used to present a quantitative measure of the spatial variability of each product. Real atmospheric gradients of moisture and stability have been identified at scales down to 300 m. Surface variability (dependent on local land use) was found to be dominant at small scales. A comparison between VAS 8 km resolution and the MAMS/VAS 100 meter resolution precipitable water structure demonstrated the

additional variability identified by using high resolution data. These results indicate that a geostationary sounding capability with better than 1 km resolution is needed if most of the meso  $\gamma$  scale variability in the atmosphere (and on the surface) is to be monitored over short temporal intervals ( $< 1$  hr).

#### ACKNOWLEDGMENTS

The authors acknowledge NASA's High Altitude Missions Branch for their efforts in collecting the MAMS data used in this paper. Scientific input from Dr. Gary Jedlovec, Marshall Space Flight Center, is also greatly appreciated. This work was supported under NASA contract NAS8-36169.

## REFERENCES

- Chesters, D., A. Mostek, and D. A. Keyser, 1986: VAS sounding images of atmospheric stability parameters. *Wea. and Forecasting*, 1, 5-22.
- Fuelberg, H. E., and P. J. Meyer, 1986: Analysis of mesoscale VAS retrievals using statistical structure functions. *J. Clim. Appl. Meteor.*, 25, 59-76.
- Hayden, C. M., 1988: GOES-VAS simultaneous temperature-moisture retrieval algorithm. *J. Appl. Meteor.*, 27, 705-733.
- Hillger, D. W., and T. H. Vonder Haar, 1979: An analysis of satellite infrared soundings at the mesoscale using statistical structure and correlation functions. *J. Atmos Sci.*, 36, 287-305.
- and T. H. Vonder Haar, 1988: Estimating noise levels of remotely sensed measurements from satellites using spatial structure analysis. *J. Atmos Oceanic Tech.*, 5, 206-214.
- Jedlovec, G. J., W. P. Menzel, G. S. Wilson, and R. J. Atkinson, 1986: Detection of mountain induced mesoscale wave structures with high resolution moisture imagery. *Second Conference on Satellite Meteorology/Remote Sensing and Applications*, May 13-16, 1986, Williamsburg, VA, AMS, Boston, 365-369.

- , K. B. Batson, R. J. Atkinson, C. C. Moeller, W. P. Menzel, and M. W. James, 1989: Improved capabilities of the Multispectral Atmospheric Mapping Sensor (MAMS). NASA Technical Memorandum 100352, Marshall Space Flight Center, Huntsville, AL, 71pp.
- , 1990: Precipitable water estimation from high-resolution split window radiance measurements. Submitted to *J. Appl. Meteor.*, July 1989.
- Menzel, P., 1980: Pre-launch study report of VAS-D performance. Report to NASA under contract NAS5-21965 from SSEC, Space Science and Engineering Center, Madison, WI.
- , T. A. Achtor, C. M. Hayden and W. L. Smith, 1984: The advantages of sounding with the smaller detectors of the VISSR Atmospheric Sounder. NOAA Technical Memorandum NESDIS 6, U.S. Department of Commerce, Washington, DC, 22pp.
- , G. J. Jedlovec, and G. S. Wilson, 1986: Verification of small scale features in VAS imagery using high resolution MAMS imagery. *Second Conference on Satellite Meteorology/Remote Sensing and Applications, May 13-16, 1986, Williamsburg, VA.* AMS, Boston, 108-111.
- Moeller, C. C., L. E. Gumley, W. P. Menzel, and K. I. Strabala, 1989: High resolution depiction of SST and SSC from MAMS data. *Fourth Conference on Satellite Meteorology and*

*Oceanography*, May 16-19, 1989, San Diego, CA, AMS, Boston,  
208-212.

- Montgomery, H. E., and L. W. Uccellini (Eds.), 1985: VAS demonstration: (VISSR Atmospheric Sounder) description and final report. NASA RP-1151, 198pp. (NTIS 86N13867).
- Mostek, A., L. W. Uccellini, R. A. Petersen, and D. Chesters, 1986: Assessment of VAS soundings in the analysis of a preconvective environment. *Mon. Wea. Rev.*, 114, 62-87.
- Rabin, R. M., S. Stadler, P. J. Wetzel, D. J. Stensrud, and M. Gregory, 1990: Observed effects of landscape variability on convective clouds. *Bull. Amer. Meteor. Soc.*, 71, 272-280.
- Robinson, W. D., D. Chesters, and L. W. Uccellini, 1986: Optimized retrievals of precipitable water fields from combinations of VAS and conventional surface observations. *J. Geophys. Res.*, 91 (D4), 5305-5318.
- Smith, W. L., V. E. Suomi, W. P. Menzel, H. M. Woolf, L. A. Sromovsky, H. E. Revercomb, C. M. Hayden, D. N. Erickson, and F. R. Mosher, 1981: First sounding results from VAS-D. *Bull. Amer. Meteor. Soc.*, 62, 232-236.
- , and H. M. Woolf, 1984: Improved vertical soundings from an amalgamation of polar and geostationary radiance observations. *Conference on Satellite Meteorology/Remote Sensing and Applications, June 25-29, 1984, Clearwater Beach, FL*, AMS, Boston, MA, pp.45-48.

-----, G. S. Wade, and H. M. Woolf, 1985: Combined atmospheric sounding/cloud imagery - a new forecasting tool. *Bull. Amer. Meteor. Soc.*, 66, 138-141.

Tarpley J. D., 1988: Some climatological aspects of satellite-observed surface heating in Kansas. *J. Appl. Meteor.*, 27, 20-29.

Velden, C. S., B. M. Goodman, and W. L. Smith, 1988: Meteorological satellite products support for project COHMEX: Final report to NASA. Available from Cooperative Institute for Meteorological Satellite Studies, Madison, WI, 11pp.

Williams, S. T., H. M. Goodman, K. R. Knupp, and J. E. Arnold, 1987: SPACE/COHMEX Data Inventory Document. NASA Technical Memorandum 4006. Marshall Space Flight Center, Huntsville, AL (available NTIS), 480pp.

Table 1. MAMS spectral channels.

<u>channel</u>	<u>bandwidth (@ 50% response)</u>
1 <sup>a</sup>	0.42 - 0.45
2	0.45 - 0.52
3	0.52 - 0.60
4	0.57 - 0.67
5	0.60 - 0.73
6	0.65 - 0.83
7	0.72 - 0.99
8	0.83 - 1.05
9 <sup>b</sup>	3.47 - 3.86
10	6.28 - 6.98
11	10.55 - 12.24
12	12.32 - 12.71

<sup>a</sup> Channel 1 is not available when 10 bit data is collected.

<sup>b</sup> Only three infrared bands are available at once. The 3 $\mu$ m and 6 $\mu$ m bands are interchangeable.

Table 2. VAS spectral channels.

<u>channel</u>	<u>bandwidth (@ 50% response)</u>
1	14.63 - 14.84
2	14.31 - 14.65
3	14.09 - 14.42
4	13.82 - 14.21
5	13.16 - 13.51
6	4.48 - 4.57
7	12.50 - 12.82
8	10.36 - 12.12
9	7.16 - 7.37
10	6.40 - 7.08
11	4.41 - 4.48
12	3.34 - 4.06

Table 3. MAMS flight track data for June 19, 1986.

<u>Track</u>	<u>Time</u> <u>(GMT)</u>	<u>Coincident</u> <u>VAS time</u>	<u>Remarks</u>
B-C	1521 - 1545	---	no VAS overlap
D-E	1553 - 1610	1600	clear skies
F-G	1621 - 1643	1600	clear skies
H-I	1650 - 1713	1600	some cirrus
F-G	1720 - 1743	1730	repeat overpass cumulus in eastern quarter
H-I	1750 - 1814	1730	repeat overpass some cirrus

Table 4. Precipitable water (PW), lifted index (LI), and skin temperature (TS) random noise estimates using structure functions. Estimates are presented for each of three locations and an average of the three locations for each product.

<u>Product</u>	<u>Extrapolated noise</u>	<u>Average</u>
PW <sub>1</sub>	0.62 mm	
PW <sub>2</sub>	0.65 mm	0.74 mm
PW <sub>3</sub>	0.93 mm	
LI <sub>1</sub>	0.22 K	
LI <sub>2</sub>	0.56 K	0.33 K
LI <sub>3</sub>	0.20 K	
TS <sub>1</sub>	2.33 K	
TS <sub>2</sub>	0.86 K	1.55 K
TS <sub>3</sub>	1.45 K	

ORIGINAL PAGE IS  
OF POOR QUALITY

FIGURE CAPTIONS

Figure 1 - MAMS instrument scanning geometry. At 20 km altitude, a MAMS instantaneous field of view (ifov) is about 100 meters on a side. Insert demonstrates overlap of ifovs from scan line to scan line.

Figure 2 - Normalized spectral response functions of MAMS and VAS 6 $\mu$ m (top), 11 $\mu$ m (middle) and 12 $\mu$ m (bottom) channels.

Figure 3 - Surface pressure and temperature (top) analysis and 500 mb height and temperature analysis (bottom) for June 19, 1986 at 1200 UTC. Temperatures in  $^{\circ}$ C. pressure in millibars, heights in decameters (from Jedlovec 1990).

Figure 4 - GOES 1600 GMT visible imagery of the COHMEX region on June 19, 1986 with the COHMEX Beta Network radiosonde locations (numbered) and the MAMS flight tracks (lettered). Note the generally clear conditions in the MAMS flight region.

Figure 5 - Guess (solid) and departure (dashed) for retrieved atmospheric profiles of temperature (T) and moisture ( $T_d$ ) for VAS (top) and MAMS/VAS (bottom) physical retrievals. The guess profile used in the MAMS/VAS retrieval is the retrieved profile in

the top panel, thus deviations from the guess in the MAMS/VAS retrieval are due to the MAMS data.

Figure 6 - MAMS/VAS precipitable water product (mm) with analysis for flight tracks D-E, F-G, and H-I (top) and for repeat overpass of flight tracks F-G and H-I (bottom) one hour later. White areas are cloud cover. See Fig. 4 for location of flight tracks. Location of Nashville, TN (BNA) is shown.

Figure 7 - MAMS/VAS lifted index stability product (deg) with analysis for same region as Fig. 6. Positive values are most stable.

Figure 8 - MAMS/VAS skin temperature product (deg) with analysis for same region as Fig. 6.

Figure 9 - COHMEX Beta Network radiosonde precipitable water (top) and lifted index (bottom) values with analysis for 1800 GMT on June 19, 1986. Radiosonde data in large numerals.

Figure 10 - GOES 1900 GMT visible imagery for June 19, 1986 over the COHMEX region with MAMS flight tracks and COHMEX Beta Network radiosonde locations overlain. Note the cumulus cloud development that has taken place from 1600 GMT (Fig. 4) to 1900 GMT.

ORIGINAL PAGE IS  
OF POOR QUALITY

Figure 11 - MAMS/VAS precipitable water isotropic structure function for flight track F-G initial (1630 UTC) and repeated (1730 UTC) overpasses of June 19, 1986.

Figure 12 - MAMS/VAS lifted index isotropic structure function for flight track F-G initial (1630 UTC) and repeated (1730 UTC) overpasses of June 19, 1986.

Figure 13 - MAMS/VAS skin temperature isotropic structure function for flight track F-G initial (1630 UTC) and repeated (1730 UTC) overpasses of June 19, 1986.

Figure 14 - MAMS/VAS and VAS-only precipitable water isotropic structure functions over the COMEX region on June 19, 1986. Note the MAMS/VAS data shows much greater structure at small separations.

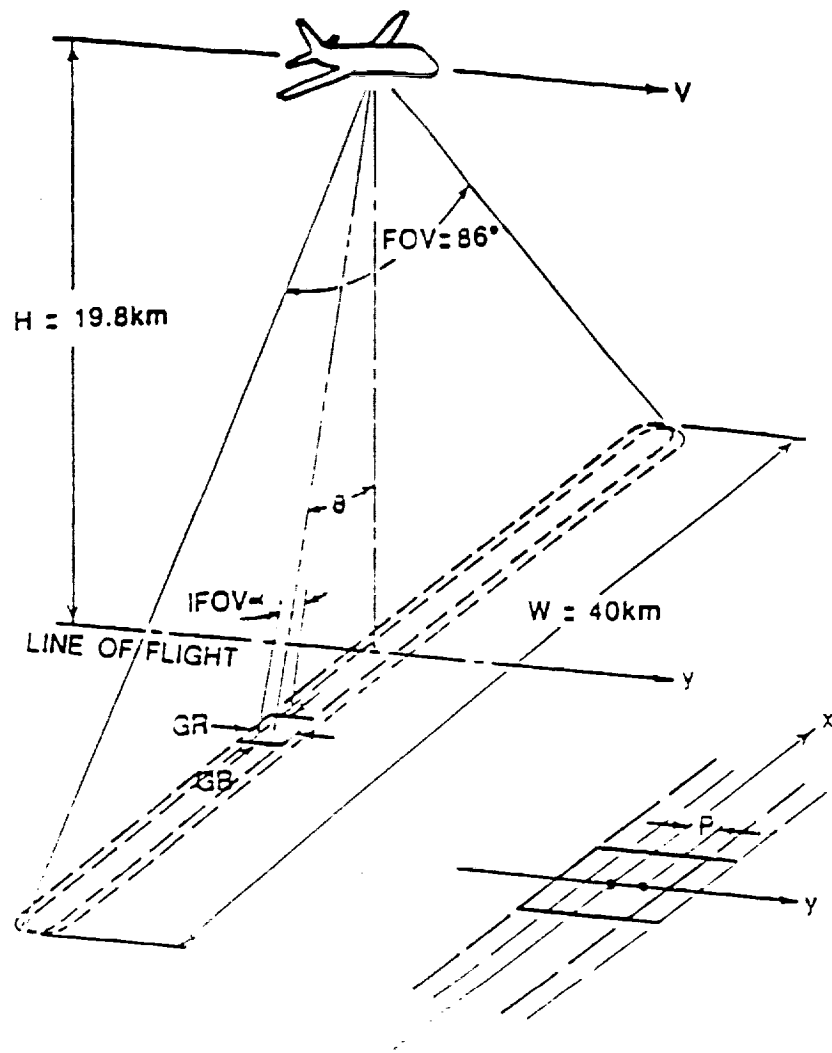


Fig. 1

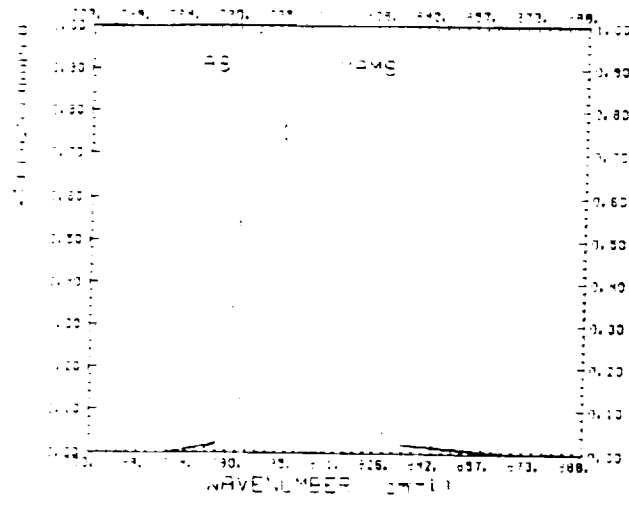
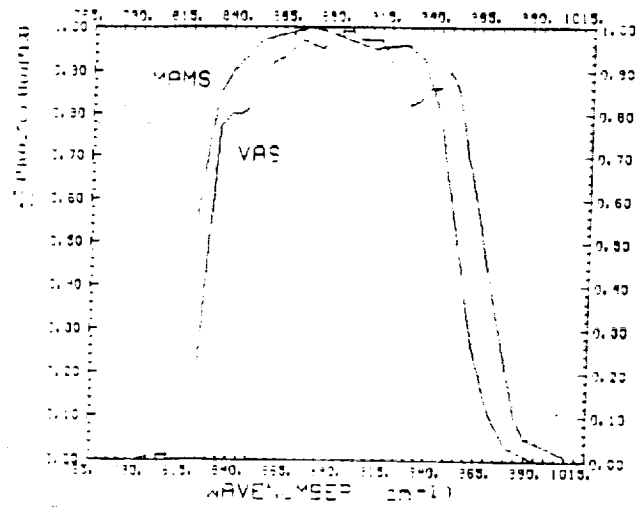
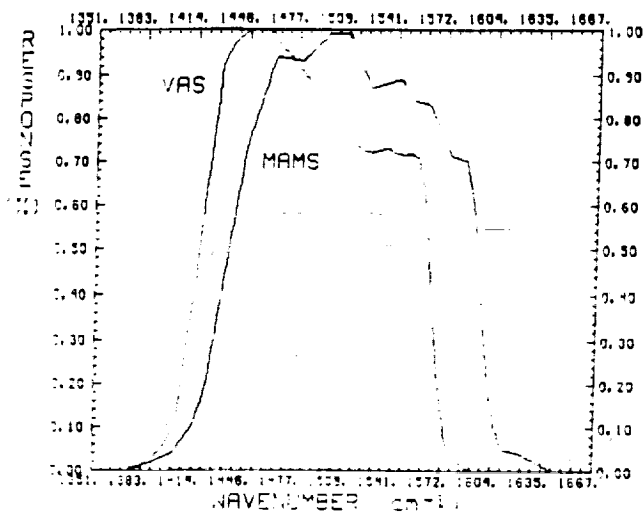


Fig. 2

ORIGINAL PAGE IS  
OF POOR QUALITY





Fig. 4

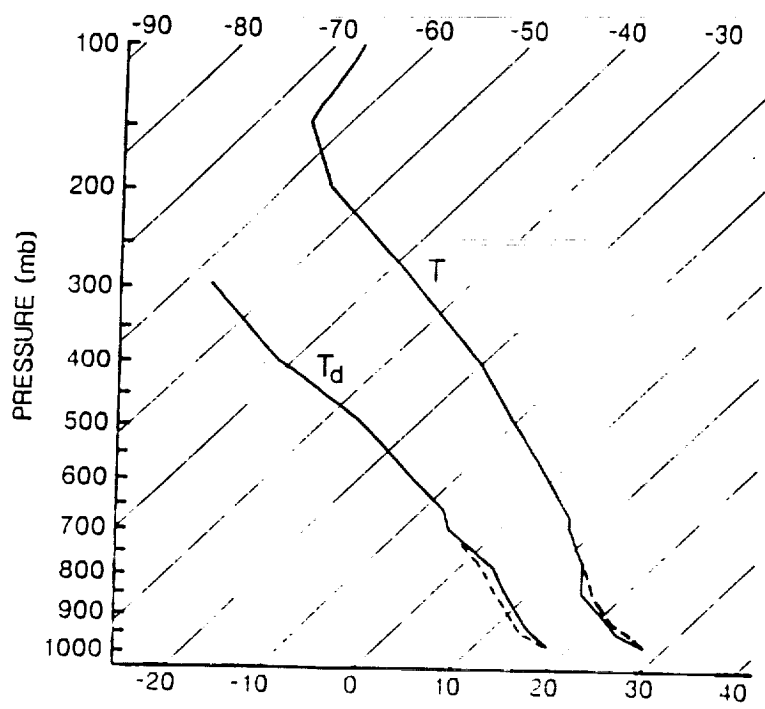
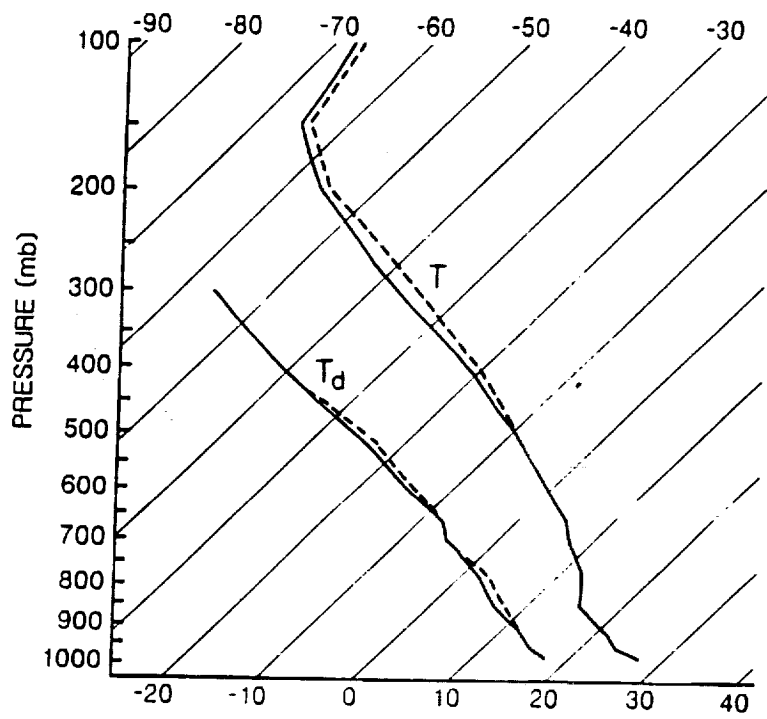


Fig. 5

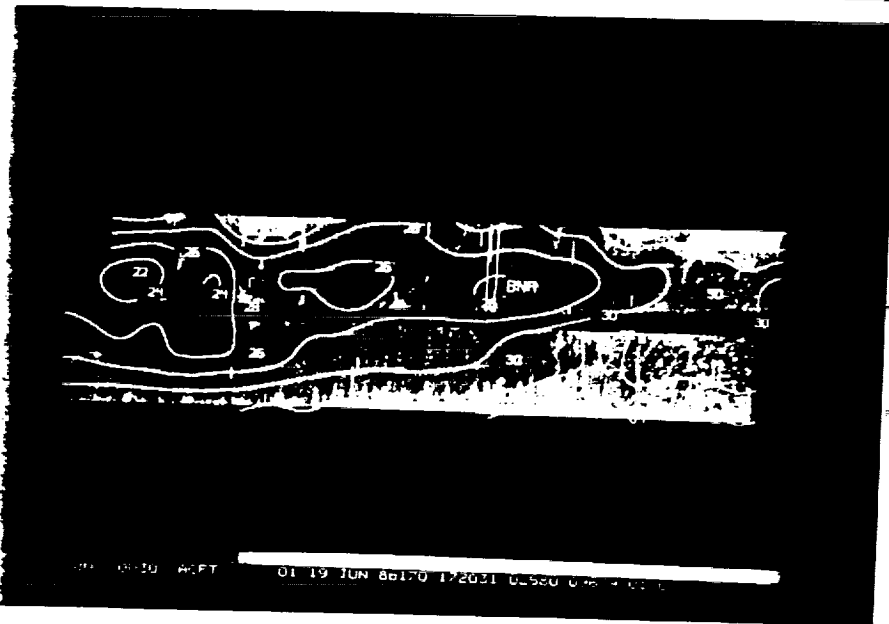
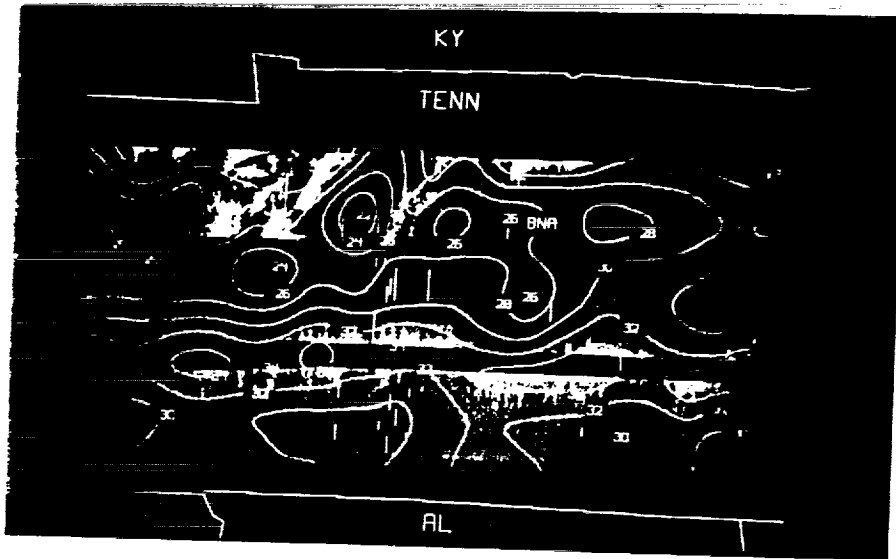
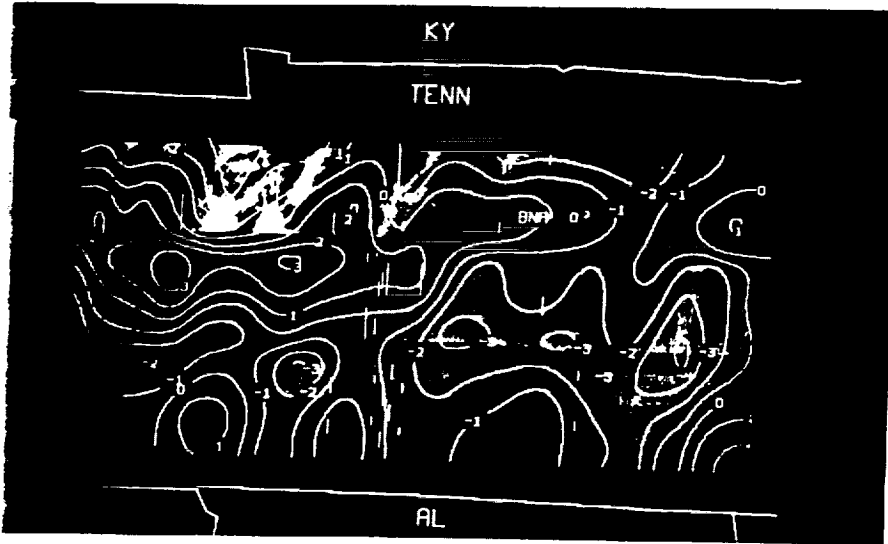


Fig. 1



01 0031 ACFT 01 19 JUN 86170 172031 02580 09679 01 00

Fig. 7

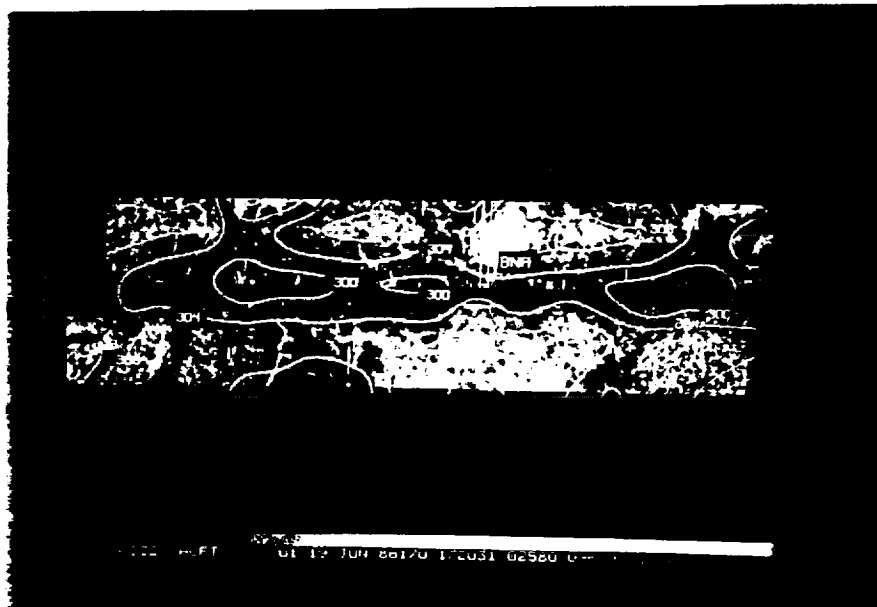
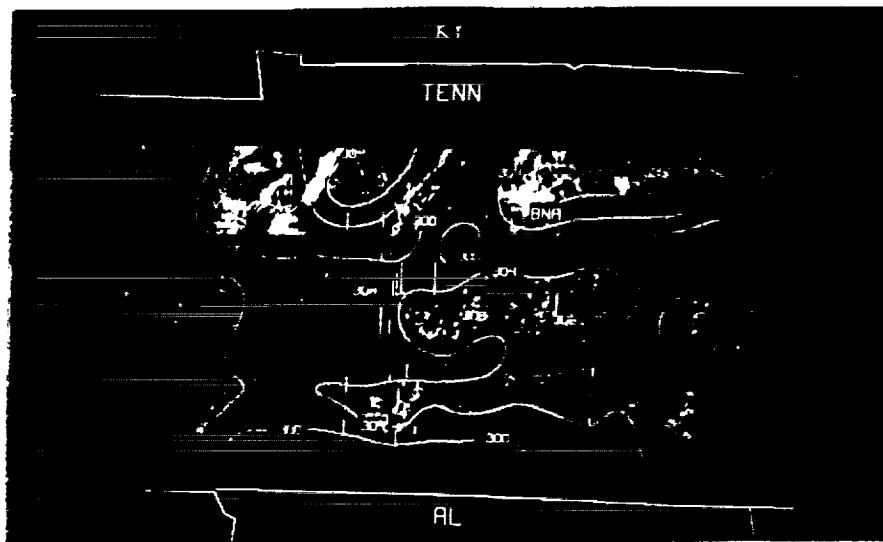


Fig. 3

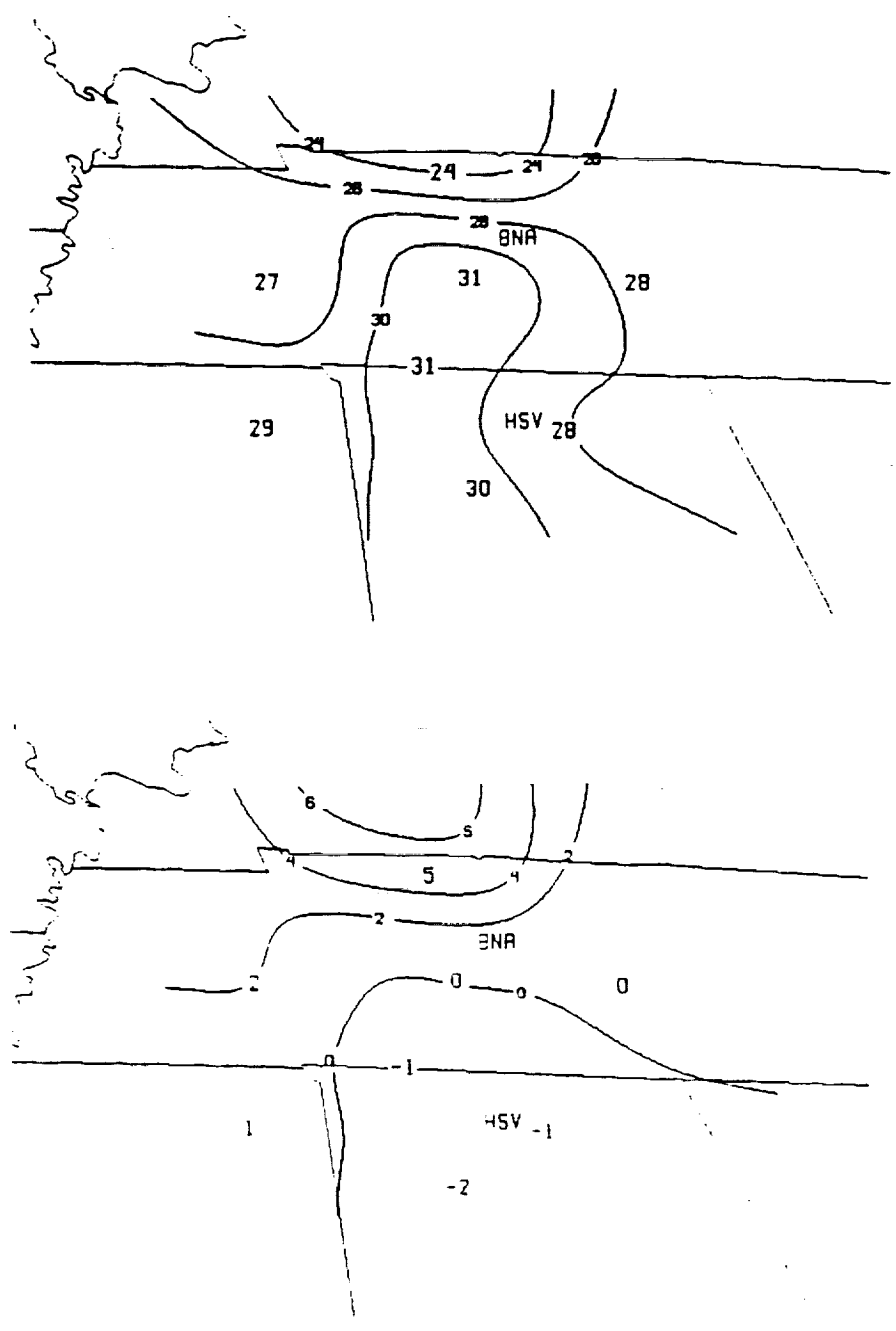


Fig. 9

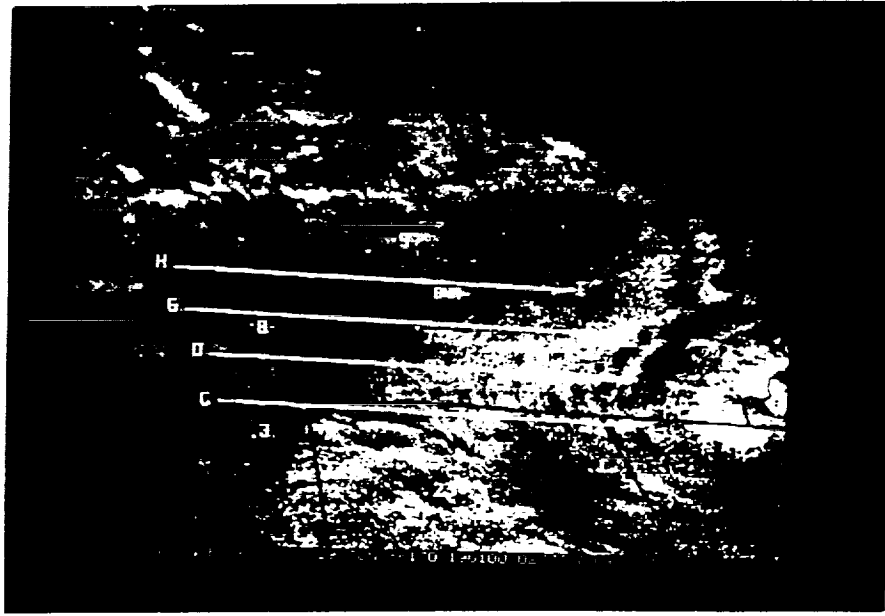


Fig. 10

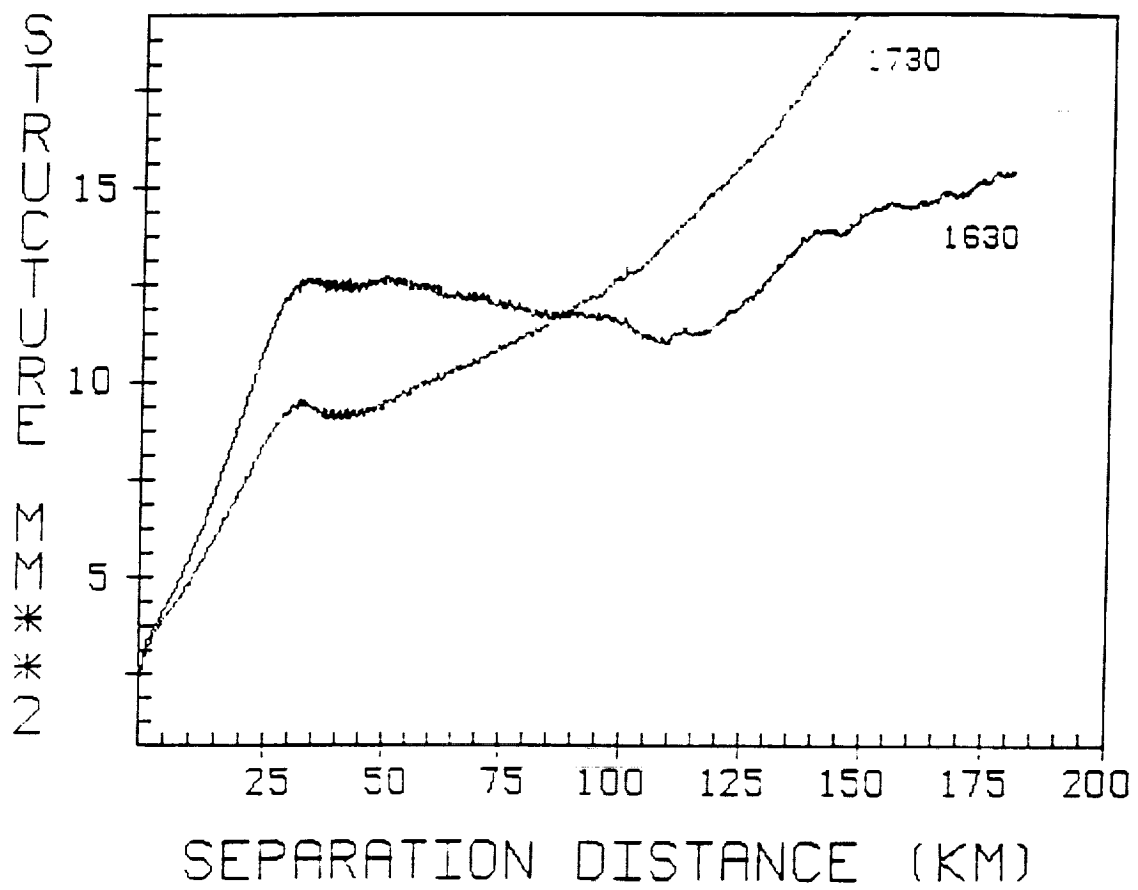


Fig. 11

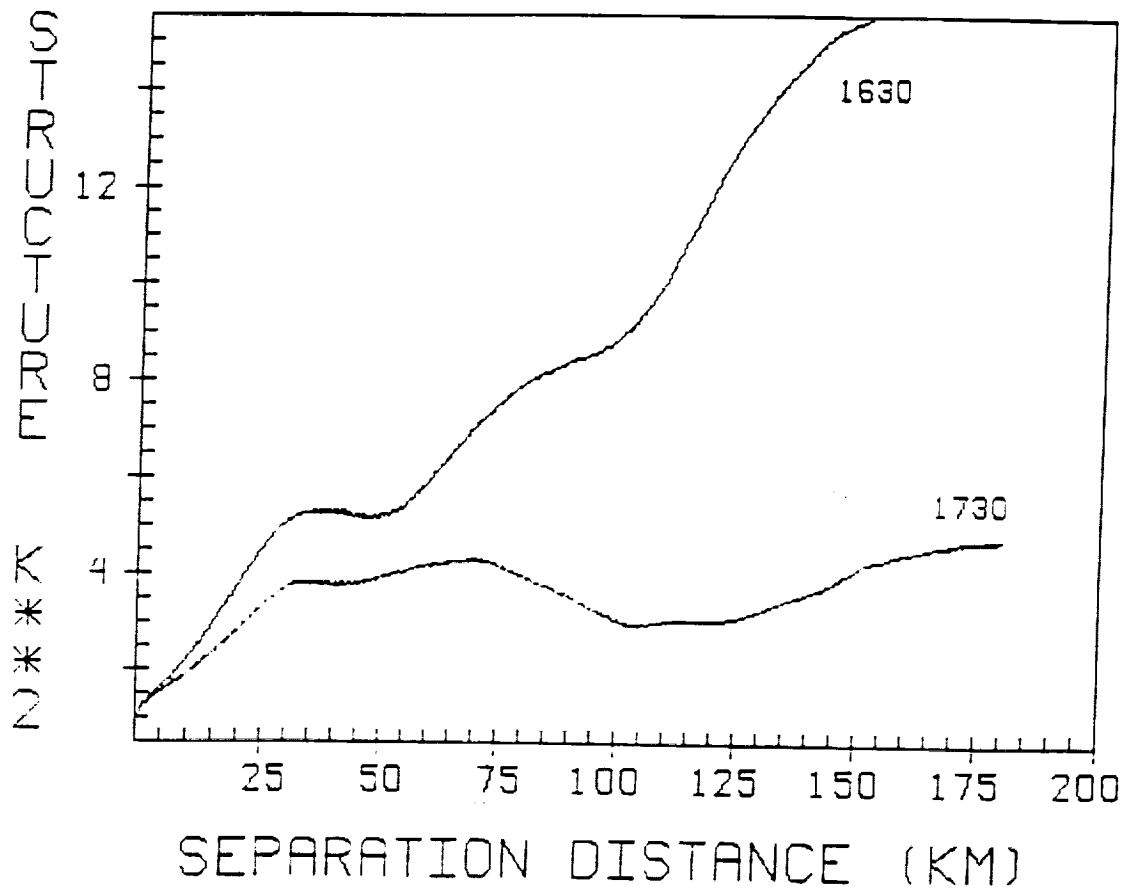


Fig. 12

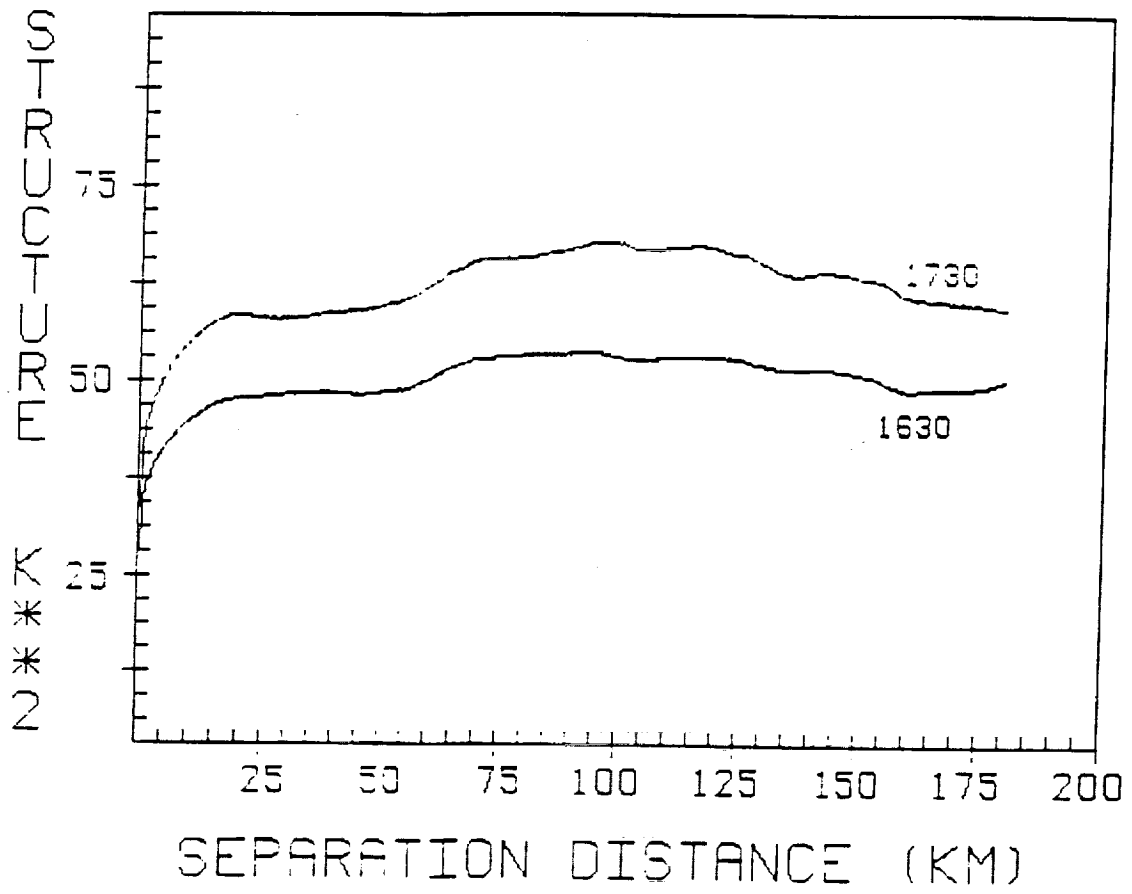


Fig. 13

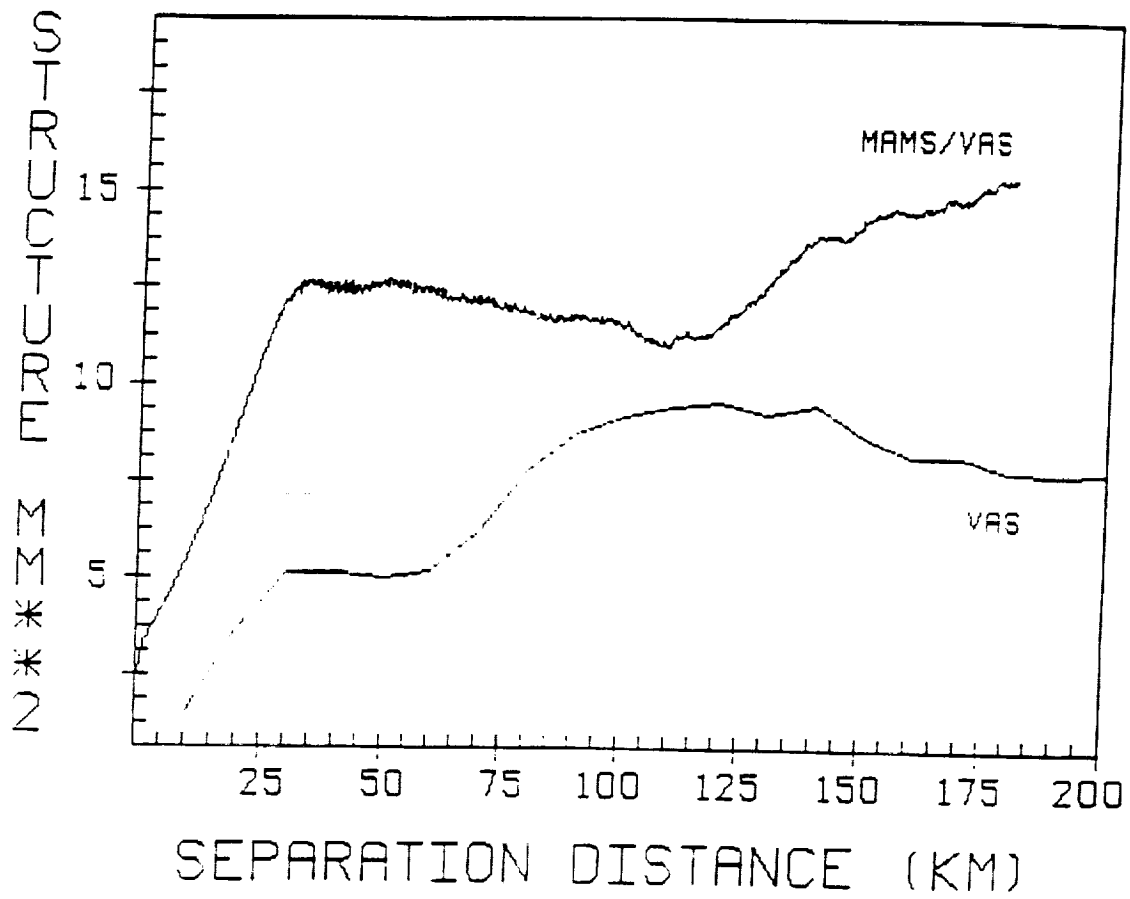


Fig. 14

53-46  
N92-98-34098  
P-13

HIGH RESOLUTION ATMOSPHERIC AND SURFACE VARIABILITY  
FROM COMBINED MAMS AND VAS RADIANCES

Christopher C. Moeller<sup>1</sup>  
W. Paul Menzel<sup>2</sup>  
Kathleen I. Strabala<sup>1</sup>

<sup>1</sup>Cooperative Institute for Meteorological Satellite Studies  
<sup>2</sup>NOAA/NESDIS Advanced Satellite Products Project  
1225 West Dayton Street  
Madison, Wisconsin 53706

NJ 925878

I. INTRODUCTION

Measuring of the variation of atmospheric and surface quantities such as moisture and stability at small scales is an important step to monitoring, understanding and forecasting mesoscale processes. While few ground based observing systems provide the high resolution coverage with sufficient areal extent necessary to study mesoscale variation, satellite observing systems have proven to be extremely useful in this endeavor. For instance, moisture and stability products from the geostationary platform VISSR Atmospheric Sounder (VAS) exhibit interesting detail at the meso B (20-200 km) level (Chesters et al., 1986; Smith et al., 1985). However, variation at the meso C scale (2-20 km) and at the lower end of the meso B scale (about 20-100 km) suffer from the effects of noise. Noise can be greatly reduced by using a high resolution data collection system. The Multispectral Atmospheric Mapping Sensor (MAMS), with its 100m resolution over a 36km swath, is well suited to provide high resolution mesoscale information about the atmosphere and surface of the earth. A more complete depiction of the atmospheric state at the smaller scales is possible through the combination of the high horizontal resolution MAMS data with the vertical sounding data of the VAS.

This paper demonstrates a procedure for combining MAMS and VAS data in a physical retrieval to produce high resolution derived products of precipitable water (PW), lifted index (LI), and skin temperature (TS). The variability of these products is evaluated in a structure function analysis similar to that of Hillger and Vonder Haar (1979). Results for 19 June 1986 from the Cooperative Huntsville Meteorological Experiment (COHMEX) are presented.

II. ALGORITHM

The MAMS/VAS combined retrieval is possible because the MAMS and VAS have spectrally similar 6, 11, and 12 micron spectral bands (Menzel et al., 1986). The MAMS high resolution data can be incorporated into the VAS retrieval process by replacing the appropriate VAS data with the MAMS data. The resulting retrieval benefits from the MAMS high resolution information as well as from the multispectral sounding information from VAS. More complete descriptions of the MAMS can be found in Jedlovec et al. (1989) and of the VAS in Montgomery and Uccellini (1985).

A physical retrieval process for producing derived imagery (Smith et al., 1985) is used, which entails a one step simultaneous solution (Smith and Woolf, 1984) to produce a retrieval for VAS data covering an area of 5 x 5 fields of view (FOV). The initial full VAS retrieval at coarse resolution is then used as the first guess for combined MAMS/VAS retrievals (where the 6, 11, and 12 micron MAMS data has replaced the equivalent VAS data) at 100m resolution. Biases with respect to the VAS radiances are removed from the MAMS radiances. Cloud checks with the infrared window are performed at each MAMS FOV; no MAMS/VAS retrieval is produced in a cloudy FOV.

III. EVALUATION OF TECHNIQUE

A. Processing of 19 June 1986 Data

On June 19, dry Canadian high pressure which had moved over the COHMEX region on the 18th began to slide off to the east, reducing the subsidence over the region as well as increasing the low level moisture, especially in the southern part of the COHMEX region. Although no significant convection occurred, sufficient moisture and surface heating were present to produce low level cumulus at the top of the boundary layer beginning about 1700 GMT. During the day this cumulus field expanded horizontally to cover much of east central Tennessee southward into northern Alabama. During the afternoon, a few of these cumulus clouds did grow sufficiently to produce brief light showers over the region.

The MAMS was flown over the COHMEX region from about 1530 GMT to 1800 GMT on this day. Figure 1 shows the COHMEX region with the straight line flight tracks that were flown. VAS dwell sounding pairs were collected at 1600 GMT and 1730 GMT.

## B. Analysis of Derived Products

The PW, LI, and TS derived products are shown in Fig. 3. Factors common to all 3 products include a varying degree of zenith angle effect, a weak left hand side bias (as the aircraft flew) and thin cirrus contamination in the NW sector.

The derived PW image shows generally higher values to the east and south and generally drier conditions to the north and west. A surge of moisture from the south can be seen penetrating into east central Tennessee. The gradient to the west and north shows a decrease of about 6 mm over a distance of about 100 km with a more concentrated gradient of about 3-4 mm over about 20 km to the northwest of the moisture maximum. This moisture surge also shows up in the more coarsely spaced COHMEX Beta Network radiosondes (not shown), though without as much certainty about its location. The radiosonde PW values show fairly good relative agreement, while absolute comparisons show a 2 to 4 mm high bias in the MAMS/VAS PW. The moist tongue is also identifiable in the repeated flight tracks one hour later, which reveal the time evolution of the feature. Interestingly, an onset of low level cumulus is seen in the repeat overpass in the moist tongue. In the next couple hours this field of cumulus expanded westward to the center of flight track F-G, in good visual correlation with the moist tongue feature.

The LI image shows that the most unstable portion of the flight exists over east-central Tennessee. This is in good agreement with the relative variation of the COHMEX 1800 GMT radiosondes, but a 3 to 4 unit bias towards unstable values is present in the MAMS/VAS LI. The general location of the low level cumulus field that developed agrees with the relatively unstable area in east central Tennessee. The repeated flight tracks indicate that much of the area is becoming less stable with time. This would be expected as solar heating warms the surface over the one hour interval. However, it appears the most rapid destabilization is taking place in the western portion. This suggests cloud development further west than actually occurred. However, the most unstable conditions (disregarding the thin cirrus region) prevail in the southeastern portion of the repeated flight tracks, in the location of the moist tongue. While sufficient low level instability (from surface heating) is apparently present as indicated by the expansive region of unstable LI values, cloud development is restricted to the moisture concentrated in east central Tennessee.

The skin temperature (TS) image shows considerable high resolution variability. The various land uses in the COHMEX region (e.g., forest, agriculture, urban) contribute strongly towards this variability. In particular, a definite heat island is observed at the location of Nashville, TN (BNA) with skin temperatures 5 to 10 K warmer than the surrounding region. Time change of TS indicates good continuity of the thermal features. Indications are that individual FOV skin temperatures increase by as little as 0 K to as much as 5 K over the one hour time interval. This is a result of the thermal properties of the various land types in the scene. Over a selected larger region (about 20 X 25 km) the average skin temperature increase was 2.75K. Such skin temperature monitoring is useful in radiation budget studies of the surface of the earth. Very warm TS values exist throughout the imagery and don't seem to be correlated to the low level cloud development. This once again points out the apparent importance of the moisture on this day to cloud development.

## C. Effect of MAMS Noise

The effect of sample noise on the derived products was evaluated by applying uniform single sample noise estimates to the retrieval coefficients. Since the retrieval coefficients were generated to represent a departure from a mean condition, the direct impact of noise can be observed by simply allowing the departure to be solely due to noise. For two retrievals in flight track F-G, the noise contribution to the PW, TS, and LI products was found to be about .75mm, .5K, and .5K respectively. This represents about 15%, 5%, and 5% of the deviation in each product respectively. Thus, real gradients of PW, TS, and LI are easily observed by the MAMS/VAS retrieval methodology.

## D. Variability of Derived Products

The spatial variability of the PW, LI, and TS fields was evaluated in a structure function calculation. This provides insight into the scales of natural variability that each derived product exhibits (Hillger and Vonder Haar, 1979). In a graph of structure versus separation distances, the slope of the plot is greater where mean horizontal gradients are greater.

The results of structure function calculations for PW, LI, and TS are shown in Fig. 2. Flight track F-G(1) was selected for the computation because it encompassed the moisture tongue identified in section III.B as well as good visual variability in the LI and TS products. Also, there were no clouds in this flight track. To reduce computation time of the structure calculation, the domain was subsampled at every 5th line and element to produce an effective resolution of 500 m; this left a domain of about 500 lines by 72 elements (250 km by 36 km). A separation interval of 1500m was used. Because the dimensions of the domain are greater in the along track direction, isotropic structures beyond 36 km will become increasingly biased in the along track direction.

The PW structure function displays a generally smooth increase from 1 km up to about 30 km separation. In this interval, PW increases from about 1.5 mm up to about 3.4 mm (including noise contributions). Small amplitude fluctuations of the structure in this interval are less than the noise level and cannot be regarded as significant. From 30 km to about 120 km separations the structure function flattens out, indicating that the gradient of PW is not increasing in this range. Beyond 120 km the PW structure again begins to increase, as PW varies significantly at larger scales (e.g., across frontal boundaries, etc.). This also indicates that the flat structure function between 30 and 120 km is not a systematic bias of the calculation, but rather represents a true lack of atmospheric variation at that scale. The indication here is that significant atmospheric variation is taking place at small scales. While this makes no statement about the meteorological importance of this variability, it does demonstrate its existence.

The LI structure shows a step-like pattern with strong increases in structure from 1-25 km, 60-75 km, and 100-120 km. This behavior is significantly different from that of the PW structure. Instead of leveling off as the PW structure does, the LI structure continues to increase as separations increase. Because the LI product is primarily dependent on the coarser resolution VAS data, the LI structure may be somewhat limited in its ability to depict the true high resolution atmospheric variability of LI. However, it is still indicated that small scale variability is certainly present and measurable.

The TS structure function exhibits behavior both similar to and different from the PW and LI structure functions. Like the PW and LI structure, the TS structure increases rapidly at small scales with most of the increase contained in the 1-15 km separation range. This rapid increase in TS structure at small separations is not surprising given the different land uses in the region. The structure flattens out over the remainder of the separation range. This is different from both PW and LI structure, and indicates a strong preference for high small scale variability of skin temperature in the COHMEX region. It is noteworthy that the TS variation of 5.6K at 1500m separation is significantly greater than the noise contribution. The implication here is that small scale variation is dominant and measurable.

#### IV. CONCLUSIONS

This paper has presented the results of merging the 8 km resolution sounding data from the VAS with the 100m resolution moisture data from the MAMS in the physical retrieval of precipitable water, atmospheric stability (lifted index), and skin temperature. The VAS provides the vertical information of the atmospheric state and the MAMS indicates the horizontal variability. Structure function analysis of the resulting derived product fields indicates that both atmospheric PW and LI products have significant variability at less than 30 km spacing. Inspection of the surface skin temperature reveals structure at less than 15 km due to differences in local land use. The implications for mesoscale monitoring of the atmospheric state are that definition of small scale variations require horizontal resolutions of better than 5 km.

#### REFERENCES

- Chesters D., A. Mostek, and D. A. Keyser, 1986: VAS sounding images of atmospheric stability parameters. Wea. and Forecasting, 1, 5-22.
- Hillger, D. W., and T. H. Vonder Haar, 1979: An analysis of satellite infrared soundings at the mesoscale using statistical structure and correlation functions. J. Atmos. Sci., 36, 287-305.
- Jedlovec, G. J., K. B. Batson, R. J. Atkinson, C. C. Moeller, W. P. Menzel, and M. W. James, 1989: Improved capabilities of the Multispectral Atmospheric Mapping Sensor (MAMS). NASA Technical Memorandum 100352, Marshall Space Flight Center, Huntsville, AL, 71pp.
- Menzel, W. P., G. J. Jedlovec, and G. S. Wilson, 1986: Verification of small scale features in VAS imagery using high resolution MAMS imagery. Second Conference on Satellite Meteorology/Remote Sensing and Applications, AMS, Boston, 108-111.
- Montgomery, H. E., and L. W. Uccellini (Eds.), 1985: VAS demonstration: (VISSR Atmospheric Sounder) description and final report. NASA RP-1151, 198pp. (NTIS 86N13867).
- Smith, W. L., and H. M. Woolf, 1984: Improved vertical soundings from an amalgamation of polar and geostationary radiance observations. Conference on Satellite Meteorology/Remote Sensing and Applications, June 25-29, 1984, Clearwater Beach, FL. American Meteorological Society, Boston, MA, 45-48.
- Smith, W. L., G. S. Wade, and H. M. Woolf, 1985: Combined atmospheric sounding/cloud imagery - a new forecasting tool. Bull. Amer. Meteor. Soc., 66, 138-141.

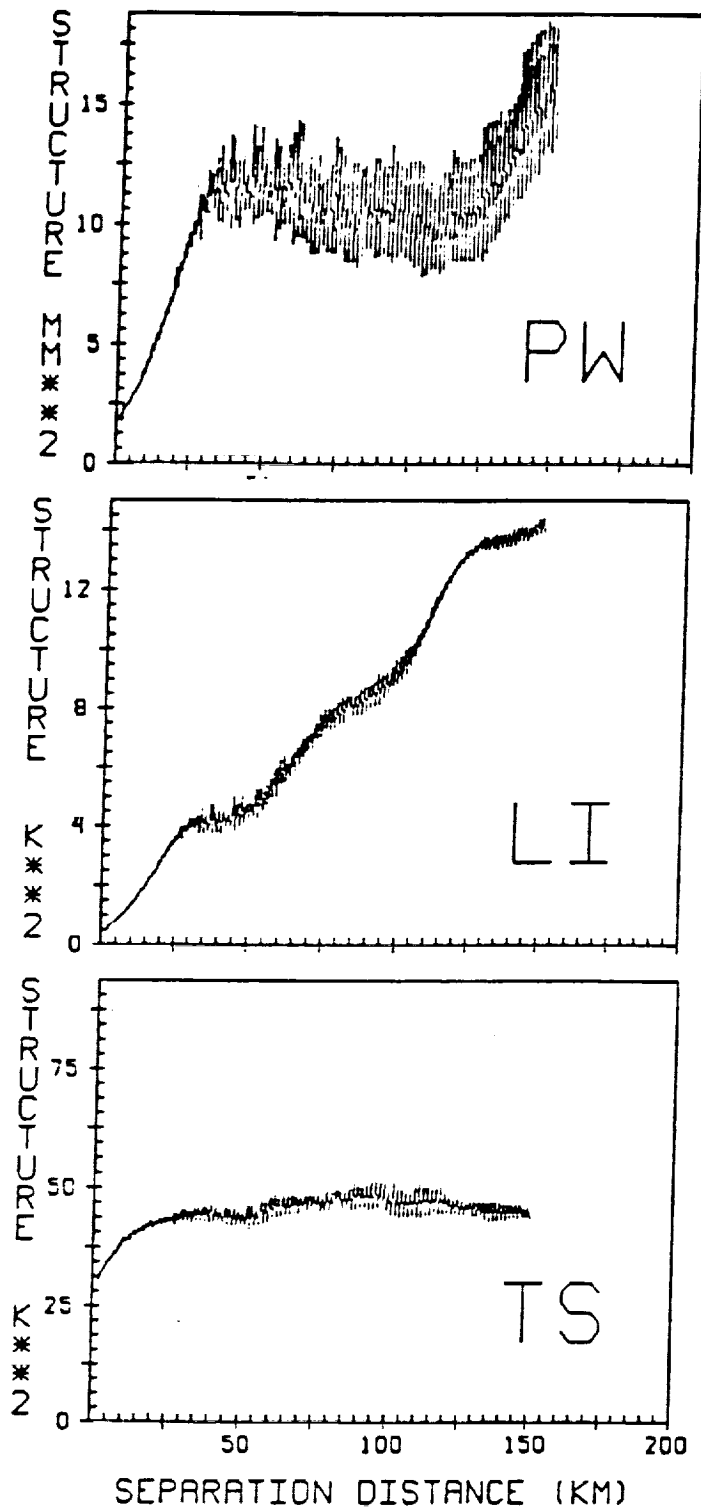


Figure 2 - Isotropic structure functions of PW, LI and TS for June 19, 1986 flight track F-G(1).

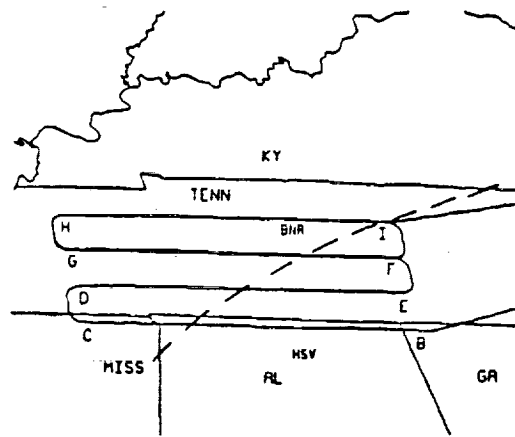


Figure 1 - MAMS flight path on June 19, 1986 over the COHMEX region. Letters identify beginning and end of straight line flight tracks. The two northernmost flight tracks (F-G,H-I) were repeated. Dashed line indicates NW boundary of cumulus cloud development at about 19 GMT.

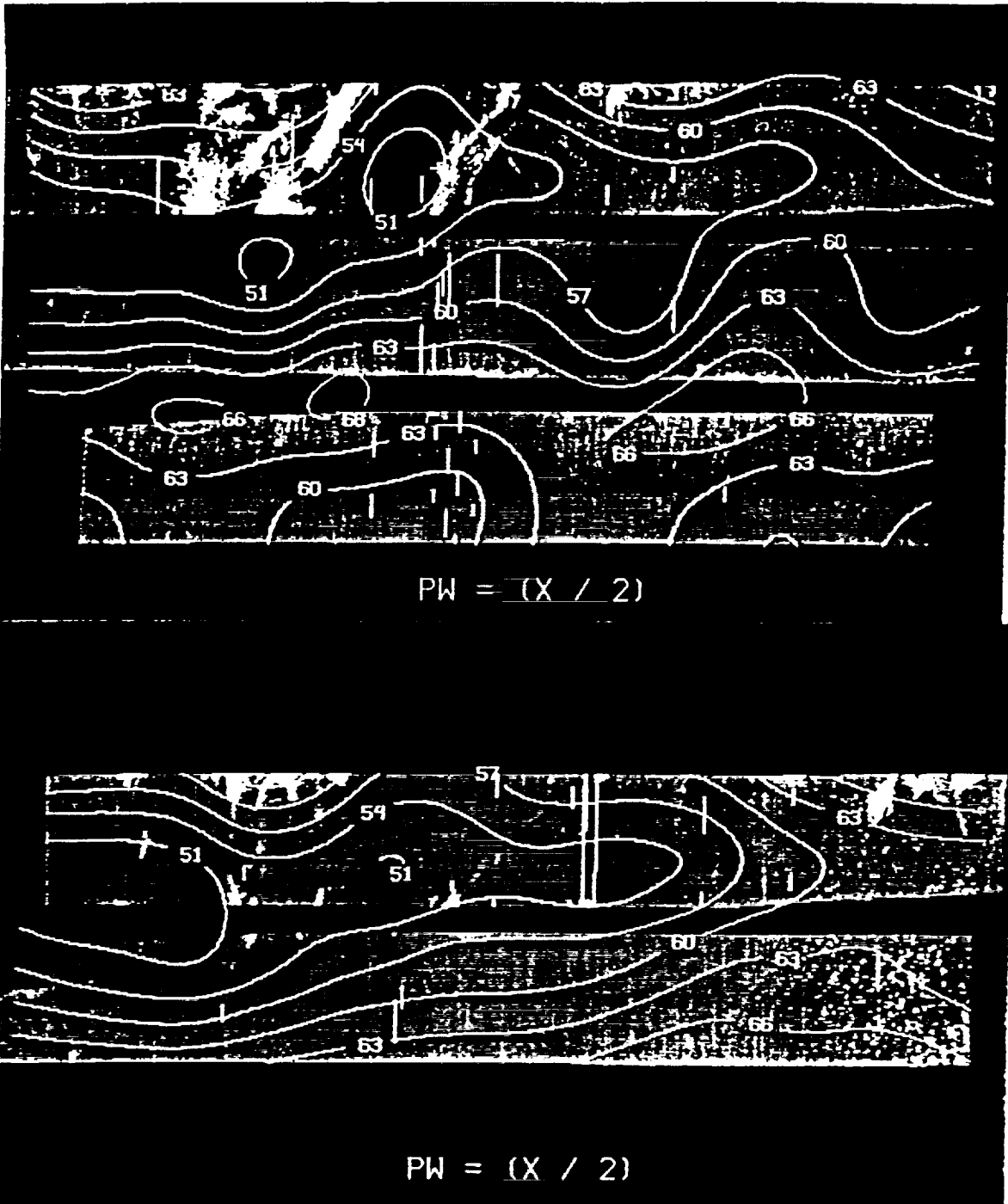


Figure 3 - Fields of precipitable water (PW), lifted index (LI) and skin temperature (TS) for the entire flight of June 19, 1986. The data has been remapped into a Mercator projection with a degradation of resolution down to .6 km so that adjacent flight tracks could be shown in a single image format. Each product consists of a composite of 3 flight tracks (D-E, F-G, H-I) and a composite of the 2 repeated flight tracks (F-G, H-I). Thus the northernmost two flight tracks of the 3 flight track composite are collocated with the composite of the repeated flight tracks. White pixels are cloud cover. Thin white vertical dashes in the imagery are a result of the remapping process.

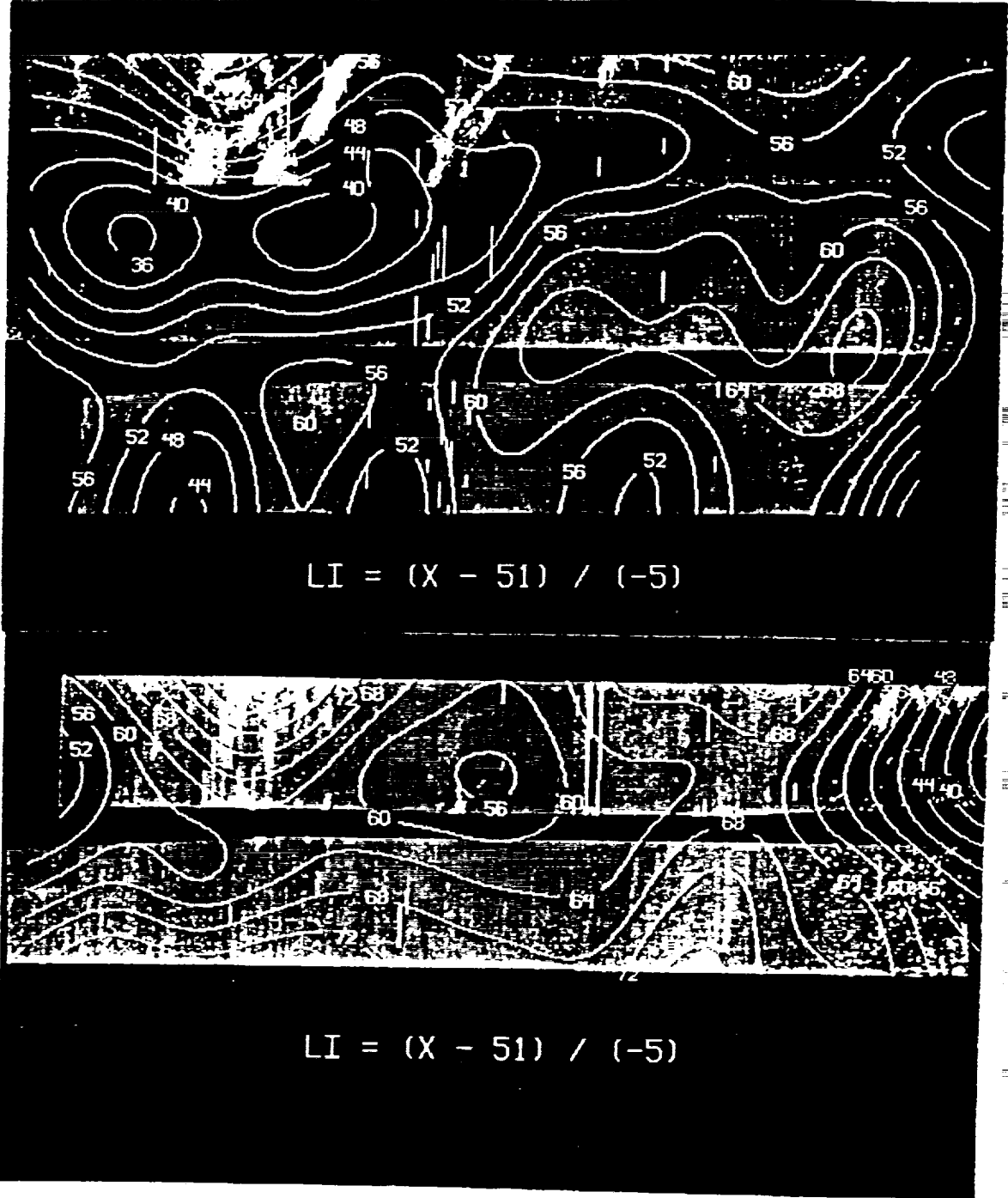


Figure 3

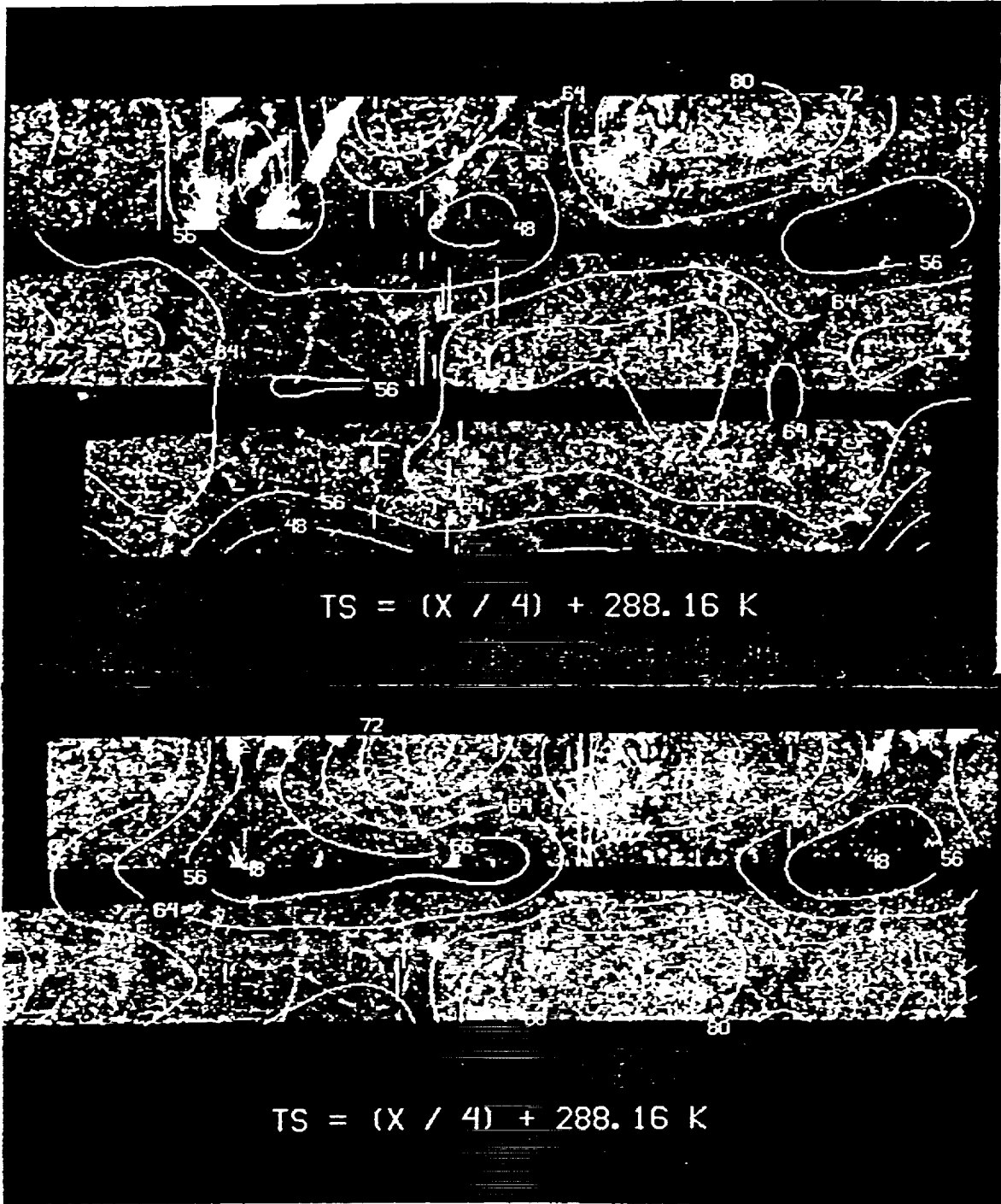


Figure 3 <sup>A</sup>

VERIFICATION OF SMALL-SCALE WATER VAPOR FEATURES IN VAS IMAGERY USING HIGH RESOLUTION MAMS IMAGERY

W. Paul Menzel

NOAA/NESDIS Advanced Satellite Products Project  
Madison, Wisconsin

Gary Jedlovec

Cooperative Institute for Meteorological Satellite Studies  
Madison, Wisconsin

Gregory Wilson

Marshall Space Flight Center  
Huntsville, Alabama

1. INTRODUCTION

The Multispectral Atmospheric Mapping Sensor (MAMS) is a new instrument designed to produce high resolution imagery in eight visible and three infrared spectral bands from an aircraft platform. Thermal emission from the earth's surface, clouds, and atmospheric water vapor is measured at 12.3, 11.2, and 6.5 microns at up to 50 meter horizontal resolution. Similar infrared spectral bands are part of the VISSR Atmospheric Sounder (VAS) which is capable of 6.9 km horizontal resolution from its geostationary orbit. Sequences of 6.7 micron VAS images have been used to track water vapor structures and to infer atmospheric motion vectors (Stewart et al., 1985). They have also been used to investigate small scale atmospheric moisture variability (Jedlovec, 1984). The high resolution MAMS data give credence to the small scale variations in the VAS water vapor imagery.

The purpose of this paper is two-fold. We shall (1) describe the MAMS instrument and the radiance characteristics, and (2) intercompare some VAS and MAMS radiances and images.

2. MAMS INSTRUMENT CHARACTERISTICS

The MAMS is a modification of NASA's Airborne Thematic Mapper (Daedalus, 1982). The MAMS has two major components, the scan head and the spectrometer (Fig. 1). The scan head consists of the primary collecting telescope, a rotating scan mirror, a motor encoder assembly, and two controlled thermal sources. The field of view is defined by the aperture which is available in two different sizes, 2.5 mrad and 5.0 mrad. The spectrometer consists of optical elements which spectrally separate the polychromatic input energy, lenses which focus the separated energy onto sensors, detectors which convert optical energy to an electrical signal, and pre-amplifiers which condition the signal. The energy collected by the spectrometer is separated into four distinct optical paths using dichroic filters: three paths for the infrared data (one for each spectral band) and one for the visible

and near infrared data. The spectrometer detectors are silicon for the visible radiation and mercury cadmium telluride for the thermal infrared radiation. The visible detector is an eight element array which converts optical energy to electrical energy. The spectral response of each band is determined by the dispersion characteristics of the prism placed in the optical path and the location of the array in the dispersed beam. The thermal infrared detectors are each housed in a vacuum dewar which contains a cooled long wave filter which defines the particular spectral band. Each infrared detector has an associated pre-amplifier to process the electrical signal. The spectral bands are summarized in Table 1. The spectral response functions for the three infrared channels of the MAMS (Fig. 2) were specified to be similar to the 6.7, 11.2, and 12.7 micron channels on VAS (also shown in Fig. 2).

The MAMS produces high resolution imagery in these visible and infrared spectral bands from a high altitude aircraft at 20 km as shown in Fig. 3. The horizontal ground resolution, GR, of each individual field of view is 100

Table 1

Range of MAMS Spectral Bands

8 visible (microns)	3 infrared (microns)
.42- .45	6.20- 6.85 (upper level water vapor)
.45- .52	10.32-12.02 (window)
.52- .60	12.20-12.56 (lower level water vapor)
.60- .62	
.63- .69	
.69- .75	
.76- .90	
.90-1.05	

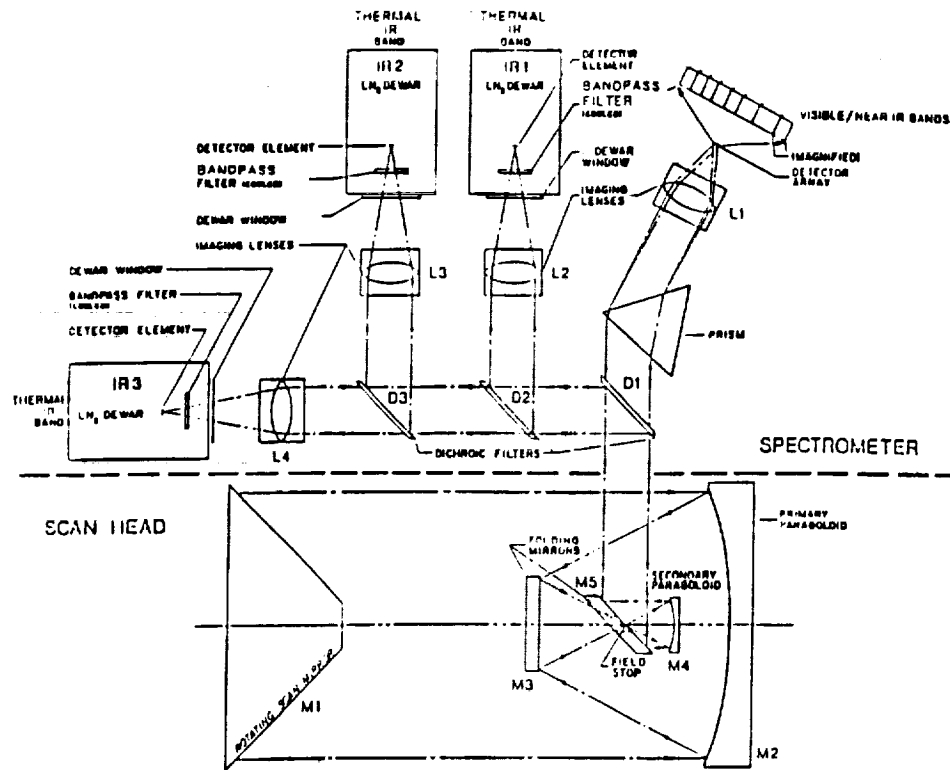


Fig. 1. Schematic of MAMS spectrometer and scan head.

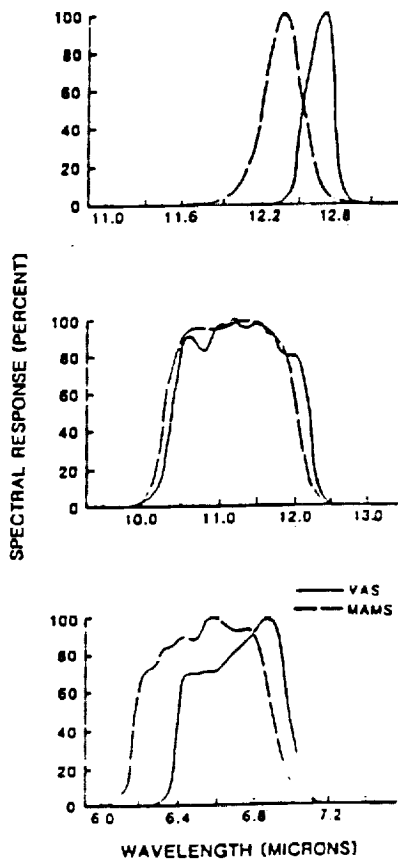


Fig. 2. Spectral response curves indicating the sensitivity of the MAMS and VAS instruments in the 12 micron, 11 micron, and 6 micron regions.

eters (50 meters if the smaller 2.5 mrad optics are used). The total field of view for one scan is  $86^\circ$  which covers the width,  $w$ , of the entire cross path of roughly 40 km. The scan rate is 6.25 revolutions per second (12.50 when the 2.5 mrad optics are used) and produces 67% overlap, I-P, of each scan line with the previous one for nominal aircraft speed (740 km/hr). On each scan line 716 samples are taken so that there is 52% overlap of neighboring pixels along a scan line (4% when the 2.5 mrad optics are used). These overlaps can be used to good advantage to reduce the noise in the scene by spatial averaging.

Radiometric calibration of the infrared data is accomplished by viewing two blackbody sources and by assuming the detector response is linear with respect to radiance (a fractional nonlinearity of less than  $5 \times 10^{-4}$  is observed). Calibration occurs every scan line by viewing a warm and then a cold blackbody of known temperature. For a given spectral band, the radiance is determined from the temperature through the convolution of the normalized spectral response and the Planck function. The calibrated radiances are transformed back into temperatures using the inverse Planck relation with the nominal spectral band center wavelength.

Prior to flight, the gain and offset for each spectral band are adjusted electronically in order to minimize the likelihood of saturation over hot scenes and to maximize the effective operating range. The 6.5 micron band is adjusted to cover 210 to 280°K, while the 11.2 and 12.3 micron bands operate from 220 to 340°K. An eight bit digitizer is used so that for the 6.5 micron band the gain is approximately .3°K per count, and for the remaining surface viewing bands it is approximately .5°K per count.

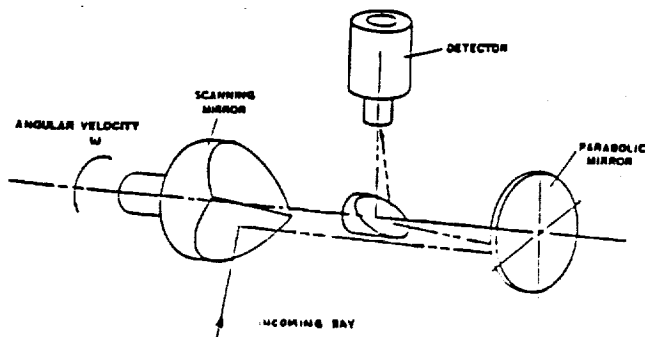


Fig. 3a. A simplified schematic of the inflight configuration of the optical elements of the MAMS.

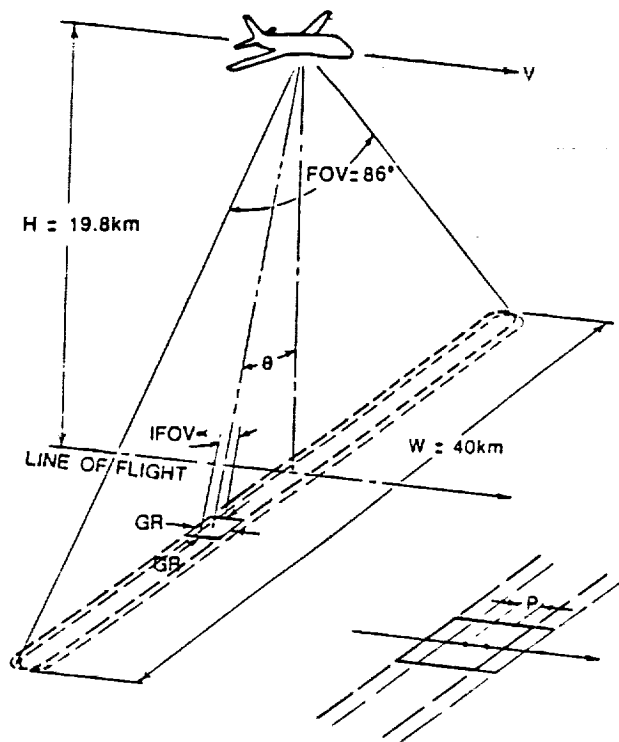


Fig. 3b. Scanning geometry for the MAMS instrument onboard a NASA U2/ER2 aircraft. Lower insert shows position of the center of the nadir Ifov for two adjacent scans.

Truncation errors are assumed to be roughly half these values.

The infrared detectors on MAMS exhibit some low frequency noise so that samples taken at 52 microsecond intervals for the spin rate of 6.25 revolutions per second (26 microsecond sampling occurs at 12.5 rps) experience noise contributions with significant correlation. An analysis of covariance (Menzel, 1950) of the noise with the 5 mrad aperture reveals that after averaging ten consecutive samples noise is reduced by a factor of .54, .52, and .37, respectively, in the three infrared spectral bands in order of increasing wavelength (uncorrelated noise would have a factor of  $1/\sqrt{10}$  or .32).

Inflight single sample noise values were determined from multiple samples over a uniform portion of the ocean. For a sample size of 100, the single sample noise values with the 5 mrad

aperture were found to be .2, .1, and .4°K, respectively, for the spectral bands in order of increasing wavelength (for the 2.5 mrad aperture the values were .5, .2, and .9°K).

### 3. DATA INTERCOMPARISONS

Radiances for the MAMS and VAS spectral responses were simulated for each band and sensor in a radiative transfer calculation. A representative atmospheric transmittance was computed using a band model and radiosonde temperature and moisture profiles. Table 2 shows that the MAMS detects radiances within one to two  $\text{mW/ster/m}^2/\text{cm}^{-1}$  of the VAS detected radiances. The MAMS spectral responses are shifted to shorter wavelengths (as shown in Fig. 2), hence less radiance is detected. This translates into brightness temperature differences of less than a degree Kelvin.

Table 2

Intercomparison of Simulated Data

	6 micron	11 micron	12 micron
R(MAMS)	7.86	96.5	109.5
T(MAMS)	254.8	287.3	286.0
R(VAS)	8.73	97.5	111.6
T(VAS)	253.9	287.3	285.4
$\Delta T_{\text{MAMS-VAS}}$	0.9°K	0.0	0.6

radiances in  $\text{mW/ster/m}^2/\text{cm}^{-1}$ , temperatures in °K

Radiances from the MAMS and VAS were collected simultaneously over a relatively isothermal area of ocean off the California coast on 18 May 1985. Table 3 presents the comparison. After compensating for the inherent spectral differences of the two instruments, the MAMS data is within .5, 2.5, and 1.5°K of the VAS data, respectively, for the spectral bands in order of increasing wavelength. The observed split window channel differences (11 micron less 12 micron) are comparable, 2.5°K for MAMS and 2.1°K for VAS and thus showing similar low level moisture concentrations. The observed water vapor channel data (6 micron) show MAMS detecting upper level moisture concentrations very much like VAS, with MAMS showing somewhat less attenuation than VAS. These comparisons

Table 3

Intercomparison of Observed Data

	6 micron	11 micron	12 micron
R(MAMS)	6.01	99.9	111.1
T(MAMS)	247.1	289.5	287.0
R(VAS)	6.80	97.0	111.1
T(VAS)	246.5	287.1	285.0
$\Delta T_{\text{MAMS-VAS}}$	.6°K	2.4	2.0

radiances in  $\text{mW/ster/m}^2/\text{cm}^{-1}$ , temperatures in °K

are quite reasonable, since the spatial resolution of each sensor is very different (VAS at 7 km and MAMS at .05 km at nadir), the navigation of the MAMS data is from visual siting of landmarks only, and non-nadir viewing of the MAMS has not yet been taken into account.

Imagery from the MAMS and VAS were compared from flights over Oklahoma and Kansas on 12 May 1985. The goal of the intercomparison is to verify small scale features observed in the VAS water vapor images with the higher resolution MAMS data. These water vapor inhomogeneities in the VAS data have been used to obtain motion vectors when several images are considered in sequence. While the imagery is often too amorphous to track winds reliably with a correlation technique, it has produced good wind fields by single pixel tracking (Stewart et al., 1985). The MAMS data tends to verify that small scale gradients (down to several single pixels) in the VAS data are real. Fig. 4a shows the VAS 6.7 micron images with the MAMS flight track superimposed while Fig. 4b shows the 6.3 micron MAMS data (at 400m resolution for display) gathered in flight from C to H. These images were enhanced to delineate the moisture features. Brighter (colder) regions represent clouds or relatively high water vapor content and darker (warmer) areas represent drier air in the middle layer of the atmosphere. The MAMS images are not limb corrected and, therefore, images appear brighter (colder) toward the edges. The moisture features compare very nicely; starting at G, MAMS shows a dry tongue giving way to a moist ridge which becomes less moist at H. Fig. 5a shows single pixel resolution of the VAS image covering the MAMS track from E to F of Fig. 4a; Fig. 5b displays the MAMS data covering the boxed region of Fig. 5a. The temperatures from brightest to darkest pixels within the boxed-in area differ by 5°K indicating that these fluctuations are not instrument noise, but real atmospheric features. Six of the VAS features are corroborated nicely by the MAMS image. This lends credence to the assertion that the VAS distinguishes moisture features which are small enough to represent a wind vector, yet large enough to exist in several successive images. The features we are examining were discernible for at least two hours in the VAS images.

#### 4. CONCLUSION

The MAMS measures thermal emission from the earth atmosphere system in eight visible and three infrared spectral bands (12.3, 11.2, and 6.5 microns) at up to 50m horizontal resolution. These infrared bands are very similar to three of the VAS infrared spectral bands. The instrument was flown aboard a NASA U-2 in May-June 1985 and corresponding VAS data was collected. MAMS radiometric performance is comparable to that of VAS. The MAMS exhibits somewhat less attenuation from water vapor than VAS because its spectral bands are shifted to shorter wavelengths away from the absorption band center. Intercomparisons of these images give credence to small scale variations in the VAS water vapor imagery. Attempts are underway to identify the scales of which these features must be tracked to depict the preconvective environment.

The MAMS has been developed to combine high resolution visible and infrared measurements to study small scale atmospheric moisture variability, to monitor and classify clouds, and to investigate the role of surface characteristics in the production of clouds, precipitation, and severe storms. As part of the Cooperative Huntsville Meteorological Experiment (COHMEX), the MAMS will be flying this summer to gather data for these studies.

#### 5. ACKNOWLEDGEMENTS

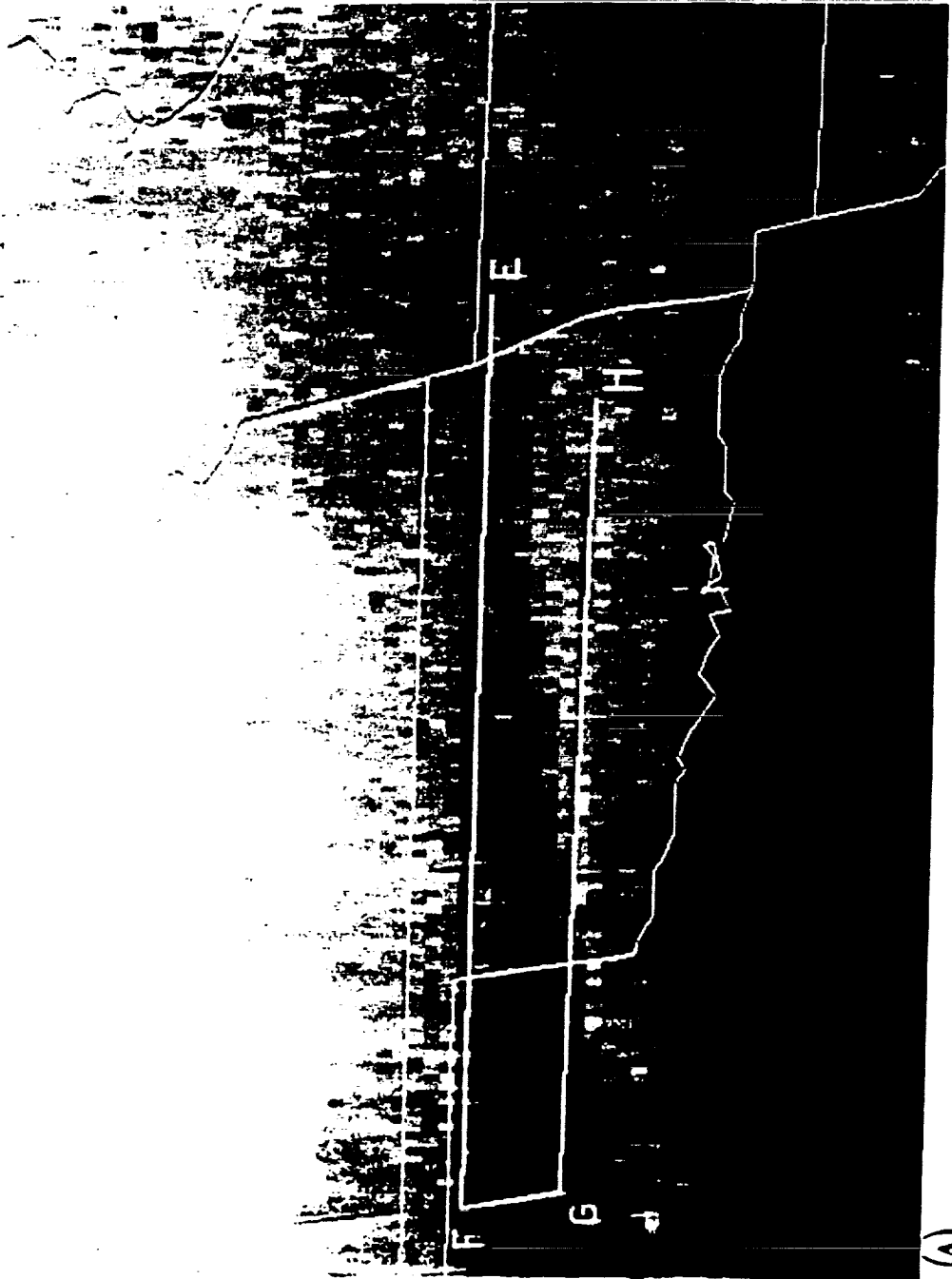
This work was performed on the University of Wisconsin Man-computer Interactive Data Access System (McIDAS) under NASA support. Mr. John Arvesen and Mr. Jeff Myers at NASA/Ames contributed to the MAMS data collection and processing. Mr. Bob Atkinson at NASA/MSFC assisted in the calibration of the flight data.

#### 6. REFERENCES

- Daedalus, 1982: Operator's Manual: AADS1268 digital multi-spectral scanner system. Daedalus Enterprises, Ann Arbor, MI.
- Jedlovec, G. J., 1984: Mesoscale analysis of 6.7 micron image data from the VISSR Atmospheric Sounder (VAS) for several case studies. Conf. on Satellite/Remote Sensing and Appl. AMS, Boston, 185-190.
- Menzel, W. P., 1980: Prelaunch study report of VAS-D performance. Report on NASA contract NAS5-21965, Space Science and Engineering Center, University of Wisconsin, Madison, WI.
- Stewart, T. R., C. M. Hayden, and W. L. Smith, 1985: A note on water-vapor wind tracking using VAS data on McIDAS. BAMS, 66, 9, 1111-1115.

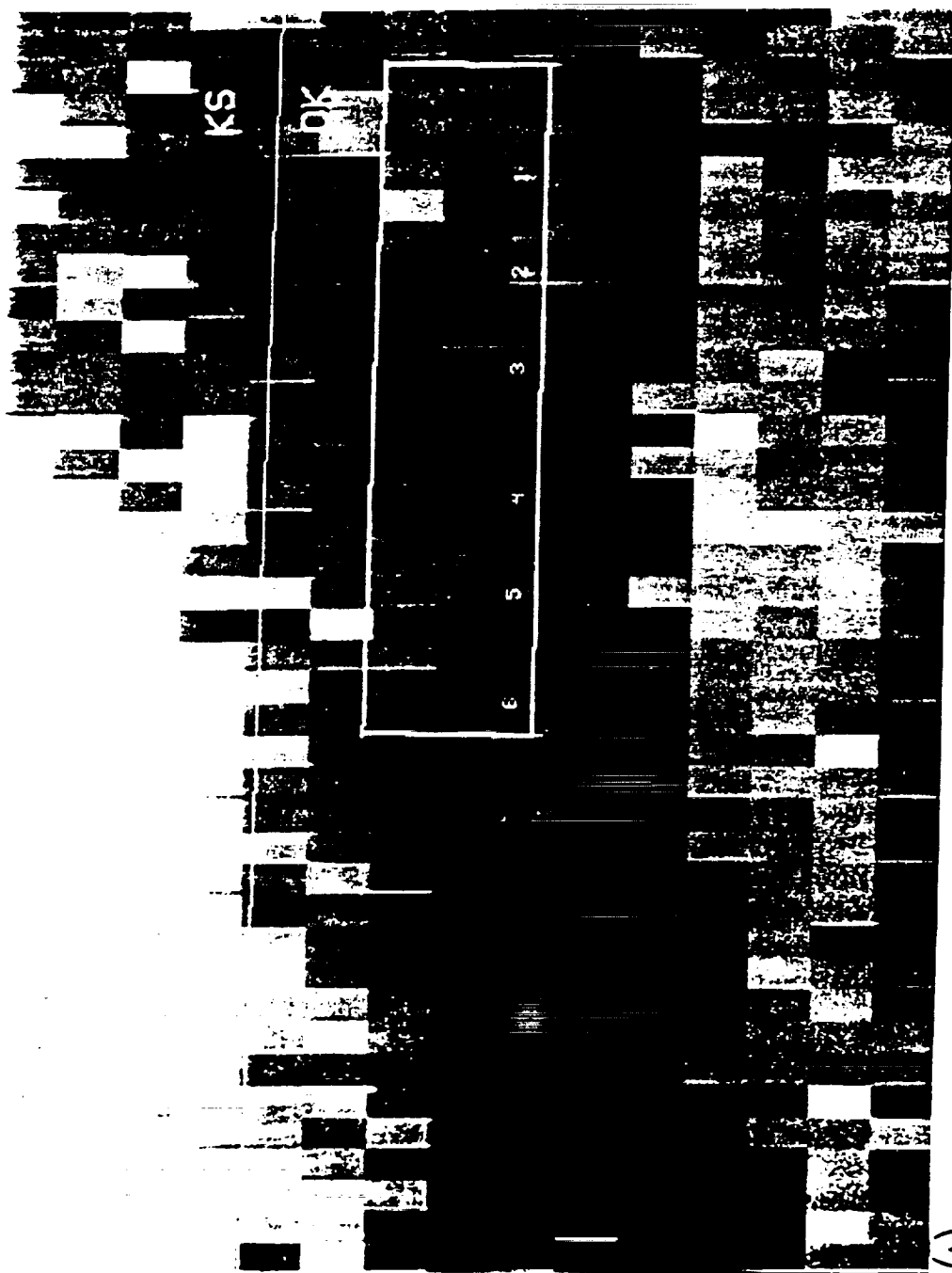


(B)

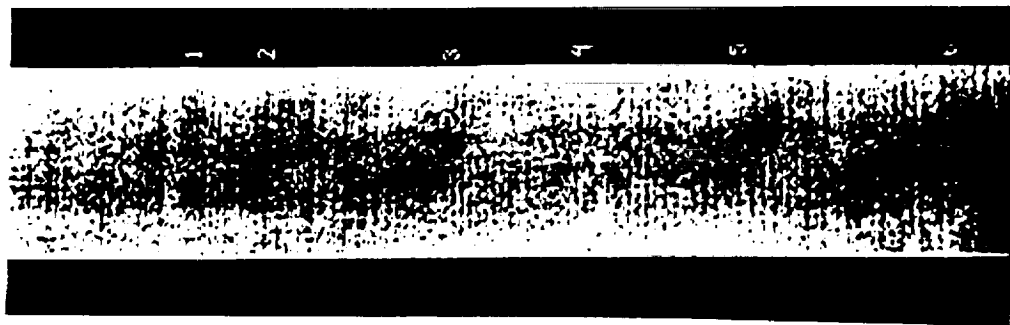


(A)

Fig. 4a. Enhanced VAS water vapor image with the MAMS flight track superimposed for 18 May 1985 at 1701 GMT.  
 Fig. 4b. Corresponding MAMS 6.3 micron enhanced image gathered in flight from G to H on 18 May 1985 at 1707 GMT.



(A)



(B)

Fig. 5a. Magnification of 4a showing single pixel variation along flight track E to F.  
 Fig. 5b. Corresponding MAMS data covering the boxed area of 5a. Six comparable water vapor gradient features are labeled.

DETECTION OF MOUNTAIN-INDUCED MESOSCALE  
WAVE STRUCTURES WITH HIGH RESOLUTION MOISTURE IMAGERY

Gary J. Jedlovec  
CIMSS, Univ. of Wisc.  
Madison, Wisc.

W. Paul Menzel  
NOAA/ASPP  
Madison, Wisc.

Gregory S. Wilson  
NASA/MSFC  
Huntsville, Al.

Robert J. Atkinson  
General Electric Co.  
Huntsville, Al.

1. INTRODUCTION

Radiosonde observations near the surface and aloft often detect pressure, temperature, and wind patterns associated with large scale atmospheric wave features which govern our daily weather conditions. The detection of small scale waves such as gravity and buoyancy oscillations however, usually require special observations to measure the perturbations directly. These waves need not always be measured or sensed directly and their observable signatures (i.e., clouds) can be detected in visible photography or satellite imagery.

The detection of mountain and lee wave structures is often done by observing cloud signatures in regions where vertical oscillations are forced by terrain. Satellite observations of these small scale clouds are possible with high resolution visible sensors. Direct observation of wind and thermodynamic parameters is achieved by instrumented aircraft, lidar, and radar measurements. From these observations, quantitative information is available about mountain and lee waves, their formation and three dimensional structure. However, because a moist environment is not necessary, many wave features may go undetected by these conventional measurements because of the absence of clouds.

During one of the flights of the Multispectral Atmospheric Mapping Sensor (MAMS) on a NASA U2 high altitude aircraft in 1985, wave features were found in water vapor channel imagery in close proximity to the Sierra Nevada mountains of California (Fig. 1). Visible channel imagery from the flight was examined for cloud features but none were found. This paper presents evidence that the waves in the imagery reflect changes in the vertical temperature and moisture distribution produced by the vertical oscillations. These features on the downwind or lee side on the mountains are called lee waves.

2. BACKGROUND

2.1 Instrument Characteristics

The MAMS is a multispectral scanner capable of producing high resolution imagery in visible and infrared bands with detailed spectral resolution. Table 1 summarizes the characteristics of the instrument and its spectral bands. The MAMS is flown on a NASA U2/ER2 at an altitude of 20km providing a resolution cell of 50-100m on the ground.

Table 1

MAMS: The Multispectral Atmospheric Mapping Sensor

Provides high resolution visible and IR scanning capabilities from a high altitude aircraft platform.

Scan rate	6.25 or 12.50 rps
Instantaneous field-of-view	2.5 or 5.0 mrad
Ground resolution (nadir, 19.8km)	50m or 100m
Total field-of-view	86°
Roll correction	+15°
Calibration sources	IR, 2 controllable bbs
Pixels per scan line	716

Spectral Bands

Channel	Wavelength (microns)	Spectral Region	Single Sample Noise(1) 2.5/5.0@6.25rps
1	.42 - .45	blue	1.0
2	.45 - .52	blue/green	.5
3	.52 - .60	green	.4
4	.60 - .62	yellow/orange	.5
5	.63 - .69	red	.5
6	.69 - .75	red/near IR	.4
7	.76 - .90	near IR	.4
8	.90 - 1.05	near IR	.4
9	6.20 - 6.90	water vapor	.40/.20
10	10.32 - 12.02	window (cold)	.15/.10
11	10.32 - 12.02	window (warm)	.15/.10
12	12.20 - 12.56	water vapor	.75/.40

(1) NEAT (mw/ster/m<sup>2</sup>/cm<sup>2</sup>) for 1-8, NEAT (°C) for 9-12.

The width of the entire cross track field-of-view is 40km, providing detailed resolution over a relatively large area.

Eight channels of the instrument are used to separate the visible and near-infrared radiation into narrow bands which sense reflected solar energy from the earth's surface and clouds. The three infrared channels (one of which is redundant) cover selected regions where infrared emission from the earth and atmosphere are of interest. These bands

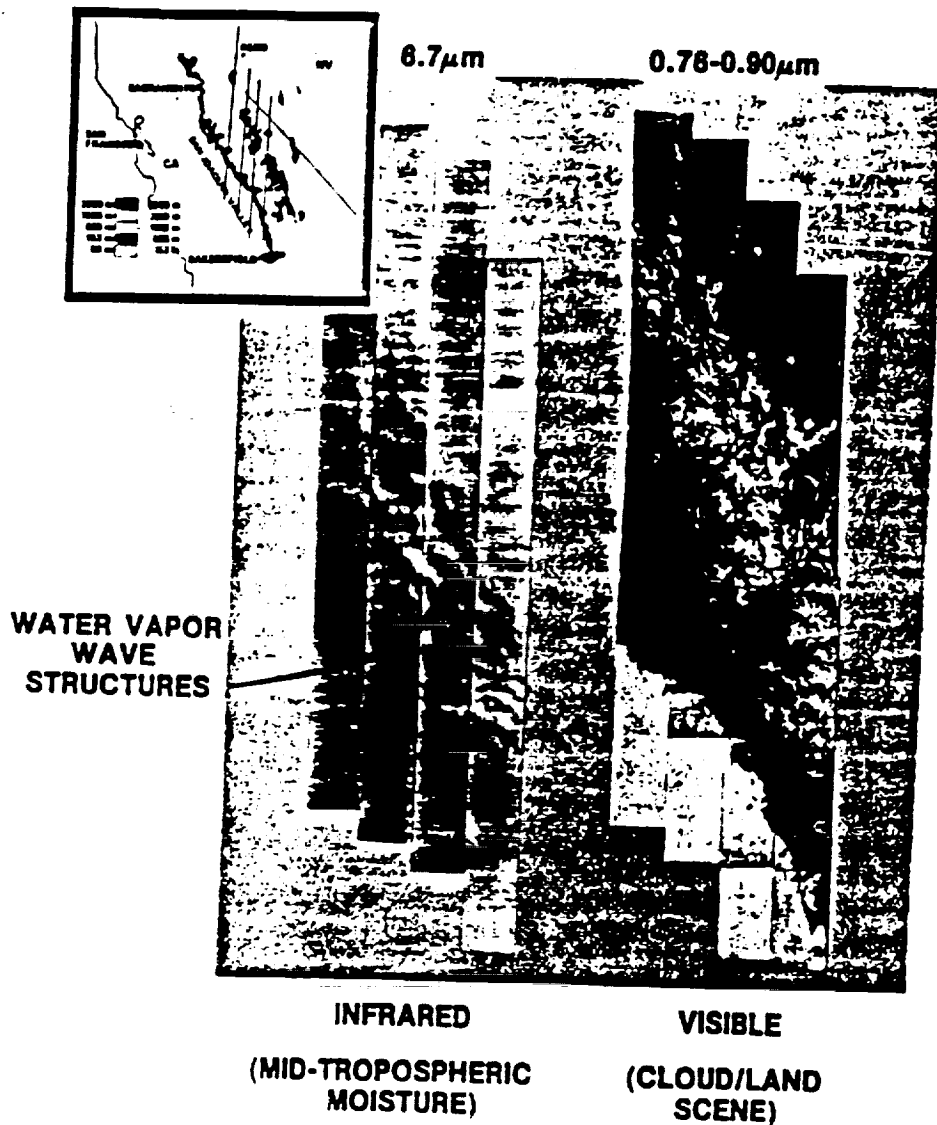


Figure 1. MAMS water vapor and visible channel composite imagery from four adjacent flight tracks on 22 January 1985 from 1942-2109 GMT. The inset shows the major terrain features of the Sierra Nevada mountains over which the imagery was collected.

include the mid-tropospheric (channel 9, 6.5 microns) and low-tropospheric (channel 12, 12.3 microns) water vapor region, and a window region (channel 10/11, 11 microns) where the atmosphere is relatively transparent. The 11 and 12 micron bands form what has become known as the split window channels (Chesters *et al.*, 1983). Further details about the instrument and spectral bands may be found in Jedlovec *et al.* (1986).

### 2.2 Structure of Lee Waves

Stationary waves such as mountain or lee waves are a local phenomena which may have significant effect on local weather conditions because of their associated cloud patterns and wind distributions. They may also feedback to the larger scales of motion. The presence of either mountain or lee waves

is due to vertical oscillations of air parcels as air is forced over the mountain. Mountain waves usually consist of one vertical oscillation of the flow pattern between two mountain peaks and are mainly governed in size by the spacing of the ridges. Lee waves, although forced by mountains, are not restricted in size to one or two vertical oscillations as with the mountain waves. In fact, the overshooting of the downward flow (the restoring force is gravity) on the lee side of the obstacle produces vertical oscillations which may extend for many wavelengths downstream.

The water vapor image in Fig. 1 shows wave structures in the lee of the Sierra Nevada mountains. Three or four waves are discernable, each having an estimated wavelength of 15-20km. The waves extend away from the face of the mountain range for about 70km and along the face for at least

120km. The waves appear somewhat irregular, possibly due to variations in the mountain peaks, tangential distortion from the scanner geometry (Jedlovac et al., 1986), limb brightening (due to increased water vapor path length at the edges of the flight track), as well as other unknown causes.

The nature of the vertical oscillation producing lee waves was studied in detail by Brunt(1927) who derived a set of equations which can be used to describe this flow pattern. From Brunt's work, a simple vertical oscillation in the atmosphere has a period given by

$$\tau = \frac{2\pi}{\left[\frac{g}{T}(\Gamma - \gamma)\right]^{1/2}} \quad (1)$$

where

- $\gamma$  is the environmental lapse rate,
- $\Gamma$  the dry adiabatic lapse rate,
- $g$  the gravitational acceleration, and
- $T$  the environmental temperature.

An air parcel moving horizontally with a velocity of  $v$  and under this vertical oscillation will complete one cycle over a distance of

$$\lambda = v\tau = \frac{2\pi v}{\left[\frac{g}{T}(\Gamma - \gamma)\right]^{1/2}} \quad (2)$$

Upon examining this equation, it becomes apparent that the horizontal wavelength ( $\lambda$ ) is governed by the wind speed and atmospheric stability. Strong winds and low stability favor long wavelengths, while weak winds and strong stability favor shorter ones.

A number of investigators have studied lee waves by observing their visible signatures and with direct measurements of temperature and wind velocity. Atkinson (1981) presents a fairly extensive review of this research. The characteristics of these waves vary from occurrence to occurrence but representative values are presented below. The wavelengths of lee waves range from 2-70km but most occurrences are in the range of 5-20km. The wavelengths tend to increase with height and seem to be related to the mean wind speed. Corby (1957) performed a linear regression of wind speed on wavelength and suggested that a high enough correlation existed for the wavelength to be determined from the wind speed alone.

Another feature which is of interest is the wave amplitude, defined as the vertical distance between the peak and trough of a streamline. This is more difficult to determine from the cloud itself and requires a number of special measurements of the wind field. From the available empirical data, these wave amplitudes are typically about 1km but amplitudes of 7km have been measured. The larger amplitudes may occur when the wavelength closely matches the size of the obstacle forcing the wave.

From these studies, it appears that two parameters control the appearance and size of lee waves: namely, stability and wind. Of course the obstacle (mountain) is necessary to initiate the vertical oscillation and may have some control over the wave amplitude. Stability and wind are also important parameters in (1), however, the importance of stability in determining wavelength seems less important than indicated by (2). A typical environmental temperature and wind profile would

consist of layers of varying stability and an absence of horizontal wind shear. In the lowest layer, the atmosphere would be neutral with a strong layer of stability aloft. This stable layer is necessary for the formation of the waves and should occur near the level of the mountain peak. A layer of weaker stability usually exists above this level. The flow should be perpendicular to the mountain at all levels and increase in speed with height. Significant horizontal shear reduces the likelihood for the development of lee waves.

### 2.3 Atmospheric Conditions

In the previous section, the atmospheric conditions required for the development of lee waves were summarized. Although they are local conditions, they are governed by the large scale atmospheric patterns. Thus, a discussion of the large scale features on 22 January 1985 corresponding to the MAMS observations is necessary. The upper air data (Fig. 2) exhibited a pronounced ridge of high pressure over the eastern Pacific ocean and over the northwestern portion of the U. S. A trough was positioned over the central part of the country with a portion of it hanging back into Utah and the southern portions of Nevada and California. This set up a prevailing flow pattern from the northeast over such of the Sierra Nevada mountains.

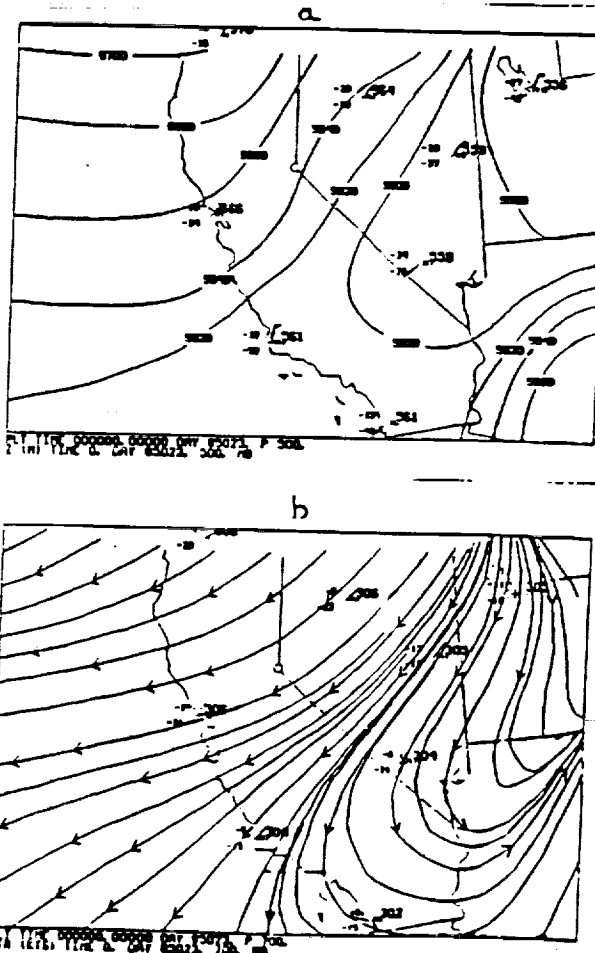


Figure 2. a) 500mb rawinsonde station plots and height analysis, and b) 700mb plots and streamlines for 23 Jan 1985 at 0000 GMT. Plots and analyses are in their standard units.

The region of interest (the Sierras) is in a data void region of the rawinsonde observing network. However, since only 3h difference exists between the MAMS and radiosonde observations, and given the stationarity of the weather systems, a reasonable estimation of the temperature, moisture, and wind profile may be available from the upwind sites. For this reason, data from two Nevada locations is presented in Fig. 3. A moderate to strong inversion exists around 700mb in both soundings. The atmosphere is quite dry above and below this level. The nearly saturated layer at the level of the inversion indicates a shallow layer of clouds. Clouds are not observed over the Sierras so the actual dewpoint will be somewhat colder. The winds are weaker at 72486 but both profiles indicate flow from the northeast without much directional shear with height. From these diagrams, it seems reasonable to assume that conditions would be favorable for lee waves over the Sierras.

### 3. DISCUSSION

Although Fig. 1 was briefly discussed in previous sections, further discussion seems appropriate at this time.

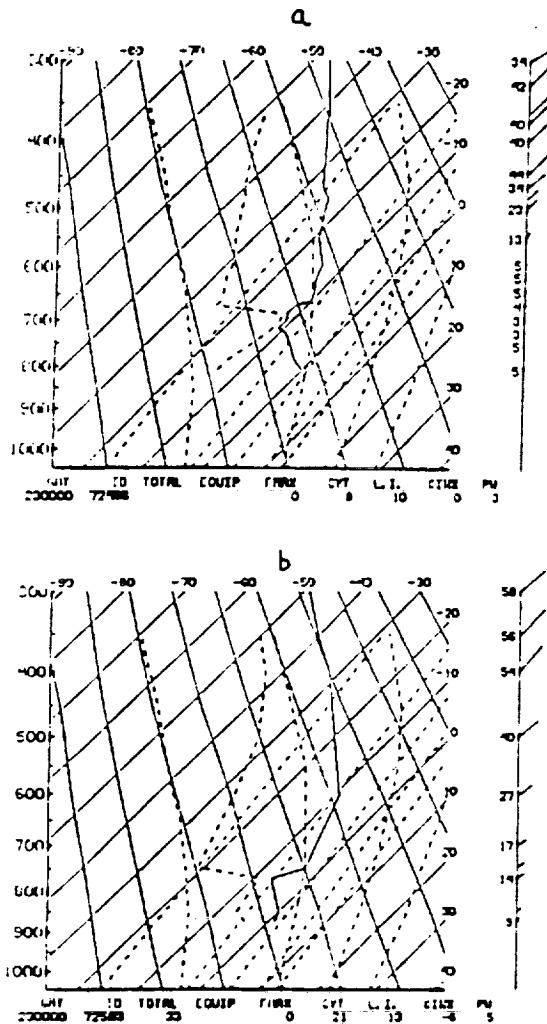


Figure 3. Skew-T-Log-P diagrams for two Nevada rawinsonde sites. a) 72486, and b) 72583 at 0000 GMT 23 Jan 1985. Winds are plotted in knots.

The MAMS 6.5 micron and visible/near-infrared channel imagery is displayed from four adjacent flight tracks on 22 January 1985. The data were collected from 1942-2109 GMT over the plateau region of Nevada, the Sierra Nevada mountains and the central valley of California as indicated by the inset map. The peaks of the Sierras climb to about 4000m and drop sharply to the southwest. Each flight track is about 40km wide making the entire ground distance of the west-east extent 160km. The north-south extent is roughly 400km. For display purposes, the resolution has been degraded to about 400m.

Many very small scale features are apparent in the water vapor imagery. In the center of this imagery, alternating bright (cold/moist) and dark (warm/dry) features exist in wave-like patterns. They are orientated in a northwest-southeast direction parallel to the mountains. It is not possible to determine the position of the waves with respect to the position of the mountains from this image alone. The accompanying flight tracks of visible data capture the cloud/land features at the same instant as the water vapor imagery. Therefore this data can be overlaid and used to determine the exact position of the waves. Several landmarks are visible in the scene, the best being the quasi-circular Lake Mono in the right hand flight track. The bright regions in the lower portion of the visible image are fog and low clouds over the central valley. The bright areas in the center represent snow in the mountains above the 2400m level. Thus the snow region can be used to outline the major mountain features. From this and the terrain map, it is clear that most of the water vapor wave features reside on the downwind side of the mountains where surface elevations are below 2000m. It should also be noted that no clouds are present in the visible imagery over this region.

The estimated wavelengths of these waves (described in section 2.2) can be compared to that obtained from (2) or estimated from the mean tropospheric wind speed. The environmental lapse rate, temperature, and wind speed used in (2) is somewhat arbitrary. A value of  $\gamma$  of  $0^\circ\text{K}/\text{km}$  ( $T=250^\circ\text{K}$ ), and  $V$  of 10 m/s, yields 3.2 km, a rather short wavelength. Since the wave structures occupy more than a single level in the vertical, it may be more appropriate to use values representative of a layer of the atmosphere. Using values from the 800-400mb layer ( $T=250^\circ$ ,  $\gamma=6.5$ , and  $V=20$ ), a wavelength of 10.7 km is obtained. This is somewhat less than the estimated length of 15-20km. As previously mentioned, Corby (1957) used an empirical relationship between wind speed and wavelength with a good correlation. The linear fit of his data (wavelength versus wind speed) produced a slope of roughly 0.45. For a mean environmental wind speed of 20m/s, a wavelength of 9km is predicted. In either case, a stronger wind speed would be needed to match the one estimated from the water vapor imagery. Considering that the actual wind profile over the Sierras is somewhat uncertain, these calculations are relatively close to the estimates from the observed data.

It is much more difficult to estimate the amplitude of these lee wave features without direct in situ measurements. However, the next section describes an approach to estimate the amplitude by simulating the MAMS water vapor channel radiances.

#### 4. RADIATIVE TRANSFER SIMULATIONS

The water vapor image presented in Fig. 1 represents energy emitted by atmospheric water vapor somewhere in the mid-troposphere. The procedure to determine this layer or level has been the subject of investigation by researchers for many years. In the case of cloud height determinations using window channel radiances, the altitude of the cloud can be estimated by comparing the measured blackbody temperature to a local rawinsonde. The water vapor signal does not come from a single level but actually a layer of the atmosphere (Jedlovec, 1984), and depends on the amount, vertical distribution, and temperature of the vapor itself. It is unclear whether blackbody temperatures in this channel can be used directly to infer a mean height from which the signal originates.

In an attempt to estimate the amplitude of the lee waves observed in Fig. 1, several approaches were considered. Table 2 presents the observed blackbody temperatures measure in the peaks and troughs of the lee wave features. Typical values indicate a 6° temperature difference from the peak to the trough of the wave. It is difficult to use one of the soundings in Fig. 3 to directly infer the levels of the peak and trough of the lee waves. It may be reasonable to assume that the level of the neutral point of the wave is 246°K (-27° C) and the peak and trough occurring at the level of their measured temperature (Table 2), however. If this is done, the estimated wave amplitude is about 1km. While this is consistent with the amplitudes of a typical lee wave, it depends heavily on the lapse rate of the sounding used. Because of the lifting of the lower level inversion by the mountains, a smaller lapse rate of temperature probably existed over the Sierras, producing a greater vertical amplitude for the lee wave.

Another approach to estimate the lee wave amplitude used a composite of the two soundings in Fig. 3. From the composite sounding, MAMS water vapor channel radiances were simulated (McMillan and Fleming, 1976; Fleming and McMillan, 1977; and Wienreb and Neuendorffer, 1973). In order to obtain a representative profile in both the peak and trough of the waves, the inversion layer near 700mb and the accompanying moisture distribution were raised and lowered adiabatically in increments of 1 km. Blackbody temperatures were computed from

Table 2

Observed and simulated blackbody temperatures for the lee waves. Units are in degrees°K.

Observed Blackbody Temperatures		
	mean	extreme
Wave peak	243.5	242.0
Wave trough	249.5	251.0
Simulated Blackbody Temperatures (4km)		
Wave peak	243.9	
Wave trough	249.5	

the channel radiances. Temperature differences of 6°K were observed (similar to the measure values from Fig. 1) as well as the appropriate blackbody temperatures when the inversion was at 2 and 6km level for the trough and peak, respectively. This 4km vertical amplitude, while larger than most lee wave amplitudes, is more consistent with the level of the mountain peaks which produce them.

#### 5. CONCLUSIONS

The above work has presented evidence for the existence of lee waves in the absence of clouds using high resolution MAMS moisture imagery. Although verifying measurements do not exist, an evaluation of wind profiles and stability in the surrounding region support the existence of these waves. Estimations of the horizontal wavelengths of the observed lee wave features are not inconsistent with those from previous studies. The estimated vertical amplitude, although less certain, seems realistic for the setting. Further work is necessary to more accurately determine this vertical amplitude.

Acknowledgements. This work was performed in part by the lead author while affiliated with several organizations. Support from the Universities Space Research Association through a NASA contract and from the Space Science and Engineering Center at the University of Wisconsin was appreciated. Mr. John Arvesen of NASA/Ames and Jeff Myers also contributed in the collection and data reduction of the MAMS flight data. Their efforts are also appreciated.

#### REFERENCES

- Atkinson, B. W., 1981: Meso-scale Atmospheric Circulations. Academic Press, New York, 495p.
- Brunt, D., 1927: The period of simple vertical oscillations in the atmosphere. Q. J. Royal Meteor. Soc., **53**, 30-31.
- Chesters, D., L. W. Uccellini, and W. D., Robinson, 1983: Low-level water vapor fields from the VISSR Atmospheric Sounder (VAS) "split window" channels. J. Climo. Appl. Meteor., **22**, 725-743.
- Corby, G. A., 1957: Preliminary study of atmospheric waves using radiosonde data. Q. J. Royal Meteor. Soc., **83**, 49-60.
- Fleming, H. E., and L. M. McMillan, 1977: Atmospheric transmittance of an absorbing gas. 2. A computationally fast and accurate transmittance model for slant paths at different zenith angles. Appl. Opt., **16**, 1366-1370.
- Jedlovec, G. J., W. P. Menzel, G. S. Wilson, R. J. Atkinson, and J. Arvesen, 1986: The Multi-spectral Atmospheric Mapping Sensor (MAMS): Instrument description and data quality. (in press).
- Jedlovec, G. J., 1984: Mesoscale analysis of 6.7µm image data from the VISSR Atmospheric Sounder (VAS) for several case studies. Preprints, Conf. on Satellite/Remote Sensing and Appl. AMS, Boston, 185-190.
- McMillan, L. M., and H. E. Fleming, 1976: Atmospheric transmittance of an absorbing gas: A computationally fast and accurate transmittance model for absorbing gases with constant mixing ratios in inhomogeneous atmospheres. Appl. Opt., **15**, 358-363.
- Wienreb, M. P., and A. C. Neuendorffer, 1973: Method to apply homogeneous-path transmittance models to inhomogeneous atmospheres. J. Atmos. Sci., **30**, 662-666.

Rough Draft

OMIT  
TO  
END

A NOTE ON THE ABSOLUTE CALIBRATION OF THE HIS AND MAMS INSTRUMENTS

C. C. Moeller, W. P. Menzel, and W. L. Smith

Cooperative Institute for Meteorological Satellite Studies  
University of Wisconsin - Madison  
1225 West Dayton Street  
Madison, WI 53706

1. INTRODUCTION

Accurate absolute calibration of radiometric data is an important component of useful remotely sensed data. Lack of absolute accuracy in the past has hindered the effectiveness of satellite radiances in budget studies, data assimilation efforts, and climatology studies, which can suffer from long term temporal instability of the calibration. Because of this problem, many efforts confine conclusions to relative variations only (e.g. Chesters et al. 1983). It is desirable that the absolute calibration of new and future satellite platform instruments be evaluated. Evaluation may be made by directly comparing collocated fields of view between two (or more) instruments. While a favorable comparison of this sort does not necessarily imply good absolute calibration, agreement between independent instruments tends to indicate that they are fairly well calibrated.

The High resolution Interferometer Sounder (HIS) and the Multispectral Atmospheric Mapping Sensor (MAMS) can be directly compared with each other for absolute calibration accuracy. The MAMS contains 3 infrared channels that are simulated by convoluting HIS high spectral resolution radiances with the MAMS spectral response functions. HIS and MAMS flew together during the COoperative Huntsville Meteorological EXperiment (COHMEX) during the summer of 1986. This note presents the

results of the absolute calibration study between MAMS and HIS  $6\mu\text{m}$ ,  $11\mu\text{m}$  and  $12\mu\text{m}$  data of June 15, 1986.

## 2. INSTRUMENT DESCRIPTIONS

### A. MAMS

The MAMS instrument is an aircraft borne 12 channel spectrometer which collects 100m resolution data across a swath of about 37 km. During COHMEX, the MAMS configuration collected 8 bit precision data in 8 visible and 4 infrared channels which include  $6\mu\text{m}$ ,  $11\mu\text{m}$ , and  $12\mu\text{m}$  bands similar to those of the VISSR Atmospheric Sounder (VAS) (Menzel et al. 1986). The infrared data is absolutely calibrated on each scan by viewing two onboard blackbodies of known temperature. Calibration noise is reduced through multiple viewings of each blackbody during a given scan. A linear relationship between blackbody radiance and digital count values is assumed. MAMS has been extensively discussed in Jedlovec et al. (1989).

### B. HIS

The airborne High-resolution Interferometer Sounder (HIS) is a Michelson interferometer which measures thermal emission from the earth's surface and clouds and atmospheric constituents in longwave (151m), midwave (6.71m) and shortwave (4.31m) bands (Fig. 1). Table 1 (Smith et al. 1983) summarizes the characteristics of the HIS aircraft instrument. With its high spectral resolution ( $< 1 \text{ cm}^{-1}$ ), HIS has several thousand spectral channels; many more than the ten or twenty spectral channels on current filter radiometers such as VAS and HIRS/2.

Detection in each of three spectral bands is performed using arsenic-doped silicon detectors contained in a single detector/dewar assembly. Three detector/filter systems are used to optimize the signal-to-noise ratio of the observations throughout the broad spectral region measured. High emissivity, temperature controlled reference blackbodies are used for an absolute calibration. Every two minutes of HIS observations consist of four cold blackbody (CBB) views, four hot blackbody (HBB) views, and twelve earth views. The four blackbody views are averaged for each blackbody and used for the calibration of the earth views. The basic approach for determining absolute radiances from the HIS nadir-viewing Michelson interferometer is the same as that used for filter radiometers and has been used successfully for other interferometric applications (Revercomb et al. 1988). The HIS is designed to yield an output which is linear in the incident radiance for all channels in the optical path difference of the instrument. The averaged HBB and CBB temperatures and counts determine the slope and offset which define the linear instrument response at each wave number (Huang 1989). The slope,  $S_t$ , is given by

$$S_t = \frac{V_t^E - V_t^C}{V_t^H - V_t^C}$$

where  $V_t^E$  is the count value in the earth scene of channel  $t$ , and  $V_t^H$  and  $V_t^C$  are the count values in the HBB and CBB scene respectively of channel  $t$ . The earth scene radiance at channel  $t$ ,  $R_t^E$ , is

$$R_t^E = S_t * (B_t^H - B_t^C) + B_t^C$$

where  $B_t$  is the Planck function of channel  $t$ . More detailed and complete calibration procedures concerning the effects of phase ambiguity, finite field of view, and other instrument effects on radiance calibration may be found in Revercomb et al. (1988). Figure 2 shows the noise spectra for the June 15, 1986 of COHMEX. In general, good signal-to-noise ratios have been realized in COHMEX HIS flights, with an average noise level of 0.2 - 0.3 K for all three bands.

### 3. HIS AND MAMS COMPARISONS

#### A. COHMEX data set

The MAMS and HIS instruments were flown repeatedly during COHMEX, which was conducted during the summer of 1986 over a portion of the mid-eastern United States. On June 15, MAMS and HIS were flown together from 1730 GMT to 2100 GMT on the NASA U2 aircraft over the central Tennessee / northern Alabama region. The flight path is shown in Figure 3. The flight region, a region of highly variant land uses and types, was partially obscured by a scattered field of low level cumulus. For further information on COHMEX and on the weather of June 15, the reader is referred to Williams et al. (1987).

#### B. Comparison procedure

In order to properly compare the MAMS and HIS radiances the data sets were equated in factors of footprint registration and size, time of observation, viewing angle, and spectral response of channels. Since MAMS and HIS flew together on June 15, footprint registration, observation time, and viewing angle considerations were easily accounted for. However, because of different data recording rates, it is unlikely

that the two data sets are exactly collocated in time and space. It is estimated though that collocation errors are less than .5 km, which is less than a quarter of a single HIS field of view. Instrument resolution differences were accounted for by averaging the observed MAMS data over the size of a HIS 4 x 2 km averaged footprint (2 fovs). The HIS and MAMS instrument impulse functions were both assumed to be symmetrical. To equate the spectral channels, MAMS spectral response functions were convoluted with two averaged HIS fov (4 x 2 km) radiances to produce "MAMS equivalent" channels from the HIS radiances. MAMS spectral response function data is given at 1 wavenumber resolution, comparable to the HIS spectral resolution. The comparison was then made between the spatially averaged MAMS radiances and the HIS radiances that had been used to produce "MAMS equivalent" channels.

C. Results of calibration comparison

The results of comparing the MAMS and HIS equated radiances are shown in Figure 4 for the 6 $\mu$ m, 11 $\mu$ m and 12 $\mu$ m MAMS channels. Statistics of the comparisons are shown in Table 2.

---

Table 2. - MAMS/HIS comparison statistics for June 15, 1986 (354 collocations).

<u>channel</u>	<u>bias(k)</u>	<u>rms(k)</u>	<u>correlation</u>
6 $\mu$ m	-0.03	0.88	0.98
11 $\mu$ m	0.93	3.30	0.94
12 $\mu$ m	-2.41	3.48	0.95

---

High correlations in Table 2 indicate excellent agreement in relative variation between the two instruments. This lends credibility to the

collocation accuracy between the two instruments. This agreement is easily seen in the  $6\mu\text{m}$  comparison of figure 4 but less so in the  $11\mu\text{m}$  and  $12\mu\text{m}$  comparisons because of the high thermal variability of the scenes. The agreement is more readily apparent in the  $11\mu\text{m}$  and  $12\mu\text{m}$  data when the U2 aircraft flew over a cumulonimbus cloud, causing both the MAMS and HIS temperatures to drop sharply. In the absolute calibration comparison, the  $6\mu\text{m}$  data shows excellent agreement between the two instruments with a total flight bias of only .03 K. The  $11\mu\text{m}$  data also shows good results with a bias of less than 1 K. The absolute calibration of the  $12\mu\text{m}$  data shows less favorable agreement. It is noteworthy that the  $11\mu\text{m}$  and  $12\mu\text{m}$  biases and RMS may be affected by some scene misregistration error, especially when the aircraft went into and came out of turns. In order to test the effect of possible misregistration errors, a filtered data set of comparisons was generated by removing comparisons that exceeded a 5 K threshold difference between the two instruments. This should exclude most misregistered comparisons. The statistics for 269 samples are shown in Table 3.

---

Table 3. - Misregistration filtered MAMS/HIS comparisons for June 15, 1986. (269 samples).

<u>channel</u>	<u>bias(k)</u>	<u>rms(k)</u>	<u>correlation</u>
$6\mu\text{m}$	-0.03	0.78	0.98
$11\mu\text{m}$	1.10	2.05	0.98
$12\mu\text{m}$	-2.27	2.62	0.98

---

The biases of the comparisons are somewhat changed, though not substantially. This indicates that collocation errors are not affecting the bias very strongly, suggesting that collocation errors cancel out.

That the  $12\mu\text{m}$  bias remains significantly larger than the  $11\mu\text{m}$  bias is probably due to the smaller bandwidth and thus noisier data in that channel. The reduction in RMS reflects the removal of the misregistered comparisons. Note that the smallest effect was on the  $6\mu\text{m}$  RMS. This is not surprising since the  $6\mu\text{m}$  spatial variability is relatively weak at small scales, and there was no cloud contamination of the  $6\mu\text{m}$  data. In other words, small scale misregistration errors should not have a significant effect on the  $6\mu\text{m}$  MAMS/HIS comparison. Also note that the  $12\mu\text{m}$  bias now accounts for almost all of the RMS while considerable unexplained RMS remains in the  $6\mu\text{m}$  and  $11\mu\text{m}$  statistics of Table 3. An investigation of MAMS data showed that the calibration "floated" with time in the  $6\mu\text{m}$  and  $11\mu\text{m}$  channels. This probably accounts for the unexplained RMS and is likely also present in the  $12\mu\text{m}$  MAMS data though it may be masked by the noisier nature of the  $12\mu\text{m}$  data. This calibration float is an undesirable characteristic of the MAMS June 15, 1986 data, however improvements to the instrument since 1986 have probably improved the performance significantly (Jedlovec et al. 1989). Also, since the calibration float introduces an uncertainty to the bias, the RMS (which includes both calibration float and true bias) serves as an upper limit to the true bias. Thus, in the worst case (and assuming that none of the remaining RMS of Table 3 is due to misregistration), the bias of the  $11\mu\text{m}$  comparison might approach 2 K (comparable to  $12\mu\text{m}$  bias) while the  $6\mu\text{m}$  bias is still less than 1 K.

This analysis suggests that the biases of Table 1 are the result of absolute calibration disagreement between the two instruments. This calibration disagreement may be caused by the choice of blackbody temperatures for data collection. MAMS blackbody temperatures were

approximately 243 K and 273 K (HIS were approximately 240 K and 300 K), thus forcing a significant linear extrapolation to the thermal scene temperatures (-300 K) of the MAMS 11 $\mu$ m and 12 $\mu$ m data on June 15. Linear extrapolation errors for AVHRR 11 $\mu$ m data exceed 1 K when scene temperatures exceed the warm blackbody temperature by 10 K (Lauritson et al. 1979 and subsequent revisions to that document). While an extrapolation correction has not been determined for the MAMS channels, it is suggested that the MAMS/HIS bias is at least partly a function of the choice of blackbody temperatures. On the other hand, the 6 $\mu$ m MAMS data, which is essentially unaffected by cloud cover or substantial small scale thermal variance, requires almost no extrapolation (scene temperatures - 245 K), and thus would be expected to be well calibrated. The HIS cold blackbody being set at 240 K makes the HIS calibration also very reliable in the 6 $\mu$ m region. Thus, of the three compared channels, the 6 $\mu$ m comparison should be the best calibrated, and indeed shows the best results. This result indicates that when blackbody temperatures are set to encompass the expected scene temperature, that good absolute accuracy of calibration is achieved.

#### 4. CONCLUSIONS

An absolute comparison of HIS and MAMS radiances has been performed in an effort to evaluate the absolute calibration of each instrument. While not conclusive, good agreement between the two independent instruments indicates that both instruments are well calibrated. Results show excellent agreement between the 6 $\mu$ m and 11 $\mu$ m data (bias < 1K) with lessor agreement in the 12 $\mu$ m data (bias - 2K).

Bias results suggest that selecting blackbody temperatures close to the expected scene temperatures improves absolute calibration.

## REFERENCES

- Chesters, D., L. W. Uccellini and W. D. Robinson, 1983: Low-level water vapor fields from the VISSR Atmospheric Sounder (VAS) "split window" channels. J. Climate Appl. Meteor., 22, 725-743.
- Huang, H.-L., 1989: An analysis of the characteristics of atmospheric profiles obtained with the High-resolution Interferometer Sounder (HIS). Ph.D. dissertation, University of Wisconsin - Madison, 145 pp.
- Jedlovec G. J., K. B. Batson, R. J. Atkinson, C. C. Moeller, W. P. Menzel, and M. W. James, 1989: Improved capabilities of the Multispectral Atmospheric Mapping Sensor (MAMS). NASA Technical Memorandum 100352, Marshall Space Flight Center, Huntsville, AL. 71pp.
- Lauritson, L., G.J. Nelson, and F. W. Porto, 1979: Data extraction and calibration of TIROS-N/NOAA radiometers. NOAA Technical Memorandum NESS 107, NOAA-NESS, Washington D.C.
- Menzel, W. P., G. J. Jedlovec, and G. S. Wilson, 1986: Verification of small scale features in VAS imagery using high resolution MAMS imagery. Second Conference on Satellite Meteorology/Remote Sensing and Applications, AMS, Boston, 108-111.
- Revercomb, H.E., H. Buijs, H.B. Howell, D.D. Laporte, W.L. Smith, and L.A. Sromovsky, 1988: Radiometric calibration of IR Fourier transform spectrometers : solution to a problem with the High-resolution Interferometer Sounder (HIS). Appl. Opt., 27, 3210-3218.

Smith, W.L., H.E. Revercomb, H.B. Howell, and H.M. Woolf, 1983: HIS - a satellite instrument to observe temperature and moisture profiles with high vertical resolution. Preprints of Fifth Conference on Atmospheric Radiation, AMS, Boston, 9pp.

Williams, S.F., H.M. Goodman, K.R. Knupp, and J.E. Arnold, 1987: Space/COHMEX Data Inventory Document. NASA Tech. Memo. 4006, 480pp.

### CHARACTERISTICS OF THE HIS AIRCRAFT INSTRUMENT

Spectral range ( $\text{cm}^{-1}$ ) :	
Band I	590 - 1070
Band II	1040 - 1930
Band III	2070 - 2750
Field of view diameter (mr) :	
Telescope	100
Interferometer	30
BlackBody reference sources :	
Emissivity	>0.998
Aperture diameter (cm)	1.5
Temperature stability (K)	$\pm 0.1$
Auto-aligned Interferometer :	modified BOMEM BBDA2.1
Beamsplitter :	
Substrate	KCL
Coatings	Ge+Sb <sub>2</sub> S <sub>3</sub>
Maximum Delay (double-sided) (cm) :	
Band I	$\pm 1.8$
Band II & III	+1.2, -0.8
Michelson mirror optical scan rate (cm/s) :	0.6-1.0
Aperture stop (at exit window) :	
Diameter (cm)	4.1
Central obscuration area fraction	0.17
Area ( $\text{cm}^2$ )	10.8
Area-solid angle product ( $\text{cm}^2\text{-sr}$ ) :	0.0076
Detectors :	
Type	Ar doped Si
Diameter (cm)	0.16
Temperature (K)	6

Table 1, characteristics of the HIS aircraft instrument

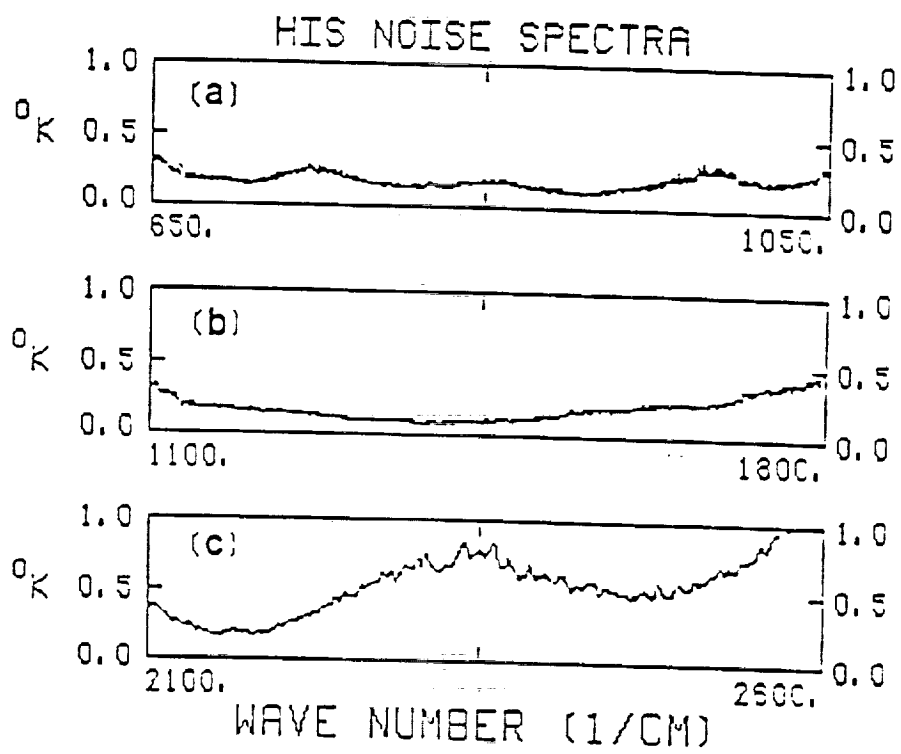


Figure 2, Noise spectrum of HIS (a), band 1; (b), band 2; and (c), band 3.

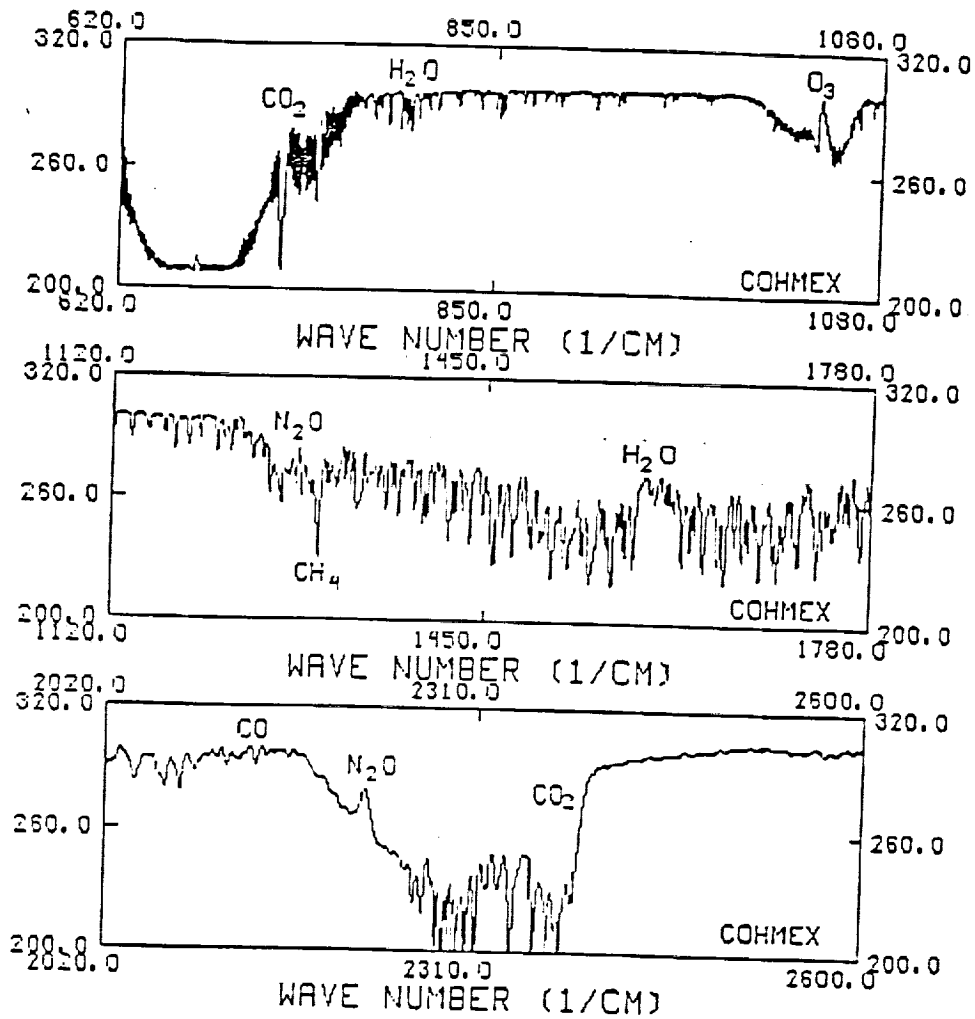
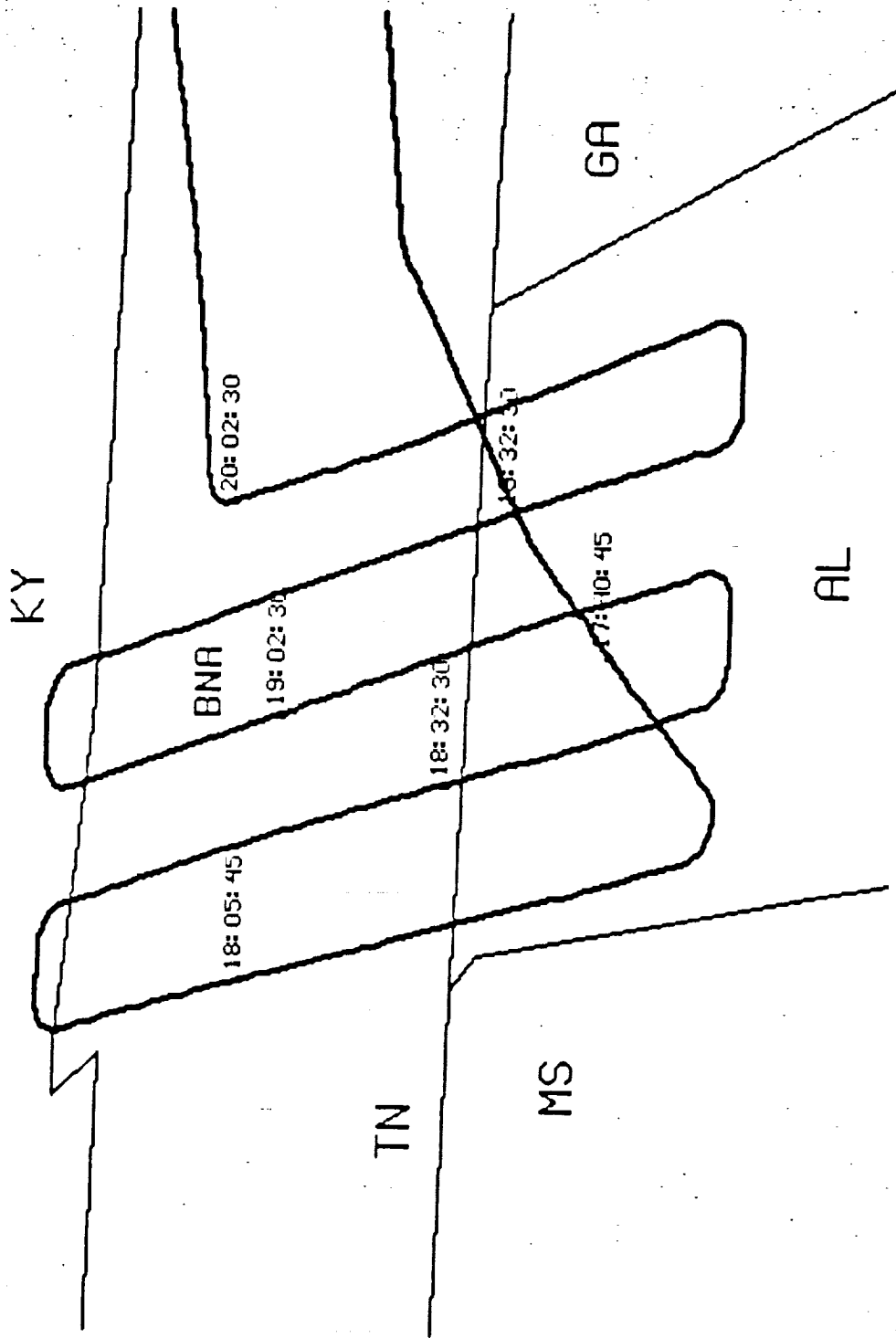


Figure 1, Brightness temperature spectra measured by HIS from NASA U2 aircraft over Huntsville, Alabama on June 15, 1986.

Fig 3 - HIS and MAMS flight path on June 15, 1986  
over the COMEX region. BNA is Nashville, TN



ORIGINAL PAGE IS  
OF POOR QUALITY

Fig 4. - MAMS (dot) and HIS (solid) 6 m comparisons  
entire flight of June 15, 1986.

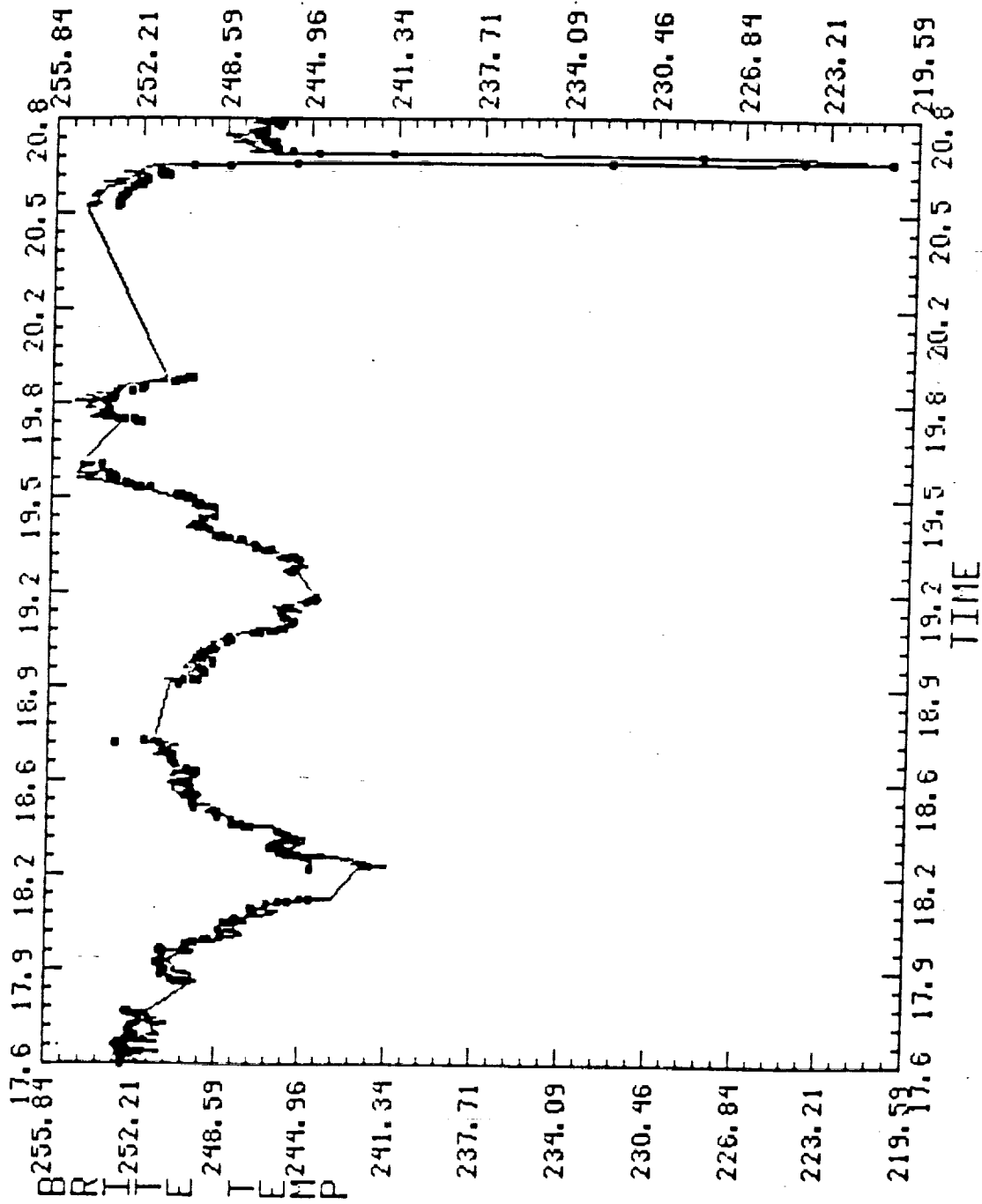


Fig 4. - MAMS (dot) and HIS (solid) 11 m comparisons  
entire flight of June 15, 1986.

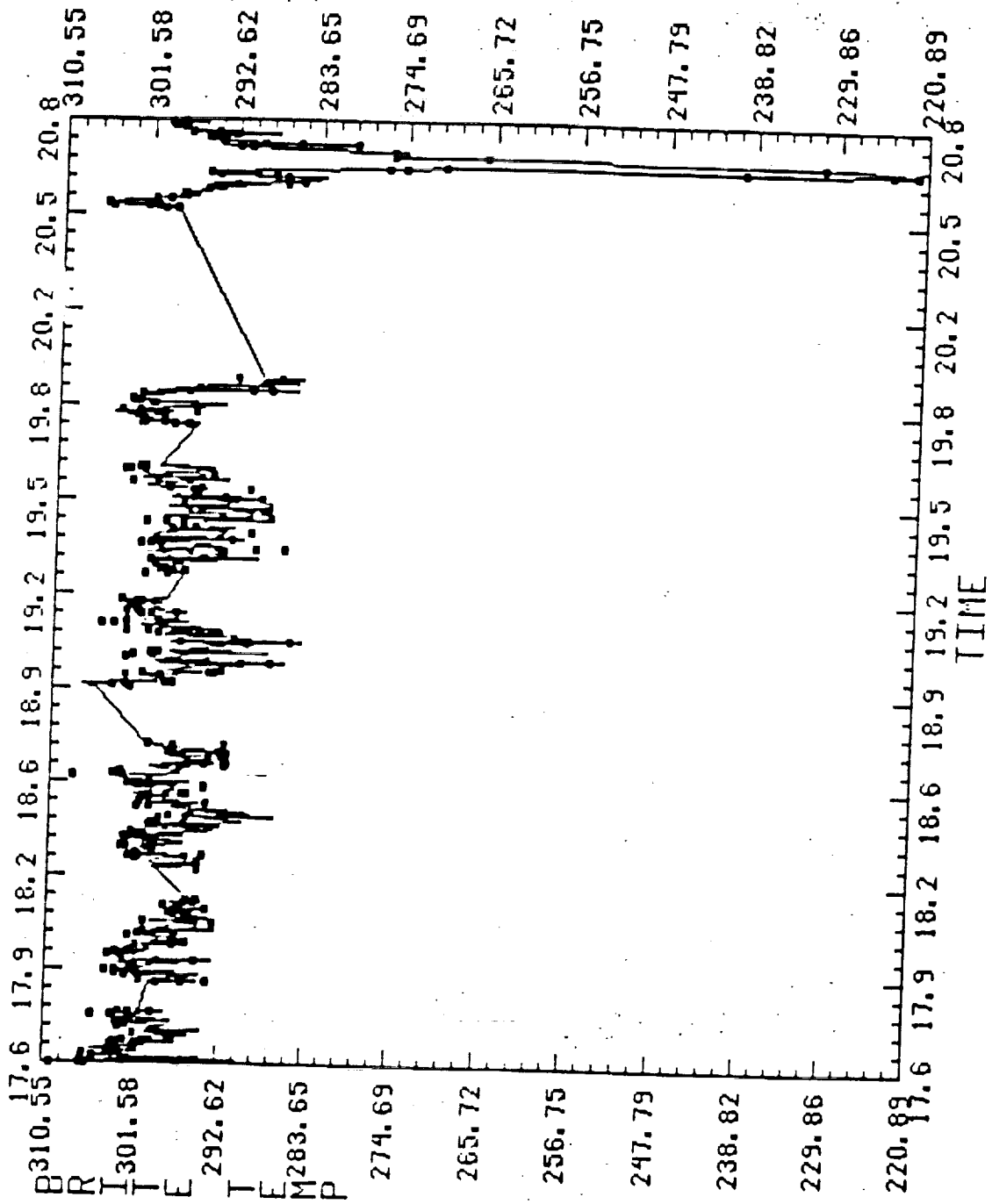


Fig 4. - MAMS (dot) and HIS (solid) 12 m comparisons  
entire flight of June 15, 1986.

